
**Scuola Normale Superiore**

CLASSE DI SCIENZE MATEMATICHE E NATURALI
Corso di Perfezionamento in Fisica della Materia Condensata

Tesi di Perfezionamento

# Hydrodynamics and plasmonics in two-dimensional materials

Candidato:
**Iacopo Torre**

Relatore:
**Prof. Marco Polini**

Correlatore:
**Prof. Alberto Diaspro**

**Anno Accademico 2017-2018**

# Acknowledgments

First of all, I really want to thank my advisor, Prof. Marco Polini, for his guidance and for teaching me a lot of things about physics and research during the last five years.

I would also like to thank all the members of the committee, my co-advisor Prof. Alberto Diaspro, and the external reviewers, Prof. Loredana Casalis and Prof. Francisco Guinea.

A special thank is due to Silvie, for convincing me to start this PhD, and for so many other reasons that would not fit into this page.

During these years I had the real pleasure to work with many wonderful people, among these I would like to mention Dr. Andrea Tomadin, for the many interesting discussion, for his infinite amount of patience in answering computer related questions at every time of day and night, and for carefully revising my Thesis, Dr. Franceso Pellegrino, for being the most fun person to work with, Dr. Ben Van Duppen, for the long discussions about physics and politics, and Dr. Achim Woessner, for sharing with me part of his experimental knowledge, and for all the beers we had together.

Much of this work wouldn't have been possible without intense collaboration with experimental groups, the Manchester University Condensed Matter Group led by Prof. Andre Geim, and the Quantum Nano-OptoElectronics at ICFO led by Prof. Frank Koppens.

I am particularly grateful to Prof. Koppens for hosting me in his group for a research visit.

I am also glad to thank all the people that made my visit in Barcelona such a nice scientific and human experience, in particular (and in totally random order) Marco, Aldo, Alessandro, Nicola, Olena, Marco, David, Peter, Sebastian, Carlotta, Angelo, Nello, Chara, Ivan, Franceso, Gabrielė, Íñigo, Laura, Sotiris, Suchi, Niels, and all the people from the NOE group.

My last years in Pisa would not have been the same without all the friends I met there, Antonella, Marcello, Stefano (I really miss "Buongiornissimo, Kaffe?"), Giacomo, and Michael, my flatmates Alex, Andrea, Azzurra, Tania, Anna and Nico, Marco, Andrea, and all the guys from the CUS Pisa Rugby team.

I also want to thank some very special friends, Alessandro (universally known as "il Brioscina"), Riccardo ("il Cinzia"), Matia ("il Merda"), Valentina, Mauro, Pietro, and Davide ("il Faco").

Last, but not least, I would like to thank my parents Teresa and Silvio (by far the best physics teachers I know), and my brother Michele for their support.

# Abstract

This Thesis is devoted to the study of two different aspects of electron behavior in two-dimensional materials, namely hydrodynamic electron transport and plasmon propagation. The Thesis is structured as follows. In Chapter 1 the main experimental facts that motivated our work on electron hydrodynamics and plasmonics are presented and critically discussed. Chapter 2 contains our main results on hydrodynamic electron transport. After deriving the basic equations of the electron hydrodynamics and discussing their limit of applicability, we use them to quantify the impact of two different transport coefficients, the shear and Hall viscosities of the electron liquid, on steady-state transport. Our results are used to propose experimental protocols that allow an experimental determination of these transport coefficients. Chapter 3 deals with plasmon propagation through inhomogeneous media. We consider three different geometries: an interface between two different materials, a one dimensional perturbation, and a zero dimensional perturbation in an otherwise uniform electron system. We calculate scattering observables for plasmons in these geometries. For the interface geometry we also investigated the presence of plasmonic bound states localized near the interface, while for the second and third geometries we quantify the impact of non-local effects. Chapter 4 presents a theory of chiral plasmons in materials with a non-trivial Berry curvature in the electronic band structure. We firstly employ the results of Chapter 3 to obtain a semi-classical theory of Chiral Berry Plasmons (CBPs) at a generic interface between two materials having different Berry fluxes across the Fermi surface. We then test the impact of different types of screened electron-electron interaction, and of a finite damping rate on the dispersion and lifetime of CBPs.

# List of publications

- **I. Torre**, A. Tomadin, R. Krane, V. Pellegrini and M. Polini. *Electrical plasmon detection in graphene waveguides*, Phys. Rev. B **91**, 081402(R) (2015). Rapid communication.
- **I. Torre**, A. Tomadin, A.K. Geim, and M. Polini. *Nonlocal transport and the hydrodynamic shear viscosity in graphene*, Phys. Rev. B **92**, 165433 (2015). Editors' suggestion.
- D.A. Bandurin, **I. Torre**, R.K. Kumar, M. Ben Shalom, A. Tomadin, A. Principi, G.H. Auton, E. Khestanova, K.S. Novoselov, I.V. Grigoreva, L.A. Ponomarenko, A.K. Geim and M. Polini. *Negative local resistance caused by viscous electron backflow in graphene*, Science **351**, 1055 (2016).
- I. Aliaj, **I. Torre**, V. Miseikis, E. di Gennaro, A. Sambri, A. Gamucci, C. Coletti, F. Beltram, F.M. Granozio, M. Polini, V. Pellegrini, S. Roddaro. *Tunnel and electrostatic coupling in graphene-$LaAlO_3/SrTiO_3$ hybrid systems*, APL Materials **4**, 066101 (2016).
- F.M.D. Pellegrino, **I. Torre**, A.K. Geim and M. Polini. *Electron hydrodynamics dilemma: Whirlpools or no whirlpools*, Phys. Rev. B **94**, 155414 (2016).
- A. Woessner, Y. Gao, **I. Torre**, M.B. Lundeberg, C. Tan, K. Watanabe, T. Taniguchi, R. Hillenbrand, J. Hone, M. Polini and F.H.L. Koppens. *Electrical $2\pi$ phase control of infrared light in a 350-nm footprint using graphene plasmons*, Nat. Photonics **11**, 421 (2017).
- **I. Torre**, M.I. Katsnelson, A. Diaspro, V. Pellegrini and M. Polini. *Lippmann-Schwinger theory for two-dimensional plasmon scattering*, Phys. Rev. B **96**, 035433 (2017).
- F.M.D. Pellegrino, **I. Torre** and M. Polini. *Non-local transport and the Hall viscosity of two-dimensional hydrodynamic electron liquids*, Phys. Rev. B **96**, 195401 (2017). Editors' suggestion.
- A. Woessner, A. Mishchenko, A. Misra, **I. Torre**, M.B. Lundeberg, K. Watanabe, T. Taniguchi, M. Polini, K.S. Novoselov, and F.H.L. Koppens. *Propagating plasmons in a charge-neutral quantum tunneling transistor*, ACS Photonics **4**, 3012 (2017).
- D. Kundys, B. Van Duppen, O.P. Marshall F. Rodriguez **I. Torre** A. Tomadin, M. Polini and A.N. Grigorenko. *Nonlinear light mixing by graphene plasmons*, Nano Lett. **18**, 282 (2018).
- A. Principi, **I. Torre**, F.H.L. Koppens, and M. Polini *General semiclassical theory of chiral Berry plasmons*, In preparation.

# Contents


**1 Introduction to relevant experimental facts** **1**
1.1 Two-dimensional materials and their heterostructures . . . 1
1.1.1 The 2D materials color box . . . 2
1.1.2 Van der Waals heterostructures . . . 7
1.1.3 h-BN encapsulated graphene . . . 7
1.2 Experimental evidence for hydrodynamic electron transport . . . 8
1.2.1 Hydrodynamic electron flow in high-mobility wires. The Gurzhi effect . . . 9
1.2.2 Negative local resistance caused by viscous electron backflow in graphene . . . 12
1.2.3 Super-ballistic flow of viscous electron fluid through graphene constrictions . . . 14
1.2.4 Observation of the Dirac fluid and the breakdown of the Wiedemann-Franz law in graphene . . . 16
1.2.5 Evidence for hydrodynamic electron flow in $PdCoO_2$ . . . 18
1.3 Experimental evidence for long-lived plasmons in graphene . . . 19
1.3.1 Graphene plasmons in far-field experiments . . . 20
1.3.2 Plasmons in near-field experiments. The s-SNOM technique . . . 21

**2 Hydrodynamic transport in encapsulated graphene** **23**
2.1 Derivation of the linearized hydrodynamic equations from the semiclassical Boltzmann equation . . . 24
2.1.1 Derivation of the boundary conditions for the linearized hydrodynamic equations . . . 26
2.2 Nonlocal transport and the hydrodynamic shear viscosity in graphene . . . 28
2.2.1 Boundary conditions . . . 30
2.2.2 Applicability of the linearized theory . . . 31
2.2.3 General solution of hydrodynamic equations in a 2D strip geometry . . . 31
2.2.4 Longitudinal transport and the Gurzhi effect . . . 32
2.2.5 Half-plane geometry . . . 34
2.2.6 The Levitov-Falkovich geometry . . . 37
2.2.7 The vicinity geometry . . . 38
2.3 Non-local transport and the Hall viscosity of 2D hydrodynamic electron liquids . . . 42
2.3.1 Single-injector setup . . . 45
2.3.2 Non-local resistances and the Hall viscosity . . . 48
2.3.3 On the solutions with no-slip BCs . . . 51
2.4 Conclusions . . . 52

**3 Scattering of plasmons in two-dimensional materials** **55**
3.1 Plasmons at an interface . . . 55
3.1.1 Interface plasmon equation . . . 56
3.1.2 The Wiener-Hopf solution for an interface . . . 57
3.1.3 Solution for an edge . . . 65
3.1.4 Interface with uniform normal conductivity . . . 65
3.2 Lippmann-Schwinger theory for two-dimensional plasmon scattering . . . 67
3.2.1 Plasmons in inhomogeneous media . . . 68
3.2.2 Lippmann-Schwinger theory for 2D plasmons . . . 69
3.2.3 Going beyond the RPA . . . 73

3.2.4 Transition Function . . . 74
3.2.5 Optical theorem . . . 75
3.2.6 The Born approximation . . . 76
3.2.7 The Eikonal Approximation . . . 78
3.2.8 The Method of Partial Waves . . . 79
3.2.9 Explicit examples . . . 80
3.3 Electrical $2\pi$ phase control of infrared light in a 350nm footprint using graphene plasmons 90
3.4 Conclusion . . . 94

**4 Plasmons in topological materials 95**
4.1 Semiclassical theory of plasmons in the presence of a Berry flux . . . 95
4.1.1 Interface Model . . . 96
4.1.2 Local capacitance approximation . . . 97
4.1.3 Fetter interaction . . . 101
4.1.4 Coulomb interaction . . . 105
4.1.5 Impact of a finite damping rate . . . 107
4.2 Conclusions . . . 108

**A Plasmons in 2D materials including retardation 109**
A.1 Constitutive equations . . . 109
A.2 Homogeneous system . . . 109
A.2.1 Confined modes . . . 110
A.2.2 Transmission and reflection coefficients . . . 112

**B Density-density response functions of inhomogeneous electron systems 115**
B.1 Non-interacting density-density response function of an inhomogeneous electron liquid . . . 115
B.1.1 Calculation of $M^{(0)}$ . . . 117
B.1.2 Calculation of $M^{(1)}$ . . . 117
B.1.3 Calculation of $M^{(2)}$ . . . 117
B.1.4 Calculation of $M^{(3)}$ . . . 118
B.2 On inhomogeneous 2D electron systems in graphene . . . 118

**C Static density-stress tensor response of a two-dimensional electron liquid 121**

**D Mathematical theorems used in the interface plasmon problem 123**
D.1 Fourier transform theorems . . . 123
D.2 Complex analysis theorems . . . 123

**E Mathematical and computational details of the two-dimensional plasmon scattering problem 125**
E.1 Effective interaction . . . 125
E.2 Real space formulation of the scattering equations . . . 126
E.2.1 Geometry in Fig. 3.1(a) . . . 126
E.2.2 Geometry in Fig. 3.1(b) . . . 126
E.3 Numerical solution of Eq. 3.165 . . . 127
E.4 Numerical solution of Eq. 3.203 . . . 128

# Chapter 1

# Introduction to relevant experimental facts

In this Chapter we summarize the physical properties of two-dimensional (2D) materials [1, 2, 3] and their heterostructures [4, 5] that are relevant for this Thesis. We focus, in particular, on heterostructures made by graphene encapsulated between slabs of hexagonal Boron Nitride (h-BN) [6]. These are crucial for all the experimental investigation discussed in this work because of the extremely high values of mobility, exceeding $10^5$ $\mathrm{cm}^2/(\mathrm{V}\cdot\mathrm{s})$, reached by charge carriers in these devices [6, 7].

In particular, both the observation of the hydrodynamic transport regime discussed in Chapter 2, and the propagation of long-lived plasmons excitation, that is the main focus of Chapter 3, require the high carriers mobilities allowed by h-BN encapsulation.

We then introduce the experimental facts that provide the motivation for the theoretical studies presented in this Thesis.

In Section 1.2 we review the experimental evidences for solid-state hydrodynamic electron flow. We start by describing early works in semiconducting nanowires [8] that provided the first experimental evidence of a hydrodynamic phenomenon in a solid-state device, namely the Gurzhi effect [9, 10]. We then discuss recent experiments that probed various hydrodynamic effects such as negative non-local resistance [11], super-ballistic electron flow trough a constriction [12], and breaking of the Wiedemann-Franz law [13], in h-BN encapsulated graphene. We finally describe an experiment that recently probed hydrodynamic flow in the high-mobility layered material $PdCoO_2$ [14].

In Section 1.3 we discuss experimental evidence for long-lived plasmon excitations in graphene [15, 16, 17] and graphene/h-BN heterostructures [18]. The existence of these collective modes and the ability to efficiently excite and detect them motivates the study of the scattering theory for two-dimensional plasmons, against different types of inhomogeneities, developed in Chapter 3. We focus in particular on the scattering-type Scanning Near Field Optical Microscopy (s-SNOM) technique that has become a highly relevant experimental tool to probe plasmons in real space, and has been used to demonstrate the functionality of the device described in Sect. 3.3 and Ref. [19].

## 1.1 Two-dimensional materials and their heterostructures

The investigation of the properties of two-dimensional (2D) materials has become one of the richest and fastest-growing research field in contemporary condensed matter physics since graphene was isolated for the first time in 2004 by A. K. Geim and K. S. Novoselov [1, 20], a discovery that earned them the 2010 Nobel prize in physics. These materials attracted a lot of interest both from the point of view of fundamental studies and for devices applications.

After more than ten years of research, higher quality samples of graphene are now available, making possible the observation of new interesting phenomena. However, in the last years the focus is shifting from graphene to other 2D materials and, more importantly, to combinations of them.

It has been demonstrated [6, 21, 22] that different 2D materials can be stacked one on top of the other to form more complex structures that are held together by the weak (compared to the in-plane covalent bonds) Van der Waals forces between the different layers. These structures are therefore known

as Van der Waals (VdW) heterostructures. This enormously enhances the number of possible devices that can be designed, both for exploring new physical phenomena and for practical applications. Thanks to stacking, the properties of different layered materials can be combined together and used to improve specific material features.

### 1.1.1 The 2D materials color box

Here we give a brief overview of the two-dimensional material that have been discovered and isolated up to now, and that can be used as building blocks for VdW heterostructures. Since the discovery of graphene this 2D materials "color box" has grown and includes now materials with very different electronic structures ranging from semi-metals to semiconductors, to large gap insulators, and recently including also ferromagnets. Importantly, the properties of 2D materials strongly depend on the number of layers and are usually very different from those of their three-dimensional (3D) counterparts.

#### Graphene

Graphene has been the first truly 2D material to be discovered and is, by far, the most studied component of the 2D materials family. Its exceptional electronic [23], mechanical [24], thermal [25], and optical [26, 27, 28] properties have been the subject of an enormous amount of publications. Many aspects like transport [29], spectroscopy [30], and many-particle effects [31] are now covered by reviews.

Here we highlight some of the fundamental electronic and optical properties that will be crucial in the next Chapters.

Graphene is a 2D allotrope of carbon in which the carbon atoms are positioned on an hexagonal lattice. There are two carbon atoms per unit cell corresponding to the two triangular sublattices A and B shown in Fig. 1.1-a. Most of graphene electronic and optical properties stem from the peculiar

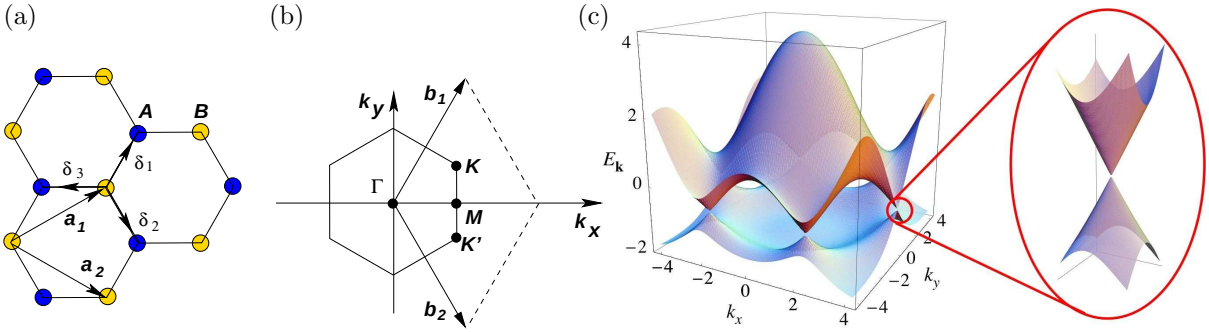


Figure 1.1: (a) A portion of graphene lattice. Atoms belonging to the two sublattices are represented in blue and yellow. The vectors $\mathbf{a}_{1-2} = [3/(2a), \pm\sqrt{3}/(2a)]$ are a possible choice of primitive vectors. The interatomic distance is $a = 0.142$ nm. (b) First Brillouin zone of the Graphene lattice. $\pi$ bands touch at the $K$ and $K'$ points at the corners of the Brillouin zone. (c) Electron band structure of graphene calculated using the the tight binding model in Ref. [32]. Taken from Ref. [23].

dispersion of its $\pi$ bands shown in Fig. 1.1-c. These are the only bands crossed by the Fermi level even under extreme doping conditions. For this reason we can disregard all the other bands when discussing transport properties or optical properties up to the Ultra-Violet (UV) spectral region, the onset for electronic transition from deeper band being in the far UV. $\pi$ bands arise from the combination of the $p_z$ atomic orbital of the carbon atoms, and they can be conveniently described using a Tight-Binding (TB) model [32]. The simplest version of this model, that considers only the nearest-neighbor hopping, gives the following dispersion for the conduction (+) and valence (−) bands

$$E_{\pm}(\mathbf{k}) = \frac{\mp t|f(\mathbf{k})|}{1 \mp s|f(\mathbf{k})|}, \tag{1.1}$$

where $t = V_{pp\pi} \approx -3.28$ eV is the hopping energy between two neighboring $p_z$ orbitals [33], $s = S_{pp\pi} \approx 0.0425$ is their overlap integral [33] (numerical values are extracted as best fit parameters to Angle

Resolved Photoelectron Emission Spectroscopy (ARPES) bands [34]), and the function $f(\boldsymbol{k})$ reads

$$f(\boldsymbol{k}) = e^{ik_y a} + e^{ik_x \frac{\sqrt{3}}{2}a - ik_y \frac{a}{2}} + e^{-ik_x \frac{\sqrt{3}}{2}a - ik_y \frac{a}{2}}, \tag{1.2}$$

with, $a \approx 1.42$ Å being the nearest-neighbor atomic distance. All the physical properties that are relevant in our work are however described by an even simpler, low-energy, one-particle Hamiltonian that can be obtained by approximating the TB Hamiltonian [32] near the $K$ or $K'$ point, called Dirac points, of the Brillouin Zone (BZ) (See Fig. 1.1-b). This procedure yields, in the sublattice basis,

$$H_{\boldsymbol{k}\zeta} = \hbar v_{\mathrm{F}} \begin{pmatrix} 0 & k_x - i\zeta k_y \\ k_x + i\zeta k_y & 0 \end{pmatrix}, \tag{1.3}$$

where $v_{\mathrm{F}} = 3|t|a/(2\hbar) \approx 1 \cdot 10^6$ m/s is the Fermi velocity, $\zeta$ is a valley index that is equal to $+1$ $(-1)$ in the valley near the $K$ $(K')$ point, and $\boldsymbol{k}$ denotes the Bloch wavevector measured from the $K$ $(K')$ point. This effective Hamiltonian is equivalent to the massless Dirac Hamiltonian in 2+1 dimensions and has a linear energy spectrum

$$E_{\boldsymbol{k}\lambda\zeta} = \pm\hbar v_{\mathrm{F}} k. \tag{1.4}$$

In ideal, free standing, graphene the valence band is completely full and the conduction band is completely empty. The Fermi energy lies therefore at the Dirac point. If the electron density $n$ is modified by impurities, doping, charge transfer from the substrate, or gating, the Fermi energy modifies according to

$$E_{\mathrm{F}} = \mathrm{sgn}(n)\hbar v_{\mathrm{F}} \sqrt{\pi|n|}, \tag{1.5}$$

where $n$ is positive for n-doping and negative for p-doping.

An extremely important characteristic of graphene and other 2D conducting materials is the possibility of electrostatically tuning the carrier density. This cannot usually be done in 3D metals because free electrons screen any external potential on a lengthscale equal to the inverse of the Thomas-Fermi wavevector [35]. This is important for studying the carrier density dependence of physical phenomena, for example, many-body effects are typically density dependent. Moreover, field effect enables the realization of Graphene based Field Effect Transistors (GFETs) [36].

In a GFET the electron density in the graphene channel depends on the gate voltage as

$$n = \frac{C(V_{\mathrm{g}} - V_0)}{e}, \tag{1.6}$$

where $C = (1/C_{\mathrm{g}} + 1/C_{\mathrm{q}})^{-1}$, $C_{\mathrm{g}}$ is the geometrical capacity per unit area between the channel and the gate and $C_q = e^2 n/E_{\mathrm{F}} \approx 2.2 \cdot \sqrt{n/\pi}$ is the so-called quantum capacitance of graphene [37, 38, 39] (here we assumed that the gate has a very large density of states at the Fermi level and therefore a negligible quantum capacitance). For high enough electron densities the total capacity $C$ is dominated by the geometrical capacity and the relation between carrier density and gate voltage is linear.

Depending on the value of the Fermi energy with respect to the thermal energy $k_{\mathrm{B}}T$ and to the amplitude of potential fluctuations induced by disorder $\delta U$ we can identify two different regimes.

When $E_{\mathrm{F}}$ is the largest energy scale, that is in the doped regime, electrons can be described according to the Fermi Liquid (FL) paradigm. This is the most interesting regime from the point of view of applications. Chapter 2 deals with hydrodynamic transport and transport coefficients in the FL regime, moreover the long-lived plasmon excitation studied in 3 occur in this regime.

Conversely, when $E_{\mathrm{F}}$ is negligible, transport is controlled by the interplay of thermally excited carriers and disorder. At low temperature disorder-induced potential fluctuations disallow the Dirac point to be reached in the whole sample at the same gate voltage and create "electron-hole puddles" [40]. This limits the precision with which the Dirac point can be approached experimentally to $\approx 1$ meV [41]. At higher temperatures, i.e. when $k_{\mathrm{B}}T \gg \delta U$, thermally excited electrons and holes coexist and form a Dirac Fluid (DF) [42, 13].

In the doped regime, the long-wavelength response of graphene to electromagnetic fields is described by its optical conductivity $\sigma(\omega) = \sigma_1(\omega) + i\sigma_2(\omega)$. At zero temperature and neglecting relaxation the real and imaginary part of the conductivity read [43, 44]

$$\sigma_1(\omega) = \frac{e^2}{h}\left\{2\pi|E_{\mathrm{F}}|\delta(\hbar\omega) + \frac{\pi}{2}\left[\Theta\left(\frac{\hbar\omega}{2|E_{\mathrm{F}}|} - 1\right) + \Theta\left(-\frac{\hbar\omega}{2|E_{\mathrm{F}}|} - 1\right)\right]\right\}, \tag{1.7}$$

$$\sigma_2(\omega) = \frac{e^2}{h}\left\{\frac{2|E_{\mathrm{F}}|}{\hbar\omega} + \frac{1}{2}\ln\left[\frac{2|E_{\mathrm{F}}| - \hbar\omega}{2|E_{\mathrm{F}}| + \hbar\omega}\right]\right\}. \tag{1.8}$$

The first term in the brackets is due to intraband transition, while the second is related to interband transitions. Absorption ($\sigma_1(\omega) \neq 0$) takes place only at zero frequency (intraband absorption) and at frequencies above $2E_F/\hbar$ (interband absorption) due to Pauli blocking. The impact of electron scattering with impurities or phonons can be taken into account using a number-conserving relaxation time approximation [45] with a relaxation rate $\gamma$. This allows kinematic constraint for electronic transitions to be violated on an energy scale $\hbar\gamma$ and leads to

$$\sigma_1(\omega) = \frac{e^2}{h}\left\{\frac{2|E_F|\hbar\gamma}{(\hbar\omega)^2+(\hbar\gamma)^2} + \frac{\pi}{2}\left[\Theta_{\tilde{\gamma}}\left(\frac{\hbar\omega}{2|E_F|}-1\right)+\Theta_{\tilde{\gamma}}\left(-\frac{\hbar\omega}{2|E_F|}-1\right)\right]\right\}, \tag{1.9}$$

$$\sigma_2(\omega) = \frac{e^2}{h}\left\{\frac{2|E_F|\hbar\omega}{(\hbar\omega)^2+(\hbar\gamma)^2} + \frac{1}{4}\ln\left[\frac{(2|E_F|-\hbar\omega)^2+(\hbar\gamma)^2}{(2|E_F|+\hbar\omega)^2+(\hbar\gamma)^2}\right]\right\}, \tag{1.10}$$

where $\tilde{\gamma} = \hbar\gamma/(2|E_F|)$, and $\Theta_\epsilon(x) = 1/2+1/\pi\arctan(x/\epsilon)$. At finite temperatures the additional thermal broadening can be taken into account by using Maldague's integral [46]

Much of this Thesis is devoted to the study of effects beyond this simple local approximation. In Chapter 2 we study the impact of a particular type of non-local effects that are related to the shear and Hall viscosity of the electron liquid hosted by graphene samples when this is driven into the hydrodynamic transport regime.

The 2D plasmon scattering theory developed in Chapter 3, and used to explain the experimental data by Woessner et al. [19], naturally takes into account non-local effects that can be relevant, and even dominant as demonstrated in Ref. [47], for plasmon experiments.

### Graphene derivatives

Although graphite is a chemically inert material, graphene can react with other elements forming new materials with different electronic properties. Elias et al. [48] have demonstrated the possibility of hydrogenating graphene, by exposition to hydrogen plasma, adding one hydrogen atom to each carbon site. The obtained material is known as graphane. Hydrogen addition changes the hybridization type of carbon atomic orbitals from $sp_2$ to $sp_3$. This has two main consequences: the graphene sheet buckles out of plane reducing the lattice constant, and the conducting $\pi$ bands are destroyed, turning the semimetal graphene into an insulator. The process can be reverted by annealing, recovering, almost completely, the original characteristics of graphene. Other ways to chemically tune graphene electrical properties, and in

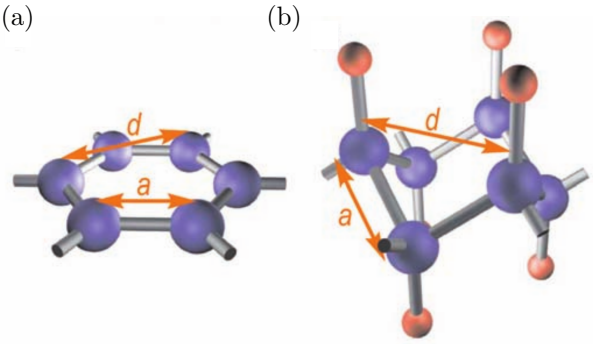


Figure 1.2: Schematic representation of the crystal structure of graphene and theoretically predicted graphane. Carbon atoms are shown as blue spheres, and hydrogen atoms are shown as red spheres. Taken from Ref. [48].

particular to open an energy gap, include fluorination of the $sp_2$ bonds. Authors of Ref. [49] demonstrated one and two-side fluorination of graphene samples, by exposition to $XeF_2$, and the opening of a gap of $\approx 3$ eV. This can be useful in optoelectronic applications [50].

### Hexagonal Boron Nitride

Hexagonal Boron Nitride is a large gap of the order of 6 eV insulator [51]. It is a layered material with a crystal structure very similar to graphite, since it is formed by monolayers with hexagonal structure held together by WdV forces. The lattice constant is also very similar to that of graphene with only a

$\approx 2\%$ mismatch. In contrast with graphene the two sublattices are occupied by different atoms, boron atoms on one sublattice and nitrogen atoms on the other. The breaking of the sublattice symmetry allows the presence of a gap at the $K$ and $K'$ points of the Brillouin zone. Hexagonal Boron Nitride can be exfoliated down to the monolayer to obtain very high quality crystals.

In this Thesis we will make use of h-BN optical properties described by the frequency-dependent dielectric tensor $\boldsymbol{\epsilon}(\omega)$. Since we are interested only to frequencies below the optical band-gap and h-BN is an insulator with no free charge carrier the dielectric response of the material is determined only by lattice vibrations. The dielectric tensor of h-BN is isotropic in the layer plane but the in-plane and the out-of-plane component can be very different

$$\boldsymbol{\epsilon}(\omega) = \begin{pmatrix} \epsilon_x(\omega) & 0 & 0 \\ 0 & \epsilon_x(\omega) & 0 \\ 0 & 0 & \epsilon_z(\omega) \end{pmatrix}. \tag{1.11}$$

Each component is well described by a simple oscillator model

$$\epsilon_i(\omega) = \epsilon_i(\infty) + \sum_n \frac{s_{n,i}\omega_{n,i}^2}{\omega_{n,i}^2 - i\gamma_{n,i}\omega - \omega^2}. \tag{1.12}$$

Slightly different sets of parameters for Eq. 1.12 are given by Refs. [52, 53, 54, 55] and are summarized in Tab. 1.1. A distinctive feature of h-BN permittivity is the presence of frequency regions called *reststrahlen*

| Model | $i$ | $n$ | $\epsilon_i(\infty)$ | $s_{n,i}$ | $\hbar\omega_{n,i}$ [meV] | $\hbar\gamma_{n,i}$ [meV] |
|---|---|---|---|---|---|---|
| Geick et al. [52] | $x$ | 1 | 4.95 | 1.868 | 169.5 | 3.6 |
| | $x$ | 2 | ” | 0.209 | 95.1 | 3.4 |
| | $z$ | 1 | 4.10 | 0.530 | 97.1 | 1.0 |
| | $z$ | 2 | ” | 0.456 | 187.2 | 9.9 |
| Cai et al. [53] | $x$ | 1 | 4.87 | 1.83 | 170.1 | – |
| | $z$ | 1 | 2.95 | 0.61 | 92.5 | – |
| Caldwell et al. [54] | $x$ | 1 | 4.9 | 2.001 | 168.6 | 0.87 |
| | $z$ | 1 | 2.95 | 0.5262 | 94.2 | 0.25 |
| Kumar et al. [55] | $x$ | 1 | 4.87 | 1.856 | 169.9 | 0.6 |
| | $z$ | 1 | 2.95 | 0.390 | 96.7 | 0.5 |

Table 1.1: Parameters for the h-BN optical response Eq. 1.12, taken from Refs. [52, 53, 54, 55].

*bands* in which the in-plane and out-of-plane components of the dielectric tensor have opposite sign [54]. In these regions h-BN is an hyperbolic materials and hosts hyperbolic phonon polaritons [54, 55].

In addition to this h-BN has an high breakdown voltage and is able to withstand electric fields up to $\approx 0.7\text{V/nm}$, this is very useful when h-BN is used as an insulating layer.

### Transition Metal Dichalcogenides

Transition metal dichalcogenides (TMDs) are chemical compounds with formula $MX_2$, where M is a transition metal, for example M=Mo, W, Ti..., and X is a chalcogenide as S, Se, or Te. All TMDs have an hexagonal lattice, each monolayer is formed by three separated layers with the M atoms occupying the central layer and the X atoms lying in the other two layers. Depending on the coordination of the transition metal atom with the other atoms in the unit cell TMDs can feature broken inversion symmetry, as it happens in $MoS_2$, and $WS_2$. TMDs can be metallic, semiconducting or insulating but the most studied crystals of this class, are the one formed by group VIB metals molybdenum and tungsten [56, 57]. These are direct gap semiconductors [56] (monolayer $MoS_2$ has a bandgap of $\approx 1.8$ eV), whose optical properties are dominated by excitonic features [58]. Mobilities exceeding 200 $\text{cm}^2/(\text{V}\cdot\text{s})$ [57] have been reported in $MoS_2$ samples.

An important feature of these TMDs is that the interband absorption near the $K$ and $K'$ points is polarization selective [59, 60, 61]. This means that it is possible to create a population imbalance between the two valleys by shining circularly polarized light on the sample. Since the two valleys have opposite Berry curvature this produces a finite off-diagonal conductivity $\sigma_{xy}$ that manifests itself in a valley Hall effect [61] in absence of magnetic field.

### Black Phosphorous

Bulk black phosphorous is a semiconducting material. Recently it has been shown that it can be exfoliated down to the monolayer [62, 63]. Mono and few-layers samples are still semiconductors with a direct or nearly direct band gap [63, 64]. It has shown high carrier mobilities, up to $10^3$ $cm^2/(V \cdot s)$ at room temperature [62].

The most peculiar feature of this semiconductor that manifests itself in both optical and transport properties [65] is the strong in-plane anisotropy of its band structure that stems from the orthorhombic wave-like structure of the crystal.

### 2D Ferromagnets

Very recently evidence of strictly 2D materials displaying ferromagnetic behavior has been reported independently by two research groups [66, 67].

Ferromagnetic behavior is forbidden for the isotropic Heisenberg model in two dimension by the Mermin-Wagner theorem [68], anisotropy is therefore an essential feature of these materials.

Authors of Ref. [67] reported hysteresis curves, measured using Magneto-Optical Kerr Effect (MOKE), of mono-, bi-, and tri-layer $CrI_3$. These are shown i Fig. 1.3. Monolayer $CrI_3$ is an anisotropic ferromagnet with a Curie temperature ($T_C \approx 45$ K) slightly lower than that of bulk $CrI_3$ ($T_C \approx 61$ K). Interestingly, the ferromagnetic behavior is found to be strongly dependent on the number of layers, with the bilayer showing no hysteresis, in striking contrast with both the mono- and the tri-layer.

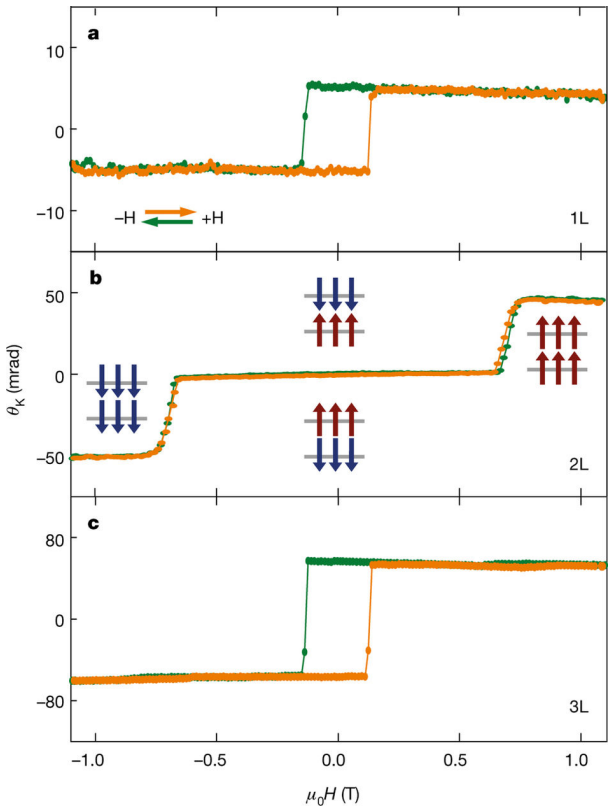


Figure 1.3: a, Magneto-Optical Kerr Effect (MOKE) signal on a monolayer (1L) $CrI_3$ flake, showing hysteresis in the Kerr rotation as a function of applied magnetic field, indicative of ferromagnetic behavior. b, MOKE signal from a bilayer $CrI_3$ showing vanishing Kerr rotation for applied fields $\pm 0.65$ T, suggesting antiferromagnetic behavior. Insets depict bilayer (2L) magnetic ground states for different applied fields. c, MOKE signal on a trilayer (3L) flake, showing a return to ferromagnetic behavior. Taken from Ref. [67].

### 1.1.2 Van der Waals heterostructures

Van der Waals heterostructures are formed by stacking different 2D crystals one on top of each other. The whole structure is then held together by the VdW forces between the different layers.

Many interesting effect can arise due to interaction between electrons in different layers. There are essentially two interaction mechanism: the Coulomb interaction and quantum tunneling between different layers.

Coulomb interaction acts without exchanging electrons between different layers, it is fundamental for the plasmonic devices described in Chapter 3, and gives rise to the phenomenon of Coulomb drag [69].

Conversely, quantum mechanical tunneling leads to exchange of electrons between different layers. This can be exploited to build Field Effect Tunneling Transistors (FETTs) [38]. Through quantum tunneling electrons in one layer can borrow some of the properties of nearby layers, an effect known as proximity effect. For example, strong spin-orbit coupling [70], superconductivity [71], and ferromagnetism [72] can be induced by proximity effect.

Advancements in fabrication techniques played a major role in the discovery of new interesting physical phenomena [4, 5]. Nowadays, the most versatile technique for assembling VdW heterostructures is direct mechanical assembly. This technique was initiated by the work of Dean et al. [6] and has been improved a lot since then.

The technique used in early VdW heterostructures works was based on depositing a 2D crystal layer on a polymer membrane, depositing it on top of another 2D flake and then chemically dissolving the membrane. The process can then be repeated to add further layers. The main drawback of this technique is the exposition of the 2D layers to the polymer membrane and to solvents that can contaminate the interfaces.

The next step in the evolution of assembly techniques was the introduction of the so-called "pick and lift" or "polymer-free" method that relies on the strong VdW interactions existing among the 2D crystals. In this technique once the first layer is picked up it is brought in contact with a second layer. Thanks to VdW forces there is a certain chance that the second layer is picked up. The process can then be repeated to pick up more layers. At the end of the process the entire stack can be released on a substrate by controlling the temperature of the membrane. In this way only the first layer comes in contact with the polymer membrane that is a possible source of contaminants, while the resulting inner interfaces are very clean.

The main disadvantage of this technique is that having the complete stack already on the substrate does not allow to evaporate surface contacts to the inner layers because selective etching is typically not possible. To circumvent this drawback an extremely powerful technique based on lateral one-dimensional contacts [7] has been developed to electrically contact the intermediate layer achieving very-low contact resistances.

An important mechanism that enhances the quality of the interfaces between certain pairs (as, for example, graphene and h-BN) of materials is the "self-cleaning". If the interaction between the two materials is stronger than the interaction between the materials and the contaminants, the later are pushed away and confined into "pockets" to achieve the most energetically favorable situation. This leaves large areas of the interface atomically flat and completely free from contaminants.

### 1.1.3 h-BN encapsulated graphene

The VdW heterostructure that is most relevant for our work is made of a graphene sheet encapsulated by flakes of h-BN. Since the work of Dean et al. [6] h-BN has proven to be the ideal substrate to enhance graphene electronic properties, allowing values of mobility even higher than those reached in suspended graphene samples. The reasons for this success are the following. First, the surface of an exfoliated h-BN flake is atomically flat and thanks to strong in-plane bonds is also almost free of dandling bonds and charge traps. Second, the presence of the h-BN flakes screens graphene from contaminants and charged impurities that may adhere to the graphene flake. Third, strong adhesion forces make the encapsulated graphene extremely flat and ripple-free. They moreover quench the out-of-plane oscillations modes (flexural phonons).

The mobility of encapsulated samples is therefore ultimately limited by the rather weak interaction with acoustic phonons as demonstrated in [7], where room temperature mobilities exceeding $10^5$ $\mathrm{cm}^2/(\mathrm{V}\cdot\mathrm{s})$ and low temperature mobilities of the order of $10^6$ $\mathrm{cm}^2/(\mathrm{V}\cdot\mathrm{s})$ are reported.

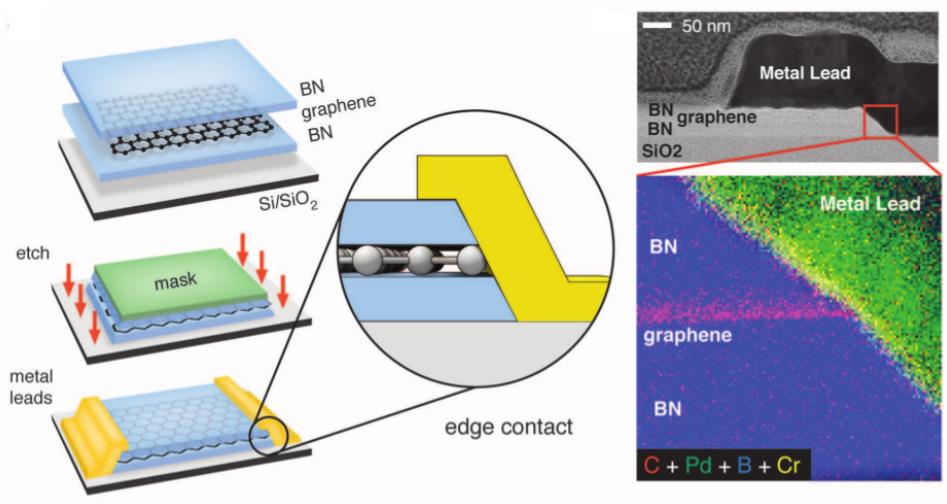


Figure 1.4: (a) Schematic of the edge-contact fabrication process. (b) High-resolution bright-field Scanning Transmission Electron Microscope image showing details of the edge-contact geometry. The expanded region shows a magnified false-color Electron Energy-Loss Spectroscopy map of the interface between the graphene edge and metal lead. Taken from Ref. [7].

The advantages of encapsulation are fully exploited using the "polymer free" stacking technique that avoids any contact between graphene and the polymer membrane used to build the stack. If this technique is used it is not possible to electrically contact the surface of graphene because no method to selectively remove the top h-BN layer exists.

The solution to this problem was found by Wang et al. [7]. These authors etched the h-BN/graphene stack at an angle of $\approx 45°$, using plasma etching to expose the edge of the graphene flake, as illustrated in Fig. 1.4-a. They subsequently evaporated metallic contacts by electron beam evaporation. Contacts were made up of a 1 nm thick chromium adhesion layer, followed by a 15 nm palladium layer, and by a 60 nm gold layer. With this combination of metals a contact resistance as low as $\approx 100\ \Omega \cdot \mu$m has been reported.

## 1.2 Experimental evidence for hydrodynamic electron transport

Hydrodynamics is a powerful, non-perturbative, theory that describes systems of many particles, either classical or quantum, undergoing very frequent inter-particle collisions, that is, when the mean-free-path for inter-particle collisions is the shortest lengthscale of the problem [73, 74]. In the hydrodynamic regime the behavior of a fluid is described by three nonlinear equations: the continuity equation, the Navier-Stokes equation and the energy transport equation, reflecting respectively the conservation of particle number, momentum, and energy during a collision.

Hydrodynamics has been used for a long time to describe transport of electrons in solid-state devices [9, 10, 75, 76, 77, 78, 79, 80, 81, 82, 83, 84, 85, 86, 87, 88, 89, 90, 91, 92]. However electron in solid state are subject to both electron-electron, momentum-conserving collisions, and electron-impurity or electron-phonon momentum-non-conserving collisions. For hydrodynamics effect to be observable the mean free path $\ell_{ee}$ for electron -electron (e-e) collisions must be the shortest length scale in the problem, i.e.

$$\ell_{ee} \ll \ell,\ W,\ v_F/\omega. \tag{1.13}$$

Here, $\ell$ is the mean free path for momentum-non-conserving collisions, $W$ is the sample size, $v_F$ is the Fermi velocity, and $\omega$ is the frequency of the external perturbations.

These requirements are difficult to meet experimentally. Indeed, at low temperatures the mean-free-path for electron-electron collisions $\ell_{ee}$ diverges as $T^{-2}\ln(T)$ in two spatial dimensions [93] (or as $T^{-2}$ in three dimensions [94]), reaching, typically, a micrometer scale around liquid-helium temperature.

On the other hand, at high temperature, collisions with phonons become the most important source of electron scattering, making $\ell$, small. Hydrodynamic behavior is therefore expected to be observed only in an intermediate temperature window and in very high quality electron systems, having large momentum-non-conserving mean-free-paths, or, equivalently, high mobilities. Fore these reasons experimental evidence for electronic hydrodynamic regime was, until recently, limited to the early work by De Jong and Molenkamp in high-mobility GaAs/AlGaAs heterostructures [8].

Recent advancement in material science and fabrication techniques [6, 7, 95] allowed to obtain very high-quality encapsulated graphene samples with mobility values exceeding $10^5$ $\mathrm{cm}^2/(\mathrm{V}\cdot\mathrm{s})$, almost reaching the theoretical limit for acoustic-phonon-limited mobility [7]. These systems are, thanks to their high purity and low electron-phonon coupling, that allows to maintain high mobilities up to room temperature, the most promising candidates to observe hydrodynamic effects in electronic transport.

Here we start by describing the pioneering work of the authors of Ref. [8]. We then review recent experiments [11, 13, 12] in h-BN encapsulated graphene that were the main motivation for the theoretical analysis of hydrodynamic transport presented in Chapter 2 of this Thesis. In particular the interpretation of the experimental data in Ref. [11] is entirely based on the theory developed in Chapter 2 and in Ref. [96].

Bandurin et al. [11] used a particular non-local measurement geometry to enhance hydrodynamic effects and used their results to measure the shear viscosity of the electron liquid. Thanks to this geometry the impact of the hydrodynamic effect is strong enough to reverse the sign of the measured signal.

More recently authors of Ref. [12] performed an experiment that is conceptually more similar to the original work of De Jong and Molenkamp but employed a channel with a constriction to maximize hydrodynamic effects.

These two experiment dealt with the doped or Fermi Liquid (FL) regime. In Ref. [13] the hydrodynamic behavior in the undoped, or Dirac Fluid (DF) regime is addressed. These authors measured a violation of the Wiedemann-Franz law that they explained as a result of the separation of charge and heat transport that happens in graphene near zero doping.

For the sake of completeness we finally mention another recent work dealing with hydrodynamic transport in ultra-pure, quasi-2D, samples of $PdCoO_2$ [14].

### 1.2.1 Hydrodynamic electron flow in high-mobility wires. The Gurzhi effect

The first evidence for hydrodynamic behavior of electrons in solid state dates back to the work by De Jong and Molenkamp in semiconducting nanowires [8, 97, 98]. These authors demonstrated experimentally for the first time the existence of the so-called Gurzhi effect [9, 10], that was predicted by Gurzhi more than thirty years earlier.

The Gurzhi effect consist in a strongly non-monotonic behavior of the resistivity of a conducting channel as a function of temperature that takes place when electrons in the channel enter the hydrodynamic regime. This effects arises because of the combined action of electron-electron (e-e) collisions and boundary scattering. Here we describe the mechanism that gives rise to the Gurzhi effect and the experiment used to probe it.

It is well known that electron-electron collisions can affect the current response of a bulk material to a uniform external electric field only through *umklapp* processes. This happens because the quasi-momentum of electron is conserved, up to a reciprocal lattice vector, during collisions.

In metals with a Fermi surface much smaller than the size of the Brillouin zone these processes are irrelevant, since they require too much momentum, and the quasi-momentum is strictly conserved. In this situation e-e collisions have no impact on the conductivity of an infinite sample.

However, as it has been demonstrated [8, 11], e-e collisions can have a dramatic effect on the resistivity of a finite width channel. This can be qualitatively explained as follows. Let's consider a 2D electron channel of width $W$, much larger than the Fermi wavelength such that quantum interference effects can be neglected and electrons can be regarded as semiclassical particles. We assume moreover that the Fermi wavelength is in turn much larger than the lattice constant, as a consequence umklapp processes are negligible. Electrons in this channel undergo three types of scattering: e-e scattering, momentum relaxing collisions against defects, impurities and phonons, and scattering against the boundaries of the channel. The first mechanism conserves both the electron number and momentum, the second conserves particle number but relaxes momentum toward zero. This mechanism is the only responsible for resistivity of wide channels. The last mechanism causes momentum losses when electrons scatter

against the boundary of the samples, due to non-specular reflection. Let us consider for the moment e-e and boundary scattering alone, leaving aside bulk momentum-relaxing collisions.

The frequency of e-e collisions is quantified by the Knudsen number [99] $K = \ell_{ee}/W$ where $\ell_{ee}$ is the average distance traveled by an electron between e-e scattering events. Based on this number we can distinguish two transport regimes: the Knudsen, or ballistic, regime when $K \gtrsim 1$ and e-e collisions are rare, and the Gurzhi or hydrodynamic regime when $K \lesssim 1$ and collisions are frequent. Electron-electron scattering acts in two very different ways in these two regimes.

In the Knudsen regime current (or momentum) is carried mainly by electrons traveling with a small angle with respect to the channel axis. These electrons travel long distances before losing momentum in boundary collisions. In this regime the main impact of e-e consists in disrupting the trajectories of electrons traveling at small angle making their collision against the boundaries more frequent. This makes the resistivity grow with the rate of e-e collisions.

Conversely, in the Gurzhi regime current is carried mainly by electrons in the center of the channel that are less prone to boundary collisions. In this regime an electron scatters many times against other electrons before hitting the boundary. Electron-electrons collisions effectively screen the boundaries, avoiding momentum losses for electrons flowing in the central part of the channel. In this situation resistivity decreases when the e-e collision rate increases because the screening becomes more and more effective. When the hydrodynamic regime is fully developed, i.e. when $K \ll 1$, this effect can be described as a decrease of the kinematic viscosity $\nu = v_F \ell_{ee}/4$ when $\ell_{ee}$ becomes shorter, as explained in Sec. 2.2.4 of Chapter 2.

Electron-electron collisions rate strongly depends on the temperature, with collisions becoming more frequent when temperature is raised. At low temperature $\ell_{ee}$ diverges as $T^{-2}\ln(T)$ making e-e scattering ineffective. This happens because of the kinematic constraints on the phase space allowed for e-e collision imposed by the sharp Fermi surface.

On these grounds we can expect the resistivity of the channel to be increasing with the temperature in the low-temperature Knudsen regime, to reach a maximum when $K \approx 1$ and then to decrease when the temperature is further raised bringing the electrons in the hydrodynamic regime.

Considering momentum-relaxing collisions modifies this picture in two ways. First, they add a contribution to the resistivity that is monotonically increasing with temperature, and, second, they help establishing the local equilibrium, shifting the transition to the hydrodynamic regime to lower temperatures. When bulk, momentum relaxing, collisions are taken into account the definition of the Knudsen number $K$ should be modified according to $K = \ell_{tot}/W$, where $\ell_{tot} = (\ell_{ee}^{-1} + \ell^{-1})^{-1}$, $\ell$ being the mean-free-path for momentum-non-conserving collisions.

The resistivity contribution arising from momentum-relaxing collisions can be large, especially in wide samples, and fast growing with temperature, completely obscuring the non-monotonic behavior of the resistivity related to the Gurzhi effect. This is the reason why Gurzhi effect was so hard to observe, and has been found only in very clean materials as the GaAs heterostructures used in Ref. [8], and in ultra-clean encapsulated graphene samples, as shown in Ref. [11].

To see a clear signature of the Gurzhi effect it is necessary to minimize the resistivity contribution arising from momentum-non-conserving collisions. The authors of Ref. [8] used two expedients to achieve this result. First, they used an electrostatically defined channel in a 2D GaAs/AlGaAs heterostructure. These structure host the cleanest electronic systems ever realized, with low-temperature mobilities exceeding $10^7$ cm$^2$/(V $\cdot$ s) [100, 101]. Second, they raised the temperature of the electron system only, by driving an heating current, while keeping the lattice temperature low. This allows to sweep the electron temperature across the transition between the Knudsen and the Gurzhi regime while preventing the momentum-relaxing scattering mechanism (especially phonon scattering), that depend mainly on the lattice temperature, from growing too fast with the temperature. The electron temperature can be directly measured as a function of the heating current by using two quantum point contacts on the sides of the channel. Measured electronic temperatures are found to be as high as 40 K above the lattice temperature. Similar results are shown in the Supplementary Material of Ref. [11] where h-BN encapsulated graphene samples are used. No signature of Gurzhi effect is found in the resistivity data as a function of the lattice temperature. However, when electrons are heated above the lattice temperature using a current the differential resistivity curves show the same behavior as in the experiment by De Jong and Molenkamp.

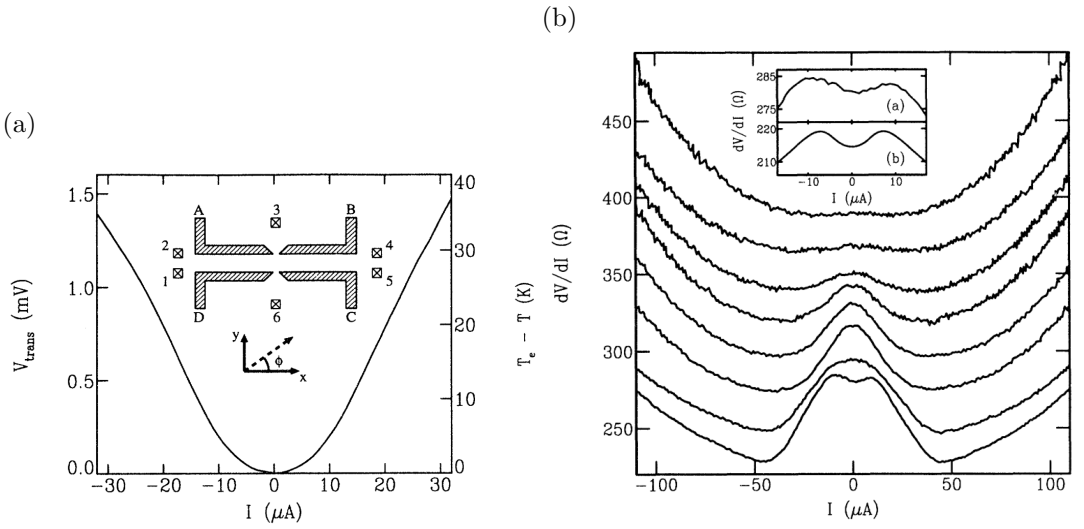


Figure 1.5: (a) Dependence of the theromovoltage $V_{\text{trans}} \equiv V_6 - V_3$ and of the difference between the electron and the lattice temperature $T_e - T$ on the heating current $I$, for $T = 1.5$ K. The inset shows the device geometry. (b) Differential resistance $dV/dI$ of the same device as a function of the current $I$ for lattice temperatures $T = 1.5,\ 4.4,\ 8.7,\ 10.4,\ 13.6,\ 17.3,\ 20.4,$ and 24.7 K. The top panel of the inset is a magnification of the 1.5 K curve. The bottom panel is the corresponding theory result. The Knudsen regime, i.e. the initial increase of the differential resistivity for small current is seen only in the 1.5 K in this sample. The Gurzhi regime, marked by a negative slope of the differential conductivity, is preserved up to 13.6 K and originates a minimum in $dV/dI$ [9]. For higher lattice temperatures the sample is already in the phonon-dominated regime, even for small applied currents. Taken from Ref. [8]

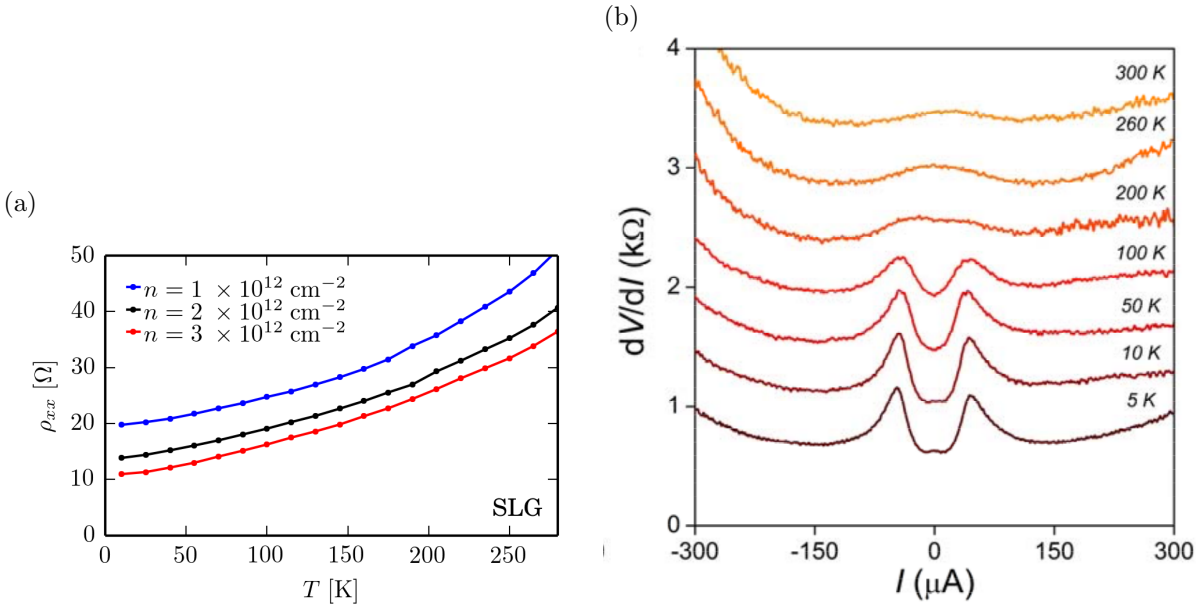


Figure 1.6: (a) Resistivity of a sample of h-BN-encapsulated Single Layer Graphene as a function of temperature for different carrier density. The resistivity grows smoothly with temperature as a consequence of enhanced electron-phonon scattering, no Gurzhi-like anomaly can be seen. (b) Differential resistance measurements in a p-doped SLG sample with width $W = 2.5$ $\mu$m, carrier density is $n = -4 \cdot 10^{11}$ cm$^2$/(V $\cdot$ s). Measurements are taken with a probe current $I_{\text{ac}} = 50$ nA in a four-probe configuration with voltage probes separated by 8 $\mu$m. Curves are offset by 300 Ω for the sake of clarity. Note the different temperature scale compared to Fig. 1.5-b. Here the positive initial slope associated to the Knudsen regime is preserved up to 100 K, while the negative slope of the differential resistance associated to the Gurzhi effect persists up to 300 K. Taken from Ref. [11]

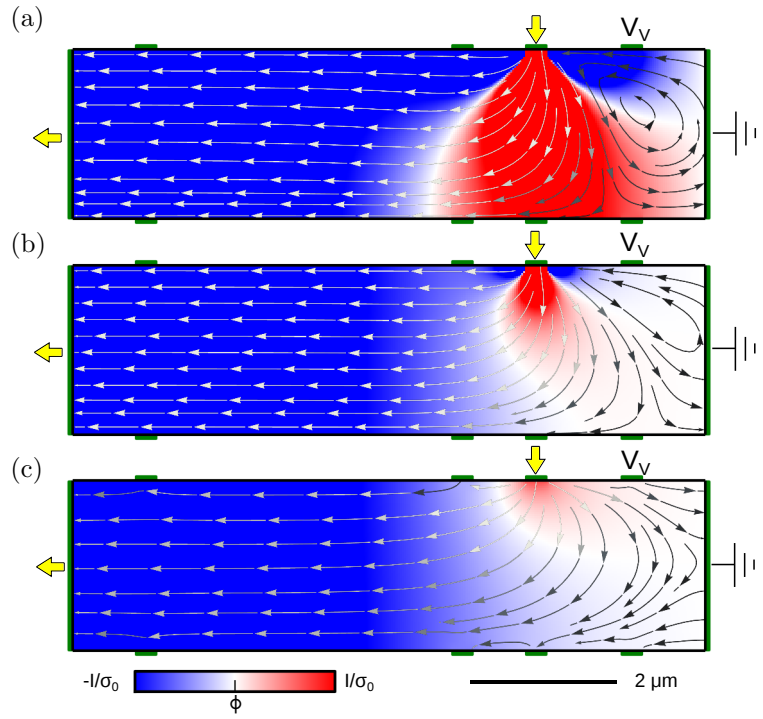


Figure 1.7: Experimental geometry used in Ref. [11]. One dimensional contacts to the graphene sheet [7] are shown in green. A current $I$ is injected from a side contact (yellow arrow on the top side of the Hall bar) and drained from the large contact on the left of the bar. The voltage $V_{\rm v}$ is measured at a nearby contact with respect to the grounded reference contact on the right of the Hall bar. The colorscale shows the values of the electric potential calculated numerically using hydrodynamic equations for three different values of the parameter $D_\nu = 2.3,\ 0.7,$ and $0$ $\mu$m (from top to bottom). Corresponding streamlines of the current are also shown, their color changes from black (low current intensity) to white (high current intensity). Adapted from Ref. [11].

### 1.2.2 Negative local resistance caused by viscous electron backflow in graphene

In the experiments of Ref. [11] electron hydrodynamics is addressed by using a special measurement geometry that amplifies effects of the shear viscosity. A viscous flow can lead to vortices appearing in the spatial distribution of the steady-state current. Such 'electron whirlpools' have a spatial scale $D_\nu = \sqrt{\nu\tau}$, which depends on electron-electron scattering through the electron liquid kinematic viscosity $\nu$ and on the electron system's quality through $\tau$, the scattering time for momentum-non-conserving collisions. To detect the whirlpools, electrical probes should be placed at a distance comparable to $D_\nu$. By using single- and bi-layer graphene (SLG and BLG, respectively) encapsulated between boron nitride crystals, $D_\nu$ of $0.3 - 0.4$ $\mu$m could be reached thanks to high viscosity of graphene's Fermi liquid and its high carrier mobility even at high $T$. For $\nu = 0.1$ m$^2$s$^{-1}$, as estimated in [102], and $\tau = 1.5$ ps (as extracted by resistivity measurements), we find $D_\nu \approx 0.4$ $\mu m$.

Such large $D_\nu$, unique to graphene, still necessitates submicron resolution to probe the electron backflow. To this end, multiterminal Hall bars with narrow ($\approx 0.3$ $\mu$m) and closely spaced ($\approx 1$ $\mu$m) voltage probes were fabricated. All the devices were first characterized in the standard geometry by applying a current $I$ along the main channel and using side probes for voltage measurements. At liquid-helium temperature, the devices exhibited $\mu = 1 - 5 \cdot 10^5$ cm$^2 \cdot$ V$^{-1} \cdot$ s$^{-1}$ over a wide range of carrier concentrations $n \approx 10^{12}$ cm$^{-2}$, and $\mu$ remained above $5 \cdot 10^4$ cm$^2 \cdot$ V$^{-1} \cdot$ s$^{-1}$ up to room $T$. Such $\mu$ allow ballistic transport with $\ell > 1$ $\mu$m at $T < 300K$. On the other hand, at $T \geq 150$ K $\ell_{\rm ee}$ decreases down to $0.1 - 0.3$ $\mu$m over the same range of $n$. This allows the essential condition for electron hydrodynamics (1.13) to be met.

Viscosity has little effect on resistivity in the conventional longitudinal geometry, essentially because

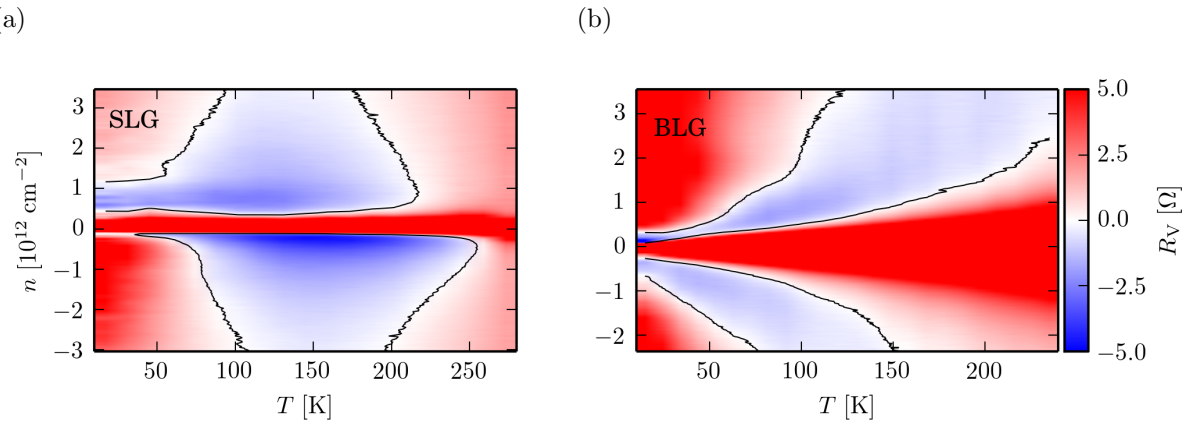


Figure 1.8: Vicinity resistance maps. (a and b) $R_v(n,T)$ for SLG and BLG, respectively; the same color coding for the $R_v$ scale. The black curves indicate zero $R_v$. For each $n$ away from the CNP, there is a wide range of $T$ over which $R_v$ is negative. $W = 2.5$ $\mu$m and $L = 1$ $\mu$m for the SLG device; $W = 2.3$ $\mu$m and $L = 1.3$ $\mu$m for the BLG one. All measurements presented for BLG were taken with zero displacement between the graphene layers. Taken from Ref. [11]

the flow in this geometry is uniform whereas the total momentum of the moving Fermi liquid is conserved in electron-electron collisions. This allows to extract $\tau$ directly from four-point resistivity measurements.

The only evidence for hydrodynamics found in the longitudinal geometry was the Gurzhi effect that appeared as a function of the electron temperature controlled by applying large $I$, similar to the observations of Ref. [8], as shown in Fig. 1.6-b.

To reveal hydrodynamic effects the geometry depicted in Fig. 1.7 was used. In this case $I$ is injected through a narrow constriction into the graphene bulk, and the voltage drop $V_v$ is measured at the nearby side contacts located at the distance $L \approx 1$ $\mu$m away from the injection point. To distinguish from the proper nonlocal geometry [103], the linear-response signal measured in this geometry is dubbed "vicinity resistance", $R_v = V_v/I$. The idea is that, in the case of a viscous flow, whirlpools emerge as shown in Fig. 1.7, and their appearance can then be detected as sign reversal of $V_v$, which is positive for the conventional current flow (Fig. 1.7-c) and negative for viscous backflow (Fig. 1.7-a-b). The relation between the appearing of a current vortex and a negative $V_v$ is discussed in details in [104] and in Chapter 2 of this Thesis.

Figure 1.8 shows maps of $R_v$ for a SLG and a BLG device as a function of carrier density $n$ and temperature $T$, other SLG and BLG devices, (for a total of seven different devices with $W$ ranging from 1.5 to 4 $\mu$m) exhibited similar behavior. Away from the Charge Neutrality Point (CNP), $R_v$ is indeed negative over a wide range of intermediate $T$. The two Fermi liquids exhibited somewhat different behavior reflecting their different electronic spectra but $R_v$ was negative over a large range of $n$ and $T$ for both of them. The same anomalous vicinity response is also be observed following the recipe of [8] and using the current $I$ to increase the electron temperature. In this case, $V_v$ changed its sign as a function of $I$ from positive to negative to positive again, reproducing the behavior of $R_v$ with increasing $T$ of the cryostat.

Comparing Figs. 1.8 and 1.6, it is clear that the vicinity geometry strongly favors the observation of hydrodynamics effects so that the measured vicinity voltage changed its sign whereas in the standard geometry the same viscosity led only to relatively small changes in $dV/dI$. The magnitude of negative $R_v$ is also found to decay rapidly with $L$, in agreement with the finite size of electron whirlpools.

Negative resistances can in principle arise from other effects such single-electron ballistic transport or quantum interference. The latter contribution is easily ruled out because quantum corrections rapidly wash out at $T > 20$ K and have a random sign that rapidly oscillates as a function of magnetic field. Also, performing numerical simulations using the Landauer-Büttiker formalism and the realistic device geometry [105] it can be shown that no negative resistance could be expected for the vicinity configuration in zero magnetic field.

Moreover the authors provided even more solid experimental evidence that the observed negative resistance cannot be attributed to ballistic effects.

First, the dependencies of the negative vicinity signal on $T$, $n$, $I$ and the device geometry allowed to unambiguously rule out any such contribution. For example, the single-electron ballistic phenomena

should become more pronounced for longer $\ell$ (that is, with decreasing $T$ and with increasing $n$), in stark contrast to the non-monotonic behavior of $V_v$.

Second, as a final proof, devices with a narrow cut between the injection contact and the vicinity voltage probe were fabricate. The cut screens the vicinity contact from the current whirlpool but does not screen electrons reflected from the opposite side of the device. In these devices no negative vicinity resistance was observed, in agreement with the prediction of hydrodynamics.

For experimentally relevant values of $D_\nu$, a vortex appears in the vicinity of the current-injecting contact. This is accompanied by the sign reversal of $V_v$ at the vicinity contact on the right of the injector, which is positive in Fig. 1.7-c (no viscosity) but becomes negative in Figs. 1.7-a and b. Because both $\nu$ and $\tau$ decrease with increasing $T$, $D_\nu$ also decreases, and stray currents start to dominate the vicinity response at high $T$. This explains why $R_V$ in Fig. 1.8 becomes positive close to room $T$, even though the hydrodynamic description has no high temperature cutoff. On the other hand, at low $T$ the electron system approaches the Knudsen regime and our hydrodynamic description becomes inapplicable because $\ell_{ee} \approx W$. In the latter regime, the whirlpools should disappear and $R_v$ become positive, in agreement with the experiment and numerical simulations based on the Landauer-Büttiker formalism.

Details of predictions of hydrodynamic theory for the vicinity resistance in this geometry are discussed in Chapter 2 and in Ref. [96] based on a fully analytical theory. In brief, current $I$ injects vorticity at the source contact, which then exponentially decays over the length scale $D_\nu$. The final result can be expressed as a quadratic relation between $D_\nu$ and $R_v$ in the form

$$R_v = (b + aD_\nu^2)\sigma_0^{-1}, \tag{1.14}$$

where $a$ and $b$ are numerical coefficients dependent only on the measurement geometry and boundary conditions, $b$ describes the Ohmic contribution from stray currents, and $\sigma_0$ is the conductivity inferred from four-point resistance measurements. For the specific device in Fig. 1.7, numerical simulations including all details of the sample geometry yield $a = -0.29\ \mu\text{m}^{-2}$ and $b = 0.056$ ($a = -0.29\ \mu\text{m}^{-2}$ and $b = 0.059$ are obtained using the fully analytical theory in Chapter 2). This allows to estimate $D_\nu(n, T)$ from measurements of $R_v$.

For the known $\tau$ and $D_\nu$, it is possible to find $\nu$. The results are plotted in Fig. 1.9 for the same SLG and BLG devices as in Fig. 1.8. It shows that, at carrier concentrations $n \approx 10^{12}\ \text{cm}^{-2}$ the Fermi liquids in both SLG and BLG are highly viscous with $\nu \approx 0.1\ \text{m}^2\text{s}^{-1}$. For the sake of comparison, liquid honey has typical viscosities of $\nu \approx 0.002 - 0.005\ \text{m}^2\text{s}^{-1}$. Figure 1.9 also plots results of fully-independent microscopic calculations of $\nu(n, T)$, which were carried out by extending the many-body theory of Ref. [102] to the case of 2D electron liquids hosted by encapsulated SLG and BLG. Within the range of applicability of this analysis in Fig. 1.9 ($n \approx 10^{12}\ \text{cm}^{-2}$), the agreement in absolute values of the electron viscosity is good, especially taking into account that no fitting parameters were used in the calculations. Because the strong inequality $\ell_{ee} \ll \ell$ required by the hydrodynamic theory cannot be reached even for graphene, it would be unreasonable to expect better agreement. In addition, this analysis does not apply near the CNP because the theory neglects contributions from thermally-excited carriers, spatial charge inhomogeneity and coupling between charge and energy flows, which can play a substantial role at low doping [42, 87, 106].

### 1.2.3 Super-ballistic flow of viscous electron fluid through graphene constrictions

As explained before, electron-electron collisions do not affect the resistance of a bulk sample, and affect the resistance of a channel of finite width $W$ only in cooperation with boundary scattering. For a sample with perfectly specularly reflecting edges electron-electron collisions become irrelevant, even for a finite $W$.

To enhance hydrodynamic effects it is necessary to use a different geometry featuring a non uniform flow pattern irrespective of the edge scattering. The first attempt in this sense was done by authors of Ref. [11] that suggested the "vicinity geometry" measurements.

Recently, Krishna Kumar et al. [12], elaborated on this idea and proposed a different geometry based on a channel with a constriction of width $w$. Here we describe briefly their findings.

A Point Contact PC is a narrow constriction between two wide conducting regions [107]. The shape of a device featuring several point contacts is shown in Fig. 1.10. If collisions can be neglected the

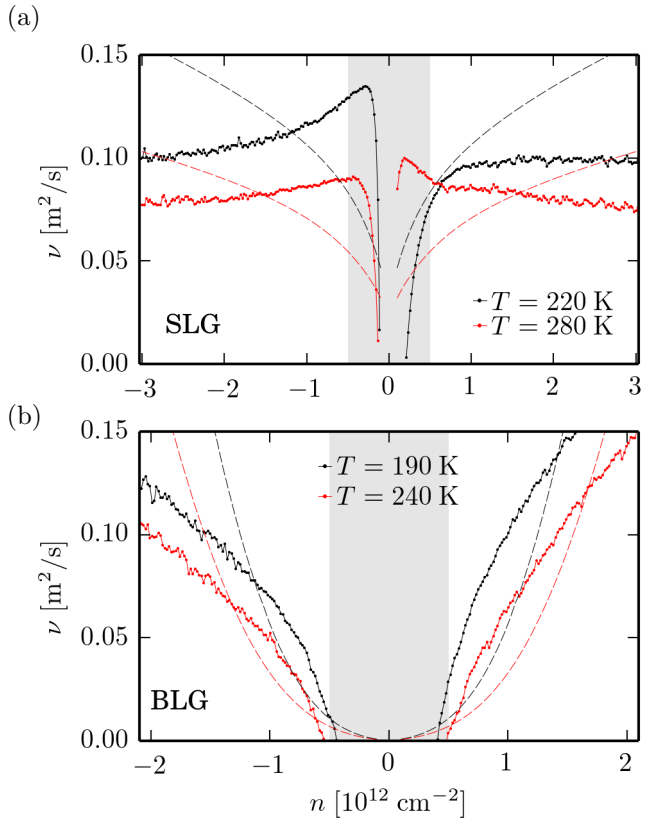


Figure 1.9: Viscosity of the Fermi liquids in graphene. (a and b) Solid curves: $\nu$ extracted from the experiment for SLG and BLG, respectively. Dashed: Calculations based on many-body diagrammatic perturbation theory [102] (no fitting parameters). The grey-shaded areas indicate regions around the CNP where the hydrodynamic model is not applicable. Taken from Ref. [11]

(a) (b)

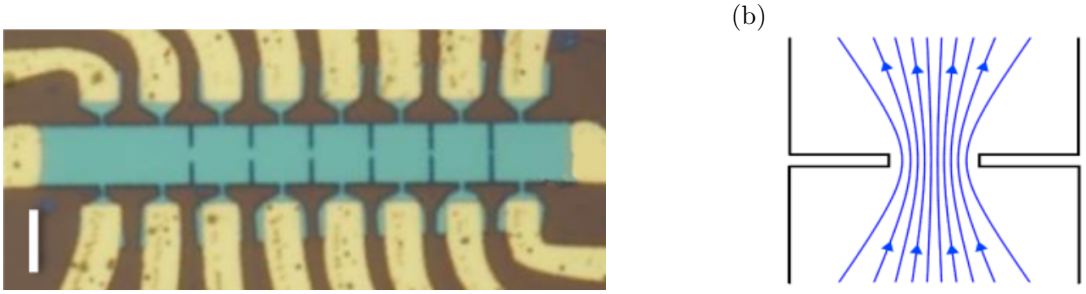

Figure 1.10: (a) Optical micrography of one of the devices used in Ref. [12]. The white scale bar is 5 $\mu$m. The left region is used to characterize the bulk resistivity of the sample by four-point measurements. The width of the point contacts varies from 1.2 $\mu$m (left) to 0.1 $\mu$m (right). (b) Schematic of viscous flow through a constriction. Taken from Ref. [12].

conductance of a PC is given by the Sharvin formula [108, 107], that is derived by counting the ballistic channel available for conduction. For a graphene PC this reads

$$G_{\rm b} = \frac{4e^2}{h}\frac{w\sqrt{\pi|n|}}{\pi}, \tag{1.15}$$

where $w$ is the width of the constriction and $n$ is the electron density. All the PC studied in Ref. [12] are in the classical regime $k_{\rm F}w \gg 1$ in which a large number of channels is available for conduction and no conductance quantization effect is expected. As shown in Fig. 1.11-a the low-temperature value of the PC resistance is well captured by Sharvin formula.

Experimental data in Fig. 1.11-a display a non-monotonic behavior of the PC resistance as a function of temperature with $R_{\rm pc}$ reaching a minimum around 100 K. The minimum value of $R_{\rm pc}$ is lower than the ballistic prediction of the Sharvin formula, that represent the maximum conductance for non-interacting electrons. This super-ballistic behavior is therefore attributed to interactions.

The presence of this minimum can again be explained in terms of Gurzhi effect [9, 10]. Raising the temperature e-e collision establish a local equilibrium and the electron flow organizes itself into low velocity streams that flow near the boundary protecting the high-velocity current-carrying stream that flows in the center of the constriction from boundary scattering (Fig. 1.10).

A quantitative theory of Gurzhi effect in this geometry can be found in [109, 110]. The conductance of a PC in the hydrodynamic regime ($\ell_{\rm ee} \ll w$), neglecting momentum-non-conserving collision is [110]

$$G_{\rm v} = \frac{4e^2}{h}\frac{\pi w^2\sqrt{\pi|n|}v_{\rm F}}{64\nu}, \tag{1.16}$$

To take into account the transition between ballistic and hydrodynamic regime and the impact of momentum-non-conserving electron-phonon collisions the resistance of the PC can be expressed as [110]

$$R_{\rm pc} = (G_{\rm b} + G_{\rm v})^{-1} + b\rho_{xx}. \tag{1.17}$$

Here $\rho_{xx}$ is the resistivity inferred by four point measurements in the unpatterned region of the sample, while $b$ is a numerical coefficient that is found by solving the Poisson equation in the actual device geometry.

The above expression with $G_{\rm b}$ given by the Sharvin formula 1.15 and $G_{\rm v}$ given by 1.16 can be used to obtain the value of the electron liquid viscosity. The result is shown in Fig. 1.11-b. The agreement with calculations based on many-body theory [102] is remarkable.

### 1.2.4 Observation of the Dirac fluid and the breakdown of the Wiedemann-Franz law in graphene

All the original results of this Thesis focus on the doped, or Fermi Liquid (FL), regime, where the chemical potential is larger than both the thermal energy $k_{\rm B}T$ and the characteristic energy of the disorder-induced chemical potential fluctuations [80, 111, 112, 113].

However, another interesting hydrodynamic theory can be developed to describe the undoped regime where the thermal energy is larger than both the average value chemical potential and the amplitude of

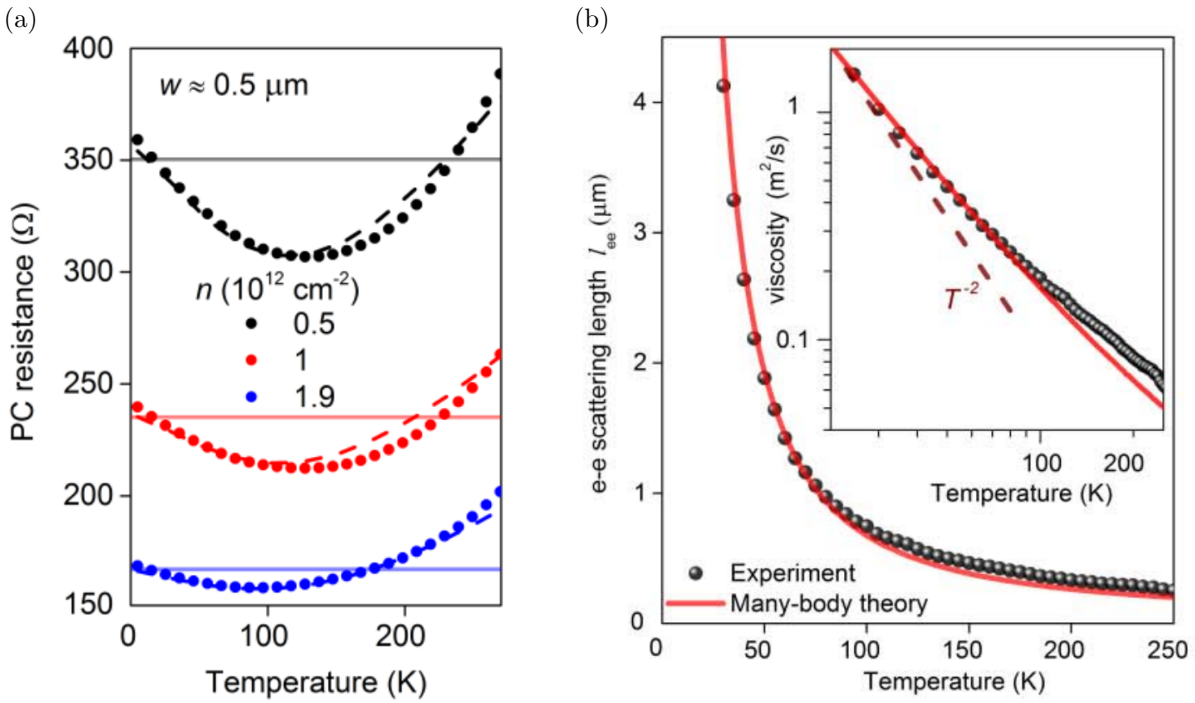


Figure 1.11: (a) $R_{\rm pc}(T)$ for a 0.5 $\mu$m constriction at representative carrier densities. Dots: Experimental data. Horizontal lines: Ballistic resistance given by Sharvin formula. Dashed curves: Theoretical prediction for a viscous electron fluid, using simplified expressions for the temperature dependence of e-e and electron-phonon scattering $T^{-2}$ and $T^{-1}$, respectively. (b) $T$ dependence of the e-e scattering length found as $\ell_{\rm ee} = 4\nu/v_{\rm F}$ (symbols) for $n = 10^{12}$ cm$^{-2}$ and $w \approx 0.5$ $\mu$m. Red curve: Microscopic calculations of $\ell_{\rm ee}$ [102]. Inset: $\nu(T)$ on a log-log scale. The data are from the main panel and color-coded accordingly. The dashed line indicates the $T^{-2}$ dependence. Taken from Ref. [12].

its fluctuation. In this regime electrons and holes are present together, as a result of thermal excitation, and form an electron-hole plasma, also known as Dirac Fluid (DF).

This regime is particularly suitable for an hydrodynamic description, because carriers are expected to collide very frequently [114], but the large density fluctuations induced by poorly screened external impurities complicate the theoretical analysis and the interpretation of experimental results.

For generic doping an hydrodynamic theory of transport in graphene must be formulated in terms of three independent currents [113]: the electric current, the energy current, and the particle imbalance current, as carefully explained in Refs. [87, 88]. In the FL regime studied in this Thesis all these three currents are proportional and transport can be described using a one-fluid model.

Another simplification happens exactly at the Dirac point. In this case the energy and particle imbalance currents are proportional and the system can be described using a two-fluids model.

The decoupling between charge and energy flow when passing from the FL to the DF regime is the key point to understand the experimental observations by Crossno et al. [13].

In the FL regime, where charge and energy current are proportionals, the electrical and (electronic) thermal conductivity are related by the Wiedemann-Franz law [115]

$$\frac{k_{\rm e}}{\sigma T} = \frac{\pi^2 k_{\rm B}^2}{3e^2} \equiv \mathcal{L}_0, \tag{1.18}$$

where $k_{\rm e}$ is the electronic thermal conductivity, $\sigma$ is the electrical conductivity, $T$ is the temperature, and $\mathcal{L}_0$ is the Lorenz number that depends only on fundamental constants. This strong prediction of the Fermi liquid theory has been verified in many different setups and has been shown to be very robust.

However, in the DF regime this prediction is violated. Authors of Ref. [13] measured independently the electrical and thermal conductivity of an ultra-clean graphene sample and found large violations of the WF law, with $k_{\rm e}$ being as high as twenty times the value predicted by the WF law. Figure 1.12 shows the ratio between the experimentally measured Lorenz number $\mathcal{L} \equiv k_{\rm e}/(\sigma T)$ and its value $\mathcal{L}_0$ predicted

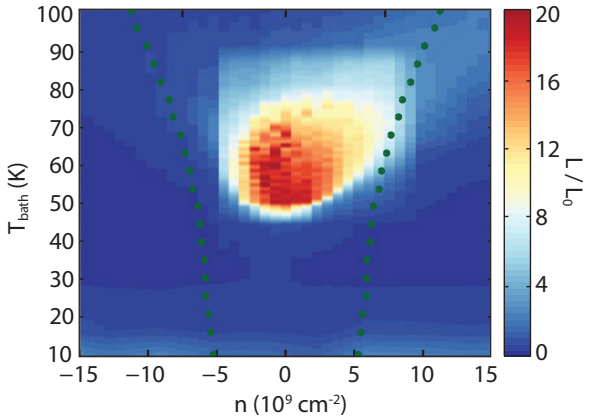


Figure 1.12: Lorenz number anomaly as a function of electron density and temperature. Taken from Ref. [13].

by the WF law.

The reason behind this striking violation is the following [116, 42]. The Dirac Fluid is made up of electrons and holes. If an electric field is applied electrons and holes are pushed in opposite directions. Collisions between electrons and holes generate a friction that manifests itself in an electron-electron contribution to the resistivity even in bulk samples. Conversely, if a temperature gradient is applied, electrons and holes move in the same direction resulting in no electron-hole friction. By this mechanism thermal conductivity is enhanced with respect to electric conductivity and produces a Lorenz ratio higher than the WF prediction.

### 1.2.5 Evidence for hydrodynamic electron flow in $PdCoO_2$

Hydrodynamic electron flow in solid state requires electron-electron collisions to be much faster than momentum-non-conserving collisions with phonons and impurities. It is therefore natural to look for signatures of hydrodynamic behavior in ultra-high quality materials.

Beside GaAs heterostructures [100, 101] used in [8] and hBN-encapsulated graphene used in [11, 12, 13], also Palladium cobaltate hosts a very high-quality electron system. Moll et al. [14] found evidences of hydrodynamic electron transport in ultra-pure samples of $PdCoO_2$.

$PdCoO_2$ is a layered material with a remarkably simple electronic structure with only one band crossing the Fermi level [117]. Its conduction properties are strongly anisotropic, with a ratio between the in-plane and out-of-plane conductivities as high as $10^3$ [118]. Its resistivity saturates around 15 K to its low temperature value that can be, in the best samples, as low as $10^{-8}\ \Omega\cdot$cm [117]. Comparison of the mean-free-path extracted from the resistivity, that is sensitive only to processes that relax momentum, to the mean-free-path extracted from the analysis of de Haas-van Alphen oscillation, that is sensitive to all scattering processes, shows that momentum-relaxing collisions are indeed slower than momentum-conserving processes [117].

In Ref. [14] two experiments were made to highlight hydrodynamic effects. First, the resistivity of thin wires was measured as a function of the wire width by successively etching the wire by Focused Ion Beam etching, to reduce progressively the wire width.

Second, Shubnikov-de Haas oscillations were observed in a meander-shaped sample.

An increase of the resistivity is observed when the wire is thinned down from a width of 60 $\mu$m to a width of 0.7 $\mu$m.

Combining the results of the two experiments provided convincing evidence that the increase of resistivity can be attributed to the viscous flow trough a narrow channel.

## 1.3 Experimental evidence for long-lived plasmons in graphene

Plasmons are collective charge density oscillations [35, 119] that occur in metals and doped semiconductors at frequency higher than the single-particle intraband excitation frequency. They are sustained by the Coulomb repulsion between electrons that tends to restore charge neutrality when a inhomogeneity is introduced in an electron system.

Bulk and surface plasmons in ordinary, highly-conductive, three dimensional metals, like copper, aluminum or noble metals, have been known for a very long time [120] and have been probed using different optical techniques [121, 122, 123] and electron energy-loss experiments [124].

The availability of 2D electron systems in semiconductor heterostructures [100, 101] and on the surface of liquid $He_3$ [125] sparked the experimental [125, 126, 123] and theoretical [127, 128, 129, 130, 131, 132] interest for plasmons and magnetoplasmons in these systems.

More recently surface-plasmons in metals (and surface-plasmon polaritons, resulting from the hybridization of surface plasmons with photons) have been used in a variety of applications ranging from lasers waveguides [133] to biosensors [134] and quantum-information [135], establishing plasmonics as an independent research field [136].

It is therefore no surprise that when truly 2D (i.e. one or few atom thick) materials became available they were considered as a new interesting plasmonic platform. Graphene plasmons [50, 137, 138] in particular attracted a lot of attention because they can be used to confine light on a length much smaller than the free-space wavelength [139], they can travel long distances [18], and can enhance the optical absorption of graphene from the $\approx 2.3\%$ value due to interband absorption to nearly 100% in patterned graphene structures [140, 141], improving the efficiency of graphene-based photodetectors [142] and photovoltaic devices.

In this Section we give a brief introduction to Graphene Plasmons (GPs) focusing on the experimental techniques used to probe GPs. These fall into two main categories: far-field techniques and near-field techniques. We discuss advantages and drawbacks of both types of methods but we focus in particular on the scattering-type Scanning Near Field Optical Microscope (s-SNOM) because it is the most relevant technique for the plasmon scattering experiments discussed in Chapter 3.

The simplest model for graphene plasmons, that considers only the intraband optical conductivity (First term in Eq. 1.8) and neglects interband transitions, non-local effects, retardation effects, and damping, predicts a dispersion relation for plasmons in graphene encapsulated between two uniform dielectrics given by [43, 143, 44]

$$\omega_{\rm pl}(q) = \sqrt{\frac{2e^2 E_{\rm F} q}{\hbar^2 \bar{\epsilon}}}, \tag{1.19}$$

where $q$ is the in-plane plasmon wavevector and $\bar{\epsilon}$ is the average dielectric constant of the media underneath and above the graphene flake. The $\sqrt{q}$ dependence of the plasmon frequency is common to every 2D electron system. The carrier density dependence $\omega_{\rm pl}(q) \propto n^{1/4}$, is instead peculiar of graphene, and different from the $\omega_{\rm pl}(q) \propto n^{1/2}$ dependence in parabolic-band 2D electron systems [35].

In the range of wavevectors where Eq. 1.19 is valid the plasmon dispersion falls well below the photon dispersion $\omega = cq$ (the hybridization of plasmons with photons that occurs when the plasmon dispersion approaches the light cone is discussed in Appendix A). This means that for a given frequency plasmons have a larger wavevector, or equivalently a shorter wavelength, than the corresponding photon.

The capacity of shrinking light is quantified by the compression factor $\beta \equiv \lambda_0/\lambda_{\rm pl}$, where $\lambda_0$ is the photon wavelength and $\lambda_{\rm pl}$ is the plasmon wavelength. Values of $\beta$ as high as 150 have been achieved using graphene plasmons [18].

This difference in wavelength is interesting from the point of view of application because it allows to shrink the size of optoelectronic components (a concrete example of a phase modulator with a footprint of only 350 nm operating on a wavelength of 10.6 $\mu$m [19] is discussed in Chapter 3) and to concentrate energy in small volumes, but forbids direct excitation of plasmon using photons because of wavevector mismatch.

All the techniques discussed in the following use a different method to overcome the wavevector mismatch.

Plasmons as collective modes of a many-body system have a finite lifetime. Mathematically this is represented by a positive imaginary part of the frequency $\omega_{\rm pl}(q)$. Another important figure of merit for plasmons is their lifetime $\tau_{\rm p}(q) \equiv /(2\Im m[\omega_{\rm p}(q)])$ or, equivalently, the inverse damping ratio $\gamma_{\rm p}^{-1}(q) \equiv \Re e[\omega_{\rm p}(q)]/(2\Im m[\omega_{\rm p}(q)])$ [17]. Lifetime of plasmons in graphene is limited by different factors [144]:

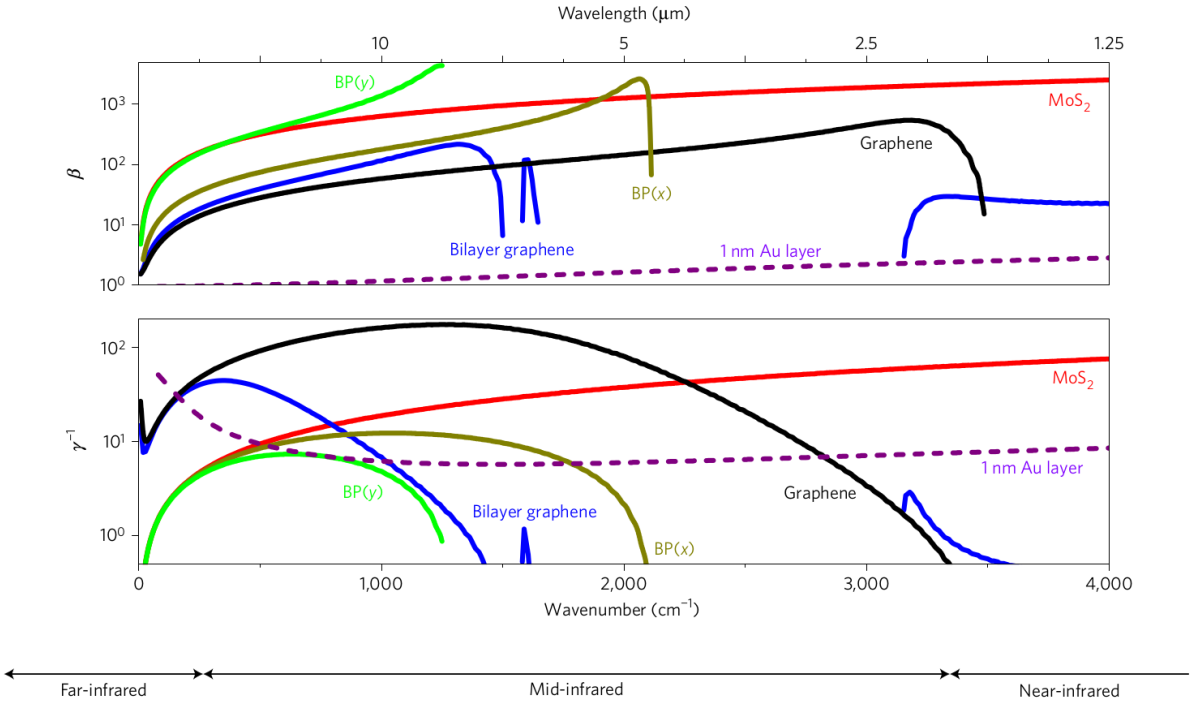


Figure 1.13: Comparison of confinement factors $\beta$ and inverse damping ratios $\gamma^{-1}$ for different two dimensional materials. Corresponding values for a 1 nm gold film are shown for comparison. Taken from Ref. [152]

interaction with disorder [145], phonons [146, 147], and intrinsic many-body effects [148]. Plasmons in samples deposited on a substrate or encapsulated between dielectrics can also suffer from losses due to energy absorption in the surrounding dielectrics [52].

Even if it is not rigorously possible to identify the plasmon lifetime $\tau_p(q)$ with the d.c. transport time $\tau$ extracted from mobility measurements [7] the two quantities are typically of the same order of magnitude, since they are limited by the same physical mechanisms [145, 147].

Typically there is a trade-off between compression $\beta$ and lifetime $\gamma^{-1}$. Very long lifetimes are possible near the light cone where the modes are essentially photon-like, but this comes at the price of compression factors $\beta$ only slightly larger than unity. Figure 1.13 shows the values of $\beta$ and $\gamma^{-1}$ for different two-dimensional materials as a function of frequency. These data highlight the potentiality of 2D materials to outperform conventional metals as plasmonic materials for many optoelectronic [149, 19] and biosensing [150, 151] applications.

### 1.3.1 Graphene plasmons in far-field experiments

Graphene plasmons are not visible in transmission or reflection experiments of uniform samples. This happens because translational invariance forces momentum conservation and the plasmon and photon wavevectors are very different. The transmission spectrum of an unpatterned graphene sample is therefore dominated by the Drude peak at low frequencies and by the constant interband absorption at frequencies greater than twice the Fermi energy (see Eq. 1.9 and Appendix A).

To study graphene plasmons using far-field radiation it is necessary to couple the radiation to plasmons. This can be done using prism coupling [153] in the Otto configuration [121] (the Kretschmann configuration is not suitable for strictly 2D materials), that allows an increase of photon wavevector up to a factor $n$, where $n$ is the refracting index of the prism. Prism-coupling has been used to probe TE modes in graphene [154, 155] and to build very sensitive Attenuated Total Reflection biosensors [150]. This technique has the advantage of requiring no fabrication or patterning process on the material under study but it is intrinsically limited to the study of modes with wavevectors smaller than $n\omega/c$.

Alternatively one needs to break translational invariance. The simplest way to do it consists in introducing a periodicity in one direction. This can be done by using a grating [156] or by patterning the

graphene itself [15, 141]. In a structure with linear periodicity $a$ the wavevector needs to be conserved only up to an integer multiple of $2\pi/a$, allowing coupling to the plasmons. The simplest example of a periodic structure is an array of graphene nanoribbons. This has been used in Ref. [15] to probe plasmonic resonances and their tunability with the gate voltage. This technique allows to probe high momentum plasmons using sufficiently narrow ribbons. The main disadvantage is that it requires a nanofabrication step. This introduces defects in the graphene sheet. Moreover the inaccuracy on the ribbons width (that must be of the same order of the plasmon wavelength, typically around 100 nm) introduces inhomogeneous broadening of the plasmon resonances.

### 1.3.2 Plasmons in near-field experiments. The s-SNOM technique

A more modern approach, that is also more relevant for this Thesis, consists in using the scattering-type Scanning Near Field Optical Microscope [16, 17, 157, 18, 158, 159, 160]. In this technique the required momentum to couple plasmons to light is provided by the sharpness of a metalized Atomic Force Microscope (AFM) tip. Since the radius of the tip is $a \approx 10$ nm ths s-SNOM technique is able to probe plasmons at wavectors up to $\approx 1/a \approx 10^6$ cm$^{-1}$.

The experimental setup works as following. A laser beam of the desired frequency is focused by a parabolic mirror on a metalized tip of an AFM. The sharpness of the tip locally enhances the field (around a factor 20) and provides the momentum to excite plasmons. Plasmons are therefore launched around the tips as cylindrical waves. These are reflected back by the boundaries of the sample toward the tip, part of the scattered field is reflected back by the tip and recollected by the parabolic mirror.

The amplitude and phase of the scattered signal are then measured at the same time using pseudo-heterodyne detection. The latter employs a beam-splitter, a vibrating mirror, and a photodetector in the configuration shown in Fig. 1.14.

Moving the s-SNOM tip across the sample allows to obtain a real-space image of the propagating plasmons [17, 16, 18], with a resolution limited only by the tip radius, and to measure their wavelength and decay length. Alternatively, plasmons can be launched by metallic contacts deposited on the sample

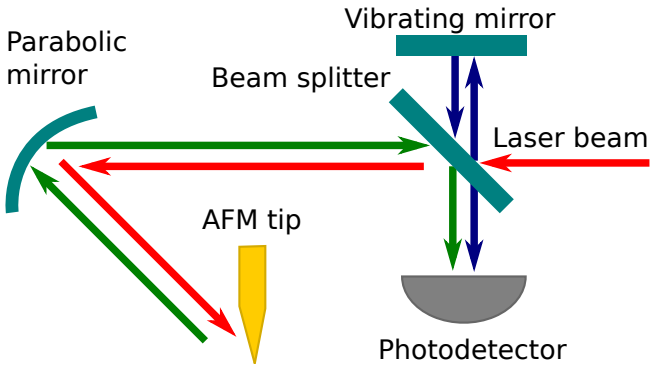


Figure 1.14: Schematic of the s-SNOM setup. The incoming beam path is represented in red, the scattered beam is represented in green, while the reference beam used for the pseudo-heterodyne detection is represented in blue.

acting as antennas [157, 19], and the tip is used only for detection.

Another interesting way of using the s-SNOM to study plasmon consists in using photocurrent nonoscopy [158, 159, 160]. In this case the tip is used to launch plasmons and is scanned across the device and the induced photocurrent between two regions of the sample having different elecronic density is measured.

Photocurrent maps can be acquired at the same time of the optical signal map and of the AFM topography. The three technique provide complementary information that allow a better characterization of the device properties.

# Chapter 2

# Hydrodynamic transport in encapsulated graphene

Transport in systems with many particles (such as gases and liquids) undergoing very frequent inter-particle collisions has been studied for more than two centuries and is described by the theory of hydrodynamics [73]. In the hydrodynamic regime, transport is described by [73] three non-linear partial-differential equations—the continuity, Navier-Stokes, and energy-transport equations—reflecting the conservation of mass, momentum and energy, respectively. The Navier-Stokes equation contains three transport coefficients [73]: the shear viscosity, $\eta$, which describes friction between adjacent layers of fluid moving with different velocities, and the bulk viscosity, $\zeta$, which describes dissipation arising in a liquid due to homogeneous compression-like deformations, and the Hall viscosity $\eta_{\mathrm{H}}$ [161, 162, 163, 164] that controls a non-dissipative term in the viscous stress tensor that is allowed when time-reversal invariance is broken. The energy transport equation contains the thermal conductivity $\kappa$, which describes dissipative heat flow between regions with different temperatures. These coefficients quantify the tendency of the liquid to restore a homogeneous state in response to a velocity or thermal gradient: they therefore control the magnitude of non-local contributions to the linear-response functions of the liquid.

Recent years have witnessed a tremendous interdisciplinary interest in the hydrodynamic flow of strongly interacting quantum fluids. This interest was sparked by a series of results [165], which were obtained via the anti-de Sitter/conformal field theory (AdS/CFT) correspondence, for the shear viscosity of a large class of strongly interacting thermal quantum field theories. These efforts culminated in 2005 when it was conjectured [166] that all quantum fluids obey the following universal lower bound: $\eta/s \geq \hbar/(4\pi k_{\mathrm{B}})$, where $s$ is the entropy density. Note that this bound does not contain the speed of light, thereby explaining why the conjecture was extended also to non-relativistic quantum field theories. Fluids that saturate this bound have been dubbed "nearly perfect fluids" (NPFs) [167], i.e. fluids that dissipate the smallest possible amount of energy and satisfy the laws of hydrodynamics at distances as short as the inter-particle spacing. Currently, two laboratory systems come closest to saturating the AdS/CFT bound: i) the quark-gluon plasma [168], which is created at Brookhaven's Relativistic Heavy Ion Collider and at CERN's Large Hadron Collider by bashing heavy (e.g. gold and lead) ions together and ii) ultracold atomic Fermi gases [169, 170] (such as $^6$Li) close to a Feshbach resonance. Although mathematical counterexamples have appeared in the literature [171], there are no known experimental violations of the AdS/CFT bound.

Our work is motivated by the following questions: Do electron liquids display hydrodynamic behavior? If so, how can it be experimentally proven that the electron system has entered the hydrodynamic transport regime? Once in the hydrodynamic regime, how can the shear and Hall viscosity of an electron liquid be measured in a solid-state device? Can an electron liquid in a solid-state device be a NPF?

This chapter is organized as follows. In Sect. 2.1 we derive the hydrodynamic equations for a (2D) electron fluid, and the corresponding boundary conditions, starting from the semiclassical Boltzmann equation. In Sect. 2.2 we apply the hydrodynamic equations to different geometries with the aim of finding an experimental signature of the hydrodynamic transport regime and establishing an experimental protocol to measure the shear viscosity of the electron liquid. In Sect. 2.3 we do the same in the presence of an external, perpendicular, magnetic field with the aim of accessing experimentally the Hall viscosity in the regime of weak magnetic fields.

## 2.1 Derivation of the linearized hydrodynamic equations from the semiclassical Boltzmann equation

For sufficiently long-wavelength ($\lambda \gg 2\pi/k_{\rm F}$) and low-frequency ($\omega \ll 2E_{\rm F}/\hbar$, where $E_{\rm F}$ is the Fermi energy) perturbations, the response of a 2D electron system can be described by using the semiclassical Boltzmann equation [172]:

$$[\partial_t + \boldsymbol{v_p}\cdot\nabla_{\boldsymbol{p}} + \boldsymbol{F}(\boldsymbol{r},\boldsymbol{p},t)\cdot\nabla_{\boldsymbol{r}}]f(\boldsymbol{r},\boldsymbol{p},t) = S\{f\}(\boldsymbol{r},\boldsymbol{p},t)\ , \tag{2.1}$$

where $\boldsymbol{v_p} \equiv \nabla_{\boldsymbol{p}}\epsilon_{\boldsymbol{p}}$ is the electron velocity, $\epsilon_{\boldsymbol{p}}$ being the band energy, $\boldsymbol{F}(\boldsymbol{r},\boldsymbol{p},t) = -e[\boldsymbol{E}(\boldsymbol{r},t) + \boldsymbol{v_p}\times \boldsymbol{B}(\boldsymbol{r},t)/c]$ is the total force acting on electrons, $\boldsymbol{B}(\boldsymbol{r},t) = \hat{\boldsymbol{z}}B(\boldsymbol{r},t)$ being the external magnetic field, and $S\{f\}(\boldsymbol{r},\boldsymbol{p},t)$ is the collision integral. The latter describes all types of electron collisions, i.e. electron-electron, electron-phonon, and electron-impurity collisions.

We solve Eq. (2.1) by using the following Ansatz:

$$f(\boldsymbol{r},\boldsymbol{p},t) = f_0(\epsilon_{\boldsymbol{p}}) - f_0'(\epsilon_{\boldsymbol{p}})\mathcal{F}(\boldsymbol{r},\theta_{\boldsymbol{p}},t)\ , \tag{2.2}$$

where $f_0(\epsilon) = \{\exp[(\epsilon-\bar{\mu})/(k_{\rm B}T)]+1\}^{-1}$ is the equilibrium Fermi-Dirac distribution function, $f_0'(\epsilon)$ is its derivative with respect to the energy $\epsilon$, and $\theta_{\boldsymbol{p}}$ is the polar angle of the vector $\boldsymbol{p}$.

Retaining only terms that are linear with respect to $\mathcal{F}(\boldsymbol{r},\theta_{\boldsymbol{p}},t)$, assuming a uniform and static magnetic field, and Fourier transforming with respect to time, we obtain the following equation for $\mathcal{F}(\boldsymbol{r},\theta_{\boldsymbol{p}},\omega)$:

$$-i\omega\mathcal{F}(\boldsymbol{r},\theta_{\boldsymbol{p}},\omega) + \boldsymbol{v_p}\cdot[\nabla\mathcal{F}(\boldsymbol{r},\theta_{\boldsymbol{p}},\omega) + e\boldsymbol{E}(\boldsymbol{r},\omega)] + \omega_{\rm c}\partial_{\theta_{\boldsymbol{p}}}\mathcal{F}(\boldsymbol{r},\theta_{\boldsymbol{p}},\omega) = S^{\rm el}\{\mathcal{F}\}(\boldsymbol{r},\theta_{\boldsymbol{p}},\omega) + S^{\rm ee}\{\mathcal{F}\}(\boldsymbol{r},\theta_{\boldsymbol{p}},\omega)\ . \tag{2.3}$$

Here $\boldsymbol{E}(\boldsymbol{r},\omega)$ is the total electric field, i.e. the sum of the external field and the field generated by the electron distribution itself (the Hartree self-consistent field), $\omega_{\rm c} = eB/(mc)$ is the cyclotron frequency, $m \equiv p_{\rm F}/v_{\rm F}$ is the effective mass, $p_{\rm F}$ and $v_{\rm F}$ being the Fermi momentum and velocity, respectively, $S^{\rm el}\{f\}$ describes momentum non-conserving collision with phonons and impurities, and, finally, $S^{\rm ee}\{f\}$ is the electron-electron collision integral.

We now introduce the Fourier decomposition of the distribution function $\mathcal{F}(\boldsymbol{r},\theta_{\boldsymbol{p}},\omega)$ with respect to the polar angle:

$$\mathcal{F}(\boldsymbol{r},\theta_{\boldsymbol{p}},\omega) = \sum_{n=-\infty}^{+\infty}\mathcal{F}_n(\boldsymbol{r},\omega)e^{in\theta_{\boldsymbol{p}}}\ , \tag{2.4}$$

where the Fourier coefficients $\mathcal{F}_n(\boldsymbol{r},\omega)$ are given by

$$\mathcal{F}_n(\boldsymbol{r},\omega) = \int\frac{d\theta_{\boldsymbol{p}}}{2\pi}e^{-in\theta_{\boldsymbol{p}}}\mathcal{F}(\boldsymbol{r},\theta_{\boldsymbol{p}},\omega)\ . \tag{2.5}$$

The lowest-order Fourier coefficients are directly related to simple physical quantities. For example, $\mathcal{F}_0$ describes an isotropic dilatation or contraction of the Fermi circle, i.e. a density perturbation

$$n(\boldsymbol{r},\omega) \equiv \int d\boldsymbol{p}[f(\boldsymbol{r},\boldsymbol{p},\omega) - f_0(\epsilon_{\boldsymbol{p}})] = \mathcal{N}_0\mathcal{F}_0(\boldsymbol{r},\omega)\ , \tag{2.6}$$

where $\mathcal{N}_0$ is the density of states at the Fermi energy.

The coefficients $\mathcal{F}_{\pm1}$ describe a rigid translation of the Fermi surface, which give rise to a finite current:

$$\boldsymbol{J}(\boldsymbol{r},\omega) \equiv \int d\boldsymbol{p}\,\boldsymbol{v_p}[f(\boldsymbol{r},\boldsymbol{p},\omega) - f_0(\epsilon_{\boldsymbol{p}})] = \frac{\mathcal{N}_0 v_{\rm F}}{2}\begin{pmatrix}\mathcal{F}_{-1}(\boldsymbol{r},\omega) + \mathcal{F}_1(\boldsymbol{r},\omega)\\ i\mathcal{F}_1(\boldsymbol{r},\omega) - i\mathcal{F}_{-1}(\boldsymbol{r},\omega)\end{pmatrix}\ . \tag{2.7}$$

The coefficients $\mathcal{F}_{\pm2}$ describe an elliptic deformation of the Fermi surface, and are related to the trace-less part of the stress tensor:

$$\begin{aligned}\boldsymbol{T}(\boldsymbol{r},\omega) &\equiv \int d\boldsymbol{p}\,\boldsymbol{p}\otimes\boldsymbol{v_p}[f(\boldsymbol{r},\boldsymbol{p},\omega) - f_0(\epsilon_{\boldsymbol{p}})] = \\ &= \frac{\mathcal{N}_0 v_{\rm F}^2 m}{2}\left[\mathcal{F}_0(\boldsymbol{r},\omega)\mathbb{I} + \frac{\mathcal{F}_2(\boldsymbol{r},\omega)+\mathcal{F}_{-2}(\boldsymbol{r},\omega)}{2}\boldsymbol{\tau}_z + \frac{\mathcal{F}_{-2}(\boldsymbol{r},\omega)-\mathcal{F}_2(\boldsymbol{r},\omega)}{2i}\boldsymbol{\tau}_x\right]\ .\end{aligned} \tag{2.8}$$

Here, $\mathbb{I}$ is the $2 \times 2$ identity matrix and $\boldsymbol{\tau}_i$ with $i = x, y, z$ are ordinary $2 \times 2$ Pauli matrices acting on Cartesian indices. Higher-order coefficients describe deformations of the Fermi surface with a more complicated angular dependence.

Following Ref. [110], we approximate the collision integrals in Eq. (2.3) with the simplest possible expression, which is linear in the coefficients $\mathcal{F}_n$ and respects relevant conservation laws. The collision integral $S^{\rm el}\{\mathcal{F}\}(\boldsymbol{r}, \theta_{\boldsymbol{p}}, \omega)$ respects particle number conservation and is described by the phenomenological time scale $\tau$. Its form is

$$S^{\rm el}\{\mathcal{F}\}(\boldsymbol{r}, \theta_{\boldsymbol{p}}, \omega) = -\frac{1}{\tau}\left[\mathcal{F}(\boldsymbol{r}, \theta_{\boldsymbol{p}}, \omega) - \mathcal{F}_0(\boldsymbol{r}, \omega)\right] \ . \tag{2.9}$$

The electron-electron collision integral should instead respect both particle number and momentum conservation and is described by the parameter $\tau_{\rm ee}$. It reads as following [110, 8]

$$S^{\rm ee}\left\{\mathcal{F}\right\}(\boldsymbol{r}, \theta_{\boldsymbol{p}}, \omega) = -\frac{1}{\tau_{\rm ee}}\mathcal{F}(\boldsymbol{r}, \theta_{\boldsymbol{p}}, \omega) + \frac{1}{\tau_{\rm ee}}\left[\mathcal{F}_0(\boldsymbol{r}, \omega) + \mathcal{F}_1(\boldsymbol{r}, \omega)e^{i\theta_{\boldsymbol{p}}} + \mathcal{F}_{-1}(\boldsymbol{r}, \omega)e^{-i\theta_{\boldsymbol{p}}}\right] \ , \tag{2.10}$$

where we impose a single relaxation rate due to the e-e interaction for all non-conserved harmonics, i.e. $\mathcal{F}_n(\boldsymbol{r}, \omega)$ with $|n| > 1$.

Multiplying Eq. (2.3) by $e^{-in\theta_{\boldsymbol{p}}}$ and averaging over the angle we get a hierarchy of equations for the moments of the distribution function:

$$\begin{aligned}
&-i\omega\mathcal{F}_n(\boldsymbol{r}, \omega) + \frac{v_{\rm F}}{2}\left\{\partial_x\left[\mathcal{F}_{n-1}(\boldsymbol{r}, \omega) + \mathcal{F}_{n+1}(\boldsymbol{r}, \omega)\right] - i\partial_y\left[\mathcal{F}_{n-1}(\boldsymbol{r}, \omega) - \mathcal{F}_{n+1}(\boldsymbol{r}, \omega)\right]\right\} \\
&+ \frac{ev_{\rm F}}{2}\left[E_x(\boldsymbol{r}, \omega)\left(\delta_{n,1} + \delta_{n,-1}\right) - iE_y(\boldsymbol{r}, \omega)\left(\delta_{n,1} - \delta_{n,-1}\right)\right] + in\omega_{\rm c}\mathcal{F}_n(\boldsymbol{r}, \omega) = \\
&- \frac{1}{\tau_{\rm ee}}\left[\mathcal{F}_n(\boldsymbol{r}, \omega) - \mathcal{F}_0(\boldsymbol{r}, \omega)\delta_{n,0} - \mathcal{F}_1(\boldsymbol{r}, \omega)\delta_{n,1} - \mathcal{F}_{-1}(\boldsymbol{r}, \omega)\delta_{n,-1}\right] - \frac{1}{\tau}\left[\mathcal{F}_n(\boldsymbol{r}, \omega) - \mathcal{F}_0(\boldsymbol{r}, \omega)\delta_{n,0}\right] \ .
\end{aligned} \tag{2.11}$$

Setting $n = 0$ in Eq. (2.11) leads to the continuity equation:

$$-i\omega n(\boldsymbol{r}, \omega) + \nabla \cdot \boldsymbol{J}(\boldsymbol{r}, \omega) = 0 \ . \tag{2.12}$$

The two equations for $n = \pm 1$ can be combined to give the Navier-Stokes equation

$$-i\omega\boldsymbol{J}(\boldsymbol{r}, \omega) + \frac{1}{m}\nabla \cdot \hat{\boldsymbol{T}}(\boldsymbol{r}, \omega) + \frac{ev_{\rm F}^2\mathcal{N}_0}{2}\boldsymbol{E}(\boldsymbol{r}, \omega) + \omega_{\rm c}\boldsymbol{J}(\boldsymbol{r}, \omega) \times \hat{\boldsymbol{z}} = -\frac{1}{\tau}\boldsymbol{J}(\boldsymbol{r}, \omega) \ . \tag{2.13}$$

To obtain a closed set of equations we truncate the series of equations (2.11) neglecting all the coefficients $\mathcal{F}_n$ with $|n| \geq 3$. By doing this we are able to close the equations for $n = \pm 2$ and we obtain

$$\mathcal{F}_{\pm 2}(\boldsymbol{r}, \omega) = -\frac{v_{\rm F}}{2}\frac{(\partial_x \mp i\partial_y)\mathcal{F}_{\pm 1}(\boldsymbol{r}, \omega)}{\frac{1}{\tau} + \frac{1}{\tau_{\rm ee}} - i\omega \pm 2i\omega_{\rm c}} \ . \tag{2.14}$$

Replacing this result into the expression for the stress tensor (2.8) leads to

$$\boldsymbol{T}(\boldsymbol{r}, \omega) = \frac{\mathcal{B}}{\bar{n}}n(\boldsymbol{r}, \omega)\mathbb{I} - \boldsymbol{\sigma}'(\boldsymbol{r}, \omega) \ , \tag{2.15}$$

where

$$\mathcal{B} = \frac{\bar{n}mv_{\rm F}^2}{2} = \frac{\bar{n}^2}{\mathcal{N}_0} \tag{2.16}$$

is the bulk modulus [35] of the electron liquid, while the viscous stress tensor is given by

$$\boldsymbol{\sigma}'(\boldsymbol{r}, \omega) = m\nu(\omega)\begin{pmatrix} \partial_x J_x - \partial_y J_y & \partial_x J_y + \partial_y J_x \\ \partial_x J_y + \partial_y J_x & -\partial_x J_x + \partial_y J_y \end{pmatrix} + m\nu_{\rm H}(\omega)\begin{pmatrix} \partial_x J_y + \partial_y J_x & -\partial_x J_x + \partial_y J_y \\ -\partial_x J_x + \partial_y J_y & -\partial_x J_y - \partial_y J_x \end{pmatrix} . \tag{2.17}$$

This coincides with the expression in Eq. (2.114). Here, the frequency-dependent viscosities are given by

$$\nu(\omega) = \frac{v_{\rm F}^2}{4}\frac{\frac{1}{\tau_{\rm ee}} + \frac{1}{\tau} - i\omega}{\left(\frac{1}{\tau_{\rm ee}} + \frac{1}{\tau} - i\omega\right)^2 + 4\omega_{\rm c}^2} \tag{2.18}$$

and

$$\nu_{\rm H}(\omega) = -\frac{v_{\rm F}^2}{2}\frac{\omega_{\rm c}}{\left(\frac{1}{\tau_{\rm ee}}+\frac{1}{\tau}-i\omega\right)^2+4\omega_{\rm c}^2} \ . \tag{2.19}$$

At low frequency ($\omega \ll \tau_{\rm ee}^{-1}+\tau^{-1}$) they read

$$\nu = \frac{v_{\rm F}^2}{4}\frac{\frac{\tau_{\rm ee}\tau}{\tau_{\rm ee}+\tau}}{1+4\omega_{\rm c}^2\left(\frac{\tau_{\rm ee}\tau}{\tau_{\rm ee}+\tau}\right)^2} \ , \tag{2.20}$$

and

$$\nu_{\rm H} = -\frac{v_{\rm F}^2}{2}\frac{\omega_{\rm c}\left(\frac{\tau_{\rm ee}\tau}{\tau_{\rm ee}+\tau}\right)^2}{1+4\omega_{\rm c}^2\left(\frac{\tau_{\rm ee}\tau}{\tau_{\rm ee}+\tau}\right)^2} \ . \tag{2.21}$$

Defining $\nu_0 = v_{\rm F}^2\tau_{\rm ee}\tau/[4(\tau_{\rm ee}+\tau)]$, one immediately reaches Eqs. (2.116) and (2.117) for the magnetic-field-dependent dc viscosities.

### 2.1.1 Derivation of the boundary conditions for the linearized hydrodynamic equations

In this Section we present a brief derivation of the hydrodynamic Boundary Conditions (BCs) in Eq. (2.53-2.55-2.125) for the components of the fluid-element current $\boldsymbol{J}$, starting from simple BCs [173] for the Boltzmann distribution function.

Let us consider a portion of the boundary located at position $\boldsymbol{r}_0$ and a local "reference system" defined by the vectors $\hat{\boldsymbol{e}}_{\rm t}$ and $\hat{\boldsymbol{e}}_{\rm n}$ introduced in Sect. 2.3.1. We denote by $\theta_0$ the angle between the tangent vector $\hat{\boldsymbol{e}}_t$ and the $\hat{\boldsymbol{x}}$ direction. The distribution $\mathcal{F}(\boldsymbol{r}_0,\theta,\omega)$ represents the density of carriers impinging from the bulk on the boundary if $\theta_0 < \theta < \theta_0+\pi$, while it represents the density of carriers scattered from the boundary into the bulk for $\theta_0-\pi < \theta < \theta_0$. The density of scattered particles is related to the density of impinging particles by

$$\mathcal{F}(\boldsymbol{r}_0,\theta+\theta_0,\omega) = \int_0^\pi d\theta' r(\theta,\theta')\mathcal{F}(\boldsymbol{r}_0,\theta'+\theta_0,\omega) \ , \tag{2.22}$$

where $r(\theta,\theta')$ is the probability for a particle impinging with an angle $\theta'$ with respect to the boundary to be scattered with an angle $\theta$, and $-\pi < \theta < 0$. Making use of Eqs. (2.4) and (2.22), we obtain

$$\mathcal{F}_n(\boldsymbol{r}_0,\omega)e^{in\theta_0} = \sum_{m=-\infty}^{\infty} e^{im\theta_0}(u_{n-m}+r_{nm})\mathcal{F}_m(\boldsymbol{r}_0,\omega) \ , \tag{2.23}$$

where

$$u_n \equiv \int_0^\pi \frac{d\theta}{2\pi}e^{-in\theta} = \begin{cases} 1/2 \text{ if } n=0 \\ 0 \text{ if } n \text{ even} \\ -i/(n\pi) \text{ if } n \text{ odd} \end{cases} \tag{2.24}$$

and

$$r_{nm} \equiv \int_{-\pi}^0 d\theta e^{-in\theta}\int_0^\pi d\theta' e^{im\theta'}\frac{r(\theta,\theta')}{2\pi} \ . \tag{2.25}$$

Since the particle number is conserved in the collisions with the boundary, we have $\int_{-\pi}^0 r(\theta,\theta')d\theta = 1$. This implies

$$r_{0m} = u_{-m} \ . \tag{2.26}$$

Consistently with the procedure followed in deriving the hydrodynamic equations (see Section 2.1), we neglect all the contributions stemming from $\mathcal{F}_n$ with $|n| > 2$. Setting $n=0$ in Eq. (2.23) and making use of Eq. (2.26) yields

$$e^{i\theta_0}\mathcal{F}_1(\boldsymbol{r}_0,\omega) - e^{-i\theta_0}\mathcal{F}_{-1}(\boldsymbol{r}_0,\omega) = 0 \ . \tag{2.27}$$

Noting that

$$\hat{\boldsymbol{e}}_n \cdot \boldsymbol{J}(\boldsymbol{r}_0,\omega) = \frac{\mathcal{N}_0 v_{\rm F} i}{2}\left[e^{i\theta_0}\mathcal{F}_1(\boldsymbol{r}_0,\omega) - e^{-i\theta_0}\mathcal{F}_{-1}(\boldsymbol{r}_0,\omega)\right] \ , \tag{2.28}$$

we can rewrite Eq. (2.27) as

$$\hat{\boldsymbol{e}}_n \cdot \boldsymbol{J}(\boldsymbol{r}_0,\omega) = 0 \ . \tag{2.29}$$

Setting $n = 1, 2$ in Eq. (2.23) gives instead

$$\left(\frac{i}{\pi} + r_{12}\right) e^{2i\theta_0}\mathcal{F}_2 + \left(-\frac{1}{2} + r_{11} + r_{1-1}\right) e^{i\theta_0}\mathcal{F}_1 + \left(-\frac{i}{\pi} + r_{10}\right)\mathcal{F}_0 + \left(-\frac{i}{3\pi} + r_{1-2}\right) e^{-2i\theta_0}\mathcal{F}_2 = 0 \tag{2.30}$$

and

$$\left(-\frac{1}{2} + r_{22}\right) e^{2i\theta_0}\mathcal{F}_2 + \left(-\frac{4i}{3\pi} + r_{21} + r_{2-1}\right) e^{i\theta_0}\mathcal{F}_1 + r_{20}\mathcal{F}_0 + r_{2-2}e^{-2i\theta_0}\mathcal{F}_2 = 0 \ . \tag{2.31}$$

In what follows we use a simple one-parameter model for the scattering probability [173], which consists in the linear superposition of specular reflection with probability $p$ and diffuse reflection with probability $1-p$. This reads

$$r(\theta,\theta') = p\delta(\theta+\theta') + \frac{(1-p)}{\pi} \ . \tag{2.32}$$

This implies

$$r_{mn} = p u_{-n-m} + 2(1-p)u_{-n}u_{-m} \ . \tag{2.33}$$

Replacing Eq. (2.33) into Eqs. (2.30)-(2.31) and using Eq. (2.27) we obtain

$$\begin{pmatrix} \frac{i(3+p)}{3\pi} & -\frac{i(1+3p)}{3\pi} \\ -\frac{1}{2} & \frac{p}{2} \end{pmatrix} \begin{pmatrix} \mathcal{F}_2 e^{2i\theta_0} \\ \mathcal{F}_{-2}e^{-2i\theta_0} \end{pmatrix} = e^{i\theta_0}\mathcal{F}_1 \begin{pmatrix} \frac{1-p}{2} \\ \frac{4i(1-p)}{3\pi} \end{pmatrix} \ . \tag{2.34}$$

Solving for $\mathcal{F}_{\pm 2}$ gives

$$\mathcal{F}_2 e^{2i\theta_0} = \frac{i e^{i\theta_0}\mathcal{F}_1(9\pi^2 p - 48p - 16)}{6\pi(p+1)} \tag{2.35}$$

and

$$\mathcal{F}_{-2}e^{-2i\theta_0} = \frac{i e^{i\theta_0}\mathcal{F}_1(9\pi^2 - 48 - 16p)}{6\pi(p+1)} \ . \tag{2.36}$$

Using this solution and noting that

$$\hat{\boldsymbol{e}}_{\rm t} \cdot [\hat{\boldsymbol{\sigma}}'(\boldsymbol{r}_0,\omega)\cdot\hat{\boldsymbol{e}}_{\rm n}] = -\frac{i\mathcal{N}_0 v_{\rm F}^2 m}{4}\Big[\mathcal{F}_2(\boldsymbol{r}_0,\omega)e^{2i\theta_0} - \mathcal{F}_{-2}(\boldsymbol{r}_0,\omega)e^{-2i\theta_0}\Big] \tag{2.37}$$

and

$$\hat{\boldsymbol{e}}_{\rm t} \cdot \boldsymbol{J}(\boldsymbol{r}_0,\omega) = \mathcal{N}_0 v_{\rm F} e^{i\theta_0}\mathcal{F}_1(\boldsymbol{r}_0,\omega) \ , \tag{2.38}$$

finally leads to

$$[\hat{\boldsymbol{e}}_{\rm t} \cdot (\hat{\boldsymbol{\sigma}}' \cdot \hat{\boldsymbol{e}}_{\rm n}) + (m\nu/\ell_{\rm b})\hat{\boldsymbol{e}}_{\rm t}\cdot\boldsymbol{J}]_\Omega = 0 \ , \tag{2.39}$$

with

$$\ell_{\rm b} = \frac{6\pi}{9\pi^2 - 32}\frac{\nu}{v_{\rm F}}\frac{1+p}{1-p} \approx 0.33\frac{\nu}{v_{\rm F}}\frac{1+p}{1-p} \ . \tag{2.40}$$

Eq. (2.40) shows that $\ell_{\rm b}$ depends on both electron-electron scattering, through $\nu$, and electron-boundary scattering, through $p$. The boundary slip length diverges for $p \to 1$, recovering the free-surface BC [96, 104], while it remains finite in the limit $p \to 0$, i.e. $\lim_{p\to 0}\ell_{\rm b} \simeq 0.1\ \ell_{\rm ee}$, where $\ell_{\rm ee}$ is the electron-electron scattering length [102]. (In deriving the last result we have used $\nu \simeq v_{\rm F}\ell_{\rm ee}/4$.) For completely diffusive scattering, $\ell_{\rm b}$ is therefore ten times smaller than the electron-electron scattering length. Since the latter quantity is much smaller than the macroscopic length scales of hydrodynamic electron flow, $\ell_{\rm b}$ is negligibly small for $p \to 0$ and we obtain the no-slip BC [96, 174]. Although Eq. (2.126) has been obtained by using a very simple model for boundary scattering [173], we believe that more refined models will yield different numerical values for $\ell_{\rm b}$ but will likely not change neither the structure of Eq. (2.125) nor the qualitative conclusions we just drew.

## 2.2 Nonlocal transport and the hydrodynamic shear viscosity in graphene

Electron systems roaming in a crystal where the mean free path for electron-electron collisions is the shortest length scale of the problem can be described by conservation laws for macroscopic collective variables [10, 75, 76, 77, 78, 175, 79, 80, 112, 114, 82, 83, 84, 86, 85, 90, 91, 176, 96, 87, 88, 177, 174, 104, 42, 178].

We consider a two-dimensional electron liquid in a doped Single Layer Graphene (SLG) or BiLayer Graphene (BLG) sheet, deep in the hydrodynamic transport regime ($\ell_{\rm ee} \ll \ell, W$). For the sake of definiteness, we consider the device geometries sketched in Fig. 2.1. Panels 2.1a-b show Hall bars with different contact arrangements, the geometry of panel 2.1-a is dubbed Levitov-Falkovich (LF) geometry [174, 179], while the geometry of panel 2.1-b is referred to as vicinity geometry. The half-plane geometry depicted in Fig. 2.1-c can be considered as the limit of an Hall bar of very large width.

Since the energy-momentum dispersion of electrons in these systems is particle-hole symmetric [31], we assume, without loss of generality, that the sample hosts a back gate-controlled equilibrium electron density equal to $\bar{n}$. (The charge density is $-e\bar{n}$, $-e$ being the electron charge.) We neglect thermally-excited carriers and coupling between charge and heat flow [180, 13], which is strong only at the charge neutrality point. Finally, we consider the linear response regime and steady-state transport.

In this framework of approximations, the hydrodynamic transport equations [90, 91] for the 2D electron liquid greatly simplify and reduce to

$$\nabla \cdot \boldsymbol{J}(\boldsymbol{r}) = 0 \ , \tag{2.41}$$

and

$$\frac{\bar{n}e}{m}\nabla\phi(\boldsymbol{r}) + \nu\nabla^2\boldsymbol{J}(\boldsymbol{r}) = \frac{\boldsymbol{J}(\boldsymbol{r})}{\tau} \ . \tag{2.42}$$

In Eqs. (2.41) and (2.42) we have introduced the linearized steady-state particle current density $\boldsymbol{J}(\boldsymbol{r}) = \bar{n}\boldsymbol{v}(\boldsymbol{r})$, where $\boldsymbol{v}(\boldsymbol{r})$ is the linearized steady-state fluid-element velocity.

Eq. (2.41) is the continuity equation, while Eq. (2.42) is the Navier-Stokes equation. The latter contains three forces acting on a fluid element: i) the electric force $-e\boldsymbol{E}(\boldsymbol{r}) = e\nabla\phi(\boldsymbol{r})$, written in terms of the electric potential $\phi(\boldsymbol{r})$ in the 2D plane where electrons are moving, which is generated by the steady-state charge distribution $n(\boldsymbol{r})$ in response to the drive current $I$; ii) the internal force due to the shear viscosity $\eta = \eta(\bar{n}, T)$ of the 2D electron liquid, here written in terms of the kinematic viscosity [73, 74]

$$\nu = \frac{\eta}{m\bar{n}} \ ; \tag{2.43}$$

and iii) friction exerted on a fluid element by agents external to the electron liquid such as phonons and impurities, which dissipate the fluid-element momentum at a rate $\tau^{-1} = 1/\tau(\bar{n}, T)$. The latter is a phenomenological parameter, which depends on $\bar{n}$ and $T$ and is commonly used in modelling transport in semiconductor devices [181, 182].

In Eqs. (2.42) and (2.43) $m$ is a suitable effective mass defined by:

$$m = \begin{cases} m_{\rm c}, \ \text{for SLG}, \\ 0.03 \ m_{\rm e}, \ \text{for BLG} \end{cases} \ , \tag{2.44}$$

where $m_{\rm c} = \hbar k_{\rm F}/v_{\rm F}$ is the 2D massless Dirac fermion cyclotron mass [31], $k_{\rm F} = \sqrt{\pi\bar{n}}$ being the Fermi wave number and $v_{\rm F} \sim 10^6$ m/s the Fermi velocity, and $m_{\rm e}$ is the bare electron mass in vacuum. Multiplying both members of Eq. (2.42) by $\tau$, we obtain

$$\frac{\sigma_0}{e}\nabla\phi(\boldsymbol{r}) + D_\nu^2\nabla^2\boldsymbol{J}(\boldsymbol{r}) = \boldsymbol{J}(\boldsymbol{r}) \ . \tag{2.45}$$

In Eq. (2.45) we have introduced the following characteristic length scale of the problem:

$$D_\nu \equiv \sqrt{\nu\tau} \ . \tag{2.46}$$

For $\tau = 1$ ps (as in high-quality hBN/graphene/hBN samples) and $\nu = 0.1$ m$^2$/s (see Ref. [102]) we obtain $D_\nu \approx 0.3$ $\mu$m.

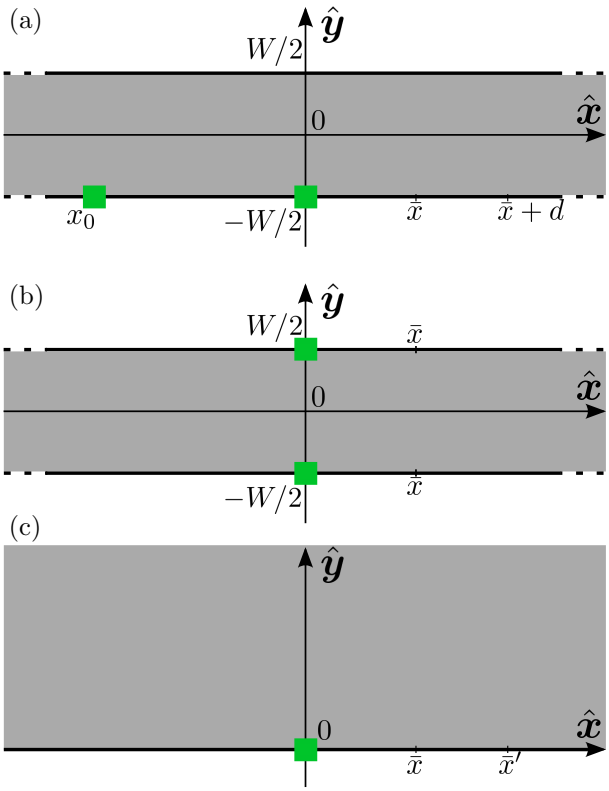


Figure 2.1: A sketch of the nonlocal transport setups analyzed in this section. Both conductive channels (grey-shaded areas) in panels (a) and (b) have infinite length in the $\hat{\boldsymbol{x}}$ direction and finite width $W$ in the $\hat{\boldsymbol{y}}$ direction. The setup in panel (c) consists in a half-plane with a single edge located at $y = 0$. Panel (a) illustrates the "vicinity" geometry [96, 11]. In this setup, current is injected into (extracted from) the green electrode located at $x = 0$ ($x = x_0 < 0$) and $y = -W/2$. The nonlocal "vicinity" resistance is defined by $R_{\rm V} \equiv [\phi(\bar{x}, -W/2) - \phi(\bar{x} + d, -W/2)]/I$, where $I$ is the injected current and $\phi(x, y)$ is the 2D electrostatic potential. For all practical purposes, we can take the limits $|x_0|, d \to +\infty$, which considerably simplify the final mathematical expression for $R_{\rm V}$. Panel (b) illustrates the LF geometry [174]. In this setup, current is injected into (extracted from) the green electrode located at $x = 0$, $y = -W/2$ ($x = 0$, $y = +W/2$). The nonlocal signal is defined by $R_{\rm LF} = [\phi(\bar{x}, -W/2) - \phi(\bar{x}, W/2)]/I$. Panel (c) illustrates the half-plane geometry. In this geometry, current is injected into a single electrode at the origin. The half-plane nonlocal resistance is defined as $R_{\rm HP} = [\phi(\bar{x}, 0) - \phi(\bar{x}', 0)]/I$.

The physical significance of $D_\nu$ can be understood as follows. We first note that we can rewrite $\nabla^2 \boldsymbol{J}(\boldsymbol{r})$ by using the following identity:

$$\nabla^2 \boldsymbol{J}(\boldsymbol{r}) = \nabla[\nabla \cdot \boldsymbol{J}(\boldsymbol{r})] - \nabla \times [\nabla \times \boldsymbol{J}(\boldsymbol{r})] \ . \tag{2.47}$$

Because of (2.41), we can drop the first term on the right-hand side of Eq. (2.47). The second term is finite and related to the vorticity [73]

$$\boldsymbol{\omega}(\boldsymbol{r}) \equiv \frac{1}{\bar{n}} \nabla \times \boldsymbol{J}(\boldsymbol{r}) = \omega(\boldsymbol{r}) \hat{\boldsymbol{z}} \ , \tag{2.48}$$

which in 2D is oriented along the $\hat{\boldsymbol{z}}$ axis. We can then rewrite Eq. (2.45) as following

$$\frac{\sigma_0}{e} \nabla \phi(\boldsymbol{r}) - \bar{n} D_\nu^2 \nabla \times \boldsymbol{\omega}(\boldsymbol{r}) = \boldsymbol{J}(\boldsymbol{r}) \ . \tag{2.49}$$

Taking the curl of Eq. (2.49) and using the identities $\nabla \times \nabla \phi(\boldsymbol{r}) = 0$ and $\nabla \cdot \boldsymbol{\omega}(\boldsymbol{r}) = 0$ (the latter being valid because $\boldsymbol{\omega}$'s only non-vanishing component is along $\hat{\boldsymbol{z}}$, while $\nabla$ acts only on the 2D $\hat{\boldsymbol{x}}$-$\hat{\boldsymbol{y}}$ plane), we

obtain a damped-diffusion equation for the vorticity

$$D_\nu^2 \nabla^2 \omega(\boldsymbol{r}) = \omega(\boldsymbol{r}) \ . \tag{2.50}$$

We therefore see that $D_\nu$ plays the role of a diffusion length for $\omega(\boldsymbol{r})$.

In Eq. (2.45) we have also introduced a "Drude-like" conductivity,

$$\sigma_0 \equiv \frac{e^2 \bar{n} \tau}{m} \ . \tag{2.51}$$

Since we are in the hydrodynamic regime, $\sigma_0$ should not be confused [91] with the ordinary dc conductivity in the diffusive transport regime: once again, $\tau = \tau(\bar{n}, T)$ represents a phenomenological parameter that should be fit to experimental data, as we discuss below in Sect. 2.2.4. This naïve description of momentum-non-conserving collisions in the hydrodynamic transport regime can be relaxed by following similar arguments to those in Ref. [83]: this is however well beyond the scope of the present work and will be the topic of future studies. In the absence of viscosity, Eq. (2.42) reduces to a local version of Ohm's law, i.e. $\boldsymbol{J}(\boldsymbol{r}) = \sigma_0 \nabla \phi(\boldsymbol{r})/e$.

Finally, we note that taking the divergence of Eq. (2.45) and making use of Eq. (2.41) we obtain the Laplace equation $\nabla^2 \phi(\boldsymbol{r}) = 0$ for the electric potential $\phi(\boldsymbol{r})$ on the 2D plane. This should not be confused with the usual three-dimensional (3D) Poisson equation for the 3D electrostatic potential $\Phi(\boldsymbol{r}, z)$,

$$\left( \nabla^2 + \frac{\partial^2}{\partial z^2} \right) \Phi(\boldsymbol{r}, z) = 4\pi e n(\boldsymbol{r}) \delta(z) \ . \tag{2.52}$$

The 2D potential in Eq. (2.42) is $\phi(\boldsymbol{r}) = \Phi(\boldsymbol{r}, z = 0)$. On the right-hand side of Eq. (2.52) we note the steady-state charge density distribution $-en(\boldsymbol{r})$ which occurs in the sample in response to the drive current $I$. Eq. (2.52) needs to be solved in 3D space with suitable boundary conditions—depending on the dielectric environment, gates, etc. surrounding the graphene sheet—if one is interested in determining $n(\boldsymbol{r})$. In the following we will focus our attention on $\boldsymbol{J}(\boldsymbol{r})$ and $\phi(\boldsymbol{r})$.

Eqs. (2.41) and (2.45) will be used to describe transport in the Hall bar geometry pictorially represented in Fig. 2.1. Mathematically, it is convenient to work in a Hall bar of infinite length in the longitudinal direction $\hat{\boldsymbol{x}}$, since this allows us to use the Fourier transform to solve the equations of motion. The width $W$ of the Hall bar will be kept finite. In the next Section we will describe a crucially important ingredient of the theory: boundary conditions.

### 2.2.1 Boundary conditions

In order to find $\phi(\boldsymbol{r})$ and $\boldsymbol{J}(\boldsymbol{r})$ in the Hall bar geometry depicted in Fig. 2.1, we need to solve Eqs. (2.41) and (2.45) in the rectangle $(-\infty, \infty) \times [-W/2, W/2]$, with appropriate boundary conditions (BCs) at the edges, i.e. at $y = \pm W/2$. These have been derived rigorously in Section 2.1.1.

Lateral electrodes acting as current injectors/collectors are described through BCs on the component of the current *perpendicular* to the edges (See (2.29)):

$$J_y \left( x, y = \pm W/2 \right) = \mathcal{J}_\pm(x) \ . \tag{2.53}$$

Here $\mathcal{J}_\pm(x)$ is a function that describes a distribution of current injectors and collectors on the upper (lower) edge of the multi-terminal Hall bar. It is through Eq. (2.53) that the total drive current $I$ injected into the system at the boundaries enters the problem.

Following Abanin *et al.* [103], we model the electrodes as point-like (i.e. delta-function) sources and sinks. (A more realistic modeling of electrodes has been carried out in Ref. [11], where finite-width effects and metallic boundary conditions at extended electrodes have been taen into account in a fully numerical solution of Eqs. (2.41) and (2.45)). Such details have essentially no impact on the physics we are going to highlight below.) For example, for the setup depicted in Fig. 2.1-a with a current injector at $x = 0$, a current collector at $x = -x_0$, and no injectors/collectors on the upper edge, we will use:

$$\mathcal{J}_-(x) = -\frac{I}{e} \delta(x) + \frac{I}{e} \delta(x + x_0) \ , \tag{2.54}$$

and $\mathcal{J}_+(x) = 0$.

In the presence of a finite shear viscosity $\nu$, we need an additional BC on the *tangential* component of the current at the top ($y = +W/2$) and bottom ($y = -W/2$) edges of the Hall bar. We use the following BC, obtained from (2.39) in our specific geometry:

$$[\partial_y J_x(x,y) + \partial_x J_y(x,y)]_{y=\pm W/2} = \mp \frac{J_x(x, y = \pm W/2)}{\ell_\mathrm{b}} \ , \tag{2.55}$$

where $\ell_\mathrm{b}$ is a "boundary slip length", i.e. a length scale describing friction at the physical boundaries of the sample. This BC can be explained as following. The left-hand side of Eq. (2.55) is proportional to the off-diagonal component of the stress tensor [73], calculated at the edges of the Hall bar. It represents the tangential component of the frictional force exerted by the boundaries of the Hall bar on the 2D electron liquid [73]. This force depends on the tangential velocity of the 2D electron liquid and boundary roughness: in the linear-response regime, it is natural to replace such unknown dependence with a linear law characterized by the single parameter $\ell_\mathrm{b}$, as in the right-hand side of Eq. (2.55).

In the description of transport of molecular liquids in constrained geometries, like water in a pipe, where the interactions between the molecules of the fluid and the walls of the container are of the same nature as of those between molecules of the fluid, the most used BCs are the so-called "no-slip" BCs [73], in which the component of the current tangential to the boundary vanishes. The no-slip BCs can be obtained from Eq. (2.55) by taking the limit $\ell_\mathrm{b} \to 0$. In the opposite limit of a free-surface geometry, like the surface of water in an open bucket, the tangential force applied from the boundary to the fluid element vanishes at the boundary. These "free-surface" BCs [73, 91] can be obtained from Eq. (2.55) by taking the limit $\ell_\mathrm{b} \to +\infty$.

Which of these BCs should be used to model the experiments in Ref. [11] will become clear at the end of Sect. 2.2.4.

### 2.2.2 Applicability of the linearized theory

The validity of the linearized Navier-Stokes equation (2.45) relies on the smallness of the Reynolds number [73] $\mathcal{R}_W$. This is a dimensionless parameter (which depends on the sample geometry) that controls the smallness of the non-linear term $[\boldsymbol{v}(\boldsymbol{r},t)\cdot\nabla]\boldsymbol{v}(\boldsymbol{r},t)$ in the convective derivative with respect to the viscous term. In our case we can define the Reynolds number as following:

$$\left| \frac{[\boldsymbol{v}(\boldsymbol{r},t)\cdot\nabla]\boldsymbol{v}(\boldsymbol{r},t)}{\nu\nabla^2\boldsymbol{v}(\boldsymbol{r},t)} \right| \simeq \frac{\bar{v}W}{\nu} = \frac{I}{e\bar{n}\nu} \equiv \mathcal{R}_W \ , \tag{2.56}$$

where $\bar{v}$ is the typical value of the fluid-element velocity. For an injected current [11] $I = 2\times10^{-7}$ A, a Hall bar width $W = 1$ $\mu$m, and an equilibrium density $\bar{n} = 10^{12}$ cm$^{-2}$, we obtain $\bar{v} \sim I/(e\bar{n}W) \approx 10^4$ cm/s. We note that $\bar{v}$ is much smaller than the graphene Fermi velocity $v_\mathrm{F} \sim 10^6$ m/s and the flow is therefore "non-relativistic". The corresponding value of the Reynolds number is $\mathcal{R}_W \sim 10^{-3} \ll 1$, obtained by using a kinematic viscosity $\nu \sim 10^3$ cm$^2$/s of the 2D electron liquid in graphene [102]. Our linearized theory in Eqs. (2.41) and (2.45) is therefore fully justified.

### 2.2.3 General solution of hydrodynamic equations in a 2D strip geometry

In this Section we briefly review the theoretical approach that was introduced in Refs. [11, 96, 104] to study nonlocal transport in viscous 2D electron systems.

Since all the setups in Fig. 2.1 are translationally-invariant in the $\hat{\boldsymbol{x}}$ direction, it is useful to introduce the Fourier transform with respect the spatial coordinate $x$:

$$\tilde{\phi}(k,y) = \int_{-\infty}^{+\infty} dx \ e^{-ikx} \phi(\boldsymbol{r}) \tag{2.57}$$

and

$$\tilde{\boldsymbol{J}}(k,y) = \int_{-\infty}^{+\infty} dx \ e^{-ikx} \boldsymbol{J}(\boldsymbol{r}) \ . \tag{2.58}$$

The three coupled partial-differential equations (2.41)-(2.42) can be combined into a $4 \times 4$ system of first-order ordinary differential equations:

$$\partial_y \boldsymbol{w}(k,y) = \mathcal{M}(k)\boldsymbol{w}(k,y) \ , \tag{2.59}$$

where $\boldsymbol{w}(k,y)$ is a four-component vector,

$$\boldsymbol{w}(k,y) = \begin{pmatrix} k\tilde{J}_x(k,y) \\ k\tilde{J}_y(k,y) \\ \partial_y \tilde{J}_x(k,y) \\ \frac{k^2\sigma_0\tilde{\phi}(k,y)}{e} \end{pmatrix} \tag{2.60}$$

and

$$\mathcal{M}(k) = k \begin{pmatrix} 0 & 0 & 1 & 0 \\ -i & 0 & 0 & 0 \\ 1+1/(kD_\nu)^2 & 0 & 0 & -i/(kD_\nu)^2 \\ 0 & 1+(kD_\nu)^2 & i(kD_\nu)^2 & 0 \end{pmatrix} , \tag{2.61}$$

with $D_\nu \equiv \sqrt{\nu\tau}$ and $\sigma_0 \equiv \bar{n}e^2\tau/m$. The quantity $D_\nu$ represents the vorticity diffusion length [11, 96], while $\sigma_0$ represents a Drude-like conductivity.

It can be easily checked that the matrix $\mathcal{M}(k)$ has four eigenvalues: $\lambda_{1/2}(k) = \pm|k|$ and $\lambda_{3/4}(k) = \pm q$, where we have introduced the shorthand

$$q \equiv q(k) = \sqrt{k^2 + 1/D_\nu^2} \, . \tag{2.62}$$

The corresponding eigenvectors are:

$$\boldsymbol{w}_{1/2}(k) = \begin{pmatrix} i \\ \pm\mathrm{sgn}(k) \\ \pm i\mathrm{sgn}(k) \\ 1 \end{pmatrix} , \; \boldsymbol{w}_{3/4}(k) = \begin{pmatrix} \pm\frac{k}{q} \\ -i\frac{k^2}{q^2} \\ 1 \\ 0 \end{pmatrix} . \tag{2.63}$$

Eqs. (2.59)-(2.62) show that viscous transport is intrinsically nonlocal on the scale given by $D_\nu$.

The general solution of Eq. (2.59) can be therefore written as a linear combination of exponentials of the form $\sum_{j=1}^{4} a_j(k)\boldsymbol{w}_j(k)\exp(\lambda_j y)$, where $\boldsymbol{w}_j(k)$ and $\lambda_j(k)$ are eigenvectors and eigenvalues of the matrix $\mathcal{M}$, respectively. The four coefficients $a_j(k)$ can be determined from the enforcement of suitable boundary conditions (BCs).

### 2.2.4 Longitudinal transport and the Gurzhi effect

We first consider the situation in which no current is injected or extracted laterally at the Hall bar edges, i.e. $\mathcal{J}_\pm(x) = 0$.

In this case the local current $\boldsymbol{J}(\boldsymbol{r})$ does not depend on the longitudinal coordinate $x$ and all the spatial derivatives with respect to $x$ in Eqs. (2.41), (2.45), and (2.55) vanish. The continuity equation implies that $J_y$ does not depend on $y$ and vanishes identically because of Eq. (2.53). Therefore also the $y$ component of the electric field must vanish. The $x$ component of the current respects the following equation: $J_x(y) - D_\nu^2\partial_y^2 J_x(y) = -\sigma_0 E_x/e$, where $\boldsymbol{E} = -\nabla\phi(\boldsymbol{r})$ is the electric field. Note that $E_x$ cannot depend on $y$ because $E_y$ vanishes and $\nabla\times\boldsymbol{E} = 0$. The solution of this equation that fulfils the BC (2.55) is

$$J_x(y) = -\frac{\sigma_0}{e}E_x\left[1 - \frac{D_\nu}{\xi}\cosh\left(\frac{y}{D_\nu}\right)\right] , \tag{2.64}$$

where we have introduced the length

$$\xi \equiv \ell_\mathrm{b}\sinh\left(\frac{W}{2D_\nu}\right) + D_\nu\cosh\left(\frac{W}{2D_\nu}\right) \, . \tag{2.65}$$

We can calculate the total longitudinal current $I$ carried by the flow by integrating Eq. (2.64) in the transverse direction, i.e.

$$I = -e\int_{-W/2}^{W/2} dy J_x(y) = \sigma_0 W E_x(1-\mathcal{F}) \, , \tag{2.66}$$

where we have defined the dimensionless quantity

$$\mathcal{F} \equiv 2\frac{D_\nu^2}{W\xi}\sinh\left(\frac{W}{2D_\nu}\right) \, . \tag{2.67}$$

Measuring the longitudinal potential drop $\Delta V$ between two lateral contacts at positions $x$ and $x + L$ yields a four-point longitudinal conductivity $\sigma_{xx}$ of the form:

$$\sigma_{xx} \equiv \frac{I}{\Delta V}\frac{L}{W} = \sigma_0(1 - \mathcal{F}) \ . \tag{2.68}$$

Eq. (2.68) is the most important result of this Section. In the limit $\ell_b \to \infty$ (i.e. free-surface BCs)

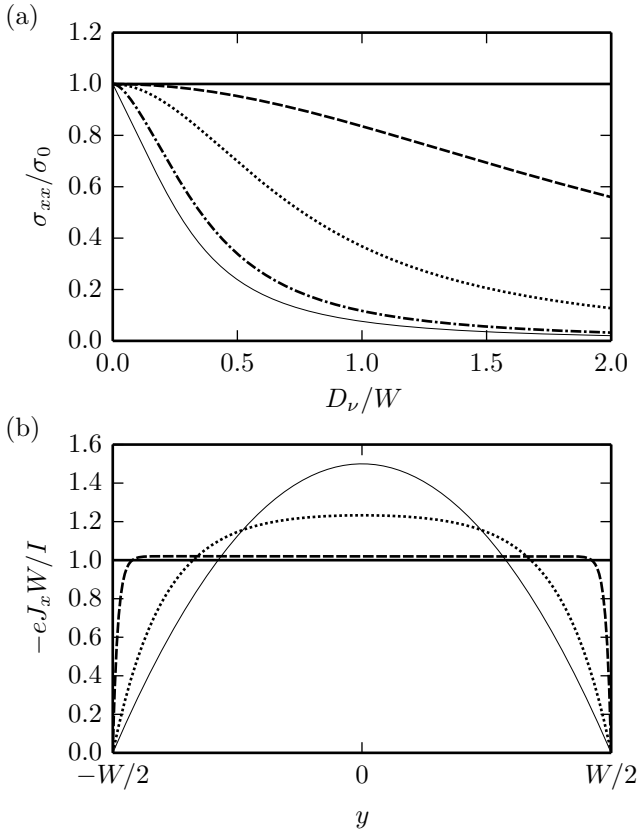


Figure 2.2: Panel (a) The longitudinal conductivity (2.68) (in units of $\sigma_0$) is plotted as a function of the ratio $D_\nu/W$ for different values of the boundary scattering length $\ell_b$: $\ell_b = \infty$ (thick solid line), $\ell_b = 10\ W$ (dashed line), $\ell_b = W$ (dotted line), $\ell_b = 0.1\ W$ (dash-dotted line), and $\ell_b = 0$ (thin solid line). Panel (b) The current-density profile $-eJ_x(y)$, normalized by the total current $I/W$, is plotted as a function of $y$ for $\ell_b = 0$ (no-slip BCs) and different values of $D_\nu$: $D_\nu = 0$ (thick solid line), $D_\nu = 0.01\ W$ (dashed line), and $D_\nu = 0.1\ W$ (dotted line). The case $D_\nu \gg W$, corresponding to Poiseuille flow, is represented by a thin solid line.

$\mathcal{F} \to 0$. For this choice of BCs the longitudinal conductivity $\sigma_{xx}$ depends only on the rate of momentum-non-conserving collisions $\tau^{-1}$ (through $\sigma_0$) and is independent of $\nu$.

On the other hand, in the limit $\ell_b \to 0$ (i.e. no-slip BCs) Eq. (2.68) reduces to

$$\sigma_{xx} = \sigma_0 \left[1 - 2\frac{D_\nu}{W}\tanh\left(\frac{W}{2D_\nu}\right)\right] \ . \tag{2.69}$$

We can easily understand two asymptotic limits of Eq. (2.69). In the limit $D_\nu \ll W$ Eq. (2.69) yields $\sigma_{xx} = \sigma_0(1 - 2D_\nu/W)$: the small correction to the Drude-like conductivity $\sigma_0$ is due to a reduction of the fluid-element velocity in a thin region of width $D_\nu$ near the top and bottom edges of the Hall bar. In the opposite limit, $D_\nu \gg W$, we obtain $\sigma_{xx} = \sigma_0 W^2/(12D_\nu^2) = e^2\bar{n}W^2/(12m\nu)$. In this limit the problem is equivalent to that of Poiseuille flow in a pipe [73], with a velocity profile $v_x(y)$ that depends quadratically on the transverse coordinate $y$ and a resistance that is entirely due to viscosity.

A summary of our main results for longitudinal electron transport in the presence of a finite viscosity is reported in Fig. 2.2.

**The Gurzhi effect**

We now would like to make a remark on the temperature dependence of $\sigma_{xx}$ in Eq. (2.68). For the sake of simplicity, we assume that $\ell_{\rm b}$ does not depend on temperature. We observe that the derivative of $\sigma_{xx}$ with respect to $T$,

$$\frac{d\sigma_{xx}}{dT} = \frac{d\sigma_0}{dT}(1-\mathcal{F}) - \sigma_0 \frac{d\mathcal{F}}{dD_\nu}\frac{dD_\nu}{dT} \ , \tag{2.70}$$

is the sum of two contributions with opposite signs. The first term on the right-hand side of Eq. (2.70) is negative, because $\mathcal{F} < 1$ and $d\sigma_0/dT < 0$. The latter inequality holds because the scattering rate $\tau^{-1}$ describing momentum non-conserving collisions is a monotonically increasing function of temperature [11]. On the contrary, the second term is positive, because the $d\mathcal{F}/dD_\nu > 0$ and $dD_\nu/dT < 0$. The vorticity diffusion length $D_\nu$ decreases with increasing temperature because both $\nu$ and $\tau$ are decreasing functions of $T$. We therefore conclude that, due to viscosity, $\sigma_{xx}$ ($\rho_{xx}$) can increase (decrease) upon increasing temperature. This is the so-called Gurzhi effect [10]. The existence of this effect relies crucially on the nature of BCs that are used to solve the hydrodynamic equations. In particular, it disappears for free-surface BCs. All previous experimental studies of transport in graphene and other 2D electron liquids we are aware of have reported monotonic temperature dependencies (i.e. no evidence of the Gurzhi effect) in the ordinary longitudinal geometry in the linear-response regime. We therefore conclude that free-surface BCs are the most appropriate for a weak driving current $I$. In this case, $\sigma_{xx}$ depends only on the unknown damping rate $\tau^{-1}$, which can therefore be determined from an ordinary four-point longitudinal transport measurement at every value of $\bar{n}$ and $T$, i.e. $\tau^{-1} = e^2\bar{n}/(m\sigma_{xx})$.

In the next Section, we will discuss another hydrodynamic phenomenon occurring in 2D electron liquids, i.e. the formation of whirlpools in electron flow [11], yielding a clear-cut experimental signal of hydrodynamic transport in weakly non-local linear-response transport measurements. Since the experimental data in Ref. [11] do not show any Gurzhi effect in the linear-response regime, in the next Section we will utilize only the free-surface BCs ($\ell_{\rm b} \to \infty$). Whirlpools in hydrodynamic electron flow, however, do exist also when no-slip BCs are used [11]. In this sense whirpools are a much more robust phenomenon that the Gurzhi effect in longitudinal transport. Whirpools are also more dramatic in experimental appearance.

### 2.2.5 Half-plane geometry

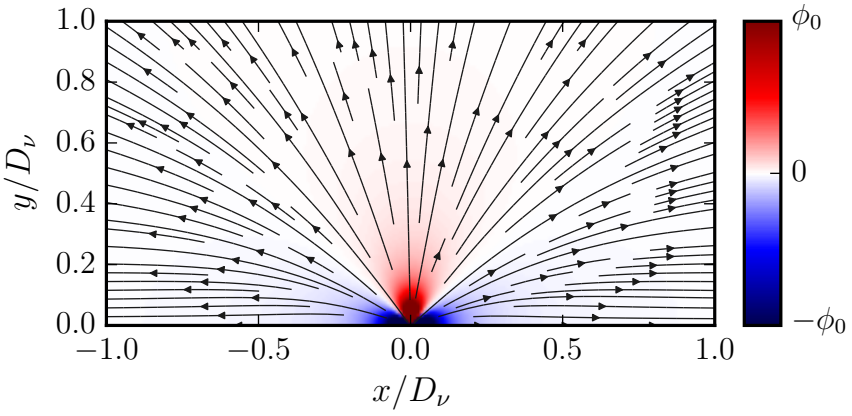


Figure 2.3: Nonlocal transport in a viscous 2D electron system confined to a half-plane geometry, as in Fig. 2.1(c). The color map shows the 2D electric potential $\phi(\boldsymbol{r})$ (in units of $\phi_0 = 100I/\sigma_0$). The vector field represents the 2D charge current profile $\boldsymbol{J}(\boldsymbol{r})$. Notice the absence of current whirlpools in this geometry. Asymptotically near the injector, we find $\boldsymbol{J}(\boldsymbol{r}) \to 2I\sin^2(\theta)\boldsymbol{r}/(\pi r^2)$, where $\theta$ is the polar angle of $\boldsymbol{r}$. This result does not depend on the boundary conditions that are used to solve the problem, free-surface (this work and Refs. [11, 96]) versus no-slip [174] boundary conditions.

In the half-plane geometry, depicted in Fig. 2.1(c), we consider a single current injector, which is described by the usual [103] point-like BC for the component of the velocity field perpendicular to the

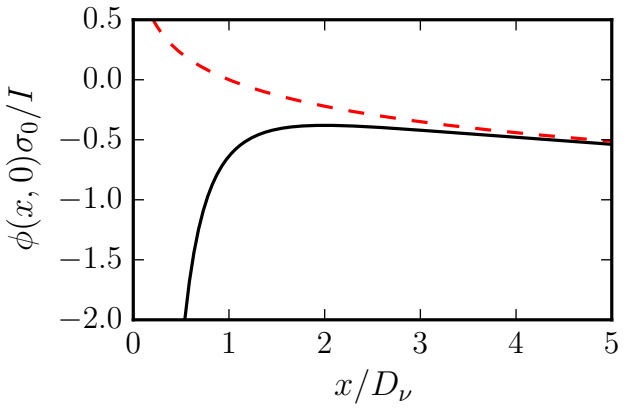


Figure 2.4: (Color online) The solid line represents the dependence of the 2D electric potential $\phi(\boldsymbol{r})$ on $x/D_\nu$ for a viscous 2D electron system confined to a half-plane. The potential is measured in units of $I/\sigma_0$ and is evaluated at the edge of the system, i.e. at $y = 0$. The Ohmic result in the absence of viscosity is also plotted (dashed line). We clearly see that viscosity introduces a region $\sim 2D_\nu$ near the injector where the 2D electrical potential is large and negative.

edge:

$$J_y(x, y = 0) = -\frac{I}{e}\delta(x) \ , \tag{2.71}$$

where $I$ in the dc drive current. The solution of the viscous problem requires an additional BC on the tangential component of the velocity at the $y = 0$ edge. Following Ref. [96], one can work with a generic BC of the type

$$\left[\partial_y J_x(\boldsymbol{r}) + \partial_x J_y(\boldsymbol{r})\right]_{y=0} = \frac{1}{\ell_\mathrm{b}} J_x(x, y = 0) \ , \tag{2.72}$$

where $\ell_\mathrm{b}$ is a boundary slip length [96]. Finally, we also impose the following BCs at $y = +\infty$: $v_x(x, y \to +\infty) = 0$ and $v_y(x, y \to +\infty) = 0$. Note that the second term in square brackets in the left-hand side of Eq. (2.72), i.e. $\partial_x v_y(\boldsymbol{r})$, is non-zero at the $y = 0$ edge and must be retained. Indeed, inserting Eq. (2.71) in Eq. (2.72), we can rewrite the BC (2.72) more explicitly as

$$\left[\partial_y J_x(\boldsymbol{r})\right]_{y=0} - \frac{I}{e}\delta'(x) = \frac{1}{\ell_\mathrm{b}} J_x(x, y = 0) \ . \tag{2.73}$$

In Fourier transform with respect to $x$, the BCs become

$$\left[\partial_y \tilde{J}_x(k, y) + ik\tilde{J}_y(k, y)\right]|_{y=0} = \frac{1}{\ell_\mathrm{b}} \tilde{J}_x(k, y = 0) \ , \tag{2.74}$$

$\tilde{J}_y(k, y = 0) = -I/(e)$, $\tilde{J}_x(k, y \to +\infty) = 0$, and $\tilde{J}_y(k, y \to +\infty) = 0$.

Imposing them we find the complete solution of the problem in Fourier transform with respect to $x$:

$$\tilde{\phi}(k, y) = -\frac{I}{\sigma_0}\frac{1}{|k|}\frac{e^{-|k|y}\left[\ell_\mathrm{b}\left(k^2 + q^2\right) + q\right]}{(|k| - q)[\ell_\mathrm{b}(|k| + q) + 1]} \ , \tag{2.75}$$

$$\tilde{J}_x(k, y) = -\frac{I}{e}\frac{ik}{|k|}\left\{\frac{\left[\ell_\mathrm{b}\left(k^2 + q^2\right) + q\right]e^{-|k|y}}{(|k| - q)[\ell_\mathrm{b}(|k| + q) + 1]} - \frac{q(2|k|\ell_\mathrm{b} + 1)e^{-qy}}{(|k| - q)[\ell_\mathrm{b}(|k| + q) + 1]}\right\} \ , \tag{2.76}$$

and

$$\tilde{J}_y(k, y) = \frac{I}{e}\left\{\frac{\left[\ell_\mathrm{b}\left(k^2 + q^2\right) + q\right]e^{-|k|y}}{(|k| - q)[\ell_\mathrm{b}(|k| + q) + 1]} - \frac{|k|(2|k|\ell_\mathrm{b} + 1)e^{-qy}}{(|k| - q)[\ell_\mathrm{b}(|k| + q) + 1]}\right\} \ . \tag{2.77}$$

In the case of the *free-surface* BCs, which are obtained by taking the limit $\ell_\mathrm{b} \to +\infty$ in Eqs. (2.72) and (2.74), the inverse Fourier transforms of Eqs. (2.75), (2.76), and (2.77) can be calculated analytically.

Simple mathematical manipulations allow us to find the electric potential and the steady-state charge current for $\ell_{\rm b} \to +\infty$:

$$\phi(\boldsymbol{r}) = -\frac{I}{\sigma_0}(1 - 2D_\nu^2\partial_x^2)\mathcal{F}(\boldsymbol{r}) \tag{2.78}$$

and

$$\boldsymbol{J}(\boldsymbol{r}) \equiv -e\bar{n}\boldsymbol{v}(\boldsymbol{r}) = I\Big\{\nabla\mathcal{F}(\boldsymbol{r}) + \nabla \times [\hat{\boldsymbol{z}}\mathcal{G}(D_\nu;\boldsymbol{r})]\Big\} \ . \tag{2.79}$$

In Eqs. (2.78)-(2.79) we have introduced the following auxiliary functions:

$$\mathcal{F}(\boldsymbol{r}) = \frac{1}{\pi}\ln(r/D_\nu) \tag{2.80}$$

and

$$\mathcal{G}(D_\nu;\boldsymbol{r}) \ \ = \ \ 2D_\nu^2\partial_x\partial_y\big[\mathcal{F}(\boldsymbol{r}) + \frac{1}{\pi}K_0(r/D_\nu)\big] \ , \tag{2.81}$$

where $K_0(r/D_\nu)$ is the zeroth-order modified Bessel function of the second kind.

Note that Eqs. (2.78) and (2.79) are manifestly universal, provided that one measures $x$ and $y$ in units of $D_\nu$, the potential in units of $I/\sigma_0$, and $\boldsymbol{J}$ in units of $I/D_\nu$. This stems, of course, from the fact that in the half-plane geometry there is one length scale, i.e. the vorticity diffusion length $D_\nu$.

In Eq. (2.78) we clearly see that the electric potential is the sum of an Ohmic contribution and a viscous one, which is proportional to $D_\nu^2$. Along the edge of the half-plane, the Ohmic result is positive definite, while the result in the presence of viscosity is large and negative: the viscous contribution to the potential dominates in the proximity of the current injector. Note that the Ohmic contributions to the potential and charge current density do *not* depend on $D_\nu$. Indeed, the Ohmic potential depends on $D_\nu$ only through a trivial constant, which has been introduced to make sure that the argument of the logarithm is dimensionless. Similarly, the Ohmic contribution to the current density does not depend on $D_\nu$, since the spatial derivative of a constant is zero.

Fig. 2.4 shows the 2D electric potential $\phi(\boldsymbol{r})$ evaluated at the $y = 0$ edge. In this figure, we only show $x > 0$ since $\phi(-x, 0) = \phi(x, 0)$. Note that the electric potential is an increasing function of $x$ for $0 < x \leq 2D_\nu$. Defining the nonlocal voltage along the edge as

$$R_{\rm HP}(\bar{x}) = \frac{\phi(\bar{x}, 0) - \phi(\bar{x}', 0)}{I} \ , \tag{2.82}$$

we conclude that, in this ultra-simplified geometry, a clear signature of the role of viscosity in transport requires to probe the 2D electric potential in the close proximity of the injector, i.e. for $\bar{x}, \bar{x}' < 2D_\nu$.

We conclude this Section with two remarks on the steady-state charge current distribution pertaining the half-plane geometry:

(a) Fig. 2.3 shows the universal spatial map of the 2D electric potential and the universal charge current streamlines in the half-plane geometry: independently of the value of $D_\nu$, *no current vortices and backflow occur in this geometry.*

(b) The current distribution $\boldsymbol{J}(\boldsymbol{r})$ near the injector is *independent* of the BCs that are used. Indeed, for the case of free-surface BCs, expanding Eq. (2.79) near the current injector located at the origin, we find:

$$\lim_{r/D_\nu \to 0} \boldsymbol{J}(\boldsymbol{r}) = \frac{2I\sin^2(\theta)}{\pi r^2}\boldsymbol{r} \ , \tag{2.83}$$

where $\theta$ is the polar angle of the vector $\boldsymbol{r}$. With no-slip BCs, i.e. for $\ell_{\rm b} = 0$, one finds exactly the same result.

The analytical solution of the problem in the half-plane geometry offers a situation in which negative nonlocal resistance near current injectors—Fig. 2.4—occurs in the absence of current whirlpools, i.e. in the absence of backflow—Fig. 2.3. A natural question therefore arises: how general is this fact? Sects. 2.2.6 and 2.2.7 below answer this question.

### 2.2.6 The Levitov-Falkovich geometry

Here, we present analytical results for the setup [174, 179] reported in Fig. 2.1(b).

In the Levitov-Falkovich (LF) geometry [174, 179], the BCs are:

$$J_y(x, y = \pm W/2) = -\frac{I}{e}\delta(x) \tag{2.84}$$

and

$$[\partial_y J_x(\boldsymbol{r}) + \partial_x J_y(\boldsymbol{r})]\,|_{y=\pm W/2} = \mp\frac{1}{\ell_{\rm b}} J_x(x, y = \pm W/2)\ . \tag{2.85}$$

Following the procedure outlined in Sects. 2.2.3-2.2.5, the solution in Fourier space for arbitrary boundary scattering length $\ell_{\rm b}$ reads as following:

$$\begin{aligned}\tilde{\phi}(k,y) &= \frac{I}{\sigma_0}\sinh(ky)\big[\ell_{\rm b}\left(k^2+q^2\right)\cosh\left(qW/2\right)+q\sinh\left(qW/2\right)\big]/\big\{k\cosh\left(kW/2\right) \\ &\times \big[\ell_{\rm b}\left(k^2-q^2\right)\cosh\left(qW/2\right)-q\sinh\left(qW/2\right)\big]+k^2\sinh\left(kW/2\right)\cosh\left(qW/2\right)\big\}\ ,\end{aligned} \tag{2.86}$$

$$\begin{aligned}\tilde{J}_x(k,y) &= -\frac{I}{e}i\big\{q\sinh(qy)\left[2k\ell_{\rm b}\cosh\left(kW/2\right)+\sinh\left(kW/2\right)\right]-\sinh(ky)\big[q\sinh\left(qW/2\right) \\ &+ \ell_{\rm b}\left(k^2+q^2\right)\cosh\left(qW/2\right)\big]\big\}/\big\{\cosh\left(kW/2\right)\big[\ell_{\rm b}\left(k^2-q^2\right)\cosh\left(qW/2\right) \\ &- q\sinh\left(qW/2\right)\big]+k\sinh\left(kW/2\right)\cosh\left(qW/2\right)\big\}\ ,\end{aligned} \tag{2.87}$$

and

$$\begin{aligned}\tilde{J}_y(k,y) &= -\frac{I}{e}\big\{k\cosh(qy)\left[2k\ell_{\rm b}\cosh\left(kW/2\right)+\sinh\left(kW/2\right)\right]-\cosh(ky)[q\sinh\left(qW/2\right) \\ &+ \ell_{\rm b}\left(k^2+q^2\right)\cosh\left(qW/2\right)]\big\}/\big\{\cosh\left(kW/2\right)\big[\ell_{\rm b}\left(k^2-q^2\right)\cosh\left(qW/2\right) \\ &- q\sinh\left(qW/2\right)\big]+k\sinh\left(kW/2\right)\cosh\left(qW/2\right)\big\}\ .\end{aligned} \tag{2.88}$$

Once again, the use of free-surface BCs, which are obtained by taking the limit $\ell_{\rm b} \to +\infty$, allows us to calculate analytically the inverse Fourier transforms of Eqs. (2.86), (2.87) and (2.88). After straightforward mathematical manipulations, we find

$$\phi(\boldsymbol{r}) = -\frac{I}{\sigma_0}(1 - 2D_\nu^2\partial_x^2)[F(x, y + W/2) - F(x, y - W/2)] \tag{2.89}$$

and

$$\boldsymbol{J}(\boldsymbol{r}) = I\Big\{\nabla[F(x,y+W/2)-F(x,y-W/2)]+\nabla\times\hat{\boldsymbol{z}}[G(D_\nu;x,y+W/2)-G(D_\nu;x,y-W/2)]\Big\}\ , \tag{2.90}$$

where we have introduced the following auxiliary functions

$$F(\boldsymbol{r}) = \frac{1}{2\pi}\ln[\cosh(\pi x/W) - \cos(\pi y/W)]\ , \tag{2.91}$$

$$G(D_\nu;\boldsymbol{r}) = 2D_\nu^2[\partial_x\partial_y F(\boldsymbol{r}) + S(\boldsymbol{r})]\ , \tag{2.92}$$

and

$$S(\boldsymbol{r}) \equiv \sum_{n=1}^{\infty}\sin\left(\frac{n\pi y}{W}\right)\frac{n\pi}{W^2}\mathrm{sgn}(x)e^{-|x|\sqrt{(n\pi/W)^2+1/D_\nu^2}}\ . \tag{2.93}$$

In this geometry, the nonlocal resistance was defined as [174]

$$R_{\rm LF}(\bar{x}) \equiv \frac{\phi(\bar{x}, -W/2) - \phi(\bar{x}, W/2)}{I} = \frac{2\phi(\bar{x}, -W/2)}{I}\ . \tag{2.94}$$

Replacing Eq. (2.89) in Eq. (2.94) we find

$$R_{\rm LF}(\bar{x}) = -\frac{1}{\sigma_0}\left\{\frac{1}{\pi}\ln\left[\tanh^2\left(\frac{\pi\bar{x}}{2W}\right)\right] + 4\pi\left(\frac{D_\nu}{W}\right)^2\frac{\cosh(\pi\bar{x}/W)}{\sinh^2(\pi\bar{x}/W)}\right\}\ . \tag{2.95}$$

We note that, for each lateral displacement $\bar{x}$ from the injector/collector electrodes in Fig. 2.1(b), we can define the following critical vorticity diffusion length scale:

$$D^*_{\rm LF}(\bar{x}) = \frac{W}{2\pi}\left\{-\frac{\sinh^2\left(\frac{\pi\bar{x}}{W}\right)}{\cosh\left(\frac{\pi\bar{x}}{W}\right)}\ln\left[\tanh^2\left(\frac{\pi\bar{x}}{2W}\right)\right]\right\}^{1/2} , \tag{2.96}$$

which is such that $R_{\rm LF}(\bar{x}) = 0$. Fig. 2.5 shows $D^*_{\rm LF}$ as a function of $\bar{x}$. The physical meaning of the quantity $D^*_{\rm LF}(\bar{x})$ is the following. For $D_\nu > D^*_{\rm LF}(\bar{x})$, the nonlocal resistance $R_{\rm LF}(\bar{x})$ is *negative*. Note that $D^*_{\rm LF}(\bar{x}) \to 0$ for $\bar{x} \ll D_\nu$ and $D^*_{\rm LF}(\bar{x}) \to W/(\sqrt{2}\pi)$ for $\bar{x} \gg W$. The first limit implies that, in the close proximity of the injector/collector electrodes, the nonlocal resistance $R_{\rm LF}(\bar{x})$ is negative for arbitrarily small values of the kinematic viscosity $\nu$.

Now, the key question is: what about current whirlpools in this geometry? Without loss of generality, we can focus on the right side of the conductive channel, i.e. for $x > 0$. The setup in Fig. 2.1(b) is clearly symmetric with respect to the inversion $x \to -x$. Also, because of the symmetric location of the electrodes, the horizontal component of the current is identically zero along the $y = 0$ axis, i.e. $J_x(x, 0) = 0$. If a current vortex exists in this geometry, it must be centered on the $y = 0$ axis. Fig. 2.6 shows the vertical component $J_y(x, 0)$ of the current density as a function of $x$, for $y = 0$. It is easy to show that $J_y(x, 0)$ is positive at $x = 0$, independently of the value of $D_\nu$. At large $x \gg W$ distances, on the other hand, one can approximate the current density along the $y = 0$ axis as:

$$J_y(x \gg W, 0) \to \frac{2I}{W}\left\{[1 - 2\pi^2(D_\nu/W)^2]e^{-\pi x/W} + 2\pi^2(D_\nu/W)^2 e^{-x\sqrt{\frac{1}{D_\nu^2}+\frac{\pi^2}{W^2}}}\right\} . \tag{2.97}$$

Using Eq. (2.97), we find that $J_y(x \to +\infty, 0) = 0^+$ for $D_\nu < W/(\sqrt{2}\pi)$, while $J_y(x \to +\infty, 0) = 0^-$ for $D_\nu > W/(\sqrt{2}\pi)$. We therefore conclude that $J_y(x, 0)$ is positive for all the values of $x$ as long as $D_\nu < W/(\sqrt{2}\pi)$. In this geometry, current whirlpools do not exist for $D_\nu < W/(\sqrt{2}\pi)$. Plots of $J_y(x, 0)$ for different values of $D_\nu$ are shown in Fig. 2.6.

On the contrary, for $D_\nu > W/(\sqrt{2}\pi)$, there is a finite value of $x$, i.e. $x_{\rm whirl}$, such that $J_y(x, 0) < 0$ for $x > x_{\rm whirl}$. This means that, for $D_\nu > W/(\sqrt{2}\pi)$, two current whirlpools appear in the LF geometry at positions $(\pm x_{\rm whirl}, 0)$. In particular, in the limit of a very large viscosity, i.e. for $D_\nu \gg W$, one can write a closed-form expression for the current density. Indeed, in this limit, the auxiliary function $G(D_\nu; \boldsymbol{r})$ in Eq. (2.92) tends to the following expression

$$G(D_\nu \gg W; \boldsymbol{r}) = -\frac{(x/W)\sin(\pi y/W)}{2[\cosh(\pi x/W) - \cos(\pi y/W)]} . \tag{2.98}$$

In this limit, $x_{\rm whirl}$ is the root of the transcendental equation $\pi x_{\rm whirl}\tanh(\pi x_{\rm whirl}/W)/W = 2$, yielding $x_{\rm whirl} \approx 0.66W$.

In summary, in the LF geometry whirlpools emerge only above a threshold value of viscosity, i.e. for $D_\nu \geq W/(\sqrt{2}\pi)$. At $D_\nu = W/(\sqrt{2}\pi)$, whirlpools form at infinity. For $D_\nu \gg W/(\sqrt{2}\pi)$, whirlpools approach the position $(\pm 0.66W, 0)$. Typical results for 2D electric potential $\phi(\boldsymbol{r})$ and charge current density $\boldsymbol{J}(\boldsymbol{r})$ in this geometry are shown in Fig. 2.7. For a highly viscous and clean electron system such as that in graphene, one can reach $D_\nu$ of $\sim$ 0.3-0.4 $\mu$m (Ref. [11]), which necessitates devices with $W \lesssim$ 1.3-1.8 $\mu$m to be able to create whirlpool currents.

### 2.2.7 The vicinity geometry

In this Section we present analytical results for the vicinity setup [96, 11] in Fig. 2.1(a).

In this geometry, the BCs read as following

$$J_y(x, y = +W/2) = 0 , \tag{2.99}$$

$$J_y(x, y = -W/2) = -\frac{I}{e}[\delta(x) - \delta(x - x_0)] , \tag{2.100}$$

while the free-surface BC on the tangential component of the fluid-element velocity reduces to

$$[\partial_y J_x(\boldsymbol{r}) + \partial_x J_y(\boldsymbol{r})]\,|_{y=\pm W/2} = 0 . \tag{2.101}$$

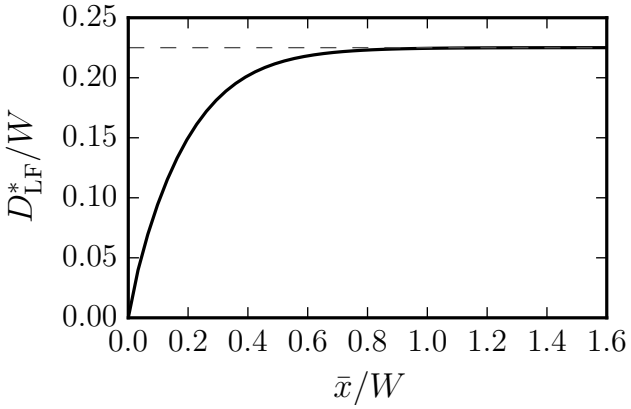


Figure 2.5: The critical vorticity diffusion length $D^*_{\rm LF}(\bar{x})$ (in units of $W$) defined in Eq. (2.96) is plotted as a function of $\bar{x}/W$. For $\bar{x} \gg W$, $D^*_{\rm LF}(\bar{x}) \to W/(\sqrt{2}\pi)$ (horizontal dashed line).

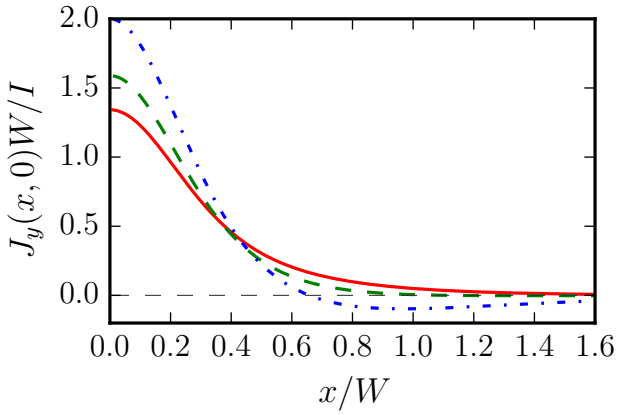


Figure 2.6: The quantity $J_y(x,0)$ (in units of $I/W$), calculated from Eq. (2.90), is plotted as a function of $x/W$. The solid line refers to $D_\nu = 0.15\ W$, the dashed line to $D_\nu = 0.25\ W$, and the dash-dotted line to $D_\nu = 10\ W$.

Repeating the same algebraic steps outlined in the previous Sections, we find that the electric potential and charge current distribution in this geometry can be written as:

$$\begin{aligned} \phi(\boldsymbol{r}) &= -\frac{I}{\sigma_0}(1 - 2D_\nu^2\partial_x^2)[F(x, y + W/2) \\ &- F(x - x_0, y + W/2)] \end{aligned} \tag{2.102}$$

and

$$\boldsymbol{J}(\boldsymbol{r}) = I\Big\{\nabla[F(x,y+W/2) - F(x-x_0,y+W/2)] + \nabla\times\hat{\boldsymbol{z}}[G(D_\nu;x,y+W/2) - G(D_\nu;x-x_0,y+W/2)]\Big\}\,, \tag{2.103}$$

where the auxiliary function $F(\boldsymbol{r})$ and $G(D_\nu;\boldsymbol{r})$ have been defined in Eqs. (2.91) and (2.92), respectively.

The nonlocal vicinity voltage can be defined as

$$R_{\rm V}(\bar{x}) \equiv \frac{\phi(\bar{x}, -W/2) - \phi(\bar{x} + d, -W/2)}{I}\,. \tag{2.104}$$

The expression of the vicinity resistance notably simplifies in the limit $x_0 \to -\infty$ and $d \to +\infty$: taking these limits we find [96]

$$R_{\rm V}(\bar{x}) = -\frac{1}{2\sigma_0}\left\{\frac{1}{\pi}\ln\left[4\sinh^2\left(\frac{\pi\bar{x}}{2W}\right)\right] - \frac{\bar{x}}{W} + \pi\left(\frac{D_\nu}{W}\right)^2\frac{1}{\sinh^2\left(\pi\bar{x}/(2W)\right)}\right\}\,. \tag{2.105}$$

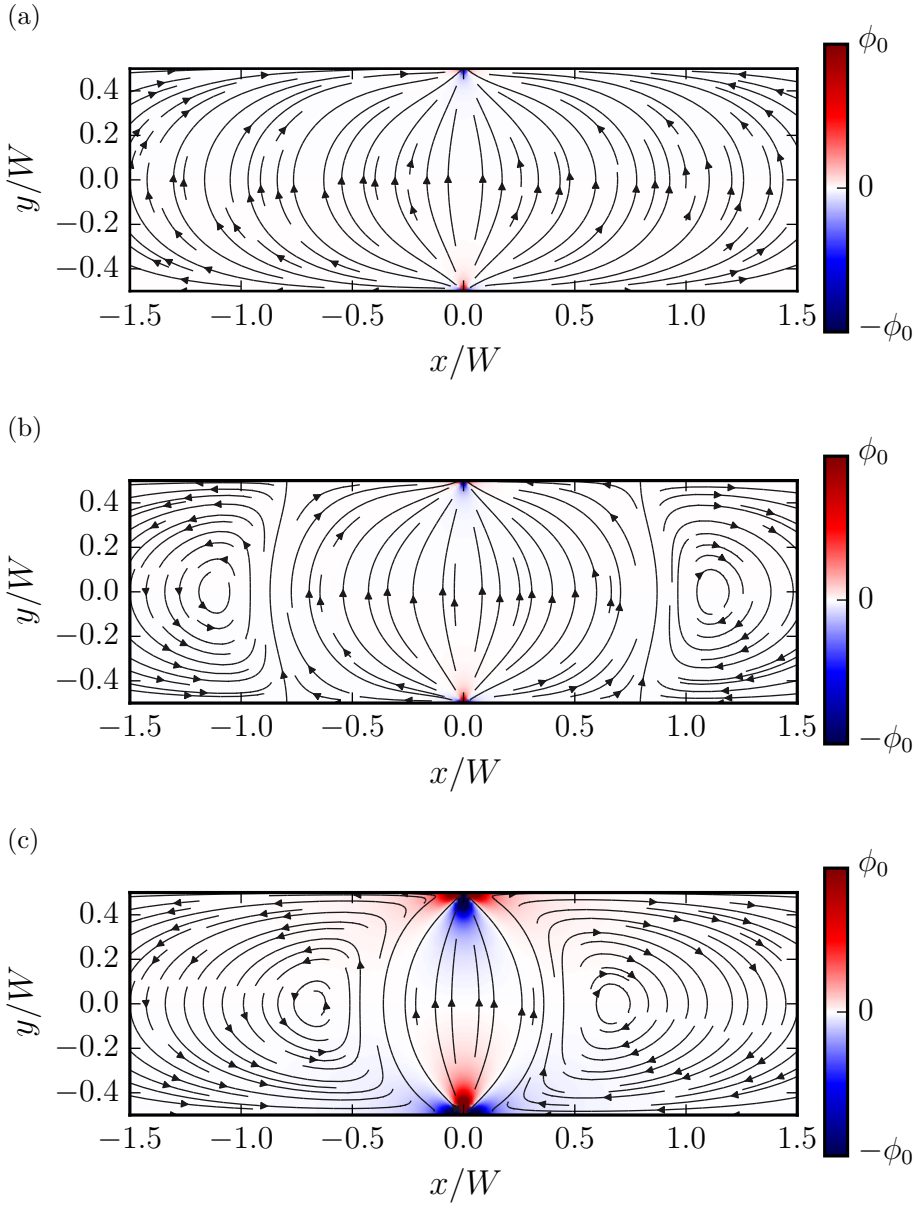


Figure 2.7: Nonlocal transport in the LF geometry—Fig. 2.1(b). The color map denotes the spatial distribution of the 2D electric potential $\phi(\boldsymbol{r})$ (in units of $\phi_0 = 100I/\sigma_0$). The vector field denotes the charge current density $\boldsymbol{J}(\boldsymbol{r})$. Panel (a): $D_\nu = 0.20W$. Panel (b): $D_\nu = 0.25W$. Panel (c): $D_\nu = W$. We clearly see current whirlpools in panels (b) and (c) because both values of $D_\nu$ that have been used to make these two plots are above the threshold value $D_\nu = W/(\sqrt{2}\pi) \simeq 0.225W$.

Similarly to what was done in Sect. 2.2.6, we can define a critical vorticity diffusion length scale $D^*_{\rm V}(\bar{x})$ as following:

$$D^*_{\rm V}(\bar{x}) \equiv W \sinh\left(\frac{\pi\bar{x}}{2W}\right)\left\{\frac{\bar{x}}{\pi W} - \frac{1}{\pi^2}\ln\left[4\sinh^2\left(\frac{\pi\bar{x}}{2W}\right)\right]\right\}^{1/2}. \tag{2.106}$$

For $D_\nu > D^*_{\rm V}(\bar{x})$ the vicinity resistance $R_{\rm NL}(\bar{x})$ is negative. Fig. 2.8 illustrates the functional dependence of $D^*_{\rm V}(\bar{x})$ on $\bar{x}$. As in the case of $D^*_{\rm LF}(\bar{x})$, $D^*_{\rm V}(\bar{x})$ tends to the asymptotic value $W/(\sqrt{2}\pi)$ for $\bar{x} \gg W$.

Unlike the LF geometry, the vicinity one exhibits a more direct relation between negative nonlocal voltage and current whirlpools. In the proximity of the current injector, i.e. for $x \ll D_\nu, W$ and $y \to$

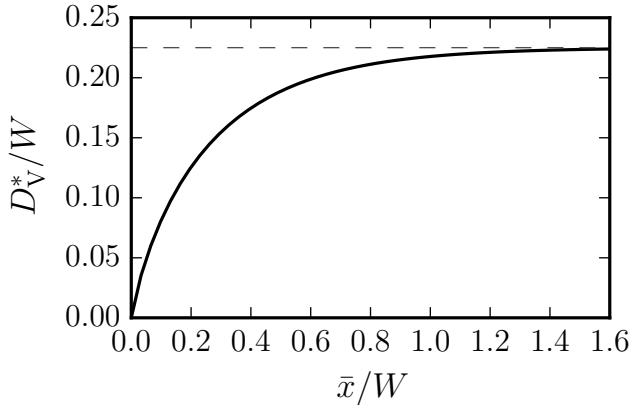


Figure 2.8: The critical vorticity diffusion length $D_{\rm V}^*(\bar{x})$ (in units of $W$) defined in Eq. (2.106) is plotted as a function of $\bar{x}/W$. For $\bar{x} \gg W$, $D_{\rm V}^*(\bar{x}) \to W/(\sqrt{2}\pi)$ (horizontal dashed line).

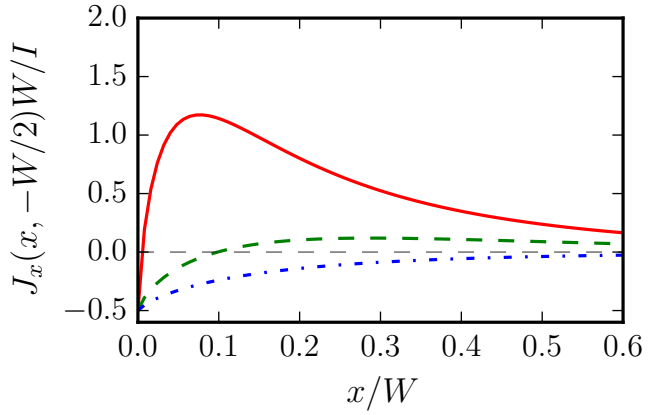


Figure 2.9: The quantity $J_x(x,-W/2)$ (in units of $I/W$), calculated from Eq. (2.103), is plotted as a function of $x/W$. The solid line refers to $D_\nu = 0.05\ W$, the dashed line to $D_\nu = 0.15\ W$, and the dash-dotted line to $D_\nu = 0.25\ W$.

$-W/2$, and in polar coordinates, the current density (2.103) behaves like

$$\boldsymbol{J}(\boldsymbol{r}) \to I\left[-\frac{1}{2W}\hat{\boldsymbol{x}} + \frac{2\sin^2(\theta)}{\pi r^2}\boldsymbol{r}\right] , \tag{2.107}$$

where we have used the asymptotic expansion (2.83) for the half-plane geometry. In Eq. (2.107) we have taken the origin of the polar plane to lie at $(0,-W/2)$. Note the presence of the first term in the square brackets in Eq. (2.107), i.e. $-I/(2W)$, which is due to the collector at $x_0 \to -\infty$. This term has crucial implications on the occurrence of whirlpools in the vicinity geometry [96, 11]. Indeed, from the BC (2.100), we see that $J_y(x,-W/2) = 0$ for $x > 0$. Eq. (2.107) implies that $J_x(0,-W/2) = -I/(2W) < 0$, independently of the value of $D_\nu$. *This implies that in the vicinity geometry there is always backflow in the proximity of the injector, independently of the value of* $D_\nu$.

As we now proceed to demonstrate, the precise value of $D_\nu$ sets only the spatial extension of the current whirlpool. At large lateral separations from the injector, one can approximate the current density (2.103) along the bottom edge as

$$J_x(x \gg W,-W/2) \to \frac{I}{W}\left\{[1-2\pi^2(D_\nu/W)^2]e^{-\pi x/W} + 2\pi^2(D_\nu/W)^2 e^{-x\sqrt{\frac{1}{D_\nu^2}+\frac{\pi^2}{W^2}}}\right\} . \tag{2.108}$$

Using the previous result, we find that $J_x(x \gg W,-W/2) = 0^+$ for $D_\nu < W/(\sqrt{2}\pi)$, while $J_x(x \gg W,-W/2) = 0^-$ for $D_\nu > W/(\sqrt{2}\pi)$. This implies that $J_x(x,-W/2)$ is negative for *all* values of $x > 0$ for $D_\nu > W/(\sqrt{2}\pi)$. This is clearly seen in Fig. 2.9 for $D_\nu = 0.25\ W$ (dash-dotted line). On the contrary,

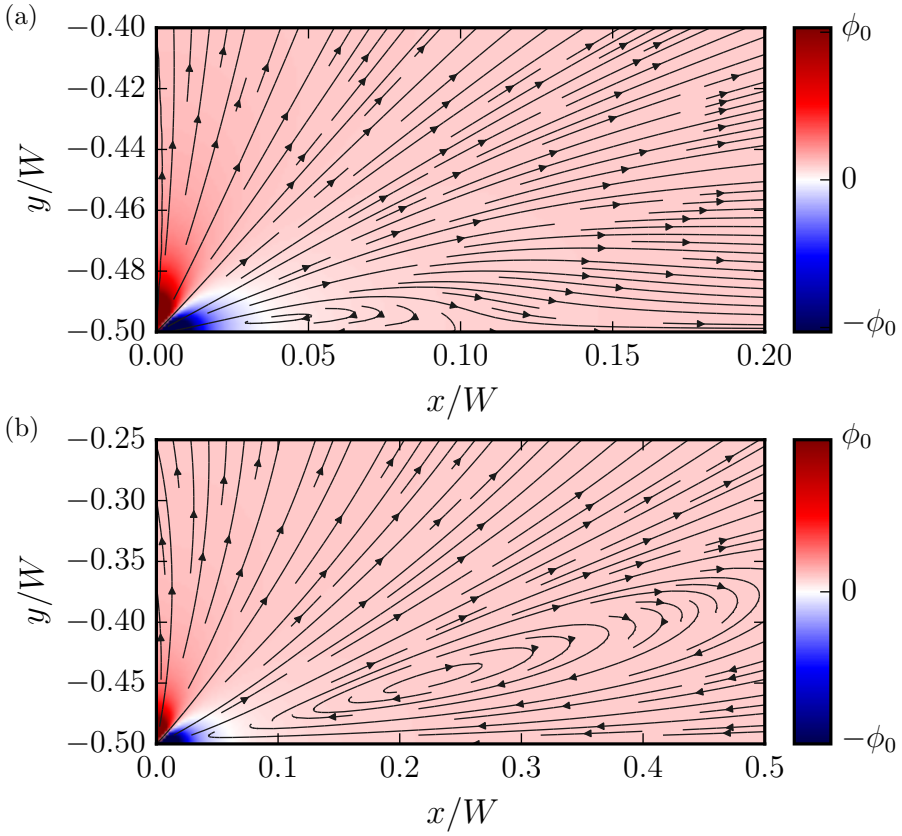


Figure 2.10: Nonlocal transport in the vicinity geometry—Fig. 2.1(a). The color map denotes the spatial distribution of the 2D electric potential $\phi(\boldsymbol{r})$ (in units of $\phi_0 = 100I/\sigma_0$). The vector field denotes the charge current density $\boldsymbol{J}(\boldsymbol{r})$. Data in this plot refer to the spatial region $x > 0$ in Fig. 2.1(a). Panel (a): $D_\nu = 0.15W$. Panel (b) $D_\nu = 0.25W$. While backflow is present in both panels, the precise value of $D_\nu$ sets the spatial extension of current whirlpools.

for $D_\nu < W/(\sqrt{2}\pi)$, $J_x(x, -W/2)$ is negative in a *finite* range of values of $x > 0$, as one can see in Fig. 2.9 for $D_\nu = 0.05W$ (solid line) and $D_\nu = 0.15W$ (dashed line).

In Fig. 2.10 we show that, independently of the value of $D_\nu$, viscosity induces a vortex to the right of the current injector. For $D_\nu < W/(\sqrt{2}\pi)$, the vortex is "localized" in an increasingly smaller region in the close proximity of the current injector, as shown in Fig. 2.10(a), while for $D_\nu > W/(\sqrt{2}\pi)$ the vortex spreads out in space far away from the location of the current injector, as in Fig. 2.10(b).

In the experiments [11], devices with $W$ ranging from 1.5 to 4 $\mu$m were employed which, for $D_\nu \approx 0.4$ $\mu$m, yields $D_\nu/W \approx 0.27$ to 0.1, respectively. For a vicinity contact placed at a distance of 1 $\mu$m, we have checked numerically that *backflow at the contact* is expected if $W \gtrsim 1.8$ $\mu$m. In reality, however, this condition is softened by the fact that both injector and detector contacts had a finite (relatively large) width of $\approx 0.3$ $\mu$m, which should allow backflow at a nominal distance to the injector larger than 2 $\mu$m. Nonetheless, even the device with $W = 4$ $\mu$m exhibited negative vicinity resistance, in agreement with the fact that the latter is a necessary but not sufficient condition for the existence of backflow at the vicinity contact.

## 2.3 Non-local transport and the Hall viscosity of 2D hydrodynamic electron liquids

In the presence of time-reversal symmetry, the response of an hydrodynamic electron system to slowly-varying external fields is fully determined by the bulk $\zeta$ and shear $\eta$ viscosities and the thermal conductivity $\kappa$. However, when time-reversal symmetry is broken (for example due to the presence of an external magnetic field), a dissipationless term, controlled by the so-called Hall viscosity [183, 184, 185,

186, 187, 188, 161, 163, 189, 190, 162, 164] $\eta_{\rm H}$, appears in the viscous stress tensor [73] $\sigma'_{ij}$. In two spatial dimensions one has

$$\sigma'_{ij} = \sum_{k,\ell} \eta_{ij,k\ell} v_{k\ell} \ , \tag{2.109}$$

where $i, j, k$ and $\ell$ denote Cartesian indices, $v_{k\ell} \equiv (\partial_k v_\ell + \partial_\ell v_k)/2$, and $\eta_{ij,k\ell}$ is a rank-4 tensor, usually called "viscosity" tensor [163],

$$\eta_{ij,k\ell} \equiv \zeta \delta_{ij}\delta_{k\ell} + \eta(\delta_{ik}\delta_{j\ell} + \delta_{i\ell}\delta_{jk} - \delta_{ij}\delta_{k\ell}) + \eta_{\rm H}(\delta_{jk}\epsilon_{i\ell} - \delta_{i\ell}\epsilon_{kj}) \ . \tag{2.110}$$

In Eq. (2.110), $\eta_{\rm H}$ parametrizes the portion of $\eta_{ij,k\ell}$ which is antisymmetric with respect to the exchange $ij \leftrightarrow k\ell$ and is non-zero only when time-reversal symmetry is broken.

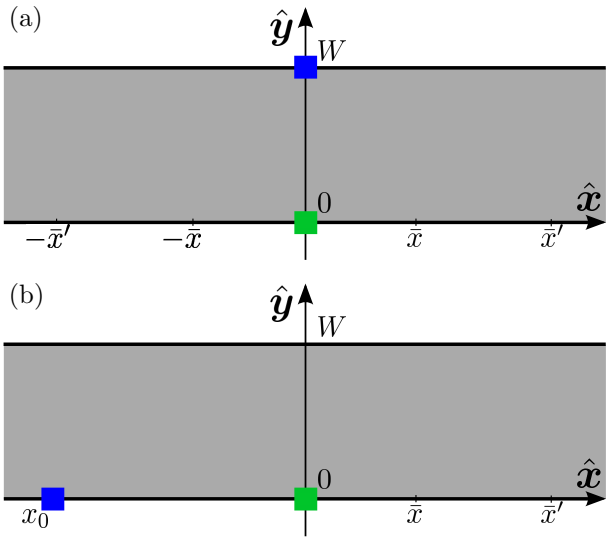


Figure 2.11: A sketch of the non-local transport setups analyzed in this work. All setups have infinite length in the $\hat{\boldsymbol{x}}$ direction and finite width $W$ in the $\hat{\boldsymbol{y}}$ direction. Panel (a) illustrates the "transverse" geometry [174, 104]. In this setup, current is injected into (extracted from) the green (blue) electrode located at $x = 0$, $y = 0$ ($x = 0$, $y = W$). Panel (b) illustrates the "vicinity" geometry [96, 104, 11]. In this setup, current is injected into (extracted from) the green (blue) electrode located at $x = 0$ ($x = x_0 < 0$) and $y = 0$.

Recent theoretical [96, 174, 104, 179] and experimental [11, 13, 14, 12] work has attracted interest in the flow of viscous electron liquids. In particular, two experiments [11, 12] in high-quality encapsulated graphene sheets have demonstrated two unique qualitative features of viscous electron transport (negative quasi-local resistance [11] and super-ballistic electron flow [12]), providing, for the first time, the ability to directly measure the dissipative shear viscosity $\eta$ of a two-dimensional (2D) electron system.

In this Section, we focus on the role of the Hall viscosity $\eta_{\rm H}$ on the non-local electrical transport characteristics of 2D electron systems subject to a perpendicular magnetic field. Solving suitable magneto-hydrodynamic equations for the rectangular geometries sketched in Fig. 2.11, we demonstrate how one can directly measure $\eta_{\rm H}$ by purely electrical non-local measurements.

In Sect. 2.3.1 we present the solution of the magneto-hydrodynamic equations in the case of a rectangular setup, with infinite length in the $\hat{\boldsymbol{x}}$ direction and finite width in the $\hat{\boldsymbol{y}}$ direction, in the presence of a single current injector on one side of the setup. This solution is then used in Sect. 2.3.2 as a building block to construct the solutions for the "transverse" and "vicinity" geometries, sketched in Figs. 2.11 (a) and (b), respectively.

In the linear-response and steady-state regimes, electron transport in the hydrodynamic regime in the presence of a static magnetic field $\boldsymbol{B} = B\hat{\boldsymbol{z}}$ is described by the continuity equation

$$\nabla \cdot \boldsymbol{J}(\boldsymbol{r}) = 0 \ , \tag{2.111}$$

and the Navier-Stokes equation

$$-\nabla P(\boldsymbol{r})+\nabla\cdot\boldsymbol{\sigma}'(\boldsymbol{r})+e\bar{n}\nabla\varphi(\boldsymbol{r})-\frac{e}{c}\boldsymbol{J}(\boldsymbol{r})\times\boldsymbol{B}=\frac{m}{\tau}\boldsymbol{J}(\boldsymbol{r})\ . \tag{2.112}$$

Here, $\boldsymbol{J}(\boldsymbol{r})=\bar{n}\boldsymbol{v}(\boldsymbol{r})$ is the particle current density, $\boldsymbol{v}(\boldsymbol{r})$ is the fluid element velocity, $\bar{n}$ is the ground-state uniform density, $P(\boldsymbol{r})$ is the pressure, $\boldsymbol{\sigma}'(\boldsymbol{r})$ is the viscous stress tensor whose Cartesian components have been explicitly reported in Eqs. (2.109)-(2.110), $\varphi(\boldsymbol{r})$ is the 2D electrostatic potential in the plane where electrons move, $-e$ is the electron charge, $m$ is the electron effective mass, and $\tau$ is a phenomenological transport time describing momentum-non-conserving collisions [96] (e.g. scattering of electrons against acoustic phonons). The gradient of the pressure is proportional to the gradient of the density via $\nabla P(\boldsymbol{r})=(\mathcal{B}/\bar{n})\nabla n(\boldsymbol{r})$, where $\mathcal{B}=\bar{n}^2/\mathcal{N}_0$ is the bulk modulus [35] of the homogeneous electron liquid, $\mathcal{N}_0$ being the density of states at the Fermi energy [35]. It is useful to define the electrochemical potential as $\phi(\boldsymbol{r})=\varphi(\boldsymbol{r})+\delta\mu(\boldsymbol{r})/(-e)$ where $\delta\mu(\boldsymbol{r})=[n(\boldsymbol{r})-\bar{n}]/\mathcal{N}_0$ is the chemical potential measured with respect to the equilibrium value, e.g. $\bar{\mu}=\hbar v_{\rm F}\sqrt{\pi\bar{n}}$ for the case of single-layer graphene [31] and $\bar{\mu}=\hbar^2\pi\bar{n}/(2m)$ for bilayer graphene [31]. Since experimental probes are usually sensitive to $\phi(\boldsymbol{r})$, from now on we will focus our attention on the electrochemical potential rather than on $\varphi(\boldsymbol{r})$.

We now note that the viscous stress tensor in Eqs. (2.109)-(2.110) can be written in the following compact form

$$\boldsymbol{\sigma}'=(\eta\mathbb{I}+i\eta_{\rm H}\boldsymbol{\tau}_y)[(\partial_x v_x-\partial_y v_y)\boldsymbol{\tau}_z+(\partial_x v_y+\partial_y v_x)\boldsymbol{\tau}_x]+\zeta\nabla\cdot\boldsymbol{v}, \tag{2.113}$$

where $\boldsymbol{\tau}_i$ with $i=x,y,z$ are standard $2\times2$ Pauli matrices acting on Cartesian indices and $\mathbb{I}$ is the $2\times2$ identity matrix. As in Eq. (2.112) above, in the linear-response and steady-state regimes we can write $\boldsymbol{v}(\boldsymbol{r})=\boldsymbol{J}(\boldsymbol{r})/\bar{n}$. We then note that the bulk viscosity $\zeta$ couples to $\nabla\cdot\boldsymbol{J}$, which vanishes because of the continuity equation (2.111). The bulk viscosity term in the viscous stress tensor therefore drops out of the problem at hand. In summary, Eq. (2.113) simplifies to:

$$\boldsymbol{\sigma}'=m(\nu\mathbb{I}+i\nu_{\rm H}\boldsymbol{\tau}_y)[(\partial_x J_x-\partial_y J_y)\boldsymbol{\tau}_z+(\partial_x J_y+\partial_y J_x)\boldsymbol{\tau}_x]\ , \tag{2.114}$$

where $\nu\equiv\eta/(m\bar{n})$ is the kinetic shear viscosity and $\nu_{\rm H}\equiv\eta_{\rm H}/(m\bar{n})$ is the kinetic Hall viscosity. Replacing Eq. (2.114) into Eq. (2.112) and introducing the electrochemical potential $\phi(\boldsymbol{r})$, we can write the Navier-Stokes equation (2.112) as

$$\frac{\sigma_0}{e}\nabla\phi(\boldsymbol{r})=(1-D_\nu^2\nabla^2)\boldsymbol{J}(\boldsymbol{r})+\omega_{\rm c}\tau\left(1+D_{\rm H}^2\nabla^2\right)\boldsymbol{J}(\boldsymbol{r})\times\hat{\boldsymbol{z}}\ , \tag{2.115}$$

where $\sigma_0=ne^2\tau/m$, $D_\nu\equiv\sqrt{\nu\tau}$ has been introduced in Refs. [96, 11, 104], $D_{\rm H}\equiv\sqrt{-\nu_{\rm H}/\omega_{\rm c}}$, and $\omega_{\rm c}\equiv eB/(mc)$ is the usual cyclotron frequency. As we will see below, $\nu_{\rm H}$ and $\omega_{\rm c}$ have opposite signs so that $D_{\rm H}$ is a well defined length scale. Notice that the Hall viscosity parametrizes a correction to the ordinary Lorentz force due to the spatial dependence of the velocity $\boldsymbol{v}(\boldsymbol{r})$.

We now resort to useful results of semiclassical Boltzmann transport theory (see Section 2.1), which capture the dependence of the shear and Hall viscosities on the magnitude of the applied magnetic field [191]:

$$\nu=\nu_0\frac{B_0^2}{B_0^2+B^2} \tag{2.116}$$

$$\nu_{\rm H}=-\nu_0\frac{BB_0}{B_0^2+B^2}\ , \tag{2.117}$$

where $\nu_0$ is the kinematic shear viscosity at zero magnetic field and $B_0\equiv c\bar{n}/(4e\mathcal{N}_0\nu_0)$ is a characteristic magnetic field. For example, for bilayer graphene [31] with carrier density $\bar{n}=10^{12}$ cm$^{-2}$, we find $B_0\approx0.1$ Tesla for [11, 12] $\nu_0\approx0.1$ m$^2$/s. For the same set of parameters we find, for $|B|\ll B_0$, a finite value of $D_{\rm H}\approx1\mu$m. Despite Eq. (2.117) has been derived in the weak-field limit, it yields sensible results even for high magnetic fields. In the limit $|B|\gg B_0$, indeed, we find $\nu_{\rm H}\approx-{\rm sgn}(B)\ell_B^2\bar{n}/(4\hbar\mathcal{N}_0)$, $\ell_B=\sqrt{c\hbar/(e|B|)}$ being the magnetic length, in agreement with the quantum Hall regime results derived in Ref. [189].

Since all the setups in Fig. 2.11 are translationally-invariant in the $\hat{\boldsymbol{x}}$ direction, it is useful to introduce the following Fourier Transforms [96, 104] (FTs) with respect to the spatial coordinate $x$: $\tilde{\phi}(k,y)=$

$\int_{-\infty}^{+\infty} dx\ e^{-ikx}\phi(\boldsymbol{r})$ and $\tilde{\boldsymbol{J}}(k,y) = \int_{-\infty}^{+\infty} dx\ e^{-ikx}\boldsymbol{J}(\boldsymbol{r})$. The three coupled partial-differential equations (2.111)-(2.112) can be combined into a $4\times 4$ system of first-order ordinary differential equations:

$$\partial_y \boldsymbol{w}(k,y) = \mathcal{M}(k)\boldsymbol{w}(k,y)\ , \tag{2.118}$$

where $\boldsymbol{w}(k,y)$ is a four-component vector, i.e.

$$\boldsymbol{w}(k,y) = \begin{pmatrix} k\tilde{J}_x(k,y) \\ k\tilde{J}_y(k,y) \\ \partial_y \tilde{J}_x(k,y) \\ e\bar{n}\tilde{\phi}(k,y)/(m\nu) \end{pmatrix}, \tag{2.119}$$

and

$$\mathcal{M}(k) = k\begin{pmatrix} 0 & 0 & 1 & 0 \\ -i & 0 & 0 & 0 \\ 1+1/(kD_\nu)^2 & \nu_{\rm r}+\omega_{\rm c}\tau/(kD_\nu)^2 & i\nu_{\rm r} & -i \\ (\nu_{\rm r}-\omega_{\rm c}\tau)/(kD_\nu)^2 & 1+\nu_{\rm r}^2+(1+\nu_{\rm r}\omega_{\rm c}\tau)/(kD_\nu)^2 & i(1+\nu_{\rm r}^2) & -i\nu_{\rm r} \end{pmatrix}, \tag{2.120}$$

where $\nu_{\rm r}\equiv\nu_{\rm H}/\nu$. The matrix $\mathcal{M}(k)$ has four eigenvalues: $\lambda_{1/2}(k)=\pm|k|$ and $\lambda_{3/4}(k)=\pm q$, where we have introduced the shorthand

$$q \equiv \sqrt{k^2+1/D_\nu^2}\ . \tag{2.121}$$

The corresponding eigenvectors are:

$$\boldsymbol{w}_{1/2}(k) = \begin{pmatrix} i \\ \pm{\rm sgn}(k) \\ \pm i\,{\rm sgn}(k) \\ \frac{1\mp i\,{\rm sgn}(k)\omega_{\rm c}\tau}{D_\nu^2 k^2} \end{pmatrix},\ \boldsymbol{w}_{3/4}(k) = \begin{pmatrix} \pm\frac{k}{q} \\ -i\frac{k^2}{q^2} \\ 1 \\ \frac{(\nu_{\rm r}-\omega_{\rm c}\tau)}{D_\nu^2 q^2} \end{pmatrix}\ . \tag{2.122}$$

Note that the eigenvalues are independent of the cyclotron frequency and Hall viscosity, while the eigenvectors explicitly depend on them. The general solution of Eq. (2.118) can be therefore written as a linear combination of exponentials of the form $\sum_{j=1}^{4} a_j(k)\boldsymbol{w}_j(k)\exp(\lambda_j y)$. The four coefficients $a_j(k)$ can be determined from the enforcement of suitable boundary conditions (BCs).

### 2.3.1 Single-injector setup

We consider a single current injector in a rectangular setup with infinite length in the $\hat{\boldsymbol{x}}$ direction and finite width $W$ in the $\hat{\boldsymbol{y}}$ direction. This plays the role of "building block", allowing us to solve the magneto-hydrodynamic problem posed by Eqs. (2.111)-(2.112) in more complicated setups like the ones sketched in Figs. 2.11(a) and (b).

A current injector is mathematically described by the usual point-like BC for the component of the current density perpendicular to the $y=0$ edge:

$$J_y(x,0) = -I\delta(x)/e\ , \tag{2.123}$$

where $I$ in the dc drive current [103]. On the edge opposite to the injector (i.e. at $y=W$), the orthogonal component of the current density must vanish:

$$J_y(x,W) = 0\ . \tag{2.124}$$

The solution of the viscous problem requires additional BCs on the tangential components of the current density at both edges. We impose that the current density on the boundary $\Omega$ of the sample is proportional to the off-diagonal component of the stress [96, 104]:

$$[\hat{\boldsymbol{e}}_{\rm t}\cdot(\hat{\boldsymbol{\sigma}}'\cdot\hat{\boldsymbol{e}}_{\rm n}) + (m\nu/\ell_{\rm b})\hat{\boldsymbol{e}}_{\rm t}\cdot\boldsymbol{J}]_\Omega = 0\ , \tag{2.125}$$

where $\hat{\boldsymbol{e}}_{\rm n}$ denotes the outer normal unit vector to the boundary, $\hat{\boldsymbol{e}}_{\rm t}=\hat{\boldsymbol{e}}_{\rm n}\times\hat{\boldsymbol{z}}$, and $\ell_{\rm b}$ is the so-called "boundary slip length". Using Boltzmann equation and the well-known Reuter-Sondheimer model of boundary scattering [173], we obtain (Section 2.1.1)

$$\ell_{\rm b} = \frac{\nu}{v_{\rm F}}\frac{6\pi}{9\pi^2-32}\frac{(1+p)}{(1-p)}\ , \tag{2.126}$$

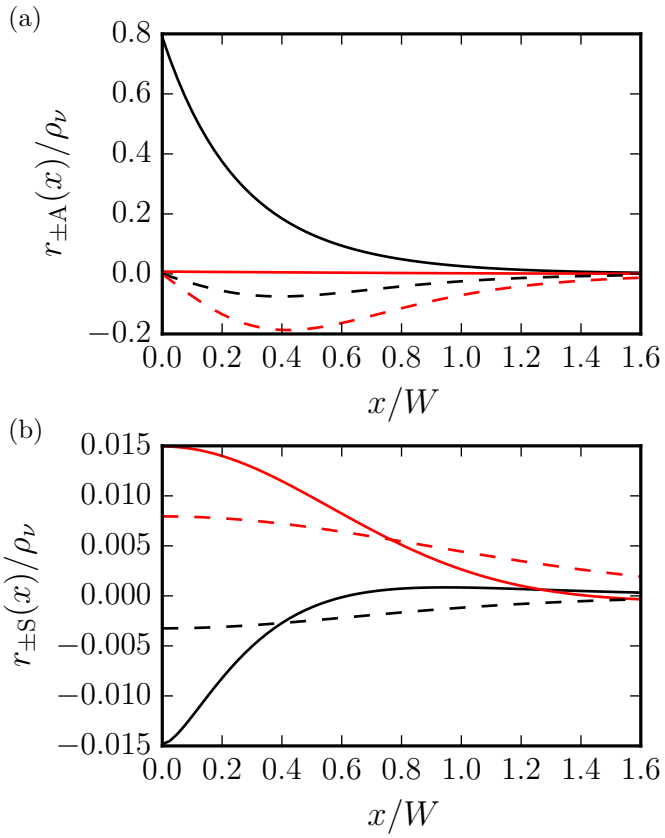


Figure 2.12: Panel (a) [Panel (b)] shows the inverse Fourier Transform of $\tilde{r}_{\pm\mathrm{A}}(k)$ [$\tilde{r}_{\pm\mathrm{S}}(k)$] in units of $\rho_\nu = mW^2/(\bar{n}e^2\nu)$ and plotted as a function of $x/W$. Results in both panels refer to a bilayer graphene sample with $W = 2.5$ $\mu$m, $\bar{n} = 10^{12}$ cm$^{-2}$, $B = 0.1$ $B_0$, $\nu_0 = 0.1$ m$^2$/s, and free-surface BCs ($\ell_\mathrm{b} = \infty$). Different colors refer to different values of $\tau$. Black: $\tau = 2$ ps. Red: $\tau = 200$ ps. Solid lines refer to $\tilde{r}_{+\mathrm{A}}(x)$ and $\tilde{r}_{+\mathrm{S}}(x)$. Dashed lines to $\tilde{r}_{-\mathrm{A}}(x)$ and $\tilde{r}_{-\mathrm{S}}(x)$.

where $0 \leq p \leq 1$ is the probability of specular scattering for an electron at the boundary [173]. Here, $p = 1$ for perfectly specular scattering and $p = 0$ for completely diffusive scattering. The boundary slip length diverges for $p \to 1$, recovering the free-surface BC [96, 104], while it remains finite in the limit $p \to 0$, i.e. $\lim_{p\to 0} \ell_\mathrm{b} \simeq 0.1\ \ell_\mathrm{ee}$, where $\ell_\mathrm{ee}$ is the electron-electron scattering length [102]. (In deriving the last result we have used $\nu \simeq v_\mathrm{F}\ell_\mathrm{ee}/4$, see Appendix 2.1.) For completely diffusive scattering, $\ell_\mathrm{b}$ is therefore ten times smaller than the electron-electron scattering length. Since the latter quantity is much smaller than the macroscopic length scales of hydrodynamic electron flow, $\ell_\mathrm{b}$ is negligibly small for $p \to 0$ and we obtain the no-slip BC [96, 174].

For the setups in Fig. 2.11, we have $\hat{\boldsymbol{e}}_\mathrm{n} = \hat{\boldsymbol{y}}$ ($\hat{\boldsymbol{e}}_\mathrm{n} = -\hat{\boldsymbol{y}}$) for the upper (lower) edge at $y = W$ ($y = 0$), respectively. In FT with respect to $x$, the BCs become

$$\partial_y \tilde{J}_x(k,0) + ik\tilde{J}_y(k,0) = (2ik\nu_\mathrm{r} + \ell_\mathrm{b}^{-1})\tilde{J}_x(k,0)\ , \tag{2.127}$$

$$\tilde{J}_y(k,0) = -I/e\ , \tag{2.128}$$

$$\partial_y \tilde{J}_x(k,W) = (2ik\nu_\mathrm{r} - \ell_\mathrm{b}^{-1})\tilde{J}_x(k,W)\ , \tag{2.129}$$

$$\tilde{J}_y(k,W) = 0\ . \tag{2.130}$$

In the remainder of this Section, we consider the case of free-surface BCs [96, 104], which are obtained by taking the limit $\ell_\mathrm{b} \to +\infty$. This choice is physically justified by the measured [11] *monotonic* temperature dependence (i.e. no Gurzhi effect) of the ordinary longitudinal resistance in the linear-response regime and in the case of a uniform steady-state flow. For more details, we refer the reader to Refs. [96, 104, 11]. To study the impact of a boundary slip length $\ell_\mathrm{b} < +\infty$, we have carried out the same calculations described in this Section in the opposite limit, i.e. for $\ell_\mathrm{b} = 0$ (See Appendix 2.3.3). The results obtained for $\ell_\mathrm{b} \to +\infty$ and $\ell_\mathrm{b} = 0$ are compared in Sect. 2.3.2, see Fig. 2.13.

The FT of the electrochemical potential along the edges reads as following:

$$\begin{aligned}\tilde{\phi}_+(k) \equiv \tilde{\phi}(k,0) = \frac{I\rho_0}{k}\Big\{ &\sinh(\bar{q})[(1+2D_\nu^2k^2)\cosh(\bar{k}) + i\omega_c\tau\sinh(\bar{k})] \\ &+ i4\nu_H\nu\tau^2k^2q\{q\sinh(\bar{k})\sinh(\bar{q}) - k[\cosh(\bar{k})\cosh(\bar{q})-1]\} \\ &+ i2\nu_H^2\tau^2k^2\big\{2kq(2\omega_c\tau-\nu_r)[1-\cosh(\bar{k})\cosh(\bar{q})] \\ &- \sinh(\bar{q})\{iD_\nu^{-2}\cosh(\bar{k}) - 2\sinh(\bar{k})[k^2(\omega_c\tau-\nu_r)+q^2\omega_c\tau]\}\big\}\Big\} \\ &\times\Big\{\sinh(\bar{k})\sinh(\bar{q}) + 4\nu_H^2\tau^2k^2\{(2k^2+D_\nu^{-2})\sinh(\bar{k})\sinh(\bar{q}) + 2kq[1-\cosh(\bar{k})\cosh(\bar{q})]\}\Big\}^{-1},\end{aligned} \tag{2.131}$$

$$\begin{aligned}&\tilde{\phi}_-(k) \equiv \tilde{\phi}(k,W) \\ &= \frac{I\rho_0}{k}\Big\{(1+2D_\nu^2k^2)\sinh(\bar{q}) + 2\nu_H\tau k^2\{\nu_r\sinh(\bar{q}) + 2ikqD_\nu^2(1+\nu_r^2)[\cosh(\bar{k})-\cosh(\bar{q})]\}\Big\} \\ &\times\Big\{\sinh(\bar{k})\sinh(\bar{q}) + 4\nu_H^2\tau^2k^2\{(2k^2+D_\nu^{-2})\sinh(\bar{k})\sinh(\bar{q}) + 2kq[1-\cosh(\bar{k})\cosh(\bar{q})]\}\Big\}^{-1},\end{aligned} \tag{2.132}$$

where $\bar{k} = kW$, $\bar{q} = qW$, $\rho_0 = \sigma_0^{-1}$, and $\sigma_0 = \bar{n}e^2\tau/m$ represents a Drude-like conductivity. It is useful to express the edge electrochemical potentials (2.131)-(2.132) as

$$\tilde{\phi}_+(k) = I[\tilde{r}_+(k) - i\rho_H/k + 2i\rho_{\nu_H}kW^2 + \tilde{r}_{+S}(k) + \tilde{r}_{+A}(k)]\ , \tag{2.133}$$

$$\tilde{\phi}_-(k) = I[\tilde{r}_-(k) + \tilde{r}_{-S}(k) + \tilde{r}_{-A}(k)]\ , \tag{2.134}$$

where $\rho_H = -m\omega_c/(\bar{n}e^2) = B/(-e\bar{n}c)$ and $\rho_{\nu_H} = m\nu_H/(\bar{n}e^2W^2) = \rho_H D_H^2/W^2$. The former quantity is the usual Hall resistivity. The resistances $\tilde{r}_\pm(k)$ physically represent the solutions at zero magnetic field [96, 104] and are given by

$$\tilde{r}_+(k) = \frac{\rho_0 + 2\rho_\nu k^2W^2}{k\tanh(kW)} \tag{2.135}$$

and

$$\tilde{r}_-(k) = \frac{\rho_0 + 2\rho_\nu k^2W^2}{\sinh(kW)k}\ , \tag{2.136}$$

where $\rho_\nu = m\nu/(\bar{n}e^2W^2)$. The inverse FT of $\tilde{r}_+(k)$ and $\tilde{r}_+(-)$ can be calculated analytically. We find

$$r_+(x) = -\frac{\rho_0}{2\pi}\ln\Big[\sinh^2\Big(\frac{\pi x}{2W}\Big)\Big] - \frac{\pi\rho_\nu}{2\sinh^2\left(\frac{\pi x}{2W}\right)} \tag{2.137}$$

and

$$r_-(x) = -\frac{\rho_0}{2\pi}\ln\Big[\cosh^2\Big(\frac{\pi x}{2W}\Big)\Big] + \frac{\pi\rho_\nu}{2\cosh^2\left(\frac{\pi x}{2W}\right)}\ . \tag{2.138}$$

In Eqs. (2.133) and (2.134), the quantity $\tilde{r}_{\pm S}(k)$ ($\tilde{r}_{\pm A}(k)$) is a real (imaginary) function and it is non zero only for a finite value of the kinematic Hall viscosity $\nu_H$.

Furthermore, $\tilde{r}_{\pm S}(k)$ ($\tilde{r}_{\pm A}(k)$) is even (odd) under the exchange $k \to -k$, implying that the corresponding inverse FTs are even (odd) real functions of the coordinate $x$. At zero magnetic field, $\omega_c$ and $\nu_H$ vanish, implying that $\tilde{r}_{\pm S}(k) = 0$ and $\tilde{r}_{\pm A}(k) = 0$.

After straightforward mathematical manipulations, we find:

$$\phi_+(x) = I\Big\{-\frac{\rho_0}{2\pi}\ln\Big[\sinh^2\Big(\frac{\pi x}{2W}\Big)\Big] - \frac{\pi\rho_\nu}{2\sinh^2\left(\frac{\pi x}{2W}\right)} + \frac{\rho_H}{2}\mathrm{sgn}(x) + 2\rho_{\nu_H}\delta'\Big(\frac{x}{W}\Big) + r_{+S}(x) + r_{+A}(x)\Big\} \tag{2.139}$$

and

$$\phi_-(x) = I\Big\{-\frac{\rho_0}{2\pi}\ln\Big[\cosh^2\Big(\frac{\pi x}{2W}\Big)\Big] + \frac{\pi\rho_\nu}{2\cosh^2\left(\frac{\pi x}{2W}\right)} + r_{-S}(x) + r_{-A}(x)\Big\}\ , \tag{2.140}$$

where the third term on the right hand side of Eq. (2.139) is the usual contribution due to the Lorentz force, the fourth term in the same equation is a singular contribution (proportional to the derivative of

the Dirac delta function) localized at the position of the injector and due to the Hall viscosity, while $r_{\pm S}(x)$ and $r_{\pm A}(x)$ are the inverse FTs of $\tilde{r}_{\pm S}(k)$ and $\tilde{r}_{\pm A}(k)$, which must be calculated numerically. Fig. 2.12(a) (Fig. 2.12(b)) shows the resistance $r_{\pm A}(x)$ ($r_{\pm S}(x)$), in units of $\rho_\nu$, plotted as a function of $x/W$. These calculations refer to the massive ($m = 0.03\ m_e$, where $m_e$ is the bare electron mass in vacuum) chiral 2D electron system [31] in a bilayer graphene sample with $W = 2.5\ \mu$m, $\bar{n} = 10^{12}\ \text{cm}^{-2}$, $B = 0.1\ B_0$, $\nu_0 = 0.1\ \text{m}^2/\text{s}$, with the black lines referring to $\tau = 2$ ps and the red lines to the ultra-clean limit, $\tau = 200$ ps. The quantities $r_{+A}(x)$ and $r_{+S}(x)$ are denoted by solid lines, while $r_{-A}(x)$ and $r_{-S}(x)$ are denoted by dashed lines. For small magnetic fields and in the ultra-clean $\tau \to \infty$ limit we can linearize $r_{\pm A}(x)$ with respect to $B$ and $1/\tau$, obtaining the following analytical expressions:

$$r_{+A}(x) \approx \frac{\rho_{\nu_H} W^2}{4 D_\nu^2} \left[ \coth\left(\frac{\pi x}{2W}\right) - \text{sgn}(x) - \frac{\frac{\pi x}{2W}}{\sinh^2\left(\frac{\pi x}{2W}\right)} \right] \tag{2.141}$$

and

$$r_{-A}(x) \approx \rho_{\nu_H} \left[ \frac{\pi^2 \tanh\left(\frac{\pi x}{2W}\right)}{2\cosh^2\left(\frac{\pi x}{2W}\right)} - \frac{\pi W x}{8 D_\nu^2 \cosh^2\left(\frac{\pi x}{2W}\right)} \right], \tag{2.142}$$

which are in excellent agreement with the numerical results shown for $\tau = 200$ ps in Fig. 2.12(a). In the limit $B/B_0 \ll 1$, the quantities $\tilde{r}_{\pm S}(k)$ start at order $(B/B_0)^2$.

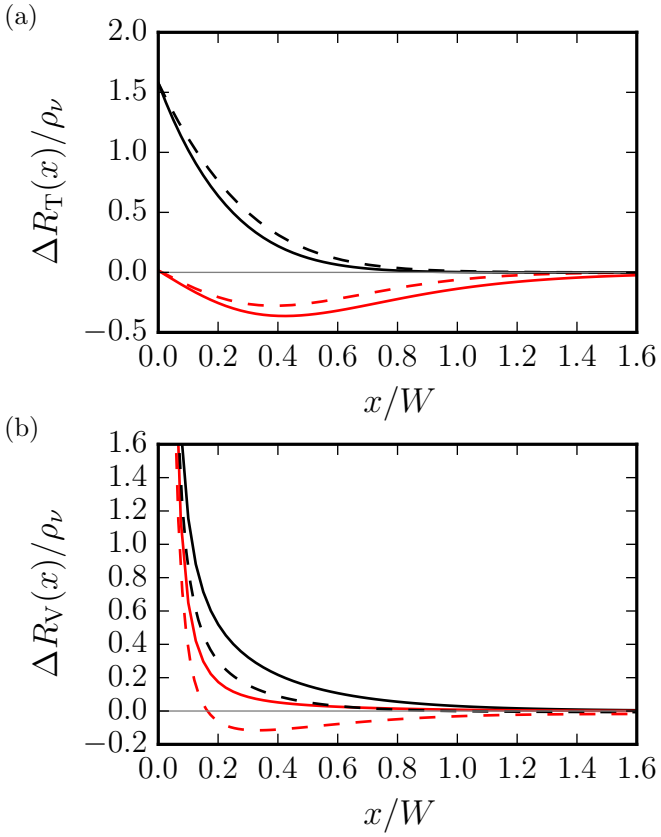


Figure 2.13: Panel (a) The transverse resistance difference (2.146), in units of $\rho_\nu$, plotted as a function of $x/W$. Panel (b) The vicinity resistance difference (2.151), in units of $\rho_\nu$, plotted as a function of $x/W$. Results in both panels refer to a bilayer graphene sample with $W = 2.5\ \mu$m, $\bar{n} = 10^{12}\ \text{cm}^{-2}$, $B = 0.1\ B_0$, and $\nu_0 = 0.1\ \text{m}^2/\text{s}$. Different colors refer to different values of $\tau$. Black: $\tau = 2$ ps. Red: $\tau = 200$ ps. Solid lines refer to $\ell_b \to \infty$ (free-surface BCs). Dashed lines to $\ell_b \to 0$ (no-slip BCs).

### 2.3.2 Non-local resistances and the Hall viscosity

We now turn to discuss explicitly the impact of the Hall viscosity on non-local electrical transport measurements carried out in the two setups sketched in Fig. 2.11(a) and (b). We start from the setup

depicted in Fig. 2.11(a), where the current $I$ is injected into the green electrode at $x = 0$ and $y = 0$, and extracted from the blue electrode at $x = 0$ and $y = W$. As in the case of the single-injector setup we just discussed, we treat each electrode with the usual point-like BC for the component of current density orthogonal to the edge.

Exploiting the linearity of the problem, it is possible to write the electrochemical potentials along the edges of the setup in Fig. 2.11(a) in terms of the potentials $\phi_+(x)$ and $\phi_-(x)$ along the lower and upper edges of the single-injector setup, respectively:

$$\phi(x,0) = \phi_+(x) - \phi_-(-x) \ , \tag{2.143}$$

$$\phi(x,W) = \phi_-(x) - \phi_+(-x) \ . \tag{2.144}$$

We remind the reader that $\phi_+(x)$ and $\phi_-(x)$ are the inverse FTs of $\tilde{\phi}_+(k)$ and $\tilde{\phi}_-(k)$, respectively. For the case of the free-surface BCs ($\ell_{\rm b} \to +\infty$), explicit expressions for the latter quantities have been given in Eqs. (2.131) and (2.132). For the no-slip BCs, we refer the reader to Eqs. (2.152)-(2.158) in Appendix 2.3.3.

We now introduce the "transverse" non-local resistance, which is measured in the setup sketched in Fig. 2.11(a), as

$$\begin{aligned} R_{\rm T}(x) \equiv \frac{\phi(x,0) - \phi(-x,0)}{I} &= \rho_{\rm H}{\rm sgn}(x) + 4\rho_{\nu_{\rm H}}\delta'\Big(\frac{x}{W}\Big) \\ &+ 2[r_{+{\rm A}}(x) + r_{-{\rm A}}(x)] \ . \end{aligned} \tag{2.145}$$

We note that $R_{\rm T}(x) \to \rho_{\rm H}{\rm sgn}(x)$ for $|x| \gg W$, because, in the same limit, $[r_{+{\rm A}}(x) + r_{-{\rm A}}(x)] \to 0$, independently of the value of $\ell_{\rm b}$. In order to have a clear signature of the Hall viscosity it is therefore convenient to perform two measurements of the transverse resistance $R_{\rm T}$, i.e. one at position $0 < x \lesssim W$ and a second one at position $x' \gg W$. The difference

$$\Delta R_{\rm T}(x) \equiv R_{\rm T}(x) - \lim_{x' \to \infty} R_{\rm T}(x') = 2[r_{+{\rm A}}(x) + r_{-{\rm A}}(x)] \tag{2.146}$$

is independent of $\rho_{\rm H}$ and non-zero only in the presence of a finite Hall viscosity. Results in the transverse geometry show a weak dependence on the BCs (2.125). Fig. 2.13(a) shows the quantity $\Delta R_{\rm T}(x)$ as a function of $x/W$, as calculated by using the BCs (2.125) in the two limiting cases, $\ell_{\rm b} \to +\infty$ (solid lines) and $\ell_{\rm b} \to 0$ (dashed lines). For the calculations we have used two different values of $\tau$: $\tau = 2$ ps (black) and $\tau = 200$ ps (red). From Fig. 2.13 we clearly see a weak dependence of $\Delta R_{\rm T}(x)$ on $\ell_{\rm b}$, independently of the value of $\tau$.

We now follow similar algebraic steps for the setup in Fig. 2.11(b). In this case the current $I$ is injected into the green electrode at $x = 0$ and $y = 0$, and extracted from the blue electrode at $x = x_0 < 0$ and $y = 0$. We find

$$\phi(x,0) = \phi_+(x) - \phi_+(x - x_0) \ , \tag{2.147}$$

$$\phi(x,W) = \phi_-(x) - \phi_-(x - x_0) \ . \tag{2.148}$$

We define the "vicinity" resistance [96, 11, 104] as

$$R_{\rm V}(x) \equiv \frac{\phi(x,0) - \phi(x' \to +\infty, 0)}{I} \ . \tag{2.149}$$

The mathematical expression of $R_{\rm V}(x)$ notably simplifies in the limit $x_0 \to -\infty$, becoming

$$R_{\rm V}(x) = r_+(x) + \frac{\rho_* x}{2W} + r_{+{\rm A}}(x) + r_{+{\rm S}}(x) - [r_{+{\rm A}}(+\infty) + r_{+{\rm S}}(+\infty)] \ , \tag{2.150}$$

where $x > 0$ and the resistance $\rho_*$ is obtained by the asymptotic relation $\rho_* = -2W \lim_{x\to\infty} r_+(x)/|x|$. In the limit $\ell_{\rm b} \to \infty$ (i.e. free-surface BCs) and using Eq. (2.139) we find $\rho_* = \rho_0$. In the opposite limit, $\ell_{\rm b} \to 0$ (i.e. no-slip BCs), we find $\rho_* = \rho_0\{1 - 2D_\nu/W \tanh[W/(2D_\nu)]\}^{-1}$ (see Appendix 2.3.3).

Since we are interested in the impact of the Hall viscosity on hydrodynamic electrical transport, it is useful to concentrate our attention on the difference between the vicinity resistance in the presence of an applied magnetic field and in the absence of it:

$$\Delta R_{\rm V}(x) \equiv R_{\rm V}(x) - R_{\rm V}(x)|_{B=0} \ . \tag{2.151}$$

The vicinity geometry displays a non-trivial dependence on the BCs (2.125). In Fig. 2.13(b) we show the quantity $\Delta R_{\rm V}(x)$ as a function of $x/W$, as calculated by using the BCs (2.125) in the two limiting cases, $\ell_{\rm b} \to +\infty$ (solid lines) and $\ell_{\rm b} \to 0$ (dashed lines). As in panel (a) of the same figure, we have carried out calculations for two different values of $\tau$: $\tau = 2$ ps (black) and $\tau = 200$ ps (red). In the ultra-clean limit ($\tau = 200$ ps) the dependence of $\Delta R_{\rm T}(x)$ on $\ell_{\rm b}$ is large. Indeed, by comparing the solutions with free-surface and no-slip BCs, we note from Fig. 2.13(b) that even the sign of $\Delta R_{\rm T}(x)$ depends on $\ell_{\rm b}$.

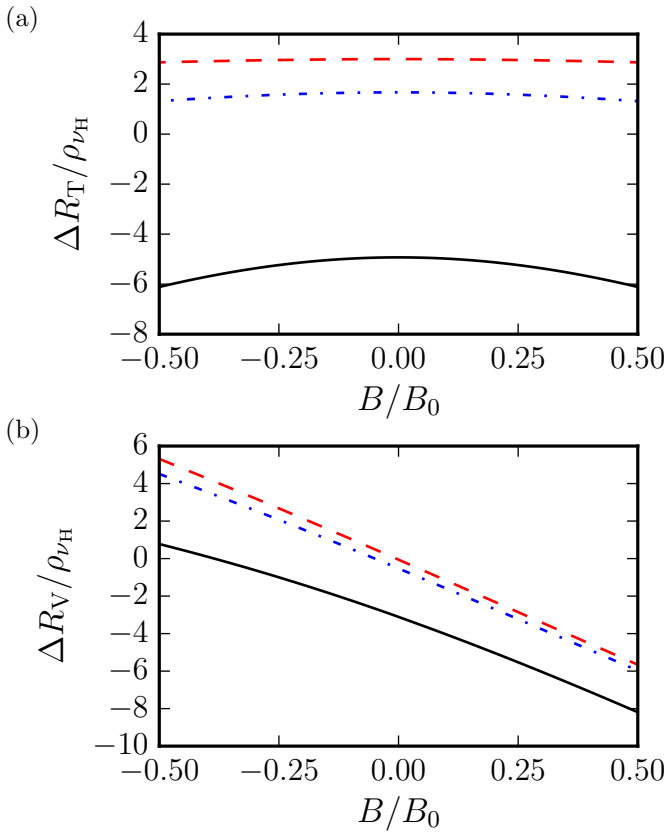


Figure 2.14: Panel (a) The transverse resistance difference (2.146), in units of $\rho_{\nu_{\rm H}}$ and evaluated at $x = 0.25\ W$, is plotted as a function of $B/B_0$. Panel (b) The vicinity resistance difference (2.151), in units of $\rho_{\nu_{\rm H}}$ and evaluated at $x = 0.25\ W$, is plotted as a function of $B/B_0$. Results in both panels refer to a bilayer graphene sample with $W = 2.5\ \mu$m, $\bar{n} = 10^{12}$ cm$^{-2}$, and $\nu_0 = 0.1$ m$^2$/s. All results shown in this figure have been evaluated by using the free-surface BCs ($\ell_{\rm b} = +\infty$). Solid line: $\tau = 2$ ps. Dash-dotted line: $\tau = 20$ ps. Dashed line: $\tau = 200$ ps.

Before concluding, in Fig. 2.14(a) and (b) we illustrate the dependence of $\Delta R_{\rm T}(x)$ and $\Delta R_{\rm V}(x)$ on $B/B_0$, respectively. In this case, these quantities have been calculated by using the free-surface BCs and evaluated at a given position $x \lesssim W$. In the weak-field $B \ll B_0$ limit, $\Delta R_{\rm T}$ is given by the product of $\rho_{\nu_{\rm H}}$ and a function that depends only on $x$, $\tau$, and $\nu(B = 0)$. A measurement of $\Delta R_{\rm T}$ therefore yields immediately the value of the Hall viscosity, provided that $\tau$ is measured from the ordinary longitudinal resistance [11] $\rho_{xx}$ and $\nu(B = 0)$ from one of the protocols discussed in Refs. [11, 12]. We emphasize that this way of accessing $\nu_{\rm H}$ is insensitive to the classical Hall resistivity $\rho_{\rm H}$ and to ballistic effects like transverse magnetic focusing [105]. The latter statement holds true as long as $\nu_{\rm H}$ is extracted from a measurement of $\Delta R_{\rm T}$ at values of $B$ that are well below those that are necessary to focus electron trajectories [192, 105], for typical sample sizes.

The vicinity geometry is in practice less convenient to probe $\nu_{\rm H}$. This is because—as seen in Fig. 2.14(b)—the range of values of $B/B_0$ over which $\Delta R_{\rm V}$ depends on $B$ solely through the Hall viscosity is smaller than in the highly-symmetric geometry shown in Fig. 2.11(a). We also mention once more that the geometry sketched in Fig. 2.11(a) is more convenient for accessing $\nu_{\rm H}$ with respect to the one in Fig. 2.11(b), because in the former one the detailed nature of BCs does not influence in a significant matter the role played by the Hall viscosity on non-local electrical measurements. In other words,

in the case of Fig. 2.11(a) and corresponding $\Delta R_{\rm T}(x)$, a precise estimate of $\ell_{\rm b}$ is unnecessary. This is at odds with a recently studied geometry [164], where the impact of $\nu_{\rm H}$ on the electrochemical potential at the boundaries of the setup exists only for finite values of the boundary slip length ($\ell_{\rm b} < +\infty$). In our case, the electrochemical potential at the boundaries depends non-trivially on $\nu_{\rm H}$ for both free-surface ($\ell_{\rm b} = +\infty$) and no-slip ($\ell_{\rm b} = 0$) BCs.

### 2.3.3 On the solutions with no-slip BCs

In the previous sections we have focused on the free-surface BCs. Here, we discuss how the results for the single-injector setup depend on the BCs, by analysing the no-slip—$\ell_{\rm b} = 0$ in Eq. (2.125)—BCs. We start by noting that Eqs. (2.133) and (2.134), i.e.

$$\tilde{\phi}_+(k) = I[\tilde{r}_+(k) - i\rho_{\rm H}/k + 2i\rho_{\nu_{\rm H}} kW^2 + \tilde{r}_{+{\rm S}}(k) + \tilde{r}_{+{\rm A}}(k)] \tag{2.152}$$

and

$$\tilde{\phi}_-(k) = I[\tilde{r}_-(k) + \tilde{r}_{-{\rm S}}(k) + \tilde{r}_{-{\rm A}}(k)] \ , \tag{2.153}$$

hold true *independently* of the chosen BCs. In the special case of the no-slip BCs ($\ell_{\rm b} = 0$), we find

$$\tilde{r}_+(k) = \rho_0 \frac{q^2\cosh(\bar{k})\sinh(\bar{q}) - kq\cosh(\bar{q})\sinh(\bar{k})}{k\{2kq[1-\cosh(\bar{k})\cosh(\bar{q})] + (k^2+q^2)\sinh(\bar{k})\sinh(\bar{q})\}} \ , \tag{2.154}$$

$$\tilde{r}_-(k) = \rho_0 \frac{q[q\sinh(\bar{q}) - k\sinh(\bar{k})]}{k\{2kq[1-\cosh(\bar{k})\cosh(\bar{q})] + (k^2+q^2)\sinh(\bar{k})\sinh(\bar{q})\}} , \tag{2.155}$$

$$\tilde{r}_{\pm{\rm S}}(k) = 0 \ , \tag{2.156}$$

$$\tilde{r}_{+{\rm A}}(k) = -i\rho_{\nu_{\rm H}} \frac{q(3\bar{k}^2+\bar{q}^2)[1-\cosh(\bar{k})\cosh(\bar{q})] + k(3\bar{q}^2+\bar{k}^2)\sinh(\bar{k})\sinh(\bar{q})}{2kq[1-\cosh(\bar{k})\cosh(\bar{q})] + (k^2+q^2)\sinh(\bar{k})\sinh(\bar{q})} \ , \tag{2.157}$$

$$\tilde{r}_{-{\rm A}}(k) = i\rho_{\nu_{\rm H}} \frac{q(\bar{q}^2-\bar{k}^2)[\cosh(\bar{k})-\cosh(\bar{q})]}{2kq[1-\cosh(\bar{k})\cosh(\bar{q})] + (k^2+q^2)\sinh(\bar{k})\sinh(\bar{q})} \ . \tag{2.158}$$

Here, $\bar{k} = kW$, $\bar{q} = qW$, $q = \sqrt{k^2 + 1/D_\nu^2}$, $D_\nu = \sqrt{\nu\tau}$, $\rho_0 = m/(\bar{n}e^2\tau)$, $\rho_{\rm H} = -m\omega_{\rm c}/(\bar{n}e^2)$, and $\rho_{\nu_{\rm H}} = m\nu_{\rm H}/(\bar{n}e^2W^2)$. The resistance $\tilde{r}_\pm(k)$ coincides with that in the absence of the external magnetic field. Straightforward mathematical manipulations lead to the following asymptotic behavior in the limit $k \to 0$:

$$\tilde{r}_\pm(k) \to \frac{\rho_0}{k^2W\{1 - 2D_\nu/W\tanh[W/(2D_\nu)]\}} \ . \tag{2.159}$$

This means that the asymptotic behavior of the corresponding inverse FT for $|x| \gg W$ is $r_\pm(x) \to -\rho_0|x|/(2W)\{1-2D_\nu/W\tanh[W/(2D_\nu)]\}^{-1}$.

The quantities $\tilde{r}_{\pm{\rm A}}(k)$ are proportional to the kinematic Hall viscosity $\nu_{\rm H}$ and they are imaginary and odd with respect to the exchange $k \to -k$. This implies that the corresponding inverse FTs are odd and real functions of the spatial coordinate $x$.

In the clean $\tau \to \infty$ limit, we find

$$\tilde{r}_+(k) = -\rho_\nu \frac{2W\bar{k}[2\bar{k} + \sinh(\bar{k})]}{1 + 2\bar{k}^2 - \cosh(2\bar{k})} \ , \tag{2.160}$$

$$\tilde{r}_-(k) = -\rho_\nu \frac{4W\bar{k}[\bar{k}\cosh(\bar{k}) + \sinh(\bar{k})]}{1 + 2\bar{k}^2 - \cosh(2\bar{k})} \ , \tag{2.161}$$

$$\tilde{r}_{+{\rm A}}(k) = -i\rho_{\nu_{\rm H}} \frac{4W\bar{k}^3}{1 + 2\bar{k}^2 - \cosh(2\bar{k})} \ , \tag{2.162}$$

$$\tilde{r}_{-{\rm A}}(k) = i\rho_{\nu_{\rm H}} \frac{4W\bar{k}^2\sinh(\bar{k})}{1 + 2\bar{k}^2 - \cosh(2\bar{k})} \ . \tag{2.163}$$

$$\tag{2.164}$$

Finally, we consider the case of the half-plane geometry with a current injector placed at the origin [104]. We obtain this case by taking the limit $W \to \infty$ in Eqs. (2.152)-(2.158)

$$\tilde{r}_{+}(k) = \rho_0 \left[ \frac{1}{|k|} + D_\nu^2 \left( q + |k| \right) \right] \ , \tag{2.165}$$

$$\tilde{r}_{+\mathrm{A}}(k) = i\rho_0 \frac{\nu_\mathrm{H}}{\nu} D_\nu^2 \mathrm{sgn}(k) \left( q - |k| \right) \ , \tag{2.166}$$

while both the resistances $\tilde{r}_{-}(k)$ and $\tilde{r}_{-\mathrm{A}}(k)$ vanish. Eqs. (2.165) and (2.166) can be transformed back analytically in real space as

$$r_{+}(x) = -\rho_0 \left[ \frac{1}{\pi} \ln \left( \frac{|x|}{D_\nu} \right) + \frac{D_\nu^2}{\pi x^2} + \frac{D_\nu}{\pi |x|} K_1 \left( \frac{|x|}{D_\nu} \right) \right] \ , \tag{2.167}$$

$$r_{+\mathrm{A}}(x) = \rho_0 \frac{\nu_\mathrm{H}}{\nu} \frac{D_\nu}{2x} \left[ -I_1 \left( \frac{|x|}{D_\nu} \right) + \mathbf{L}_1 \left( \frac{|x|}{D_\nu} \right) \right] \ , \tag{2.168}$$

where $I_1(x)$ ($K_1(x)$) is the modified Bessel function of first (second) kind and order one, and $\mathbf{L}_1(x)$ is the modified Struve function of order one.

## 2.4 Conclusions

In this Chapter we studied hydrodynamic transport in 2D electron system. In Section 2.1 we gave a derivation of the hydrodynamic equations based on the semiclassical Boltzmann equation. This provided a link between the microscopic quantities $\tau$, $\tau_{\mathrm{ee}}$, and $p$, (parametrizing momentum-relaxing collisions, electron-electron collisions, and boundary collisions respectively) and the macroscopic coefficients appearing in the hydrodynamic equations, namely $\nu$ (See Eq. (2.18)), $\nu_\mathrm{H}$ (See Eq. (2.19)) and $\ell_\mathrm{b}$ (See Eq. (2.40)).

In Section 2.2 we studied the impact of the shear viscosity on non-local transport measurements, focusing in particular on the role of geometric effects in two-dimensional solid-state hydrodynamic transport [104]. We have been able to demonstrate that they play a crucial role in the establishment of so-called current whirlpools [11, 96].

The half-plane geometry—sketched in Fig. 2.1(c)—hosts negative nonlocal resistances due to viscosity but no current whirlpools.

The geometry analyzed in Ref. [174], which is depicted in Fig. 2.1(b), allows the formation of current whirlpools only if the electron liquid viscosity, at a given carrier density and temperature, overcomes a threshold value, i.e. $D_\nu > W/(\sqrt{2}\pi)$ or, more explicitly, $\nu > W^2/(2\pi^2\tau)$.

In contrast to the above two geometries, the vicinity geometry introduced in Refs. [11, 96] and sketched in Fig. 2.1(a) exhibits backflow *near* the injector electrode for arbitrarily small values of $D_\nu$. The value of $D_\nu$ affects the spatial extent of current whirlpools, as shown in Fig. 2.10. To detect current backflow in this geometry, either a local probe should be in the immediate vicinity of the injector or the width $W$ of the conductive channel should be chosen sufficiently small. For the case of graphene with its typical vorticity diffusion length $\approx$ 0.3-0.4 $\mu$m and a distance of 1 $\mu$m between a narrow probe and a current injector, $W$ should be $<$ 1.5-2 $\mu$m.

We hope that this helps clarifying the subtle connection between backflow and negative nonlocal resistances due to viscosity in 2D electron liquids [179]. We also hope that it will spark experimental quests of current whirlpools based on scanning probe potentiometry and magnetometry, as suggested in Ref. [96].

In Section 2.3, we have proposed an all-electrical scheme that allows a determination of the Hall viscosity $\nu_\mathrm{H}$ of a two-dimensional electron liquid in a solid-state device [193]. We have carried out extensive calculations for two device geometries, illustrated in Figs. 2.11(a) and (b), and a family of boundary conditions, reported in Eq. (2.125), which depends on one parameter, the so-called boundary slip length $\ell_\mathrm{b}$. The latter allows to interpolate between the widely used no-slip ($\ell_\mathrm{b} = 0$) and free-surface ($\ell_\mathrm{b} = +\infty$) boundary conditions.

We have demonstrated that the transverse geometry in Fig. 2.11(a) is particularly suitable for extracting $\nu_\mathrm{H}$ from experimental data. Indeed, we have shown that a measurement of $\Delta R_\mathrm{T}(x)$—Eq. (2.146)—yields immediately the value of the Hall viscosity, provided that $\tau$ is measured from the ordinary longitudinal resistance [11] $\rho_{xx}$ and $\nu(B = 0)$ from one of the protocols discussed in Refs. [11, 12]. We have also

shown that $\Delta R_{\mathrm{T}}(x)$ is insensitive to the value of the boundary slip length, a finding that further enforces the robustness of this quantity as a diagnostic tool of the Hall viscosity. A similar experiments has been recentely proposed by Delacretaz and Gromov [194]. These Authors however focus on the ultra-clean regime neglecting the impact of momentum-non-conserving collisions.

# Chapter 3

# Scattering of plasmons in two-dimensional materials

Plasmons in 2D materials [137, 50, 195, 152] have attracted a lot of attention because they can confine light on lengthscales much shorter than the corresponding free-space wavelength [139, 18], can travel long distances [18, 152], and can be tuned by field effect [17, 16, 196]. Graphene plasmons have been proposed as a platform for many interesting optoelectronic [19] and biosensing [151] applications.

Most of the theoretical works dealing with 2D plasmons consider translationally invariant samples where the equations describing these collective modes can be solved by the power of Fourier transforms. Technically, this allows to reduce the integral equations describing the plasmonic response to algebraic equations. Notable exceptions to this rule are Refs. [197, 198, 199] that treat the scattering of plasmons against different type of sample inhomogeneities. Nevertheless, the behavior of plasmons in inhomgeneous setups is important both for the investigation of the optical response of defects [200, 198, 201, 202] and interfaces [203], and for many device applications [19].

In this Chapter we address the problem of plasmon scattering in three different geometries.

In Sect. 3.1 we consider two half-planes whose optical response is described by different *local* conductivities, and we calculate transmission and reflection amplitudes for plasmons across the interface, as well as the spectrum of bound plasmon resonances.

In Sect. 3.2 we develop a theory that closely parallels the Lippmann-Schwinger theory of quantum scattering to study the scattering of plasmons off zero and one-dimensional inhomogeneities. In this case the impact of *non-local* effects and of exchange-correlation effects beyond the Random Phase Approximation (RPA) is taken into account.

Finally, in Sect. 3.3 we present experimental work [19] carried out at ICFO (Spain) in which our Lippmann-Schwinger theory has been put to test producing striking agreement with experimental results.

## 3.1 Plasmons at an interface

In this Section we study 2D plasmons in one of the simplest non-homogenous setups that is a system made up of two half-planes, each one having a different conductivity tensor, comprising a normal (i. e. diagonal) part and an antisymmetric Hall part. This second part is non-vanishing in systems with broken time reversal symmetry, as normal conductors in the presence of an external magnetic field [127, 128, 126], ferromagnetic materials [67] or topological materials with an induced population imbalance between the two valleys [59, 60, 61, 204, 205].

Our theory relies on few basic assumptions that are: locality (i. e. independence of the conductivities on wavevector), isotropy (that allows us to split the 2D conductivity tensor in a diagonal part and an antisymmetric part), and sharpness of the interface, compared with the relevant plasmon wavelengths. Since no assumptions is made on the frequency dependence of the conductivities our theory is very general and can describe many different experimental situations, including normal plasmons at edges and interfaces [130], magnetoplasmons [127, 128, 206], and chiral Berry plasmons [204]. In addition to this, our theory is completely general with respect to the screening of the electron-electron interaction and is therefore able to treat on the same footing the standard 2D plasmons with a $\omega \sim \sqrt{q}$ dispersion

relation and the acoustic ($\omega \sim q$) plasmons that occur in structures where the Coulomb interaction is strongly screened by a conducting gate [207, 47].

Depending on the values of the normal part of the conductivity we identify three different situations.

When the normal conductivity has two different non-zero values on both sides, our theory describes an interface between two different media that can host propagating plasmons. In this situation we can find localized plasmon resonances at the interface, scattering (that is reflection and transmission) of bulk plasmons impinging from one side of the interface, as well as total internal reflection of plasmons coming from one side of the interface if the matching of plasmon wavevectors on the two sides of the interface cannot be realized. This is is in close analogy to what happens to light at the interface between two media with different refraction indices.

When the conductivity is zero on one side of the interface our theory describes the edge of a semi-infinite system. This can host localized plasmonic resonance known as edge plasmons, moreover plasmon propagating from the bulk of the sample are reflected at the edge with a certain reflection phase.

In both these case the resulting plasmon equation is an integral equation that can be solved with the help of a very elegant mathematical technique due to Wiener and Hopf [208, 130, 206], that relies on the analyticity properties of the Fourier transforms of functions that are non-zero only on half of the real line.

A particular type of interface, with the two sides having the same normal conductivity but different Hall conductivities is discussed separately, since it can be solved without resorting to the Wiener-Hopf technique. This type of interface cannot support total internal reflection since the plasmon wavevector is exactly the same on the two sides of the interface, and the matching is therefore always possible.

The remainder of this Section is structured as follows: in Sect. 3.1.1 the equation describing 2D plasmons at a generic interface is derived. This is then solved in Sect. 3.1.2 for an interface between two media using the Wiener-Hopf method. The particular case of an edge is analyzed in Sect. 3.1.3, while the case of uniform normal conductivity is dealt with in Sect. 3.1.4.

### 3.1.1 Interface plasmon equation

We consider a two-dimensional (2D) electron system whose electromagnetic response is described by a position-dependent local conductivity

$$J_i(\boldsymbol{r},\omega) = \sigma_{ij}(\boldsymbol{r},\omega)E_j(\boldsymbol{r},\omega), \tag{3.1}$$

where $J_i(\boldsymbol{r},\omega)$ are the components of the electric current density, $E_j(\boldsymbol{r},\omega)$ are the components of the total electric field, and $\sigma_{ij}(\boldsymbol{r},\omega)$ is a local conductivity tensor in the form

$$\sigma_{ij}(x,\omega) = \sigma(x,\omega)\delta_{ij} + \sigma_{\mathrm{H}}(x,\omega)\epsilon_{ij}. \tag{3.2}$$

From now on we will drop, for the sake of space, all the $\omega$ dependencies since $\omega$ will be considered as a fixed parameter. We now specify the spatial dependence of the normal and Hall conductivity to describe an abrupt interface at $x = 0$

$$\sigma(x) = \sigma_L\Theta(-x) + \sigma_R\Theta(x), \tag{3.3}$$
$$\sigma_{\mathrm{H}}(x) = \sigma_{\mathrm{H}L}\Theta(-x) + \sigma_{\mathrm{H}R}\Theta(x). \tag{3.4}$$

Here $\Theta(x)$ is the Heaviside step function.

The normal modes of charge density oscillation are therefore described by the following equations.

$$i\omega\rho(x) = \partial_x J_x(x) + iq_y J_y(x), \tag{3.5}$$
$$J_x(x) = -\sigma(x)\partial_x\phi(x) - iq_y\sigma_{\mathrm{H}}(x)\phi(x), \tag{3.6}$$
$$J_y(x) = \sigma_{\mathrm{H}}(x)\partial_x\phi(x) - iq_y\sigma(x)\phi(x), \tag{3.7}$$

where we used the translational invariance in time and in the $y$ direction, as well as the absence of external driving fields. Making use of (3.5-3.6-3.7) we obtain the charge density

$$\begin{aligned} i\omega\rho(x) &= -\partial_x[\sigma(x)\partial_x\phi(x)] + q_y^2\sigma(x)\phi(x) - iq_y\partial_x\sigma_{\mathrm{H}}(x)\phi(x) \\ &= -\partial_x[\sigma_L\Theta(-x)\partial_x\phi(x) + \sigma_R\Theta(x)\partial_x\phi(x)] + q_y^2[\sigma_L\Theta(-x)\phi(x) + \sigma_R\Theta(x)\phi(x)] - iq_y\delta\sigma_{\mathrm{H}}\delta(x)\phi(0). \end{aligned} \tag{3.8}$$

Here, $\delta\sigma_{\rm H} = \sigma_{{\rm H}R} - \sigma_{{\rm H}L}$. Fourier transforming with respect to the variable $x$ we obtain

$$\rho(q_x) = -\frac{iq^2}{\omega}[\sigma_R\hat{\phi}_R(q_x) + \sigma_L\hat{\phi}_L(q_x)] + \phi(0)\frac{q_x\delta\sigma - q_y\delta\sigma_{\rm H}}{\omega}, \tag{3.9}$$

where $\hat{\phi}_{R/L}(q_x)$ is the right (left) Fourier transform of $\phi$ (See Appendix D for definitions), $q \equiv \sqrt{q_x^2 + q_y^2}$, and $\delta\sigma = \sigma_R - \sigma_L$. In calculating this Fourier transform we made use of the property (D.3).

The charge density is in turn related to the electric potential by the interaction potential

$$\phi(x) = \int_{-\infty}^{\infty} dx' L_{q_y}(x - x')\rho(x'). \tag{3.10}$$

Here

$$L_{q_y}(x) = \int \frac{dq_x}{2\pi} e^{iq_x x} L(q), \tag{3.11}$$

and $L(q)$ is the interaction potential in wavevector space, i. e. $L(q) = 2\pi/q$ for unscreened 2D Coulomb interaction. The Fourier transform of (3.10) yields

$$\hat{\phi}_L(q_x) + \hat{\phi}_R(q_x) = L(q)\rho(q_x). \tag{3.12}$$

In the following we make use of the fact that $L(q)q^2 \to +\infty$ for $q \to \infty$, this is true for all the relevant types of interaction.

Combining (3.9-3.12) and defining

$$\epsilon_{R/L}(q) = 1 + \frac{i\sigma_{R/L}q^2 L(q)}{\omega}, \tag{3.13}$$

we get

$$\epsilon_R(q)\hat{\phi}_R(q_x) + \epsilon_L(q)\hat{\phi}_L(q_x) = \phi(0)\frac{L(q)(q_x\delta\sigma - q_y\delta\sigma_{\rm H})}{\omega}. \tag{3.14}$$

Next, we note that

$$\frac{L(q)}{\omega} = -i\frac{\epsilon_R(q) - \epsilon_L(q)}{q^2\delta\sigma}. \tag{3.15}$$

Here we assumed $\sigma_R \neq \sigma_L$, the case $\sigma_R = \sigma_L$ does not need the Wiener-Hopf technique to be solved and is dealt with in Sect. 3.1.4 starting from Eq. 3.14.

Eq. (3.14) then becomes

$$\epsilon_R(q)\hat{\phi}_R(q_x) + \epsilon_L(q)\hat{\phi}_L(q_x) = \phi(0)\frac{\epsilon_R(q) - \epsilon_L(q)}{q^2}f(q_x), \tag{3.16}$$

where we defined

$$f(q_x) = -i\frac{\delta\sigma q_x - \delta\sigma_{\rm H} q_y}{\delta\sigma}. \tag{3.17}$$

Eq. (3.16) is solved for the unknown functions $\hat{\phi}_{R/L}(q_x)$ by means of the Wiener-Hopf method in the following Section.

Since $\hat{\phi}_{R/L}(q_x)$ need to be the right (left) Fourier transform of a function it needs to be analytical in the lower (upper) half of the complex plane (see theorem (i) in Appendix D).

We moreovere require the potential $\phi(x)$ to be continuous. This implies that its Fourier transform goes to zero at least as $q_x^{-2}$ for $|q_x| \to \infty$. $\phi_{R/L}(x)$ have instead a jump discontinuity at $x = 0$, their Fourier transforms $\hat{\phi}_{R/L}(q_x)$ are therefore allowed to go to zero as $q_x^{-1}$.

### 3.1.2 The Wiener-Hopf solution for an interface

The zeros of $\epsilon_{R/L}(q)$ define a plasmon wavevector on the two sides of the interface. In the following we assume that $\epsilon_{R/L}(q)$ has a only one simple (i. e. first order) zero as a function of $q$. This allows us to unambiguously define the right (left) plasmon wavevector as

$$\epsilon_{R/L}\left(q^{R/L}\right) \equiv 0. \tag{3.18}$$

Depending on the relative values of $q_y$ and $q^{R/L}$ we can have three different situations. For $|q_y| > \max[q^R, q^L]$ we have localized solutions, for $\min[q^R, q^L] < |q_y| < \max[q^R, q^L]$ Total Internal Reflection, and for $|q_y| < \min[q^R, q^L]$ propagating states. Here we discuss separately the three different cases.

**Localized solutions**

If $|q_y| > q^{R/L}$ the permeabilities $\epsilon_{R/L}(q)$ are negative for every real value of $q_x$. We can therefore define a function $R(q_x)$ that is positive on the whole real axis and approaches 1 for $q_x \to \infty$

$$R(q_x) \equiv \frac{\sigma_L}{\sigma_R}\frac{\epsilon_R(q)}{\epsilon_L(q)} = \frac{R_R(q_x)}{R_L(q_x)}. \tag{3.19}$$

This function can be split according to property (D.6) into the ratio of a function $R_R(q_x)$ that is analytic in for $\Im m[q_x] \leq 0$ and a function $R_L(q_x)$ that is analytic for $\Im m[q_x] \geq 0$. With this definition Eq. (3.16) becomes

$$\sigma_R R_R(q_x)\hat{\phi}_R(q_x) + \sigma_L R_L(q_x)\hat{\phi}_L(q_x) = \phi(0)X(q_x)f(q_x), \tag{3.20}$$

where the function $X(q_x)$ is defined by

$$X(q_x) = \frac{\sigma_R R_R(q_x) - \sigma_L R_L(q_x)}{q_x^2 + q_y^2} = X_R(q_x) + X_L(q_x). \tag{3.21}$$

Using the property (D.4) this function can be split into the sum of a function that is analytic in for $\Im m[q_x] \leq 0$ and a function that is analytic for $\Im m[q_x] \geq 0$. The functions $X_{R/L}(q_x)$ can be explicitly calculated and read

$$X_{R/L}(q_x) = \pm\frac{1}{q^2}\left[\sigma_{R/L}R_{R/L}(q_x) - \bar{\sigma}\frac{iq_x\sinh(I(|q_y|)) + |q_y|\cosh(I(|q_y|))}{|q_y|}\right]. \tag{3.22}$$

Here $I(|q_y|)$ is defined by the integral

$$I(|q_y|) = \frac{1}{\pi}\int_0^\infty \ln\left[\frac{\epsilon_R(|q_y|\sqrt{1+t^2})}{\epsilon_L(|q_y|\sqrt{1+t^2})}\right]\frac{dt}{1+t^2}, \tag{3.23}$$

and $\bar{\sigma} = \sqrt{\sigma_R\sigma_L}$.

For large values of $|q_x|$ $X_{R/L}(q_x)$ behave asymptotically as

$$X_{R/L}(q_x) \sim \mp\frac{i\bar{\sigma}\sinh(I)}{|q_y|q_x}. \tag{3.24}$$

We can then rearrange Eq. (3.20) into

$$\sigma_R R_R(q_x)\hat{\phi}_R(q_x) - \phi(0)X_R(q_x)f(q_x) = -\sigma_L R_L(q_x)\hat{\phi}_L(q_x) + \phi(0)X_L(q_x)f(q_x). \tag{3.25}$$

The left (right) hand side of (3.25) is analytic in in the lower (upper) half of the complex plane, with the equality holding on the real line. This defines a function that is analytic in the whole complex plane. Using the asymptotic behaviors for large $|q_x|$: $R_{R/L}(q_x) \sim 1$, $\hat{\phi}_{R/L}(q_x) \sim q_x^{-1}$, $f(q_x) \sim q_x$, and (3.24) we can show that the two sides of (3.25) behave at most as a constant for $|q_x| \to \infty$. Since an entire function that behaves asymptotically as a constant is constant on the whole complex plane we can set the two sides of (3.25) independently equal to a constant $A$.

We are now in position to solve for $\hat{\phi}_{R/L}(q_x)$ obtaining

$$\hat{\phi}_{R/L}(q_x) = \frac{\phi(0)X_{R/L}(q_x)f(q_x) \pm A}{\sigma_{R/L}R_{R/L}(q_x)}. \tag{3.26}$$

The constant $A$ must be chosen such that $\hat{\phi}_{R/L}(q_x)$ has the correct asymptotic behavior $\sim q_x^{-1}$ for large $q_x$. This leads to

$$A = \frac{\phi(0)\bar{\sigma}\sinh[I(|q_y|)]}{|q_y|}. \tag{3.27}$$

We finally obtain

$$\hat{\phi}_{R/L}(q_x) = \\ \pm\phi(0)\left\{\frac{f(q_x)}{q_x^2+q_y^2} + \frac{iq_x\left[|q_y|\delta\sigma\cosh(I) - iq_y\delta\sigma_{\mathrm{H}}\sinh(I)\right] - iq_y\left[iq_y\delta\sigma\sinh(I) + |q_y|\delta\sigma_{\mathrm{H}}\cosh(I)\right]}{\bar{\sigma}^{-1}\sigma_{R/L}R_{R/L}(q_x)(q_x^2+q_y^2)|q_y|\delta\sigma}\right\}. \tag{3.28}$$

As expected $\hat{\phi}_{R/L}(q_x)$ go to zero as $q_x^{-1}$ for large $q_x$. We can extract the limiting behavior taking the limit

$$\lim_{q_x\to\infty} q_x\hat{\phi}_{R/L}(q_x) = \mp i\phi(0)\left(1+c_{R/L}\right), \tag{3.29}$$

where

$$c_{R/L} = \frac{iq_y\delta\sigma_{\rm H}\sinh(I) - |q_y|\delta\sigma\cosh(I)}{2|q_y|\delta\sigma\bar{\sigma}^{-1}\sigma_{R/L}}. \tag{3.30}$$

This allows to write $\hat{\phi}_{R/L}(q_x)$ as

$$\hat{\phi}_{R/L}(q_x) = \mp\frac{i\phi(0)}{q_x\mp i\xi}\left(1+c_{R/L}\right) + \hat{g}^{(\xi)}_{R/L}(q_x), \tag{3.31}$$

where $\xi$ is a positive quantity whose value do not affect the result, and $\hat{g}^{(\xi)}_{R/L}(q_x)$ behaves at infinity as $\mathcal{O}(q_x^{-2})$, and shares the same analyticity properties of $\hat{\phi}_{R/L}(q_x)$. The inverse Fourier transform $g^{(\xi)}_{R/L}(x)$ is identically zero for $x < (>)0$ and is continuous. This means that $g^{(\xi)}_{R/L}(0) = 0$. We can therefore extract the value of $\phi_{R/L}(0)$ using the Fourier transform

$$\mathcal{F}_x[\Theta(\pm x)e^{-\zeta|x|}](q_x) = \frac{\mp i}{q_x\mp i\zeta}. \tag{3.32}$$

This leads to

$$\phi_{R/L}(0^{\pm}) = \phi(0)\left(1+c_{R/L}\right). \tag{3.33}$$

Non trivial solutions are possible if and only if

$$c_R = c_L = 0, \tag{3.34}$$

that is equivalent to [130]

$$\coth[I(|q_y|)] = i\frac{\delta\sigma_{\rm H}}{\delta\sigma}{\rm sgn}(q_y), \tag{3.35}$$

with $I(|q_y|)$ defined in (3.23).

This equation is the most important result of this section and allows determination of the spectrum of bound-states at the interface.

We note that since $I(|q_y|)$ is a real quantity $|\coth(I)| > 1$. This means that no bound state is allowed for $|\delta\sigma_{\rm H}| < |\delta\sigma|$.

Equation (3.35) must be, in general, solved numerically. However we note that for $|q_y| \gg q^{R/L}$ the integral $I$ can be approximated by

$$I(|q_y|) \approx \frac{1}{2}\ln\left(\frac{\sigma_R}{\sigma_L}\right), \tag{3.36}$$

substituting into (3.35) gives the much simpler equation

$$\sigma_R + \sigma_L = i\delta\sigma_{\rm H}{\rm sgn}(q_y), \tag{3.37}$$

from which the asymptotic, large $q_y$ behavior of bounded resonances can be calculated.

For small $\delta\sigma$ the integral (3.23) can be approximated by

$$I(|q_y|) \approx \frac{i\delta\sigma|q_y|}{\omega}J(|q_y|), \tag{3.38}$$

where

$$J(0,|q_y|) = |q_y|\int_0^\infty \frac{dt}{\pi}\frac{L(|q_y|\sqrt{1+t^2})}{\epsilon(|q_y|\sqrt{1+t^2})}. \tag{3.39}$$

Equation (3.35) then reduces to

$$1 + \frac{q_y\delta\sigma_{\rm H}J(|q_y|)}{\omega} = 0, \tag{3.40}$$

in agreement with the result of Sect. 3.1.4.

**Total internal reflection**

If the modulus of the $y$ component of the wavevector $q_y$ is larger than $\min[q^R, q^L]$ but smaller than $\max[q^R, q^L]$ total internal reflection takes place at the interface. Throughout this section we assume, without loss of generality, that $q^R < q^L$. This means that the following chain of inequalities: $q^R < q_y < q^L$ holds. Plasmons can therefore propagate in the left half plane ($x < 0$) with a real $q_x$ wavevector, corresponding to a traveling solution, while they are forced to have an imaginary wavevector, corresponding to an evanescent wave for $x > 0$. This mathematically describe the well known phenomenon of the total internal reflection of a wave at the interface of two media.

We start analyzing this case by defining two auxiliary polynomials

$$P_R(q_x) \equiv q_x^2 + q_y^2, \tag{3.41}$$

$$P_L(q_x) \equiv \left(q_x + q_x^L\right)\left(q_x - q_x^L\right), \tag{3.42}$$

where the $x$ component of the left plasmon wavevector is defined by

$$q_x^L = \sqrt{\left(q^L\right)^2 - q_y^2}. \tag{3.43}$$

We define again a well-behaved function

$$R(q_x) \equiv \frac{\sigma_L}{\sigma_R}\frac{\epsilon_R(q)P_L(q_x)}{\epsilon_L(q)P_R(q_x)} = \frac{R_R(q_x)}{R_L(q_x)}, \tag{3.44}$$

that is regular and positive on the whole real line and tends to one for $q_x \to \infty$.

With these definitions Eq. (3.16) becomes

$$\sigma_R R_R(q_x)P_R(q_x)\hat{\phi}_R(q_x) + \sigma_L R_L(q_x)P_L(q_x)\hat{\phi}_L(q_x) = \phi(0)[X(q_x) + \delta\sigma]f(q_x), \tag{3.45}$$

where the function $X(q_x)$ is defined by

$$X(q_x) \equiv \frac{\sigma_R R_R(q_x)P_R(q_x) - \sigma_L R_L(q_x)P_L(q_x)}{q_x^2 + q_y^2} - \delta\sigma. \tag{3.46}$$

Using the property (D.4) we can split this function into the sum of two parts that are analytic in the lower (upper) half of the complex plane respectively. This procedure yields

$$X_{R/L}(q_x) = \pm\,\sigma_{R/L}\left[\frac{R_{R/L}(q_x)P_{R/L}(q_x)}{q_x^2 + q_y^2} - 1\right] \mp \frac{iq^L\bar{\sigma}e^{-I}}{q_x - i|q_y|}, \tag{3.47}$$

where $I \equiv I(|q_y|)$ is defined by the integral

$$I(|q_y|) = \ln(2) + \frac{1}{\pi}\int_0^\infty \ln\left[\frac{\epsilon_R(|q_y|\sqrt{1+t^2})\left[(t^2+1)\frac{q_y^2}{(q^L)^2} - 1\right]}{\epsilon_L(|q_y|\sqrt{1+t^2})\left[1+t^2\right]}\right]\frac{dt}{1+t^2}. \tag{3.48}$$

Equation (3.49) can then be rearranged into

$$\begin{aligned}&\sigma_R R_R(q_x)P_R(q_x)\hat{\phi}_R(q_x) - \phi(0)[X_R(q_x) + \sigma_R]f(q_x) = \\ &= -\sigma_L R_L(q_x)P_L(q_x)\hat{\phi}_L(q_x) + \phi(0)[X_L(q_x) - \sigma_L]f(q_x),\end{aligned} \tag{3.49}$$

where the left hand side is analytic for $\Im m[q_y] \leq 0$, while the right hand side is analytic for $\Im m[q_y] \geq 0$, the equality holding on the real line. The two sides of this equation therefore an entire function. Taking into account the asymptotic behaviors for large $|q_x|$: $R_{R/L}(q_x) \sim 1$, $P_{R/L}(q_x) \sim q_x^2$, $\phi_{R/L}(q_x) \sim q_x^{-1}$, $X_{R/L}(q_x) \sim q_x^{-1}$, and $f(q_x) \sim q_x$, we can show that both sides of (3.49) behave at most linearly for large values of the argument. This means that they are both equal to the same first degree polynomial $A + Bq_x$. This gives

$$P_{R/L}(q_x)\hat{\phi}_{R/L}(q_x) = \frac{\phi(0)[X_{R/L}(q_x) \pm \sigma_{R/L}]f(q_x) \pm A \pm Bq_x}{\sigma_{R/L}R_{R/L}(q_x)}. \tag{3.50}$$

We can extract the leading $\mathcal{O}(q_x^{-1})$ part of $\hat{\phi}_{R/L}(q_x)$ for large $q_x$ by taking the limit

$$\lim_{q_x\to\infty} q_x\hat{\phi}_{R/L}(q_x) = \mp i\left(\phi(0) + i\frac{B}{\sigma_{R/L}}\right), \tag{3.51}$$

by following the same steps as in Eqs. (3.29-3.31) we obtain

$$\phi(0^{\pm}) = \phi(0) + i\frac{B}{\sigma_{R/L}}. \tag{3.52}$$

To ensure the continuity of the potential at $x = 0$ we must therefore fix $B = 0$.

We can now solve for the potentials $\hat{\phi}_{R/L}(q_x)$. Let's consider $\hat{\phi}_R(q_x)$ first. Dividing by $P_R(q_x)$ in Eq. (3.50) can introduce poles at $\pm i|q_y|$. While a pole at $i|q_y|$ is acceptable, no pole should arise at $-i|q_y|$ since $\hat{\phi}_r(q_x)$ is required to be analytic in the lower half of the complex plane. The numerator of (3.50) should therefore vanish at $q_x = -i|q_y|$. This fixes the constant $A$ to be

$$A = -\phi(0)\left[X_R(-i|q_y|) + \sigma_R\right] f(-i|q_y|) = -\phi(0) f(-i|q_y|)\frac{\bar{\sigma}q^L\cosh(I)}{|q_y|}. \tag{3.53}$$

Solving (3.50) for $\hat{\phi}_L(q_x)$ in the *distribution* sense yields

$$\hat{\phi}_L(q_x) = \mathcal{P}\frac{\phi(0)[X_L(q_x) - \sigma_L]f(q_x) - A}{\sigma_L R_L(q_x)P_L(q_x)} + C^+\delta\left(q_x - q_x^L\right) + C^-\delta\left(q_x + q_x^L\right), \tag{3.54}$$

where the two constants $C^{\pm}$ must be determined by requiring that $\phi_L(x)$ vanishes for $x > 0$. With the help of the Fourier transform

$$\mathcal{F}_x[\Theta(\pm x)e^{iq_0x}](q_x) = \mp\mathcal{P}\frac{i}{q_x - q_0} + \pi\delta(q_x - q_0) = \frac{\mp i}{q_x - q_0 \mp i\eta}, \tag{3.55}$$

we find

$$C^{\lambda} = -i\pi\lambda\phi(0)\frac{\phi(0)[X_L(\lambda q_x^L) - \sigma_L]f(\lambda q_x^L) - A}{2q_x^L\sigma_L R_L(\lambda q_x^L)}. \tag{3.56}$$

Using the second line of (3.55) we can show that this is equivalent to

$$\hat{\phi}_L(q_x) = \frac{\phi(0)[X_L(q_x) - \sigma_L]f(q_x) - A}{\sigma_L R_L(q_x)P_L(q_x + i\eta)}. \tag{3.57}$$

The right (left) Fourier transform of the potential then reads

$$\hat{\phi}_{R/L}(q_x) = \pm\phi(0)\left\{\frac{f(q_x)}{q_x^2 + q_y^2} - \frac{f(q_x)\bar{\sigma}iq^L|q_y|e^{-I} + f(-i|q_y|)\bar{\sigma}q^L(q_x - i|q_y|)\cosh(I)}{\sigma_{R/L}R_{R/L}(q_x)P_{R/L}(q_x \mp i\eta)(q_x - i|q_y|)|q_y|}\right\}. \tag{3.58}$$

The asymptotic behavior of $\phi_L(x)$ for $x \to -\infty$ is completely controlled by the poles of $\hat{\phi}_L(x)$ located near the real axis at $\pm q_x^L - i\eta$,

$$\hat{\phi}_{R/L}(q_x) \sim \frac{\alpha_L^+}{q_x - q_x^L + i\eta} + \frac{\alpha_L^-}{q_x + q_x^L + i\eta}, \tag{3.59}$$

where

$$\alpha_L^{\lambda} \equiv \lim_{q_x\to\lambda q_x^L - i\eta}\hat{\phi}_L(q_x)(q_x - \lambda q_x^L + i\eta). \tag{3.60}$$

The Fourier transform of (3.59) gives

$$\phi_L(x) \sim -i\Theta(-x)\left[\alpha_L^+ e^{iq_x^Lx} + \alpha_L^- e^{-iq_x^Lx}\right], \tag{3.61}$$

from this we can see that the reflection coefficient is given by $r \equiv \alpha_L^-/\alpha_L^+$. By straightforward manipulation we obtain

$$\alpha_L^{\lambda} = \frac{\lambda\phi(0)\bar{\sigma}q^L}{2\sigma_L q_x^L\delta\sigma}\frac{\delta\sigma[i|q_y|\cosh(I) - \lambda q_x^L\sinh(I)] + \delta\sigma_{\mathrm{H}}\mathrm{sgn}(q_y)[i\lambda q_x^L\cosh(I) + |q_y|\sinh(I)]}{R_L(\lambda q_x^L)(\lambda q_x^L - i|q_y|)}, \tag{3.62}$$

and

$$r = e^{-2i\psi_L} \frac{(q_x^L - i|q_y|)\left\{\delta\sigma[i|q_y|\cosh(I) + q_x^L \sinh(I)] + \delta\sigma_{\mathrm{H}}\mathrm{sgn}(q_y)[-iq_x^L \cosh(I) + |q_y|\sinh(I)]\right\}}{(q_x^L + i|q_y|)\left\{\delta\sigma[i|q_y|\cosh(I) - q_x^L \sinh(I)] + \delta\sigma_{\mathrm{H}}\mathrm{sgn}(q_y)[iq_x^L \cosh(I) + |q_y|\sinh(I)]\right\}}. \tag{3.63}$$

Here $I$ is given by (3.48) and the phase $\psi_L \equiv \psi_L(|q_y|)$ is defined by

$$\begin{aligned} &\psi_L(|q_y|) = \\ &= \frac{\mathcal{P}}{\pi}\int_0^\infty \frac{dt}{t^2-1} \ln\left[\frac{\epsilon_R\left(\sqrt{(q_x^L)^2 t^2 + q_y^2}\right)(t^2-1)}{\epsilon_L\left(\sqrt{(q_x^L)^2 t^2 + q_y^2}\right)\left[t^2 + \frac{q_y^2}{(q_x^L)^2}\right]}\right]. \end{aligned} \tag{3.64}$$

**Propagating solutions**

When $|q_y|$ is smaller than both the left and right plasmon wavevector, that is when $|q_y| < q^{R/L}$, we have propagating plasmons on both sides of the interface. We define the $x$ component of the plasmon wavevectors as

$$q_x^{R/L} = \sqrt{\left(q^{R/L}\right)^2 - q_y^2}, \tag{3.65}$$

and we define the auxiliary polynomials to be

$$P_{R/L}(q_x) \equiv \left(q_x + q_x^{R/L}\right)\left(q_x - q_x^{R/L}\right), \tag{3.66}$$

and a function $R(q_x)$ with no zeros or poles on the real axis

$$R(q_x) \equiv \frac{\sigma_L}{\sigma_R}\frac{\epsilon_R(q)P_L(q_x)}{\epsilon_L(q)P_R(q_x)} = \frac{R_R(q_x)}{R_L(q_x)}. \tag{3.67}$$

Splitting $R(q_x)$ into its left and right component according to (D.6) and substituting in (3.16) gives

$$\sigma_R R_R(q_x)P_R(q_x)\hat{\phi}_R(q_x) + \sigma_L R_L(q_x)P_L(q_x)\hat{\phi}_L(q_x) = \phi(0)[X(q_x) + \delta\sigma]f(q_x), \tag{3.68}$$

where the function $X(q_x)$ is

$$X(q_x) = \frac{\sigma_R R_R(q_x)P_R(q_x) - \sigma_L R_L(q_x)P_L(q_x)}{q_x^2 + q_y^2} - \delta\sigma. \tag{3.69}$$

We now split $X(q_x)$ into its left and right components according to (D.4). The two components read

$$X_{R/L}(q_x) = \pm\frac{1}{q^2}\left\{\sigma_{R/L}R_{R/L}(q_x)P_{R/L}(q_x) + \bar{\sigma}q^R q^L \frac{iq_x\sinh(I) + |q_y|\cosh(I)}{|q_y|}\right\} \mp \sigma_{R/L}\ , \tag{3.70}$$

where $\bar{\sigma} = \sqrt{\sigma_R\sigma_L}$, and $I \equiv I(|q_y|)$ is given by

$$I(|q_y|) = \frac{1}{\pi}\int_0^\infty \ln\left[\frac{\epsilon_R(|q_y|\sqrt{1+t^2})\left[1 - (1+t^2)\frac{q_y^2}{(q^L)^2}\right]}{\epsilon_L(|q_y|\sqrt{1+t^2})\left[1 - (1+t^2)\frac{q_y^2}{(q^R)^2}\right]}\right]\frac{dt}{1+t^2}. \tag{3.71}$$

Substituting into (3.68) gives

$$\begin{aligned} &\sigma_R R_R(q_x)P_R(q_x)\hat{\phi}_R(q_x) - \phi(0)[X_R(q_x) + \sigma_R]f(q_x) = \\ &= -\sigma_L R_L(q_x)P_L(q_x)\hat{\phi}_L(q_x) + \phi(0)[X_L(q_x) - \sigma_L]f(q_x). \end{aligned} \tag{3.72}$$

Repeating the same reasoning explained after (3.49) we can say that the two sides of this equation are equal to a polynomial $A + Bq_x$. We therefore obtain

$$P_{R/L}(q_x)\hat{\phi}_{R/L}(q_x) = \frac{\phi(0)[X_{R/L}(q_x) \pm \sigma_{R/L}]f(q_x) \pm A \pm Bq_x}{\sigma_{R/L}R_{R/L}(q_x)}. \tag{3.73}$$

The leading-order behavior of $\hat{\phi}_{R/L}(q_x)$ is again given by the limit

$$\lim_{q_x\to\infty} q_x\hat{\phi}_{R/L}(q_x) = \mp i\left(\phi(0) + i\frac{B}{\sigma_{R/L}}\right). \tag{3.74}$$

Repeating the steps in (3.29-3.33) we obtain

$$\phi(0^{\pm}) = \phi(0) + i\frac{B}{\sigma_{R/L}}. \tag{3.75}$$

The continuity of $\phi(x)$ in $x = 0$ then fixes $B = 0$. Inverting (3.72) yields

$$\hat{\phi}_{R/L}(q_x) = \mathcal{P}\frac{\phi(0)[X_{R/L}(q_x) \pm \sigma_{R/L}]f(q_x) \pm A}{\sigma_{R/L}R_{R/L}(q_x)P_{R/L}(q_x)} + C^{+}_{R/L}\delta\left(q_x - q_x^{R/L}\right) + C^{-}_{R/L}\delta\left(q_x + q_x^{R/L}\right). \tag{3.76}$$

The four constants must be fixed by requiring that $\phi_{R/L}(x)$ vanishes for $x < 0$ ($x > 0$). We obtain

$$C^{\lambda}_{R/L} = \pm i\pi\lambda\phi(0)\frac{\phi(0)[X_{R/L}(\lambda q_x^{R/L}) \pm \sigma_{R/L}]f(\lambda q_x^{R/L}) \pm A}{2q_x^{R/L}\sigma_{R/L}R_{R/L}(\lambda q_x^{R/L})}, \tag{3.77}$$

that, using the Sokhotski-Plemelj theorem, can be written more compactly as

$$\hat{\phi}_{R/L}(q_x) = \frac{\phi(0)[X_{R/L}(q_x) \pm \sigma_{R/L}]f(q_x) \pm A}{\sigma_{R/L}R_{R/L}(q_x)P_{R/L}(q_x \mp i\eta)}. \tag{3.78}$$

Substituting (3.70) into (3.78) we obtain the Fourier transform of the potential

$$\hat{\phi}_{R/L}(q_x) = \pm\frac{\phi(0)f(q_x)}{q_x^2 + q_y^2}\left\{1 + \frac{\bar{\sigma}q^R q^L\left[iq_x\sinh(I) + |q_y|\cosh(I)\right]}{|q_y|\sigma_{R/L}R_{R/L}(q_x)P_{R/L}(q_x \mp i\eta)}\right\} \pm \frac{A}{\sigma_{R/L}R_{R/L}(q_x)P_{R/L}(q_x \mp i\eta)}. \tag{3.79}$$

The asymptotic behavior of $\phi(x)$ for $x \to \pm\infty$ is governed by the poles of $\hat{\phi}_{R/L}(q_x)$ located near the real axis,

$$\hat{\phi}_{R/L}(q_x) \sim \frac{\alpha^{+}_{R/L}}{q_x - q_x^{R/L} \mp i\eta} + \frac{\alpha^{-}_{R/L}}{q_x + q_x^{R/L} \mp i\eta}, \tag{3.80}$$

taking the Fourier transform of this equation we obtain

$$\phi_{R/L}(x) \sim \pm i\Theta(\pm x)\left[\alpha^{+}_{R/L}e^{iq_x^{R/L}x} + \alpha^{-}_{R/L}e^{-iq_x^{R/L}x}\right], \tag{3.81}$$

where the residues $\alpha^{\lambda}_{R/L}$ of $\hat{\phi}_{R/L}(q_x)$ at $q_x = \lambda q_x^{R/L}$, with $\lambda = \pm 1$, are given by

$$\alpha^{\lambda}_{R/L} \equiv \lim_{q_x\to\lambda q_x^{R/L}\pm i\eta} \hat{\phi}_{R/L}(q_x)(q_x - \lambda q_x^{R/L} \mp i\eta). \tag{3.82}$$

Looking at the asymptotic formula (3.80) we see that in order to have an impinging wave plus a reflected wave on the left and a transmitted wave on the right we must choose the constant $A$ such that $\alpha^{-}_{R} \equiv 0$. We firstly calculate the residues explicitly using (3.79-3.82)

$$\alpha^{\lambda}_{R/L} = \pm\lambda\frac{\phi(0)\bar{\sigma}q^R q^L f(\lambda q_x^{R/L})\left[i\lambda q_x^{R/L}\sinh(I) + |q_y|\cosh(I)\right] + A|q_y|(q^{R/L})^2}{2|q_y|q_x^{R/L}(q^{R/L})^2\sigma_{R/L}R_{R/L}(\lambda q_x^{R/L})}, \tag{3.83}$$

requiring the vanishing of $\alpha^{-}_{R}$ this becomes

$$\begin{aligned}\alpha^{\lambda}_{R/L} = \pm\lambda&\frac{\phi(0)\bar{\sigma}q^L}{2|q_y|q^R q_x^{R/L}(q^{R/L})^2\sigma_{R/L}R_{R/L}(\lambda q_x^{R/L})}\\ &\times\left\{(q^R)^2 f(\lambda q_x^{R/L})\left[i\lambda q_x^{R/L}\sinh(I) + |q_y|\cosh(I)\right] - (q^{R/L})^2 f(-q_x^R)\left[-iq_x^R\sinh(I) + |q_y|\cosh(I)\right]\right\}.\end{aligned} \tag{3.84}$$

More explicitly we get

$$\alpha_R^+ = -i\phi(0)\sqrt{\frac{\sigma_L}{\sigma_R}}\frac{q^L}{q^R R_R(q_x^R)}\left[\cosh(I) - \frac{i\mathrm{sgn}(q_y)\delta\sigma_{\mathrm{H}}}{\delta\sigma}\sinh(I)\right], \tag{3.85}$$

$$\begin{aligned}\alpha_L^+ &= i\phi(0)\sqrt{\frac{\sigma_R}{\sigma_L}}\frac{q_x^R + q_x^L}{2q^R q^L q_x^L R_L(q_x^L)}\times \\ &\times\left\{(q_x^L q_x^R + q_y^2)\left[\cosh(I) - \frac{i\mathrm{sgn}(q_y)\delta\sigma_{\mathrm{H}}}{\delta\sigma}\sinh(I)\right] + i|q_y|(q_x^L - q_x^R)\left[\sinh(I) - \frac{i\mathrm{sgn}(q_y)\delta\sigma_{\mathrm{H}}}{\delta\sigma}\cosh(I)\right]\right\},\end{aligned} \tag{3.86}$$

and

$$\begin{aligned}\alpha_L^- &= -i\phi(0)\sqrt{\frac{\sigma_R}{\sigma_L}}\frac{q_x^L - q_x^R}{2\delta\sigma q^R q^L q_x^L R_L(-q_x^L)}\times \\ &\times\left\{(q_x^L q_x^R - q_y^2)\left[\cosh(I) - \frac{i\mathrm{sgn}(q_y)\delta\sigma_{\mathrm{H}}}{\delta\sigma}\sinh(I)\right] + i|q_y|(q_x^L + q_x^R)\left[\sinh(I) - \frac{i\mathrm{sgn}(q_y)\delta\sigma_{\mathrm{H}}}{\delta\sigma}\cosh(I)\right]\right\}.\end{aligned} \tag{3.87}$$

Making use of (3.80) we can write the reflection and transmission coefficients

$$\begin{aligned}r = \frac{\alpha_L^-}{\alpha_L^+} &= \frac{(q_x^R - q_x^L)}{(q_x^R + q_x^L)}e^{-2i\psi_L}\times \\ &\times\frac{(q_x^L q_x^R - q_y^2)\left[\cosh(I) - \frac{i\mathrm{sgn}(q_y)\delta\sigma_{\mathrm{H}}}{\delta\sigma}\sinh(I)\right] + i|q_y|(q_x^L + q_x^R)\left[\sinh(I) - \frac{i\mathrm{sgn}(q_y)\delta\sigma_{\mathrm{H}}}{\delta\sigma}\cosh(I)\right]}{(q_x^L q_x^R + q_y^2)\left[\cosh(I) - \frac{i\mathrm{sgn}(q_y)\delta\sigma_{\mathrm{H}}}{\delta\sigma}\sinh(I)\right] + i|q_y|(q_x^L - q_x^R)\left[\sinh(I) - \frac{i\mathrm{sgn}(q_y)\delta\sigma_{\mathrm{H}}}{\delta\sigma}\cosh(I)\right]},\end{aligned} \tag{3.88}$$

$$\begin{aligned}t = -\frac{\alpha_R^+}{\alpha_L^+} &= \frac{2\sqrt{q_x^R q_x^L}\sqrt{q^R q^L}q^L}{(q_x^R + q_x^L)}\sqrt{\frac{\sigma_L}{\sigma_R}}\sqrt{\frac{1 + \frac{q^L L'(q^L)}{2L(q^L)}}{1 + \frac{q^R L'(q^R)}{2L(q^R)}}}e^{i(\psi_L - \psi_R)}\times \\ &\times\frac{\cosh(I) - \frac{i\mathrm{sgn}(q_y)\delta\sigma_{\mathrm{H}}}{\delta\sigma}\sinh(I)}{(q_x^L q_x^R + q_y^2)\left[\cosh(I) - \frac{i\mathrm{sgn}(q_y)\delta\sigma_{\mathrm{H}}}{\delta\sigma}\sinh(I)\right] + i|q_y|(q_x^L - q_x^R)\left[\sinh(I) - \frac{i\mathrm{sgn}(q_y)\delta\sigma_{\mathrm{H}}}{\delta\sigma}\cosh(I)\right]}.\end{aligned} \tag{3.89}$$

Here $I \equiv I(|q_y|)$ is defined in (3.71), $L'(q) \equiv \partial_q L(q)$, while the phase $\psi_{R/L}(|q_y|)$ is defined by the integral

$$\psi_{R/L}(|q_y|) = \frac{\mathcal{P}}{\pi}\int_0^\infty \frac{dt}{t^2 - 1}\ln\left[\frac{\epsilon_R\left(\sqrt{\left(q_x^{R/L}\right)^2 t^2 + q_y^2}\right)\left[t^2 - \left(\frac{q_x^L}{q_x^{R/L}}\right)^2\right]}{\epsilon_L\left(\sqrt{\left(q_x^{R/L}\right)^2 t^2 + q_y^2}\right)\left[t^2 - \left(\frac{q_x^R}{q_x^{R/L}}\right)^2\right]}\right]. \tag{3.90}$$

In deriving the above result we made use of the chain of equalities

$$\begin{aligned}\frac{\sigma_L}{\sigma_R}\left|\frac{R_L(q_x^L)}{R_R(q_x^R)}\right| &= \frac{\sigma_L}{\sigma_R R(q_x^L)R(q_x^R)} = \sqrt{\frac{\epsilon_L(q^L)\epsilon_L(q^R)P_R(q_x^L)P_R(q_x^R)}{\epsilon_R(q^L)\epsilon_R(q^R)P_L(q_x^L)P_L(q_x^R)}} = \sqrt{-\frac{\epsilon_L(q^L)\epsilon_L(q^R)P_R(q_x^R)}{\epsilon_R(q^L)\epsilon_R(q^R)P_L(q_x^L)}} \\ &= \sqrt{-\frac{q_x^R\epsilon_L'(q^L)\epsilon_L(q^R)}{q_x^L\epsilon_R'(q^R)\epsilon_R(q^L)}} = \sqrt{\frac{q_x^R\sigma_L\epsilon_L'(q^L)}{q_x^L\sigma_R\epsilon_R'(q^R)}} = \sqrt{\frac{q_x^R\sigma_L^2[2q^L L(q^L) + (q^L)^2 L'(q^L)]}{q_x^L\sigma_R^2[2q^R L(q^R) + (q^R)^2 L'(q^R)]}} \\ &= \sqrt{\frac{q_x^R\sigma_L^2 q^L L(q^L)[1 + \frac{q^L L'(q^L)}{2L(q^L)}]}{q_x^L\sigma_R^2 q^R L(q^R)[1 + \frac{q^R L'(q^R)}{2L(q^R)}]}} = \sqrt{\frac{q_x^R\sigma_L q^R[1 + \frac{q^L L'(q^L)}{2L(q^L)}]}{q_x^L\sigma_R q^L[1 + \frac{q^R L'(q^R)}{2L(q^R)}]}}.\end{aligned} \tag{3.91}$$

The above results simplify considerably for $q_y \equiv 0$. In this case the scattering coefficients read [209, 210, 138]

$$r = \frac{q^R - q^L}{q^R + q^L}e^{-2i\psi_L(0)}, \tag{3.92}$$

$$t = \frac{2q^L}{q^R + q^L}\sqrt{\frac{\sigma_L}{\sigma_R}}\sqrt{\frac{1+\frac{q^L L'(q^L)}{2L(q^L)}}{1+\frac{q^R L'(q^R)}{2L(q^R)}}}e^{i[\psi_L(0)-\psi_R(0)]}. \tag{3.93}$$

The conservation of energy is expressed by

$$|r|^2 + \frac{\sigma_R q^R\left[1+\frac{q^R L'(q^R)}{2L(q^R)}\right]}{\sigma_L q^L\left[1+\frac{q^L L'(q^L)}{2L(q^L)}\right]}|t|^2 = 1 \tag{3.94}$$

### 3.1.3 Solution for an edge

The particular case of an edge, with vacuum occupying the half-plane $x > 0$ can be recovered setting $\sigma_R = 0$, $\epsilon_R(q_x) = 1$ in the final formulas of Sect. 3.1.2.

#### Localized solutions

Setting $\epsilon_R(q_x) = 1$, the integral in (3.23) can be rewritten as $I(|q_y|) = -i\pi/2 - \tilde{I}(|q_y|)$, where

$$\tilde{I}(|q_y|) = \frac{1}{\pi}\int_0^\infty \frac{dt}{1+t^2}\ln\left(-\epsilon_L(|q_y|\sqrt{1+t^2})\right). \tag{3.95}$$

We used the standard choice for the branch-cut of the ln function (i. e. $\ln(x) = \ln|x| + i\pi\Theta(-x)$ for real $x$). The final results, however, do not depend on this choice.

Taking the above definition into account, Eq. (3.35) becomes

$$\tanh[\tilde{I}(|q_y|)] = -i\frac{\sigma_{\rm HL}}{\sigma_L}\mathrm{sgn}(q_y). \tag{3.96}$$

We note that since $\tilde{I}$ is a real quantity, this equation can have solutions only if $|\sigma_{\rm HL}/\sigma_L| < 1$.

#### Propagating solutions

Setting $\epsilon_R = 1$ in Eqs. (3.71-3.90) we obtain $\psi_L(|q_y|) = \tilde{\psi}(|q_y|)$ with

$$\tilde{\psi}(|q_y|) = \frac{\mathcal{P}}{\pi}\int_0^\infty \frac{dt}{1-t^2}\ln\left[\epsilon_L\left(\sqrt{(q_x^L)^2t^2+q_y^2}\right)\frac{t^2+\frac{q_y^2}{(q_x^L)^2}}{1-t^2}\right], \tag{3.97}$$

and $I(|q_y|) = \ln(2) - i\pi/2 - \tilde{I}(|q_y|)$ with

$$\tilde{I}(|q_y|) = \frac{1}{\pi}\int_0^\infty \ln\left[\frac{\epsilon_L(|q_y|\sqrt{1+t^2})\left(1+t^2\right)}{1-(t^2+1)\frac{q_y^2}{(q^L)^2}}\right]\frac{dt}{1+t^2}. \tag{3.98}$$

The reflection phase is therefore

$$r = e^{-2i\tilde{\psi}}\frac{(q_x^L - i|q_y|)\left\{\sigma_L[i|q_y|\sinh(\tilde{I}) - q_x^L\cosh(\tilde{I})] + \sigma_{\rm HL}\mathrm{sgn}(q_y)[-iq_x^L\sinh(\tilde{I}) - |q_y|\cosh(\tilde{I})]\right\}}{(q_x^L + i|q_y|)\left\{\sigma_L[i|q_y|\sinh(\tilde{I}) + q_x^L\cosh(\tilde{I})] + \sigma_{\rm HL}\mathrm{sgn}(q_y)[iq_x^L\sinh(\tilde{I}) - |q_y|\cosh(\tilde{I})]\right\}}. \tag{3.99}$$

### 3.1.4 Interface with uniform normal conductivity

Here we analyze the particular case of an interface between two media with the same normal conductivity but with different Hall conductivities. We start from Eq. (3.14) and set $\delta\sigma \equiv 0$ and $\epsilon_R(q) = \epsilon_L(q) \equiv \epsilon(q)$

$$\epsilon(q)\hat{\phi}(q_x) = -\phi(0)\frac{\delta\sigma_{\rm H}L(q)q_y}{\omega}. \tag{3.100}$$

The dielectric function $\epsilon(q)$ vanishes at the wavevector $q^0 \equiv q^R = q^L$

$$\epsilon(q^0) = 0. \tag{3.101}$$

**Localized solutions**

If $q_y > q^0$ we can directly divide Eq. (3.100) by $\epsilon(q)$ and obtain the Fourier transform of the potential

$$\hat{\phi}(q_x) = -\phi(0)\frac{\delta\sigma_{\mathrm{H}} L(q) q_y}{\omega\epsilon(q)}. \tag{3.102}$$

Fourier transforming back to real space we get

$$\phi(x) = -\phi(0)\frac{\delta\sigma_{\mathrm{H}} q_y}{\omega} J(x, |q_y|), \tag{3.103}$$

where

$$J(x, |q_y|) = |q_y| \int_0^\infty \frac{dt}{\pi} \frac{L(|q_y|\sqrt{1+t^2})\cos(|q_y| tx)}{\epsilon(|q_y|\sqrt{1+t^2})}. \tag{3.104}$$

Setting $x = 0$ we obtain the equation for the bound states

$$1 + \frac{\delta\sigma_{\mathrm{H}} q_y}{\omega} J(0, |q_y|) = 0. \tag{3.105}$$

A simpler result can be obtained in the limit $|q_y| \gg q^0$. If this inequality holds we can approximate the integral $J(x, |q_y|)$ with

$$J(x, |q_y|) \approx -\frac{i\omega}{2\sigma|q_y|} e^{-|q_y||x|}, \tag{3.106}$$

substituting into (3.105) yields

$$1 - i\mathrm{sgn}(q_x)\frac{\delta\sigma_{\mathrm{H}}}{2\sigma} = 0. \tag{3.107}$$

**Propagating solutions**

If $q_y < q^0$ more care must be taken in dividing by $\epsilon(q)$ because this function vanishes at $q^0$. Inverting in the distribution sense we obtain

$$\hat{\phi}(q_x) = -\phi(0)\mathcal{P}\frac{L(q)\delta\sigma_{\mathrm{H}} q_y}{\epsilon(q)\omega} + C^+\delta(q_x - q_x^0) + C^-\delta(q_x + q_x^0), \tag{3.108}$$

where $C^\pm$ are two constants to be determined. By Fourier transform we obtain the corresponding real space expression

$$\phi(x) = -\phi(0)\frac{\delta\sigma_{\mathrm{H}} q_y}{\omega} J(x, |q_y|) + \frac{C^+}{2\pi} e^{iq_x^0 x} + \frac{C^-}{2\pi} e^{-iq_x^0 x}, \tag{3.109}$$

where

$$J(x, |q_y|) = |q_y|\mathcal{P}\int_0^\infty \frac{dt}{\pi} \frac{L(|q_y|\sqrt{1+t^2})\cos(|q_y| tx)}{\epsilon(|q_y|\sqrt{1+t^2})}. \tag{3.110}$$

Setting $x = 0$ in (3.109) we obtain an equation that fixes the sum of the two constants.

$$\phi(0)\left(1 + \frac{\delta\sigma_{\mathrm{H}} q_y}{\omega} J(0, |q_y|)\right) = \frac{C^+ + C^-}{2\pi}, \tag{3.111}$$

The asymptotic behavior of the potential is controlled by the diverging part of its Fourier transform

$$\hat{\phi}(q_x) \sim -\phi(0)\frac{\delta\sigma_{\mathrm{H}} q_y}{\omega}\mathcal{P}\left[\frac{\alpha^+}{q_x - q_x^0} + \frac{\alpha^-}{q_x + q_x^0}\right] + C^+\delta(q_x - q_x^0) + C^-\delta(q_x + q_x^0), \tag{3.112}$$

where

$$\alpha^\pm = \lim_{q_x \to \pm q_x^0} \frac{L\left(\sqrt{q_x^2 + q_y^2}\right)}{\epsilon\left(\sqrt{q_x^2 + q_y^2}\right)}(q_x \mp q_x^0) = \pm\frac{q^0 L(q^0)}{q_x^0 \epsilon'(q^0)}. \tag{3.113}$$

Here $\epsilon'(q) = \partial_q \epsilon(q)$.

Fourier transforming back to real space gives

$$\begin{aligned}\phi(x) = \Theta(x) &\left[\left(\frac{i\phi(0)\delta\sigma_{\rm H}q_y\alpha^+}{2\omega}+\frac{C^+}{2\pi}\right)e^{iq_x^0x}+\left(\frac{i\phi(0)\delta\sigma_{\rm H}q_y\alpha^-}{2\omega}+\frac{C^-}{2\pi}\right)e^{-iq_x^0x}\right]\\ +\Theta(-x) &\left[\left(\frac{-i\phi(0)\delta\sigma_{\rm H}q_y\alpha^+}{2\omega}+\frac{C^+}{2\pi}\right)e^{iq_x^0x}+\left(\frac{-i\phi(0)\delta\sigma_{\rm H}q_y\alpha^-}{2\omega}+\frac{C^-}{2\pi}\right)e^{-iq_x^0x}\right].\end{aligned} \tag{3.114}$$

To have only a transmitted wave for $x>0$ the constant $C^-$ must be

$$C^- = -i\pi\phi(0)\alpha^-\frac{\delta\sigma_{\rm H}q_y}{\omega}, \tag{3.115}$$

while $C^+$ reads

$$C^+ = 2\pi\phi(0)\left[1+\frac{\delta\sigma_{\rm H}q_y}{\omega}\left(J(0,|q_y|)+i\frac{\alpha^-}{2}\right)\right]. \tag{3.116}$$

The reflection (transmission) coefficient, given by the ratio between the amplitude of the reflected (transmitted) wave and the amplitude of the incident wave, is therefore

$$r = \frac{i\frac{L(q^0)q^0}{\epsilon'(q^0)q_x^0}\frac{\delta\sigma_{\rm H}q_y}{\omega}}{1+\left[J(0,|q_y|)-i\frac{L(q^0)q^0}{\epsilon'(q^0)q_x^0}\right]\frac{\delta\sigma_{\rm H}q_y}{\omega}}, \tag{3.117}$$

$$t = \frac{1+J(0,|q_y|)\frac{\delta\sigma_{\rm H}q_y}{\omega}}{1+\left[J(0,|q_y|)-i\frac{L(q^0)q^0}{\epsilon'(q^0)q_x^0}\right]\frac{\delta\sigma_{\rm H}q_y}{\omega}}. \tag{3.118}$$

## 3.2 Lippmann-Schwinger theory for two-dimensional plasmon scattering

In this Section, we are interested in the scattering properties of 2D plasmons in parabolic-band electron gases and encapsulated graphene sheets. To this end, we lay down a Lippmann-Schwinger theory that enables us to calculate complex reflection and transmission coefficients for 2D plasmons impinging on a great variety of localized perturbations.

Scattering theories for surface plasmon polaritons in noble metals have been introduced in the past [211, 212, 213, 214]. More recently, scattering of graphene plasmons against one-dimensional (1D) defects has been studied in Refs. [197, 200]. In particular, the impact of electronic quasi-bound states on the scattering properties of plasmons has been recently studied in Ref. [198]. Scattering of plasmons in more exotic electron systems has also been considered, for example in Ref. [215].

The main difference between these earlier works and the theory presented here is that we use an *electrostatic approximation*, instead of solving Maxwell equations. This offers several advantages with respect to previous works: (i) our theory is essentially semi-analytical, requires little numerical effort, and, most importantly, takes into account *nonlocal* effects; (ii) we calculate the density-density response function from the knowledge of a *microscopic* Hamiltonian, instead of assuming phenomenological models for the spatial dependence of the conductivity profile (as done in *all* papers, with the exception of Ref. [198]); (iii) we treat on equal footing many different perturbations (not only electrostatic perturbations coupling to the electron density operator); and (iv) we provide a recipe to include exchange and correlation effects *beyond* the celebrated random phase approximation (RPA) [35], as we explain below in Section 3.2.3.

The only disadvantage of our approach is that we are unable to describe scattering of plasmons into far-field modes of the electromagnetic field. In 2D electron gases in GaAs/AlGaAs heterostructures and graphene sheets, these dissipative processes are usually very weak as it has been demostrated both theoretically [197] and experimentally (see, for example, Ref. [19]) for sufficiently confined 2D plasmons. The reason is that the plasmon momenta at play in these electron systems are much larger that the photon momentum $\omega/c$. This implies that coupling to far-field modes of the electromagnetic field can occur only in the presence of extremely sharp defects/perturbations. However, experimentally realized (electrostatic) defects/perturbations for plasmons are smooth and are therefore unable to couple plasmons

to photons. The situation is particularly "extreme" in hybrid heterostructures containing graphene, hBN, and nearby metal gates [160, 47]. A metal gate in close proximity to graphene suppresses the long-range tail of the inter-electron Coulomb interaction, morphing the usual 2D unscreened plasmon [35] with $\omega_{\rm pl}(q) \propto \sqrt{q}$ into an acoustic plasmon mode [207, 160, 47] with a phase velocity that is extremely close to the electron Fermi velocity $v_{\rm F}$. For a given illumination frequency $\omega$, such acoustic plasmons have therefore momenta that are much larger that those of unscreened plasmons. Recent experiments [19] where plasmons in such stacks were launched against smooth 1D electrostatic barriers show that our approximation is fully justified and that our theory explains in a fully quantitative fashion experimental data with *no* fitting parameters.

The ramaning part of this Section is organized as following. In Sect. 3.2.1 we present a brief overview of how to approach the non-trivial problem of plasmons in inhomogeneous media [216, 217] and we introduce two fundamental quantities: a) the proper density-density response function $\tilde{\chi}_{nn}(\boldsymbol{q},\boldsymbol{q}',\omega)$ and b) the screened potential $V_{\rm sc}(\boldsymbol{q},\omega)$. In Sect. 3.2.2 we introduce two scattering geometries of interest in this work, which are schematically reported in Fig. 3.1, and a Lippmann-Schwinger equation for the screened potential, which automatically fulfils appropriate asymptotic conditions. Sect. 3.2.3 is devoted to the generalization of the theory of the previous section to include exchange and correlation effects *beyond* the RPA.

In Sect. 3.2.4 we introduce the key quantity of our 2D Lippmann-Schwinger plasmon scattering theory: the transition function $T(\boldsymbol{q},\theta,\omega)$. The latter fully controls the scattering amplitude $f(\theta_{\boldsymbol{r}},\theta,\omega)$ in the geometry in Fig. 3.1(a) and reflection $r_{\theta,\omega}$ and transmission $t_{\theta,\omega}$ coefficients in the geometry in Fig. 3.1(b). In Sect. 3.2.5 we derive a useful relation between the amplitude of forward scattering and the total scattering cross section, which is known, in the context of electromagnetic scattering, as optical theorem. Paralleling single-particle quantum-mechanical scattering theory [218], in Sections 3.2.6, 3.2.7, and 3.2.8 we present three approximations for the evaluation of the scattering observables: the *Born* approximation, the *eikonal* approximation, and the *method of partial waves*, respectively. Finally, two concrete problems, i.e. scattering of a plasmon in a 2D parabolic-band electron system against an electrostatic potential generated by i) a point-like charged impurity and ii) a 1D line of charges, are explicitly solved in Sect. 3.2.9. These are used to compare exact numerical results—obtained from the full solution of the Lippmann-Schwinger equation—with approximate results based on the Born and eikonal approximations. In the second geometry, we also explicitly quantify the impact of nonlocal effects. A summary of our main results and a brief set of conclusions and perspectives is finally reported in Sect. 3.4. The evaluation of the transition function requires exact expressions for the proper density-density response function of an inhomogeneous 2D electron system, which are carefully derived in Appendix B.1. We here stress the importance of the results contained in Eqs. (B.24), (B.30), and (B.32): these give the high-frequency behavior of the density-density response function of an *inhomogeneous* 2D electron liquid subject to a very general perturbation, up to next-to-leading order in the frequency. In Appendix B.2 we extend these results to the case of an inhomogeneous electron liquid hosted in a graphene sheet. Other mathematical and computational details are contained in Appendix E

### 3.2.1 Plasmons in inhomogeneous media

The linear density response $n_1(\boldsymbol{q},\omega)$ induced by an external scalar potential in an electron liquid can be expressed in terms of the screened potential $V_{\rm sc}(\boldsymbol{q},\omega)$ and the *proper* density-density response function [35] according to

$$n_1(\boldsymbol{q},\omega) = \sum_{\boldsymbol{q}'} \tilde{\chi}_{nn}(\boldsymbol{q},\boldsymbol{q}',\omega) V_{\rm sc}(\boldsymbol{q}',\omega) \ . \tag{3.119}$$

The screened potential is in turn related to the induced density via

$$V_{\rm sc}(\boldsymbol{q},\omega) = V_{\rm ext}(\boldsymbol{q},\omega) + \sum_{\boldsymbol{q}'} v(\boldsymbol{q},\boldsymbol{q}',\omega) n_1(\boldsymbol{q}',\omega) \ , \tag{3.120}$$

where $V_{\rm ext}(\boldsymbol{q},\omega)$ is the external potential and $v(\boldsymbol{q},\boldsymbol{q}',\omega)$ is the Fourier transform of the electron-electron interaction potential. For example, $v(\boldsymbol{q},\boldsymbol{q}',\omega) = \delta_{\boldsymbol{q},\boldsymbol{q}'} 2\pi e^2/[q\bar{\epsilon}(\omega)]$ for a 2D electron system ($q = |\boldsymbol{q}|$) surrounded by a homogeneous and isotropic dielectric, with a frequency-dependent permittivity $\bar{\epsilon}(\omega)$. The interaction potential $v(\boldsymbol{q},\boldsymbol{q}',\omega)$ accounts for all screening effects stemming from nearby dielectrics. Note that we are neglecting retardation effects ($c = \infty$).

Plasmons are self-sustained charge density oscillations that occur in absence of an external field. They correspond to non-trivial solutions of the integral equation

$$\sum_{\boldsymbol{q}'} \epsilon(\boldsymbol{q},\boldsymbol{q}',\omega) V_{\rm sc}(\boldsymbol{q}',\omega) = 0 \ , \tag{3.121}$$

where we have introduced the dynamical dielectric function:

$$\epsilon(\boldsymbol{q},\boldsymbol{q}',\omega) = \delta_{\boldsymbol{q},\boldsymbol{q}'} - \sum_{\boldsymbol{q}''} v(\boldsymbol{q},\boldsymbol{q}'',\omega)\tilde{\chi}_{nn}(\boldsymbol{q}'',\boldsymbol{q}',\omega) \ . \tag{3.122}$$

For electron systems that are invariant under spatial translations, $\tilde{\chi}_{nn}(\boldsymbol{q},\boldsymbol{q}',\omega) = \delta_{\boldsymbol{q},\boldsymbol{q}'}\tilde{\chi}_{nn}(\boldsymbol{q},\omega)$, $v(\boldsymbol{q},\boldsymbol{q}',\omega) = \delta_{\boldsymbol{q},\boldsymbol{q}'}v(\boldsymbol{q},\omega)$, and Eq. (3.121) reduces to the familiar equation [35]

$$\left[1 - v(\boldsymbol{q},\omega)\tilde{\chi}_{nn}(\boldsymbol{q},\omega)\right] V_{\rm sc}(\boldsymbol{q},\omega) \equiv \epsilon(\boldsymbol{q},\omega) V_{\rm sc}(\boldsymbol{q},\omega) = 0 \ . \tag{3.123}$$

The solutions of Eq. (3.123) for $V_{\rm sc}(\boldsymbol{q},\omega)$ are delta functions peaked at the zeroes of $\epsilon(\boldsymbol{q},\omega)$ and correspond to *plane waves* in real space.

### 3.2.2 Lippmann-Schwinger theory for 2D plasmons

We now specialize Eq. (3.121) to describe the scattering of a plasmon off a spatially-localized inhomogeneity in the 2D electron system. We consider two types of inhomogeneities: (a) one that is localized inside a circle of radius $a$ around the origin and (b) one that is invariant under spatial translations in one direction (the $\hat{\boldsymbol{y}}$ direction) and is confined to a strip of finite width $2a$ in the $\hat{\boldsymbol{x}}$ direction, i.e. for $-a < x < a$. These are sketched in Fig. 3.1(a) and (b), respectively.

We now write the proper density-density response function $\tilde{\chi}_{nn}(\boldsymbol{q},\boldsymbol{q}',\omega)$ as the sum of a homogeneous part $\tilde{\chi}_{\rm h}(q,\omega)\delta_{\boldsymbol{q},\boldsymbol{q}'}$, plus a perturbation $\delta\tilde{\chi}(\boldsymbol{q},\boldsymbol{q}',\omega)$, the latter describing the inhomogeneity present in the 2D electron system:

$$\tilde{\chi}_{nn}(\boldsymbol{q},\boldsymbol{q}',\omega) = \tilde{\chi}_{\rm h}(q,\omega)\delta_{\boldsymbol{q},\boldsymbol{q}'} + \frac{1}{S}\delta\tilde{\chi}(\boldsymbol{q},\boldsymbol{q}',\omega) \ . \tag{3.124}$$

Here, $S = L_x L_y$ is the 2D electron system area. In writing the above equation we assumed, for the sake of simplicity, that the 2D electron system in the absence of perturbations is homogeneous and isotropic—this implies that the homogeneous part $\tilde{\chi}_{\rm h}(q,\omega)$ of the density-density response function depends only on $q = |\boldsymbol{q}|$.

In what follows, we introduce, without loss of generality, the following parametrization of the uniform part of the proper density-density response function:

$$\tilde{\chi}_{\rm h}(q,\omega) = \frac{D}{e^2\pi}\frac{q^2}{\omega^2}\mathcal{G}(q,\omega) \ , \tag{3.125}$$

where $D$ is the so-called Drude weight [219] and $\mathcal{G}(q,\omega)$ is a correction factor that takes into account all the effects beyond simple Drude theory, including *nonlocal* effects.

Similarly, we split the interaction potential into two parts:

$$v(\boldsymbol{q},\boldsymbol{q}',\omega) = \delta_{\boldsymbol{q},\boldsymbol{q}'}v(q,\omega) + \frac{1}{S}\delta v(\boldsymbol{q},\boldsymbol{q}',\omega) \ , \tag{3.126}$$

where

$$v(q,\omega) = \frac{2\pi e^2}{\bar{\epsilon}(\omega)q}\mathcal{F}(q,\omega) \tag{3.127}$$

represents the homogeneous part of the interaction, which does not depend on the direction of $\boldsymbol{q}$, while $\delta v(\boldsymbol{q},\boldsymbol{q}',\omega)$ stems from an inhomogeneity in the dielectric environment surrounding the 2D electron system.

In Eq. (3.127), $\bar{\epsilon}(\omega)$ is a suitable frequency-dependent permittivity and $\mathcal{F}(q,\omega)$ is a form factor that takes into account deviations from the pure 2D Coulomb law [35] $2\pi e^2/q$. These may occur in quantum wells of GaAs/AlGaAs where $\mathcal{F}$ takes into account the finite thickness of the quantum well and its geometric form [220] or in graphene sheets encapsulated between slabs of hBN crystals, where $\mathcal{F}$ captures effects stemming from the finite thickness of hBN [221].

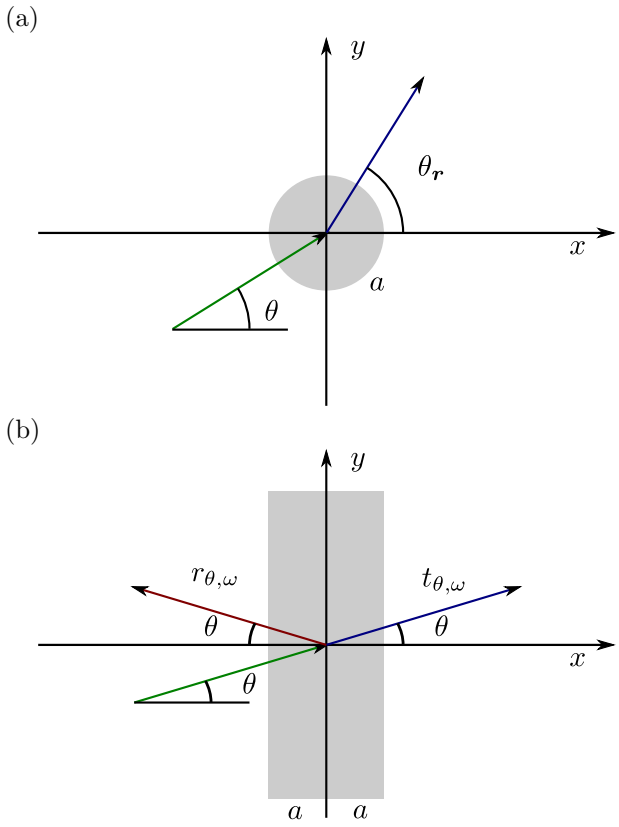


Figure 3.1: The two scattering geometries considered in this work. In panel (a), the perturbation is localized within a circle of radius $a$ (grey-shaded area). In panel (b), the perturbation is confined in the rectangular strip $-a < x < a$ (grey-shaded area). Translational invariance is assumed in the $\hat{\boldsymbol{y}}$ direction. The perturbations $\delta\tilde{\chi}(\boldsymbol{r}, \boldsymbol{r}', \omega)$ and $\delta v(\boldsymbol{r}, \boldsymbol{r}', \omega)$ introduced in the main text in Eqs. (3.128)-(3.129) are negligible if either $\boldsymbol{r}$ or $\boldsymbol{r}'$ lie outside the scattering region.

In real space, Eqs. (3.124) and (3.126) read as following:

$$\tilde{\chi}_{nn}(\boldsymbol{r},\boldsymbol{r}',\omega) = \tilde{\chi}_{\rm h}(|\boldsymbol{r}-\boldsymbol{r}'|,\omega) + \frac{1}{S}\delta\tilde{\chi}(\boldsymbol{r},\boldsymbol{r}',\omega) \tag{3.128}$$

and

$$v(\boldsymbol{r},\boldsymbol{r}',\omega) = v(|\boldsymbol{r}-\boldsymbol{r}'|,\omega) + \frac{1}{S}\delta v(\boldsymbol{r},\boldsymbol{r}',\omega)\ . \tag{3.129}$$

We assume that the perturbations $\delta\tilde{\chi}(\boldsymbol{r},\boldsymbol{r}',\omega)$ and $\delta v(\boldsymbol{r},\boldsymbol{r}',\omega)$ are negligible if either $\boldsymbol{r}$ or $\boldsymbol{r}'$ lie outside the scattering region, see Fig. 3.1.

We now introduce the homogeneous part of the dielectric function

$$\epsilon_{\rm h}(q,\omega) \equiv 1 - v(q,\omega)\tilde{\chi}_{\rm h}(q,\omega) = 1 - \frac{2D}{\bar{\epsilon}(\omega)\omega^2}q\mathcal{F}(q,\omega)\mathcal{G}(q,\omega)\ , \tag{3.130}$$

the inverse of the effective interaction

$$W_{\rm h}^{-1}(q,\omega) \equiv \frac{\epsilon_{\rm h}(q,\omega)}{v(q,\omega)} = \frac{q\bar{\epsilon}(\omega)}{2\pi e^2\mathcal{F}(q,\omega)}\left[1 - \frac{2D}{\bar{\epsilon}(\omega)\omega^2}q\mathcal{F}(q,\omega)\mathcal{G}(q,\omega)\right]\ , \tag{3.131}$$

and the *scattering kernel*

$$\Delta(\boldsymbol{q},\boldsymbol{q}',\omega) \equiv \delta\tilde{\chi}(\boldsymbol{q},\boldsymbol{q}',\omega) + \frac{\delta v(\boldsymbol{q},\boldsymbol{q}',\omega)}{v(q,\omega)}\tilde{\chi}_{\rm h}(q',\omega) + \frac{1}{S}\sum_{\boldsymbol{q}''}\frac{\delta v(\boldsymbol{q},\boldsymbol{q}'',\omega)}{v(q,\omega)}\delta\tilde{\chi}(\boldsymbol{q}'',\boldsymbol{q}',\omega)\ . \tag{3.132}$$

Note that Eq. (3.132) establishes a crucial relationship between scattering theory and microscopic many-body theory, which can be used to calculate the response function $\delta\tilde{\chi}(\boldsymbol{q},\boldsymbol{q}',\omega)$ of the inhomogeneous 2D electron system that appears in Eq. (3.132).

With these definitions, we can rewrite Eq. (3.121) in the following appealing manner:

$$W_{\rm h}^{-1}(q,\omega)V_{\rm sc}(\boldsymbol{q},\omega) = \frac{1}{S}\sum_{\boldsymbol{q}'}\Delta(\boldsymbol{q},\boldsymbol{q}',\omega)V_{\rm sc}(\boldsymbol{q}',\omega)\ . \tag{3.133}$$

Eq. (3.133) closely resembles the momentum-space version of Schrödinger's equation for an electron of mass $m$ in a generic *nonlocal* potential $U(\boldsymbol{q},\boldsymbol{q}')$:

$$\left(E - \frac{\hbar^2q^2}{2m}\right)\psi(\boldsymbol{q}) = \frac{1}{S}\sum_{\boldsymbol{q}'}U(\boldsymbol{q},\boldsymbol{q}')\psi(\boldsymbol{q}')\ . \tag{3.134}$$

Comparing Eq. (3.133) with Eq. (3.134), we clearly see that $W_{\rm h}^{-1}(q,\omega)$ plays the role of $E-\hbar^2q^2/(2m)$, $\Delta(\boldsymbol{q},\boldsymbol{q}',\omega)$ plays the role of the scattering potential $U(\boldsymbol{q},\boldsymbol{q}')$, and $V_{\rm sc}(\boldsymbol{q},\omega)$ is the analogue of the wave-function $\psi(\boldsymbol{q})$.

In the following, we assume that the unperturbed system has a single plasmon mode at a given frequency $\omega$. This means that $\epsilon_{\rm h}(q,\omega)$ has only one zero as a function of $q$ for any given $\omega$. This allows us to unambiguously define the *plasmon wavevector* of the homogeneous system as the solution $q_{\rm pl} = q_{\rm pl}(\omega)$ of the following equation:

$$\epsilon_{\rm h}(q_{\rm pl},\omega) = 0\ . \tag{3.135}$$

Our theory can be easily extended to anisotropic media, for which $q_{\rm pl}$ depends on the propagation direction, and to take into account the presence of multiple plasmon modes at a given frequency.

For the geometry in Fig. 3.1(a) and just as in the case of single-particle quantum-mechanical scattering theory [218], we are interested in solutions of Eq. (3.133) whose *asymptotic* behavior is given by the sum of an incoming plane wave plus a scattered wave:

$$V_{\rm sc}(\boldsymbol{r},\omega) \simeq e^{i\boldsymbol{q}_{\rm pl}\cdot\boldsymbol{r}} + \frac{e^{iq_{\rm pl}r}}{\sqrt{r}}f(\theta_{\boldsymbol{r}},\theta,\omega)\ , \tag{3.136}$$

where $\boldsymbol{q}_{\rm pl} \equiv q_{\rm pl}[\hat{\boldsymbol{x}}\cos(\theta) + \hat{\boldsymbol{y}}\sin(\theta)]$, $\theta$ is the polar angle of the wavevector of the incoming wave, $\theta_{\boldsymbol{r}}$ is the polar angle of $\boldsymbol{r}$, and $f(\theta_{\boldsymbol{r}},\theta,\omega)$ is the scattering amplitude induced by the inhomogeneity.

For the geometry in Fig. 3.1(b), which is translationally invariant along the $\hat{\boldsymbol{y}}$ direction, the required asymptotic behavior is given by

$$V_{\rm sc}(\boldsymbol{r},\omega) \simeq e^{iq_{\rm pl}\sin(\theta)y} \times \begin{cases} e^{iq_{\rm pl}\cos(\theta)x} + r_{\theta,\omega}e^{-iq_{\rm pl}\cos(\theta)x}, & \text{for } x \to -\infty \\ t_{\theta,\omega}e^{iq_{\rm pl}\cos(\theta)x}, & \text{for } x \to +\infty \end{cases} , \tag{3.137}$$

where $\theta$ is the angle between the wavevector of the incoming wave and the $\hat{\boldsymbol{x}}$ axis, while $r_{\theta,\omega}$ and $t_{\theta,\omega}$ are the reflection and transmission coefficients, respectively.

The asymptotic behaviors (3.136) and (3.137) can be more easily enforced using a formalism *à la* Lippmann-Schwinger [218]. Indeed, we claim that a solution of

$$V_{\rm sc}(\boldsymbol{q},\omega) = V^{(0)}(\boldsymbol{q},\omega) + W_{\rm h}(q,\omega)\frac{1}{S}\sum_{\boldsymbol{q}'}\Delta(\boldsymbol{q},\boldsymbol{q}',\omega)V_{\rm sc}(\boldsymbol{q}',\omega) , \tag{3.138}$$

with $V^{(0)}(\boldsymbol{q},\omega)$ satisfying

$$\epsilon_{\rm h}(q,\omega)V^{(0)}(\boldsymbol{q},\omega) = 0 \tag{3.139}$$

and $W_{\rm h}(q,\omega)$ satisfying the *distributional* equation

$$W_{\rm h}(q,\omega)\frac{\epsilon_{\rm h}(q,\omega)}{v(q,\omega)} = 1 , \tag{3.140}$$

is also a solution of Eq. (3.133).

To prove our assertion, it is sufficient to multiply Eq. (3.138) by $W_{\rm h}^{-1}(q,\omega)$ and use Eqs. (3.139)-(3.140). Eq. (3.138) is the desired Lippmann-Schwinger equation for 2D plasmon scattering.

The solutions of Eqs. (3.139)-(3.140) are not unique. To impose the asymptotic conditions (3.136)-(3.137), we choose: i) $V^{(0)}$ as a delta function in wavevector space (a plane wave in real space):

$$V^{(0)}(\boldsymbol{q},\omega) = (2\pi)^2\delta(\boldsymbol{q}-\boldsymbol{q}_{\rm pl}) , \tag{3.141}$$

which corresponds to the first term in Eqs. (3.136)-(3.137), and ii) the solution of Eq. (3.140) corresponding to an outgoing cylindrical wave. As shown in Appendix E.1, the solution of Eq. (3.140) corresponding to an outgoing cylindrical wave is:

$$W_{\rm h}^{(+)}(q,\omega) \equiv \frac{1}{W_{\rm h}^{-1}(q,\omega)+i0^+} = \mathcal{P}\frac{1}{W_{\rm h}^{-1}(q,\omega)} - i\pi C(\omega)\delta(q-q_{\rm pl}) , \tag{3.142}$$

where

$$C(\omega) = \lim_{q\to q_{\rm pl}}\frac{q_{\rm pl}-q}{W_{\rm h}^{-1}(q,\omega)} = \frac{2\pi e^2\mathcal{F}(q_{\rm pl},\omega)}{\bar{\epsilon}(\omega)\left[1+q_{\rm pl}\frac{\mathcal{F}'(q_{\rm pl},\omega)}{\mathcal{F}(q_{\rm pl},\omega)}+q_{\rm pl}\frac{\mathcal{G}'(q_{\rm pl},\omega)}{\mathcal{G}(q_{\rm pl},\omega)}\right]} . \tag{3.143}$$

Here, $\mathcal{F}'(q,\omega) \equiv \partial\mathcal{F}(q,\omega)/\partial q$ and $\mathcal{G}'(q,\omega) \equiv \partial\mathcal{G}(q,\omega)/\partial q$.

With these definitions we can separate the effective interaction into a *universal* function of $q$ plus a correction $\mathcal{W}(q,\omega)$:

$$W_{\rm h}^{(+)}(q,\omega) = \frac{C(\omega)}{q_{\rm pl}}\left[\mathcal{P}\frac{1}{1-\frac{q}{q_{\rm pl}}} - i\pi\delta\left(1-\frac{q}{q_{\rm pl}}\right)+\frac{q_{\rm pl}}{q}+\mathcal{W}(q,\omega)\right] , \tag{3.144}$$

where

$$\mathcal{W}(q,\omega) = \frac{\mathcal{F}(q,\omega)\left[\mathcal{F}(q_{\rm pl},\omega)\mathcal{G}(q_{\rm pl},\omega)+q_{\rm pl}\mathcal{F}'(q_{\rm pl},\omega)\mathcal{G}(q_{\rm pl},\omega)+q_{\rm pl}\mathcal{F}(q_{\rm pl},\omega)\mathcal{G}'(q_{\rm pl},\omega)\right]}{\mathcal{F}(q_{\rm pl},\omega)\frac{q}{q_{\rm pl}}\left[\mathcal{F}(q_{\rm pl},\omega)\mathcal{G}(q_{\rm pl},\omega)-\frac{q}{q_{\rm pl}}\mathcal{F}(q,\omega)\mathcal{G}(q,\omega)\right]} - \frac{q_{\rm pl}}{q_{\rm pl}-q} - \frac{q_{\rm pl}}{q} . \tag{3.145}$$

Note that $\mathcal{W}(q,\omega)$ vanishes identically if *both* $\mathcal{F}(q,\omega)$ and $\mathcal{G}(q,\omega)$ are set to one.

Since the intensity associated with a travelling plasmon with a fixed wavevector is proportional to the square of its potential, the information about the flux of energy is carried by the modulus square of the scattering amplitude $|f(\theta_{\boldsymbol{r}},\theta,\omega)|^2$ in the geometry of Fig 3.1(a) and by the square modulus of $r_{\theta,\omega}$ and $t_{\theta,\omega}$ in the geometry of Fig 3.1(b). More precisely the ratio between the amount of power scattered

into a small angle $d\theta$ around $\theta_{\boldsymbol{r}}$ and the intensity (i.e. power per unit length) of the incoming wave is $|f(\theta_{\boldsymbol{r}},\theta,\omega)|^2 d\theta$. The total scattered power divided by the intensity of the original wave is given by the total cross section

$$\Sigma(\theta,\omega) \equiv \int_{-\pi}^{\pi} d\theta_{\boldsymbol{r}} |f(\theta_{\boldsymbol{r}},\theta,\omega)|^2 \ . \tag{3.146}$$

In rotationally invariant system $\Sigma(\theta,\omega)$ obviously does not depend on the angle $\theta$ and is a function of $\omega$ only.

### 3.2.3 Going beyond the RPA

The simplest way of transcending the RPA [35] (i.e. the time-dependent Hartree approximation discussed in Sect. B.1) consists in using time-dependent density-functional theory (TDDFT) [35, 222]. This theory is appealing since, as we proceed to show, it requires very little modifications of our scattering equations.

We define the Kohn-Sham response function [35]

$$\chi^{\mathrm{KS}}_{nn}(\boldsymbol{q},\boldsymbol{q}',\omega) \equiv \frac{1}{S}\sum_{\alpha,\beta} \frac{(f_\alpha - f_\beta)\langle\alpha|n_{\boldsymbol{q}}|\beta\rangle\langle\beta|n_{-\boldsymbol{q}'}|\alpha\rangle}{\hbar\omega + \epsilon_\alpha - \epsilon_\beta + i\eta} \ , \tag{3.147}$$

where $|\alpha\rangle$, $\epsilon_\alpha$ are eigenstates and eigenvalues of the self-consistent Kohn-Sham Hamiltonian [35]. The density perturbation generated by an external field is given by [35, 222]

$$n_1(\boldsymbol{q},\omega) = \sum_{\boldsymbol{q}'} \chi^{\mathrm{KS}}_{nn}(\boldsymbol{q},\boldsymbol{q}',\omega)\Big\{V_{\mathrm{ext}}(\boldsymbol{q}',\omega) + \sum_{\boldsymbol{q}''}\left[v(\boldsymbol{q}',\boldsymbol{q}'',\omega) + f_{\mathrm{xc,L}}(\boldsymbol{q}',\boldsymbol{q}'',\omega)\right] n_1(\boldsymbol{q}'',\omega)\Big\} \ . \tag{3.148}$$

The first term in curly brackets is the response of the non-interacting Kohn-Sham electron system, while the second and third terms stem from the time variation of the Hartree and exchange-correlation potentials, respectively. The quantity $f_{\mathrm{xc,L}}(\boldsymbol{q}',\boldsymbol{q}'',\omega)$ is the wavevector- and frequency-dependent (longitudinal) exchange-correlation kernel [35]. We now introduce—cf. Eqs. (3.124) and (3.126)—the following decompositions:

$$\chi^{\mathrm{KS}}_{nn}(\boldsymbol{q},\boldsymbol{q}',\omega) = \delta_{\boldsymbol{q},\boldsymbol{q}'}\chi_0(q,\omega) + \frac{1}{S}\delta\chi^{\mathrm{KS}}_{nn}(\boldsymbol{q},\boldsymbol{q}',\omega) \ , \tag{3.149}$$

and

$$f_{\mathrm{xc,L}}(\boldsymbol{q},\boldsymbol{q}',\omega) = \delta_{\boldsymbol{q},\boldsymbol{q}'} f_{\mathrm{xc,h}}(q,\omega) + \frac{1}{S}\delta f_{\mathrm{xc}}(\boldsymbol{q},\boldsymbol{q}',\omega) \ . \tag{3.150}$$

In writing Eq. (3.149) we used the fact that the homogeneous part of the Kohn-Sham response function coincides with the non-interacting response function $\chi_0(q,\omega)$ of the homogeneous electron system in absence of perturbation.

Comparing Eq. (3.148) with Eqs. (3.119)-(3.120), it is straightforward to show that the TDDFT version of our Lippmann-Schwinger scattering theory can be written down with the following replacements:

$$\tilde{\chi}_{\mathrm{h}}(q,\omega) \mapsto \chi_0(q,\omega) \ , \tag{3.151}$$

$$\delta\tilde{\chi}(\boldsymbol{q},\boldsymbol{q}',\omega) \mapsto \delta\chi^{\mathrm{KS}}_{nn}(\boldsymbol{q},\boldsymbol{q}',\omega) \ , \tag{3.152}$$

$$\epsilon_{\mathrm{h}}(q,\omega) \mapsto 1 - \left[v(q,\omega) + f_{\mathrm{xc,h}}(q,\omega)\right]\chi_0(q,\omega) \ , \tag{3.153}$$

$$\Delta(\boldsymbol{q},\boldsymbol{q}',\omega) \mapsto \Delta(\boldsymbol{q},\boldsymbol{q}',\omega) + \Delta_{\mathrm{xc}}(\boldsymbol{q},\boldsymbol{q}',\omega) \ , \tag{3.154}$$

where

$$\Delta_{\mathrm{xc}}(\boldsymbol{q},\boldsymbol{q}',\omega) = \frac{f_{\mathrm{xc,h}}(q,\omega)}{v(q,\omega)}\delta\chi^{\mathrm{KS}}_{nn}(\boldsymbol{q},\boldsymbol{q}',\omega) + \frac{\delta f_{\mathrm{xc}}(\boldsymbol{q},\boldsymbol{q}',\omega)}{v(q,\omega)}\chi_0(q',\omega) + \frac{1}{S}\sum_{\boldsymbol{q}''}\frac{\delta f_{\mathrm{xc}}(\boldsymbol{q},\boldsymbol{q}'',\omega)}{v(q,\omega)}\delta\chi^{\mathrm{KS}}_{nn}(\boldsymbol{q}'',\boldsymbol{q}',\omega) \ . \tag{3.155}$$

Explicit calculations of the scattering kernel $\Delta_{\mathrm{xc}}(\boldsymbol{q},\boldsymbol{q}',\omega)$ requite explicit expressions for the exchange-correlation kernel $f_{\mathrm{xc,L}}(\boldsymbol{q},\boldsymbol{q}',\omega)$ of the inhomogeneous electron system. To this aim, we refer the reader to Ref. [35] and references therein.

### 3.2.4 Transition Function

We now turn to relate the scattering amplitude $f(\theta_{\boldsymbol{r}}, \theta, \omega)$ and the reflection and transmission coefficients $r_{\theta,\omega}$ and $t_{\theta,\omega}$ to the solutions of Eq. (3.138). To this end, it is useful to define the *transition function* $T$. Since the final results are slightly different for the two scattering geometries in Figs. 3.1(a) and (b), we split the discussion into two separate parts, in Sects. 3.2.4 and 3.2.4, respectively.

**Geometry in Fig. 3.1(a)**

In this geometry, the transition function is defined by

$$T(\boldsymbol{q}, \theta, \omega) \equiv \frac{1}{S} \sum_{\boldsymbol{q}'} \Delta(\boldsymbol{q}, \boldsymbol{q}', \omega) V_{\rm sc}(\boldsymbol{q}', \omega) \ , \tag{3.156}$$

where $V_{\rm sc}(\boldsymbol{q}, \omega)$ is the solution of Eq. (3.138) with $V^{(0)}(\boldsymbol{q}, \omega)$ given by (3.141) and effective interaction given by (3.142). Note that $T$ is a function of a reciprocal vector $\boldsymbol{q}$, of an angle $\theta$ giving the direction of the incoming wave, and of the frequency $\omega$.

The transition function satisfies the following integral equation

$$T(\boldsymbol{q}, \theta, \omega) = \Delta(\boldsymbol{q}, \boldsymbol{q}_{\rm pl}, \omega) + \frac{1}{S} \sum_{\boldsymbol{q}'} \Delta(\boldsymbol{q}, \boldsymbol{q}', \omega) W_{\rm h}^{(+)}(q', \omega) T(\boldsymbol{q}', \theta, \omega) \ , \tag{3.157}$$

as one can easily verify by inserting Eq. (3.138) in Eq. (3.156).

To make a link between the transition function and the scattering amplitude $f(\theta_{\boldsymbol{r}}, \theta, \omega)$ we must consider the asymptotic behavior of Eq. (3.138) in real space. This is carefully considered in Appendix E.2. The final result is

$$f(\theta_{\boldsymbol{r}}, \theta, \omega) = -\frac{e^{i\frac{\pi}{4}}}{\sqrt{2\pi}} \sqrt{q_{\rm pl}} C(\omega) T(q_{\rm pl} \hat{\boldsymbol{r}}, \theta, \omega) \ . \tag{3.158}$$

**Geometry in Fig. 3.1(b)**

Since this geometry is translationally invariant in the $\hat{\boldsymbol{y}}$ direction, we can rewrite the scattering kernel (3.132) as

$$\Delta(\boldsymbol{q}, \boldsymbol{q}', \omega) = 2\pi \delta(q_y - q'_y) \Delta(q_x, q'_x, q_y, \omega) \ . \tag{3.159}$$

Eq. (3.138) then becomes

$$V_{\rm sc}(q_x, q_y, \omega) = V^{(0)}(q_x, q_y, \omega) + W_{\rm h}^{(+)}\left(\sqrt{q_x^2 + q_y^2}, \omega\right) \frac{1}{L_x} \sum_{q'_x} \Delta(q_x, q'_x, q_y, \omega) V_{\rm sc}(q'_x, q_y, \omega) \ , \tag{3.160}$$

where $L_x$ has been defined after Eq. (3.124).

We now separate the two components of Eq. (3.141):

$$V^{(0)}(q_x, q_y) = (2\pi)^2 \delta(q_y - q_{\rm pl} \sin(\theta)) \delta(q_x - q_{\rm pl} \cos(\theta)) \ . \tag{3.161}$$

Because of translational invariance in the $\hat{\boldsymbol{y}}$ direction, we can take the solution to have the form

$$V_{\rm sc}(q_x, q_y, \omega) = 2\pi \delta(q_y - q_{\rm pl} \sin(\theta)) V_{\rm sc}(q_x, \theta, \omega) \ . \tag{3.162}$$

The Lippmann-Schwinger equation (3.138) then becomes

$$V_{\rm sc}(q_x, \theta, \omega) = 2\pi \delta(q_x - q_{\rm pl} \cos\theta) + W_{\rm h}^{(+)}\left(\sqrt{q_x^2 + q_{\rm pl}^2 \sin^2\theta}, \omega\right) \frac{1}{L_x} \sum_{q'_x} \Delta(q_x, q'_x, q_{\rm pl} \sin\theta, \omega) V_{\rm sc}(q'_x, \theta, \omega) \ . \tag{3.163}$$

In analogy to Eq. (3.156), we define

$$T(q_x, \theta, \omega) \equiv \frac{1}{L_x} \sum_{q'_x} \Delta(q_x, q'_x, q_{\rm pl} \sin(\theta), \omega) V_{\rm sc}(q'_x, \theta, \omega) \ , \tag{3.164}$$

which satisfies the following integral equation:

$$T(q_x,\theta,\omega) = \Delta(q_x, q_{\rm pl}\cos(\theta), q_{\rm pl}\sin(\theta),\omega) + \frac{1}{L_x}\sum_{q_x'} \Delta(q_x, q_x', q_{\rm pl}\sin(\theta),\omega) W_{\rm h}^{(+)}\left(\sqrt{q_x'^2 + q_{\rm pl}^2\sin^2(\theta)},\omega\right) T(q_x',\theta,\omega)\ . \tag{3.165}$$

This is the equation we solved numerically in the geometry (b) described in Section 3.2.9.

Using the asymptotic behavior of Eq. (3.163)—see Appendix E.2—and comparing the result to Eq. (3.137), we finally obtain:

$$t_{\theta,\omega} = 1 - i\frac{C(\omega)}{\cos(\theta)} T(q_{\rm pl}\cos(\theta),\theta,\omega) \tag{3.166}$$

and

$$r_{\theta,\omega} = -i\frac{C(\omega)}{\cos(\theta)} T(-q_{\rm pl}\cos(\theta),\theta,\omega)\ . \tag{3.167}$$

In the theory of single-particle quantum-mechanical scattering [218] the analytical continuation of the transition function into the upper half of the complex plane can display poles at purely imaginary values of the wavevector corresponding to the energies of single-particle bound states. Similarly, for the case of plasmon scattering, a localized plasmon resonance—i.e. a solution of Eq. (3.121) that decays exponentially, in real space, far from the perturbation—manifests as a pole in the transition function $T(q_x,\theta,\omega)$ at a purely imaginary value of $q_x$.

### 3.2.5 Optical theorem

In this Section we derive a useful relation between the amplitude of forward scattering (i.e. scattering in the same direction of the incoming wave) and the total scattering cross section. In the context of electromagnetic scattering, this is known as "optical theorem". It holds if dissipation can be neglected during the scattering process. Once again, we split the derivation into two parts, depending on the scattering geometry.

#### Geometry in Fig. 3.1(a)

Using Eq. (3.156), we can write the imaginary part of the transition function for the forward scattering process as

$$\begin{aligned}\Im m\left\{T(\boldsymbol{q}_{\rm pl},\theta,\omega)\right\} &= \Im m\left\{\frac{1}{S}\sum_{\boldsymbol{q}'}\Delta(\boldsymbol{q}_{\rm pl},\boldsymbol{q}',\omega)V_{\rm sc}(\boldsymbol{q}',\omega)\right\}\\ &= \Im m\left\{\frac{1}{S}\sum_{\boldsymbol{q}'}\int d^2\boldsymbol{q}\,\delta(\boldsymbol{q}-\boldsymbol{q}_{\rm pl})\Delta(\boldsymbol{q},\boldsymbol{q}',\omega)V_{\rm sc}(\boldsymbol{q}',\omega)\right\}\ .\end{aligned} \tag{3.168}$$

We can rewrite the delta function using the complex conjugate of the Lippmann-Schwinger equation (3.138), and Eqs. (3.141), (3.142), and (3.156):

$$\delta(\boldsymbol{q}-\boldsymbol{q}_{\rm pl}) = \frac{1}{(2\pi)^2}V_{\rm sc}^*(\boldsymbol{q},\omega) - \frac{1}{(2\pi)^2}\left[\mathcal{P}\frac{1}{W_{\rm h}^{-1}(q,\omega)} + i\pi C(\omega)\delta(q-q_{\rm pl})\right] T^*(\boldsymbol{q},\theta,\omega)\ . \tag{3.169}$$

Substituting Eq. (3.169) into Eq. (3.168) we get

$$\begin{aligned}\Im m\left\{T(\boldsymbol{q}_{\rm pl},\theta,\omega)\right\} &= -\frac{C(\omega)}{4\pi}\int d\boldsymbol{q}|T(\boldsymbol{q},\theta,\omega)|^2\delta(q-q_{\rm pl})\\ &\quad + \Im m\left\{\int\frac{d\boldsymbol{q}}{(2\pi)^2}\int\frac{d\boldsymbol{q}'}{(2\pi)^2}V_{\rm sc}^*(\boldsymbol{q},\omega)\Delta(\boldsymbol{q},\boldsymbol{q}',\omega)V_{\rm sc}(\boldsymbol{q}',\omega)\right\}\\ &= -\frac{C(\omega)q_{\rm pl}}{4\pi}\int d\theta'|T(q_{\rm pl}[\hat{\boldsymbol{x}}\cos\theta' + \hat{\boldsymbol{y}}\sin\theta'],\theta,\omega)|^2\ .\end{aligned} \tag{3.170}$$

The term in the second line of the previous equation is proportional to the power absorbed by the inhomogeneous electron system [35] and can therefore be neglected if dissipation is small.

Making use of Eqs. (3.146-3.158) this relation can be recast in the form of an optical theorem [218]

$$\Im m\left\{\frac{2\sqrt{2\pi}e^{-i\frac{\pi}{4}}}{\sqrt{q_{\rm pl}}}f(\theta,\theta,\omega)\right\}=\Sigma(\theta,\omega)\ . \tag{3.171}$$

**Geometry in Fig. 3.1(b)**

Following the same steps as those in Sect. 3.2.5, we derive a very similar relation for the forward-scattering transition function in the geometry sketched in Fig. 3.1(b):

$$\Im m\left\{T(q_{\rm pl}\cos\theta,\theta,\omega)\right\}=-\frac{C(\omega)}{2}\int dq_x|T(q_x,\theta,\omega)|^2\delta\left(\sqrt{q_{\rm pl}^2\sin^2\theta-q_x^2}-q_{\rm pl}\right)\ . \tag{3.172}$$

Using the definitions in Eqs. (3.166) and (3.167) we get

$$|r_{\theta,\omega}|^2+|t_{\theta,\omega}|^2=1\ . \tag{3.173}$$

The latter simply expresses conservation of energy in absence of dissipation.

### 3.2.6 The Born approximation

In this Section we discuss the Born approximation for the two geometries of interest in this work.

**Geometry in Fig. 3.1(a)**

Eq. (3.157) can be handled exactly in a numerical fashion, as we will discuss below, provided that the scattering kernel $\Delta(\boldsymbol{q},\boldsymbol{q}',\omega)$ is known. In this Section, however, we wish to introduce an approximate perturbative approach in powers of $\Delta(\boldsymbol{q},\boldsymbol{q}',\omega)$, which is usually termed "Born approximation" in ordinary single-particle quantum-mechanical scattering theory [218].

We start by writing the transition function as a power series:

$$T(\boldsymbol{q},\theta,\omega)\equiv\sum_{n=1}^{\infty}\lambda^n T^{(n)}(\boldsymbol{q},\theta,\omega)\ , \tag{3.174}$$

where $\lambda$ is a dimensionless bookkeeping parameter, which will be set to unity at the end of calculation. We also multiply the kernel $\Delta(\boldsymbol{q},\boldsymbol{q}',\omega)$ in Eq. (3.157) by the same parameter $\lambda$. The equation for the transition function becomes

$$\sum_{n=1}^{\infty}\lambda^n T^{(n)}(\boldsymbol{q},\theta,\omega)=\lambda\Delta(\boldsymbol{q},\boldsymbol{q}_{\rm pl},\omega)+\frac{1}{S}\sum_{\boldsymbol{q}'}\lambda\Delta(\boldsymbol{q},\boldsymbol{q}',\omega)W_{\rm h}^{(+)}(q',\omega)\sum_{n=1}^{\infty}\lambda^n T^{(n)}(\boldsymbol{q}',\theta,\omega)\ . \tag{3.175}$$

Collecting terms that appear in Eq. (3.175) with the same power of $\lambda$ and setting $\lambda=1$, we finally obtain

$$T^{(1)}(\boldsymbol{q},\theta,\omega)=\Delta(\boldsymbol{q},\boldsymbol{q}_{\rm pl},\omega) \tag{3.176}$$

and

$$T^{(n+1)}(\boldsymbol{q},\theta,\omega)=\frac{1}{S}\sum_{\boldsymbol{q}'}\Delta(\boldsymbol{q},\boldsymbol{q}',\omega)W_{\rm h}^{(+)}(q',\omega)T^{(n)}(\boldsymbol{q}',\theta,\omega)\ , \tag{3.177}$$

for $n\geq 1$. This series yields a scattering amplitude

$$f(\theta_{\boldsymbol{r}},\theta,\omega)=\sum_{n=1}^{\infty}f^{(n)}(\theta_{\boldsymbol{r}},\theta,\omega)=-\frac{e^{i\frac{\pi}{4}}}{\sqrt{2\pi}}\sqrt{q_{\rm pl}}C(\omega)\sum_{n=1}^{\infty}T^{(n)}(q_{\rm pl}\hat{\boldsymbol{r}},\theta,\omega)\ . \tag{3.178}$$

As one can see from Eq. (3.176), the leading term of the expansion in Eq. (3.174) is particularly easy to calculate since it is simply given by the scattering kernel evaluated at the outcoming and incoming wavevectors:

$$f^{(1)}(\theta_{\boldsymbol{r}},\theta,\omega) = -\frac{e^{i\frac{\pi}{4}}}{\sqrt{2\pi}}\sqrt{q_{\rm pl}}C(\omega)\Delta(q_{\rm pl}\hat{\boldsymbol{r}},\boldsymbol{q}_{\rm pl},\omega)\ . \tag{3.179}$$

Eq. (3.179) represents the first-order Born approximation for the scattering amplitude and often represents a good starting tool to understand, at least qualitatively, the behavior of 2D plasmon scattering in a purely analytical fashion.

We note that the scattering amplitude calculated using the Born approximation does not fulfil the optical theorem (3.171), order by order. For example, the right-hand side of Eq. (3.171) calculated with $f(\theta',\theta,\omega)$ at the level of the first-order Born approximation is equal to the left-hand side of Eq. (3.171) with $f(\theta,\theta,\omega)$ calculated using the second-order Born approximation.

A natural question that arises at this point is when the Born series converges and when it is legitimate to keep only the first terms of the series. The Born approximation works well when the difference between the full solution for the screened potential $V_{\rm sc}(\boldsymbol{r},\omega)$ and the incoming wave $V^{(0)}(\boldsymbol{r},\omega)$ within the scattering region is small. Looking at the real-space formulation of the Lippmann-Schwinger equation in Appendix E.2, we can write the difference between the full solution and the incoming wave for $\boldsymbol{r}\approx\boldsymbol{0}$ as

$$\begin{aligned}|V_{\rm sc}(\boldsymbol{r}\approx\boldsymbol{0},\omega) - V^{(0)}(\boldsymbol{r}\approx\boldsymbol{0},\omega)| &\approx \left|\int d\boldsymbol{r}' W_{\rm h}^{(+)}(|\boldsymbol{r}'|,\omega)\int d\boldsymbol{r}''\frac{1}{S}\Delta(\boldsymbol{r}',\boldsymbol{r}'',\omega)V_{\rm sc}(\boldsymbol{r}'',\omega)\right| \\ &\approx \left|\int d\boldsymbol{r}' W_{\rm h}^{(+)}(|\boldsymbol{r}'|,\omega)\int d\boldsymbol{r}''\frac{1}{S}\Delta(\boldsymbol{r}',\boldsymbol{r}'',\omega)V^{(0)}(\boldsymbol{r}'',\omega)\right| = \left|\frac{1}{S}\sum_{\boldsymbol{q}} W_{\rm h}^{(+)}(q,\omega)\Delta(\boldsymbol{q},\boldsymbol{q}_{\rm pl},\omega)\right|\ .\end{aligned} \tag{3.180}$$

If the above quantity is much smaller than unity, the perturbative series converges and the Born approximation is good.

**Geometry in Fig. 3.1(b)**

In the case of the geometry in Fig. 3.1(b), we can still express the transition function as a power series

$$T(q_x,\theta,\omega) = \sum_{n=1}^{\infty} T^{(n)}(q_x,\theta,\omega) \tag{3.181}$$

with coefficients given by

$$T^{(1)}(q_x,\theta,\omega) = \Delta(q_x, q_{\rm pl}\cos(\theta), q_{\rm pl}\sin(\theta),\omega) \tag{3.182}$$

and

$$T^{(n+1)}(q_x,\theta,\omega) = \frac{1}{L_x}\sum_{q_x'}\Delta(q_x,q_x',q_{\rm pl}\sin(\theta),\omega)W_{\rm h}^{(+)}\left(\sqrt{q_{\rm pl}^2\sin^2(\theta)+q_x'^2},\omega\right)T^{(n)}(q_x',\theta,\omega)\ . \tag{3.183}$$

Transmission and reflection coefficients in the first-order Born approximation read as following:

$$t_{\theta,\omega}^{(1)} = 1 - i\frac{C(\omega)}{\cos\theta}\Delta(q_{\rm pl}\cos\theta, q_{\rm pl}\cos\theta, q_{\rm pl}\sin\theta,\omega) \tag{3.184}$$

and

$$r_{\theta,\omega}^{(1)} = -i\frac{C(\omega)}{\cos\theta}\Delta(-q_{\rm pl}\cos\theta, q_{\rm pl}\cos\theta, q_{\rm pl}\sin\theta,\omega)\ . \tag{3.185}$$

In general, these expressions do not respect the conservation law (3.173), often leading to the unphysical result $|t_{\theta,\omega}^{(1)}| > 1$. For this reason, we prefer to extract the amplitude of the transmission coefficient by using Eq. (3.173), with the reflection coefficient being extracted from Eq. (3.185).

Following the same steps as in Eq. (3.180), we obtain a similar convergence criterion:

$$\left|\frac{1}{L_x}\sum_{q_x} W_{\rm h}^{(+)}\left(\sqrt{q_x^2+q_{\rm pl}^2\sin^2(\theta)},\omega\right)\Delta(q_x,q_{\rm pl}\cos(\theta),q_{\rm pl}\sin(\theta),\omega)\right| \ll 1\ . \tag{3.186}$$

### 3.2.7 The Eikonal Approximation

In the geometry depicted in Fig. 3.1(b) it is possible to introduce the simplest approximation of the full scattering theory, i.e. the "Eikonal approximation". The latter allows the calculation of the phase of the transmission coefficient. This is the most important scattering observable in all situations in which reflection is small (i.e. when $|r_{\theta,\omega}| \ll 1$).

The eikonal approximation does not rely on the smallness of the scattering kernel $\Delta(\boldsymbol{q}, \boldsymbol{q}', \omega)$ but requires the plasmon wavelength $2\pi/q_{\rm pl}$ to be much smaller than the lengthscale over which the properties of the inhomogeneous electron liquid vary appreciably.

We lay down the derivation of this approximation under the two simplifying assumptions, which can be relaxed if necessary: (i) $\delta v(\boldsymbol{q}, \boldsymbol{q}', \omega) \equiv 0$ and (ii) $\tilde{\chi}_{nn}(\boldsymbol{q}, \boldsymbol{q}', \omega) = \boldsymbol{q} \cdot \boldsymbol{q}' D_{\boldsymbol{q}-\boldsymbol{q}'}/(Se^2\pi\omega^2)$, with $D_{\boldsymbol{q}} = 2\pi\delta(q_y)D_{q_x}$. Physically, (ii) derives from the assumption of a local conductivity model $\sigma(x) = iD(x)/(\pi\omega)$, with a Drude weight that changes spatially only along the $\hat{\boldsymbol{x}}$ direction—see Fig. 3.1(b).

We start from Eq. (3.121) and use Eq. (3.122) and assumptions (i) and (ii). Dividing by $v(q, \omega)$, we obtain

$$\frac{V_{\rm sc}(q_x, \theta, \omega)}{v(q, \omega)} = \frac{1}{\pi e^2 \omega^2} \int \frac{dq'_x}{2\pi} (q_x q'_x + q_{\rm pl}^2 \sin^2\theta) D_{q_x - q'_x} V_{\rm sc}(q'_x, \theta, \omega) \ . \tag{3.187}$$

In real space, the previous equation becomes

$$\int dx' v^{-1}(x - x', q_{\rm pl}\sin\theta, \omega) V_{\rm sc}(x', \theta, \omega) = \frac{1}{\pi e^2 \omega^2} \{-\partial_x [D(x)\partial_x V_{\rm sc}(x, \theta, \omega)] + q_{\rm pl}^2 \sin^2\theta D(x) V_{\rm sc}(x, \theta, \omega)\}, \tag{3.188}$$

where

$$v^{-1}(x, q_y, \omega) \equiv \int \frac{dq_x}{2\pi} \frac{e^{iq_x x}}{v(q, \omega)} \tag{3.189}$$

with $q = \sqrt{q_x^2 + q_y^2}$. We now introduce in Eq. (3.188) the eikonal ansatz:

$$V_{\rm sc}(x, \theta, \omega) = \exp[iq_{\rm pl}\cos\theta S(x)] \ . \tag{3.190}$$

Our target is to derive an equation for the quantity $S(x)$. We find

$$\begin{aligned} &\int dx' v^{-1}(x - x', q_{\rm pl}\sin\theta, \omega) e^{-iq_{\rm pl}\cos\theta[S(x) - S(x')]} = \\ &= \frac{1}{\pi e^2 \omega^2} \left\{ q_{\rm pl}^2 \sin^2\theta D(x) - e^{-iq_{\rm pl}\cos\theta S(x)} \ \partial_x \left[ D(x) \partial_x e^{iq_{\rm pl}\cos\theta S(x)} \right] \right\} \ . \end{aligned} \tag{3.191}$$

No approximation has been yet made in the derivation of Eq. (3.191).

When $q_{\rm pl}$ is large enough, the exponential in the integrand on the left-hand side of Eq. (3.191) oscillates rapidly. In this case, only a small range of values of $x'$ (those for which $q_{\rm pl}|x - x'| \ll 1$) contributes to the integral and we can approximate $S(x') - S(x)$ with $[dS(x)/dx](x' - x)$. The left-hand side of Eq. (3.191) can therefore be estimated as

$$\simeq \left[ v\left( q_{\rm pl} \sqrt{\cos^2\theta S'(x) + \sin^2\theta}, \omega \right) \right]^{-1} \ , \tag{3.192}$$

where $S'(x) \equiv dS(x)/dx$. The right-hand side of (3.191) is instead approximated with its leading order in the limit $q_{\rm pl} \to \infty$, reducing to

$$\simeq q_{\rm pl}^2 D(x) \{\sin^2\theta + \cos^2\theta [S'(x)]^2\} \ . \tag{3.193}$$

With these approximations, Eq. (3.191) becomes

$$q_{\rm pl} \sqrt{\cos^2\theta [S'(x)]^2 + \sin^2\theta} = q_{\rm pl}(x) \ , \tag{3.194}$$

where the *local* plasmon wavevector [216, 217] $q_{\rm pl}(x)$ is defined as the solution of

$$\frac{q_{\rm pl}^2(x) v(q_{\rm pl}(x), \omega) D(x)}{\pi e^2 \omega^2} = 1 \ . \tag{3.195}$$

The corresponding solution for the potential is, up to a multiplicative constant,

$$V_{\rm sc}(x,\theta,\omega) \propto \exp\left[ i \int_0^x dx' \sqrt{q_{\rm pl}^2(x') - q_{\rm pl}\sin^2\theta} \right] \ . \tag{3.196}$$

The phase of the transmission coefficient $t_{\theta,\omega}$ is found by looking at the difference between the the solution (3.196) and the unperturbed wave, i.e. $\exp(iq_{\rm pl}\cos\theta)$:

$$\arg(t_{\theta,\omega}) = \int_{-\infty}^{\infty} dx' \left[ \sqrt{q_{\rm pl}^2(x') - q_{\rm pl}\sin^2\theta} - q_{\rm pl}\cos\theta \right] \ . \tag{3.197}$$

### 3.2.8 The Method of Partial Waves

In this Section we introduce a decomposition of the scattering kernel and transition function in their angular components. This can be useful to treat problems with rotationally-invariant scatterers, or problems in which only a few angular components of the scattering amplitude matter.

We Fourier-decompose the incoming wave, the screened potential, the scattering kernel, and the transition function with respect to the polar angles of the relevant wavevectors:

$$V_m^{(0)}(q,\omega) = \int_{-\pi}^{\pi} \frac{d\theta_{\boldsymbol{q}}}{2\pi} e^{-im\theta_{\boldsymbol{q}}} V^{(0)}(\boldsymbol{q},\omega) \ , \tag{3.198}$$

$$V_{{\rm sc},m}(q,\omega) = \int_{-\pi}^{\pi} \frac{d\theta_{\boldsymbol{q}}}{2\pi} e^{-im\theta_{\boldsymbol{q}}} V_{\rm sc}(\boldsymbol{q},\omega) \ , \tag{3.199}$$

$$\Delta_{mm'}(q,q',\omega) = \int_{-\pi}^{\pi} \frac{d\theta_{\boldsymbol{q}}}{2\pi} \int_{-\pi}^{\pi} \frac{d\theta_{\boldsymbol{q}'}}{2\pi} e^{-im\theta_{\boldsymbol{q}}+im'\theta_{\boldsymbol{q}'}} \Delta(\boldsymbol{q},\boldsymbol{q}',\omega) \ , \tag{3.200}$$

and

$$T_{mm'}(q,\omega) = \int_{-\pi}^{\pi} \frac{d\theta_{\boldsymbol{q}}}{2\pi} \int_{-\pi}^{\pi} \frac{d\theta}{2\pi} e^{-im\theta_{\boldsymbol{q}}+im'\theta} T(\boldsymbol{q},\theta,\omega) \ . \tag{3.201}$$

With these definitions, Eq. (3.138) can be written as

$$V_{{\rm sc},m}(q,\omega) = V_m^{(0)}(q,\omega) + W_{\rm h}^{(+)}(q,\omega) \sum_{m'=-\infty}^{\infty} \int_0^{\infty} \frac{dq'}{2\pi} q' \Delta_{mm'}(q,q',\omega) V_{{\rm sc},m'}(q',\omega) \ , \tag{3.202}$$

while Eq. (3.157) becomes

$$T_{mm'}(q,\omega) = \Delta_{mm'}(q,q_{\rm pl},\omega) + \sum_{n=-\infty}^{\infty} \int_0^{\infty} \frac{dq'}{2\pi} q' \Delta_{mn}(q,q',\omega) W_{\rm h}^{(+)}(q',\omega) T_{nm'}(q',\omega) \ . \tag{3.203}$$

In Section 3.2.9 we present the results of a numerical solution this equation in a concrete situation.

Once Eq. (3.203) is solved, the scattering amplitude can be easily calculated by using

$$T(\boldsymbol{q},\theta,\omega) = \sum_{m=-\infty}^{\infty} \sum_{m'=-\infty}^{\infty} e^{im\theta_{\boldsymbol{q}}-im'\theta} T_{mm'}(q,\omega) \ . \tag{3.204}$$

Even in this geometry, the presence of a localized plasmon resonanc manifests as a pole of the analytical continuation of $T_{mm'}(q,\theta,\omega)$ to the upper half of the complex plane, at a purely imaginary value of $q$.

For systems with rotational invariance, only the diagonal components of $\Delta_{mm'}$ and $T_{mm'}$ are non-zero. This greatly simplifies the solution of Eq. (3.203). In this case, the scattering amplitude depends only on the angle between the incoming and scattered waves and can be written as

$$f(\theta,\omega) \equiv f(\theta,0,\omega) = -e^{i\frac{\pi}{4}} \frac{\sqrt{q_{\rm pl}} C(\omega)}{\sqrt{2\pi}} \sum_{m=-\infty}^{+\infty} e^{im\theta} T_m(q_{\rm pl},\omega) \ , \tag{3.205}$$

where $T_m(q,\omega) \equiv T_{mm}(q,\omega)$. Using Eq. (3.205) and the optical theorem (3.171) we obtain

$$\sum_{m=-\infty}^{\infty} \frac{|q_{\rm pl} C(\omega) T_m(q_{\rm pl},\omega)|^2}{2} + \Im m[q_{\rm pl} C(\omega) T_m(q_{\rm pl},\omega)] = 0 \ . \tag{3.206}$$

Since the quantities $T_m(q_{\rm pl},\omega)$ for different values of $m$ are independent from each other, every term of the sum in Eq. (3.206) must vanish. This restricts the region of the complex plane allowed for the values of $q_{\rm pl}C(\omega)T_m(q_{\rm pl},\omega)$ to a circle of radius 1 centered in $-i$. This region can be parametrized by a single real number $-\pi/2 \leq \delta_{m,\omega} \leq \pi/2$, called phase shift, in the following way

$$q_{\rm pl}C(\omega)T_m(q_{\rm pl},\omega) = -2\sin(\delta_{m,\omega})e^{i\delta_{m,\omega}} \ . \tag{3.207}$$

We can therefore express the scattering amplitude and the total cross section in terms of the phase shifts in a compact way:

$$f(\theta,\omega) = \frac{2e^{i\pi/4}}{\sqrt{2\pi q_{\rm pl}}} \sum_{m=-\infty}^{\infty} \sin(\delta_{m,\omega})e^{i\delta_{m,\omega}+im\theta} \tag{3.208}$$

and

$$\Sigma(\omega) \equiv \int d\theta |f(\theta,\omega)|^2 = \frac{4}{q_{\rm pl}} \sum_{m=-\infty}^{\infty} \sin^2(\delta_{m,\omega}) \ . \tag{3.209}$$

### 3.2.9 Explicit examples

In this Section we illustrate the power of our Lippmann-Schwinger theory by solving two concrete problems, one for each of the geometries displayed in Fig. 3.1.

We consider the scattering of plasmons in a 2D parabolic-band electron gas subject to an external scalar perturbation generated by: (a) a charged point-like impurity with charge $Ze$, $Z$ being an integer number, positioned at $(x,y,z) = (0,0,d)$ and (b) a line of charged impurities with charge density per unit length $\lambda$, positioned at $x = 0$ and $z = d$. Here, $z = 0$ is the position of the 2D electron gas, which, in the absence of the impurities, has a uniform density $\bar{n}$. For the sake of definiteness, we take $\bar{\epsilon} = 12$ and $m = 0.067\ m_{\rm e}$, where $m_{\rm e}$ is the electron mass in vacuum. These material parameters refer to a 2D parabolic-band electron gas in a GaAs quantum well.

The electric potential generated by the external charges perturbs the uniform ground-state density inducing a non-trivial density profile $n(\boldsymbol{r}) = \bar{n} + \delta n(\boldsymbol{r})$, which depends only on $r = |\boldsymbol{r}|$ in geometry (a) and only on $x$ in geometry (b). These density profiles are shown in Fig. 3.2(a) and (b). Details on how $n(\boldsymbol{r})$ is actually calculated are reported below.

As explained in Sect. 3.2.2, we first need to calculate the homogeneous part $\tilde{\chi}_{\rm h}(q,\omega)$ of the density-density response function of the system in the absence of the perturbations, i.e. for $Z = 0$ in geometry (a) and for $\lambda = 0$ in geometry (b). To this end, we use Eqs. (B.11)-(B.12) with $\boldsymbol{q}' = \boldsymbol{q}$, retaining terms $\mathcal{O}(\omega^{-4})$ (i.e. expanding up to $\ell = 3$). The first moment is given by

$$M^{(1)}(\boldsymbol{q},\boldsymbol{q}) = \frac{\bar{n}}{m}q^2 \ , \tag{3.210}$$

the second moment $M^{(2)}(\boldsymbol{q},\boldsymbol{q})$ is identically zero, while the third moment reads as following:

$$M^{(3)}(\boldsymbol{q},\boldsymbol{q}) = \frac{3\bar{n}\epsilon_0}{m^2}q^4 + \frac{\bar{n}\hbar^2}{4m^3}q^6 \ , \tag{3.211}$$

where $\epsilon_0 = E_{\rm F}/2$ is the kinetic energy per particle of the non-interacting 2D electron system [35]. Here, $E_{\rm F} = \pi\bar{n}\hbar^2/m$ is the Fermi energy. Using these three results we find that $\tilde{\chi}_{\rm h}(q,\omega)$ can be expressed as in Eq. (3.125) with $D = \pi e^2\bar{n}/m$ and

$$\mathcal{G}(q,\omega) = 1 + \frac{3}{4}\frac{v_{\rm F}^2q^2}{\omega^2} + \frac{1}{4}\frac{\hbar^2q^4}{m^2\omega^2} \ , \tag{3.212}$$

where $v_{\rm F} = \hbar k_{\rm F}/m$ is the Fermi velocity and $k_{\rm F} = \sqrt{2\pi\bar{n}}$ is the Fermi wave number.

For the sake of simplicity, in Eq. (3.127) we neglect the frequency dependence of $\bar{\epsilon}(\omega)$, by taking $\bar{\epsilon}(\omega) \mapsto \bar{\epsilon}$, and also finite-size effects, by setting $\mathcal{F}(q,\omega) \equiv 1$. Using Eq. (3.143) we find

$$C(\omega) = \frac{2\pi e^2}{\bar{\epsilon}} \frac{1 + \frac{3}{4}\frac{v_{\rm F}^2q_{\rm pl}^2}{\omega^2} + \frac{1}{4}\frac{\hbar^2q_{\rm pl}^4}{m^2\omega^2}}{1 + \frac{9}{4}\frac{v_{\rm F}^2q_{\rm pl}^2}{\omega^2} + \frac{5}{4}\frac{\hbar^2q_{\rm pl}^4}{m^2\omega^2}} \ , \tag{3.213}$$

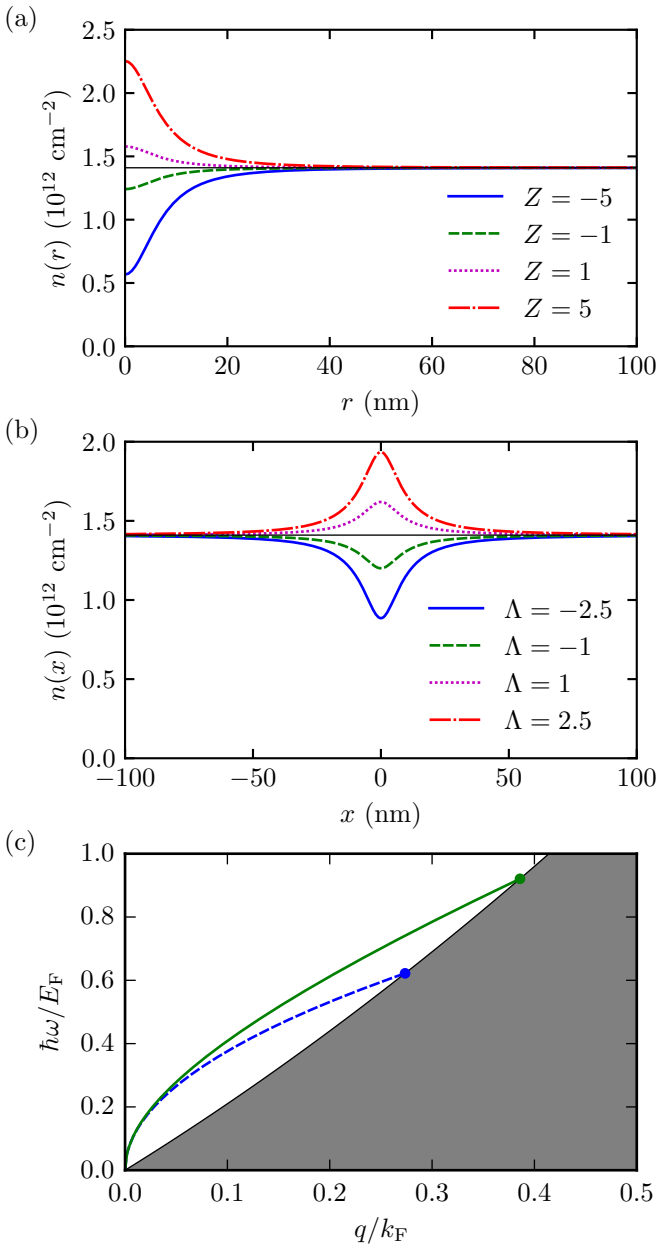


Figure 3.2: Panel (a) Spatial dependence $n(r)$ of the density profile induced by a point-like charged impurity located above a 2D parabolic-band electron gas, at $(x, y) = (0, 0)$ and $z = d = 2/k_{\rm F}$. These results have been obtained for a Wigner-Seitz density parameter [35] $r_{\rm s} = 0.5$. (It is only in this weak-coupling limit that the application of RPA is rigorously justified [35].) Different curves refer to different values of the impurity charge $Ze$. Panel (b) Same as in panel (a) but for a line of charged impurities located at $x = 0$ and $z = d = 2/k_{\rm F}$. Different curves refer to different values of the dimensionless parameter $\Lambda$ introduced in Eq. (3.235). Panel (c) RPA dispersion relation of plasmons in a uniform 2D parabolic-band electron system (evaluated at $r_{\rm s} = 0.5$). The blue dashed line is the result of the local theory, obtained by setting $\mathcal{G}(q, \omega) = 1$, while the green solid line is the result of our nonlocal theory. The grey-shaded area represents the electron-hole continuum, where plasmons suffer Landau damping [35].

while using Eq. (3.145) we obtain the nonlocal correction to the effective interaction

$$\mathcal{W}(q,\omega) = \frac{q_{\rm pl} - q}{q} \frac{E_{\rm F}^2 q_{\rm pl}^2}{\hbar^2\omega^2 k_{\rm F}^2} \frac{3\left(\frac{q}{q_{\rm pl}} + 2\right) + \frac{q_{\rm pl}^2}{k_{\rm F}^2}\left(\frac{q^3}{q_{\rm pl}^3} + \frac{2q^2}{q_{\rm pl}^2} + \frac{3q}{q_{\rm pl}} + 4\right)}{\left(1 - \frac{q}{q_{\rm pl}}\right) + \frac{3E_{\rm F}^2 q_{\rm pl}^2}{\hbar^2\omega^2 k_{\rm F}^2}\left(1 - \frac{q^3}{q_{\rm pl}^3}\right) + \frac{E_{\rm F}^2 q_{\rm pl}^4}{\hbar^2\omega^2 k_{\rm F}^4}\left(1 - \frac{q^5}{q_{\rm pl}^5}\right)} \,. \tag{3.214}$$

Plasmon modes of the uniform 2D parabolic-band electron system analyzed in this work are shown in Fig. 3.2(c). Results of the local theory (i.e. obtained by negleting $M^{(3)}(\boldsymbol{q},\boldsymbol{q}')$) are simply $\mathcal{G}(q,\omega)=1$, $C(\omega)=2\pi e^2/\bar{\epsilon}$ and $\mathcal{W}(q,\omega)=0$. We now analyze separately the two geometries (a) and (b). In case of geometry (a), we calculate the phase shifts $\delta_{m,\omega}$ and the scattering cross section $\Sigma(\omega)$ as functions of the plasmon wavevector and impurity charge $Z$, limiting ourselves to the local approximation. In the case of geometry (b), we calculate transmission and reflection coefficients as functions of the plasmon wavevector and impurity charge density $\lambda$ using the full nonlocal theory and compare these results with the corresponding ones in the local approximation.

**Scattering of a plasmon against a point-like charged impurity**

The potential generated by a charge $eZ$ located at a distance $d$ from the plane of the 2D electron gas is

$$U_{\rm ext}(r)=-\frac{e^2Z}{\bar{\epsilon}\sqrt{r^2+d^2}}\ . \tag{3.215}$$

Its Fourier transform reads as following

$$U_{\rm ext}(q)=-\frac{2\pi e^2Ze^{-qd}}{\bar{\epsilon}q}\ . \tag{3.216}$$

We can calculate the density-density response function of the non-uniform system using the results in Appendix B.1. Retaining only the first moment $M^{(1)}(\boldsymbol{q},\boldsymbol{q}')$ we obtain

$$\Delta(\boldsymbol{q},\boldsymbol{q}',\omega)=\delta\tilde{\chi}(\boldsymbol{q},\boldsymbol{q}',\omega)=\frac{\boldsymbol{q}\cdot\boldsymbol{q}'}{m\omega^2}\delta n(|\boldsymbol{q}-\boldsymbol{q}'|)\ . \tag{3.217}$$

In this approximation the scattering kernel depends only on the induced density perturbation. We now evaluate $\delta n(q)$ by using linear response theory [35] with respect to $U_{\rm ext}(r)$ and the RPA. The total potential is

$$U_{\rm tot}(q)=\frac{U_{\rm ext}(q)}{\epsilon(q)}\ , \tag{3.218}$$

where the static dielectric constant of the uniform 2D parabolic-band electron gas is [35, 223]

$$\epsilon(q)=1-\frac{2\pi e^2}{\bar{\epsilon}q}\chi_0(q,\omega=0)=1+\frac{q_{\rm TF}}{q}\left[1-\Theta(q-2k_{\rm F}\frac{\sqrt{q^2-4k_{\rm F}^2}}{q}\right]\ . \tag{3.219}$$

Here, $\chi_0(q,\omega=0)$ is the static density-density response function of a 2D parabolic-band electron gas [35, 223] and $q_{\rm TF}=2me^2/(\hbar^2\bar{\epsilon})$ is the Thomas-Fermi wave number [35, 223].

Making use of well-known analytical expressions [35, 223] for $\chi_0(q,\omega=0)$, we can write the density perturbation as

$$\delta n(q)=-N_0\left[1-\Theta(q-2k_{\rm F})\frac{\sqrt{q^2-4k_{\rm F}^2}}{q}\right]U_{\rm tot}(q)\ , \tag{3.220}$$

where $N_0=m/(\pi\hbar^2)$ is the density of states at the Fermi energy [35]. We now make a further approximation neglecting all the terms that are proportional to $\Theta(|q_x|-2k_{\rm F})$. Indeed, since the plasmon wavevector $q_{\rm pl}$ is a fraction of $k_{\rm F}$, we expect that the contribution to the scattering problem coming from wavevectors satisfying $|q_x|>2k_{\rm F}$ is negligible. This amounts to neglecting Friedel oscillations of the electron density. The total density profile in real space $n(r)=\bar{n}+\delta n(r)$ is shown Fig. 3.2(a).

Using Eqs. (3.217)-(3.220) we can calculate the dimensionless scattering kernel, obtaining the following expression

$$q_{\rm pl}C(\omega)\Delta(\boldsymbol{q},\boldsymbol{q}',\omega)=\frac{2\pi e^2Z}{\bar{\epsilon}E_{\rm F}}\frac{\boldsymbol{q}\cdot\boldsymbol{q}'e^{-d|\boldsymbol{q}-\boldsymbol{q}'|}}{|\boldsymbol{q}-\boldsymbol{q}'|+q_{\rm TF}}\ . \tag{3.221}$$

This quantity is related by Eq. (3.179) to the scattering amplitude in the first-order Born approximation:

$$f^{(1)}(\theta,\omega)=-\frac{e^{i\frac{\pi}{4}}q_{\rm pl}^{3/2}}{\sqrt{2\pi}}\frac{2\pi e^2Z}{\bar{\epsilon}E_{\rm F}}\frac{\cos(\theta)e^{-dq_{\rm pl}\sqrt{2[1-\cos(\theta)]}}}{q_{\rm pl}\sqrt{2[1-\cos(\theta)]}+q_{\rm TF}}\ . \tag{3.222}$$

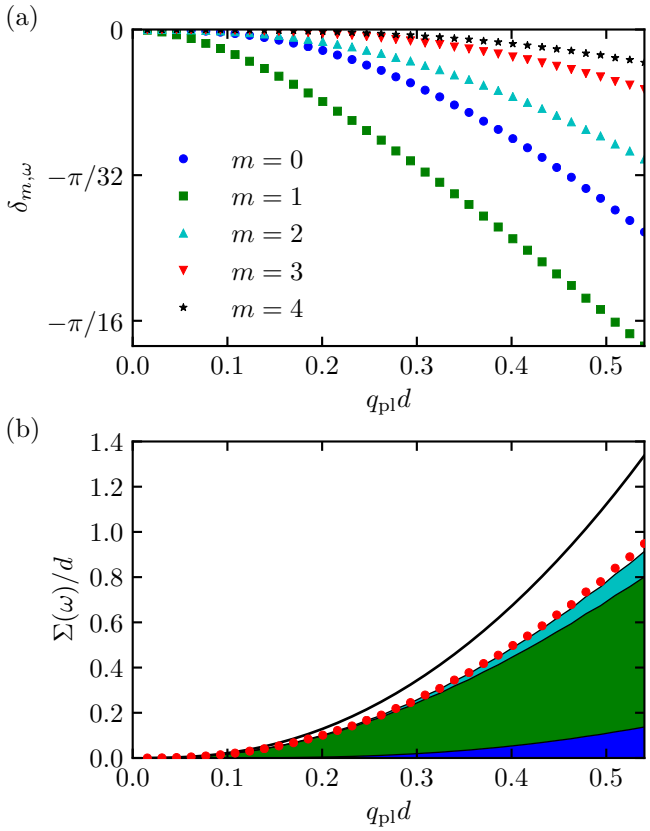


Figure 3.3: Panel (a) The numerically calculated phase shifts $\delta_{m,\omega}$ for the case of geometry (a) are plotted as functions of the plasmon wavevector $q_{\rm pl}$ for $Z = 5$ and $0 \leq m \leq 4$. Panel (b) The total cross section $\Sigma(\omega)$ (calculated by including in the numerics partial waves with $|m| \leq 5$) is plotted as a function of the plasmon wavevector $q_{\rm pl}$ for $Z = 5$ (red dots). The thick black line is the result of first-order Born approximation. The blue, green, and cyan-shaded regions denote the contributions to the total cross section of partial waves with $m = 0$, $m = \pm 1$, and $m = \pm 2$, respectively. Note that the dominant contribution comes from the $m = \pm 1$ channel ($p$-wave scattering).

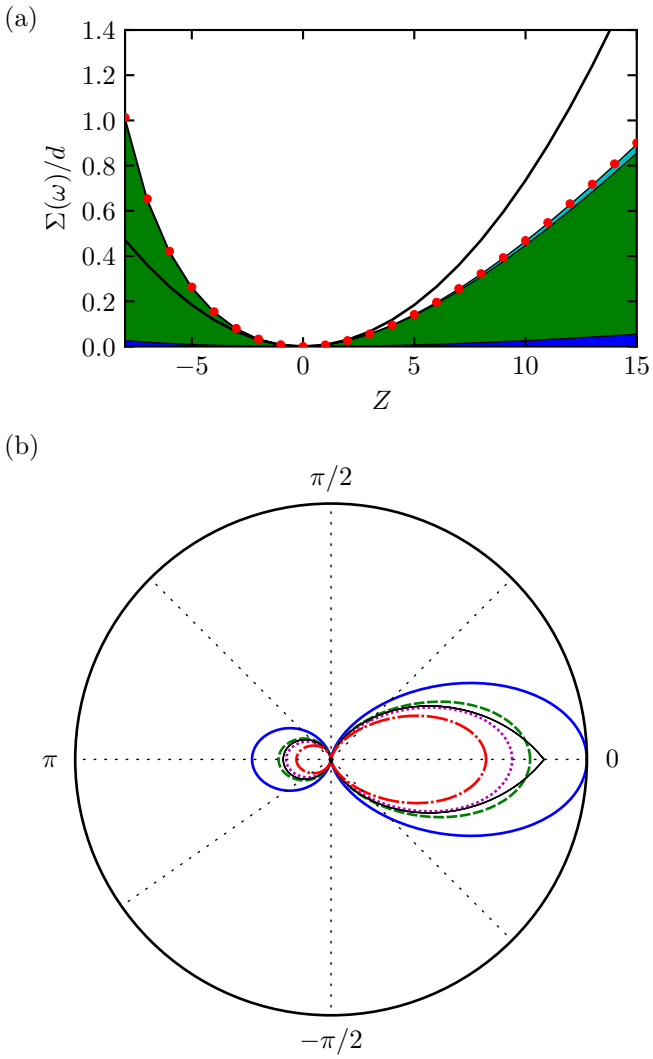


Figure 3.4: Panel (a) Total scattering cross section $\Sigma(\omega)$ as a function of the impurity charge $Z$, for a fixed value of the plasmon wavevector, i.e. $q_{\rm pl}d = 0.23$ (red dots). The thick black line is the result of the first-order Born approximation. The blue, green, and cyan-shaded regions denote the contributions to the total cross section of partial waves with $m = 0$, $m = \pm 1$, and $m = \pm 2$, respectively. Panel (b) Angular dependence of the numerically evaluated scattering cross section normalized by $Z^2$, $|f(\theta)|^2/(Z^2 d)$, for $q_{\rm pl}d = 0.23$ and different values of $Z$: $Z = -5$ (blue solid line), $Z = -1$ (green dashed line), $Z = 1$ (magenta dotted line), and $Z = 5$ (red dash-dotted line). The black line is the result of the first-order Born approximation. Again, only partial waves with $|m| \leq 5$ were kept in all numerical calculations.

This is the most important analytical result of this Section. Note the presence of the overall factor $\cos(\theta)$, which is responsible for the dominance of $p$-wave (i.e. $m = \pm 1$) scattering—see Fig. 3.3(b)— and for the suppression of scattering in the direction perpendicular to the incident one—see Fig. 3.4(b).

Since the problem at hand is rotationally symmetric, we can decompose Eq. (3.157) for the transition function into its cylindrical components, as described in Sect. 3.2.8. This procedure requires the knowledge of the angular components of the scattering kernel defined in Eq. (3.200):

$$q_{\rm pl} C(\omega) \Delta_{mm}(q, q', \omega) = \frac{2\pi e^2 Z}{\bar{\epsilon} E_{\rm F}} q q' \int_{-\pi}^{\pi} \frac{d\theta}{2\pi} e^{-im\theta} \frac{\cos(\theta) e^{-d\sqrt{q^2+q'^2-2qq'\cos(\theta)}}}{\sqrt{q^2+q'^2-2qq'\cos(\theta)} + q_{\rm TF}} \ . \tag{3.223}$$

This quantity needs to be evaluated numerically for each $m$.

**Scattering of a plasmon against a 1D line of charged impurities**

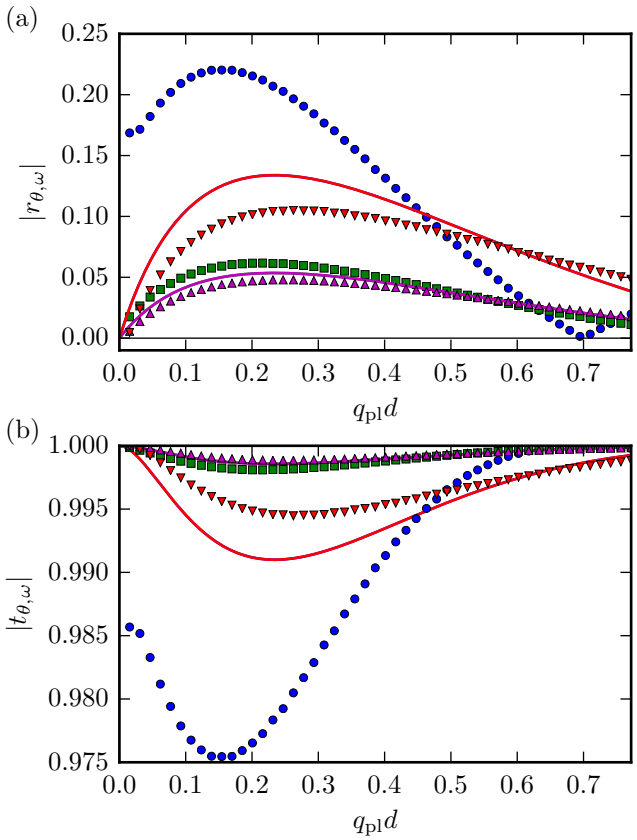


Figure 3.5: Numerically evaluated amplitudes of the reflection—panel (a)—and transmission—panel (b)—coefficients, as functions of the plasmon wavevector $q_{\rm pl}$, for different values and signs of the dimensionless parameter $\Lambda$: $\Lambda = -2.5$ (blue circles), $\Lambda = -1$ (green squares), $\Lambda = 1$ (magenta upward triangles), and $\Lambda = 2.5$ (red downward triangles). These results include nonlocal effects. The solid lines with the same color coding are the results of the first-order Born approximation. In this approximation the results are even in $\Lambda$, therefore only curves corresponding to positive values of $\Lambda$ are shown.

The external potential generated by a line of charges can be calculated via Gauss theorem and reads

$$U_{\rm ext}(x) = \frac{e\lambda}{\bar{\epsilon}} \ln\left(1 + \frac{x^2}{d^2}\right) \ . \tag{3.224}$$

Its Fourier transform is

$$U_{\rm ext}(q_x) = -\frac{2\pi e\lambda e^{-d|q_x|}}{\bar{\epsilon}|q_x|} \ . \tag{3.225}$$

We are clearly in the case of Fig. 3.1(b), with translational invariance along the $\hat{\boldsymbol{y}}$ direction.

We are now in the position to calculate the scattering kernel. Using Eq. (3.132) and the results (B.24), (B.30), and (B.32) we find:

$$\begin{aligned}\Delta(q_x, q_x', q_y, \omega) = &\frac{(q_x q_x' + q_y^2)}{m\omega^2}\delta n(q_x - q_x') \\ &+ \frac{3(q_x q_x' + q_y^2)}{m^2\omega^4}\left[q_x q_x' \delta T_{xx}(q_x - q_x') + q_y^2 \delta T_{yy}(q_x - q_x')\right] \\ &+ \frac{\hbar^2}{m^3\omega^4}(q_x q_x' + q_y^2)\left[\frac{3}{4}q_x q_x'(q_x - q_x')^2 + \frac{1}{4}(q_x q_x' + q_y^2)^2\right]\delta n(q_x - q_x') \\ &+ \frac{1}{m\omega^4} q_x q_x' \left\langle \partial_{xx} U_{\rm tot} n_{\hat{\mathbf{x}}(q_x - q_x')}\right\rangle \ .\end{aligned} \tag{3.226}$$

Here $\delta n(q_x)$ is the variation of the electron density with respect to its equilibrium value $\bar{n}$, while $\delta T_{ij}(q_x)$ represents the variations of the stress-tensor components with respect to their the equilibrium values. To get an explicit analytical expression for the scattering kernel, we evaluate the expectation values in

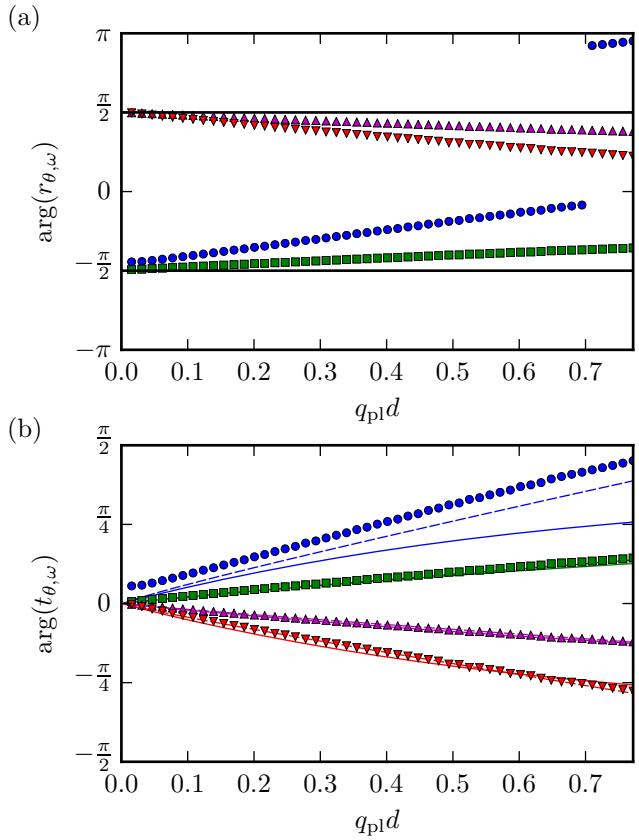


Figure 3.6: Numerically evaluated phases of the reflection—panel (a)—and transmission—panel (b)—coefficients, as functions of the dimensionless product $q_{\rm pl}d$, for different values and signs of the dimensionless parameter $\Lambda$: $\Lambda = -2.5$ (blue circles), $\Lambda = -1$ (green squares), $\Lambda = 1$ (magenta upward triangles), and $\Lambda = 2.5$ (red downward triangles). The black solid lines in panel (a) represent the result of the first-order Born approximation. The solid lines in panel (b) represent the result of the first-order Born approximation, while the dashed lines are the results of the eikonal approximation.

Eq. (3.226) by using linear response theory [35] with respect to $U_{\rm ext}(x)$ and the RPA. We follow the same steps as in the previous Section. We start again by calculating the Fourier transform of the total potential $U_{\rm tot}(x)$:

$$U_{\rm tot}(q_x) = \frac{U_{\rm ext}(q_x)}{\epsilon(|q_x|)} \ . \tag{3.227}$$

The density perturbation reads as following

$$\delta n(q_x) = -N_0 \left[1 - \Theta(|q_x| - 2k_{\rm F}) \frac{\sqrt{q_x^2 - 4k_{\rm F}^2}}{|q_x|}\right] U_{\rm tot}(q_x) \ . \tag{3.228}$$

The resulting inverse Fourier transform of the density profile $n(x) = \bar{n} + \delta n(x)$ is plotted as a function of $x$ in Fig. 3.2(b).

The expectation value of the second derivative of the potential is, to linear order in $U_{\rm ext}$,

$$\langle \partial_{xx} U_{\rm tot}(x) n_{\hat{\boldsymbol{x}} q_x} \rangle = -q_x^2 \bar{n} U_{\rm tot}(q_x) \ . \tag{3.229}$$

The components of the stress tensor can be evaluated using the density-stress tensor response function calculated in Appendix C. We find

$$\delta T_{xx}(q_x) = -N_0 E_{\rm F} f_x(|q_x|) U_{\rm tot}(q_x) \tag{3.230}$$

and

$$\delta T_{yy}(q_x) = -N_0 E_{\rm F} f_y\left(|q_x|\right) U_{\rm tot}(q_x) \ . \tag{3.231}$$

Here,

$$f_x(q) = 1 + \frac{q^2}{2k_{\rm F}^2} - \Theta(q - 2k_{\rm F}) \frac{q}{2k_{\rm F}^2} \sqrt{q^2 - 4k_{\rm F}^2} \tag{3.232}$$

and

$$f_y(q) = 1 - \frac{q^2}{6k_{\rm F}^2} - \Theta(q - 2k_{\rm F}) \frac{2\sqrt{q^2 - 4k_{\rm F}^2}}{3q} \left(1 - \frac{q^2}{4k_{\rm F}^2}\right) \ . \tag{3.233}$$

We neglect again all the terms in the expectation values that are proportional to $\Theta(|q_x| - 2k_{\rm F})$. In summary, our final result for the dimensionless scattering kernel is

$$C(\omega)\Delta(q_x, q_x', q_y, \omega) = \frac{\Lambda e^{-d|q_x - q_x'|}(q_x q_x' + q_{\rm pl}^2 \sin^2\theta)}{q_{\rm pl}\left(|q_x - q_x'| + q_{\rm TF}\right)} \mathcal{K}(q_x, q_x', q_y, \omega) \ , \tag{3.234}$$

where

$$\Lambda = \frac{2\pi e \lambda}{\bar{\epsilon} E_{\rm F}} \tag{3.235}$$

is the dimensionless "impurity" concentration (for $\Lambda > 0$ the external potential is attractive for the electron system, while for $\Lambda < 0$ it is repulsive) and $\mathcal{K}(q_x, q_x', q_y, \omega)$ is a function that takes into account nonlocal effects:

$$\begin{aligned} &\mathcal{K}(q_x, q_x', q_y, \omega) = \\ &= \frac{1 + \frac{2E_{\rm F}^2}{\hbar^2\omega^2 k_{\rm F}^2}\left[3(q_x q_x' + q_y^2) + \frac{q_x q_x'(q_x - q_x')^2}{q_x q_x' + q_y^2}\right] + \frac{E_{\rm F}^2}{\hbar^2\omega^2 k_{\rm F}^4}\left[(6q_x q_x' - q_y^2)(q_x - q_x')^2 + (q_x q_x' + q_y^2)^2\right]}{1 + \frac{9E_{\rm F}^2 q_{\rm pl}^2}{\hbar^2\omega^2 k_{\rm F}^2} + \frac{5E_{\rm F}^2 q_{\rm pl}^4}{\hbar^2\omega^2 k_{\rm F}^4}} \ . \end{aligned} \tag{3.236}$$

We can now make use of Eqs. (3.184)-(3.185) to evaluate the transmission and reflection coefficients in the first-order Born approximation. We find

$$t_{\theta,\omega}^{(1)} = 1 - i \frac{\Lambda q_{\rm pl}}{q_{\rm TF} \cos\theta} \mathcal{K}(q_{\rm pl}\cos\theta, q_{\rm pl}\cos\theta, q_{\rm pl}\sin\theta, \omega) \tag{3.237}$$

and

$$r_{\theta,\omega}^{(1)} = i \frac{\Lambda q_{\rm pl} \cos(2\theta) e^{-2d q_{\rm pl}\cos\theta}}{\cos\theta(2q_{\rm pl}\cos\theta + q_{\rm TF})} \mathcal{K}(-q_{\rm pl}\cos\theta, q_{\rm pl}\cos\theta, q_{\rm pl}\sin\theta, \omega) \ . \tag{3.238}$$

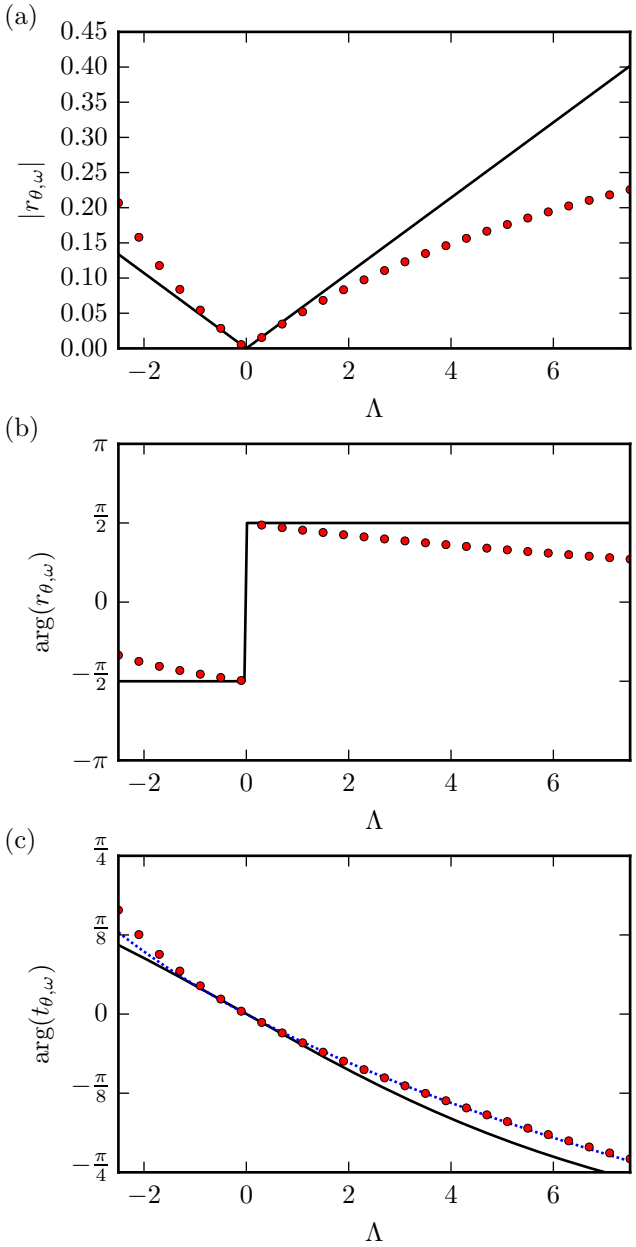


Figure 3.7: Coupling constant dependence of $|r|$, $\arg(r)$, and $\arg(t)$. Panel (a) The quantity $|r|$ as a function of $\Lambda$, for $q_{\rm pl}d = 0.23$. For this value of $q_{\rm pl}d$, the reflection coefficient displays a maximum. Red circles are numerical data (including nonlocal corrections) while the solid black line is the result of the first-order Born approximation. Panel (b) Same as in panel (a) but for the phase of the reflection coefficient. Panel (c) Same as in panel (b) for $\arg(t)$. In this panel, the blue dashed line is the result of the eikonal approximation.

### Numerical results

In the case of geometry (a), we solved numerically Eq. (3.203) by using a first-order finite-element method for partial waves with $0 \leq m \leq 5$ and the local results for $C(\omega)$ and $\mathcal{W}(q,\omega)$, together with Eq. (3.221). From the resulting angular components of the transition matrix we extracted the corresponding phase shifts $\delta_{m,\omega}$ by inverting Eq. (3.207). (Results for negative values of $m$ are readily obtained by using $\delta_{m,\omega} = \delta_{-m,\omega}$.) Numerical results for the phase shifts are shown in Fig. 3.3(a). We then used the phase shifts to calculate the scattering amplitude $f(\theta,\omega)$ and the total cross section $\Sigma(\omega)$ according to Eqs. (3.208)-(3.209). Numerical results for the cross section are shown in Figs. 3.3(b) and 3.4(a) and

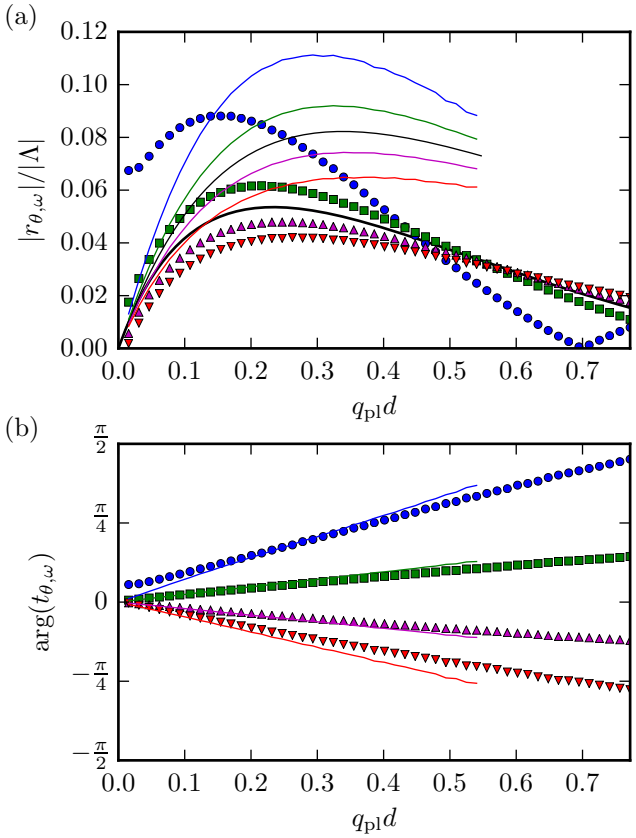


Figure 3.8: Numerical results of the full nonlocal theory (symbols) are compared with the corresponding results of the local theory (thin lines). Color coding is identical to that used in Fig. 3.5. The black line in panel (a) is the result of the first-order Born approximation (which is "universal", provided that $|r_{\theta,\omega}|$ is rescaled by $|\Lambda|$). As expected, the local theory is a good approximation in the long-wavelength $q_{\rm pl}d \to 0$ limit.

compared to the results of the first-order Born approximation. Fig. 3.4 shows the angular distribution of the scattered power (proportional to the square modulus of the scattering amplitude) for a fixed value of the plasmon wavevector $q_{\rm pl}$ and different values of $Z$. We note that most of the power is scattered in the forward direction inside an angle of $\approx \pm 45°$ from the incidence direction. A smaller fraction of the power is backscattered, while "lateral" scattering is almost negligible.

For the case of geometry (b), we solved numerically Eq. (3.165) by using a first-order finite-element method, making use of the expressions in Eqs. (3.213), (3.214), (3.234), and (3.236). All numerical results for $r_{\theta,\omega}$ and $t_{\theta,\omega}$ have been obtained by setting $\theta = 0$ and evaluating $\omega$ at the plasmon dispersion. This implies that $\omega$ changes with $q_{\rm pl}$, as dictated by the RPA equation (3.135). A summary of our main results for the transmission and reflection coefficients as functions of the plasmon wavevector $q_{\rm pl}$ is presented in Figs. 3.5-3.6. Full numerical results (denoted by symbols) are compared with the results of the first-order Born and eikonal approximations. We clearly see that the first-order Born approximation works well for the amplitude of reflection and transmission coefficients (Fig. 3.5) in the weak-coupling limit $|\Lambda| \ll 1$. The same approximation works well in the same limit for the phase of the transmission coefficient, as shown in Fig. 3.6(b). From the same figure, it is also clear that the eikonal approximation performs better than the first-order Born approximation in predicting $\arg(t)$, especially at strong coupling.

In Fig. 3.7 we illustrate the dependence of $|r|$, $\arg(r)$, and $\arg(t)$ on the coupling constant $\Lambda$. Full numerical results (symbols) are compared with the results of the first-order Born and eikonal approximations. The perturbative validity of the former is again clear. The validity of the eikonal approximation for $\arg(t)$ and its non-perturbative nature are also clear.

Finally, in Fig. 3.8 we compare our full numerical results with the results of the local theory, which is obtained by setting $C(\omega) \equiv 2\pi e^2/\bar{\epsilon}$, $\mathcal{W}(q,\omega) \equiv 0$, and $\mathcal{K}(q_x, q'_x, q_y, \omega) \equiv 1$ in the general equations. As expected, the local theory fails spectacularly in predicting $|r|$ for large values of the product $q_{\rm pl}d$.

## 3.3 Electrical $2\pi$ phase control of infrared light in a 350nm footprint using graphene plasmons

Modulating the amplitude and phase of light is at the heart of many applications such as wavefront shaping, [224] transformation optics [225, 149], phased arrays [226], modulators [227], and sensors [228]. Performing this task with high efficiency and small footprint is a formidable challenge [229, 230]. Metasurfaces [231, 227] and plasmonics [232] are promising, but metals exhibit weak electro-optic effects. Two-dimensional materials, such as graphene, have shown great performance as modulators with small drive voltages [233, 234]. Here we show a graphene plasmonic phase modulator which is capable of tuning the phase between 0 and $2\pi$ *in situ*. With a footprint of 350 nm it is more than 30 times smaller than the 10.6 $\mu$m free space wavelength. The modulation is achieved by spatially controlling the plasmon phase velocity in a device where the spatial carrier density profile is tunable. We provide a scattering theory for plasmons propagating through spatial density profiles. This work constitutes a first step towards two-dimensional transformation optics [149] for ultra-compact modulators [229] and biosensing [151].

The graphene plasmon phase velocity (and thus wavelength) is *in situ* tunable, and can be varied spatially, making it a unique platform for for transformation optics in two dimensions [149, 7]. The full spatial and dynamic control of the plasmon velocity profile makes completely new device concepts possible. This includes on-chip interferometers and tunable metamaterials such as phased arrays for a full dynamical beam manipulation [226]. This full control has thus far remained a great challenge and the plasmon propagation was mainly controlled by physical features in the graphene [200, 203, 157].

Here, we manipulate for the first time the spatial profile of the plasmon phase velocity actively employing local metal gates, achieving *in situ* control of the plasmon wavelength, as sketched in Fig. 3.9. A plasmon (launched by scattering light on a gold edge) that propagates trough the tunable spatial carrier density profile picks up a phase, that is transferred to the photon after scattering of a metallized atomic force microscopy probe tip. In this way, we are able to continuously tune the phase shift of the plasmon and the outcoming photons from 0 to $2\pi$, and experimentally measure this phase in the far-field with an interferomete [235, 236].

We present a simple model based on the optical path length of light to explain our observations and to provide guidelines for designing such graphene plasmonic phase modulators. Moreover we rigorously calculate the expected phase shift and reflections using a Lippmann-Schwinger scattering theory approach derived in Section 3.2. Indeed our work is the first time for graphene plasmons that such an approach has been used.

This strongly improved understanding both theoretically and experimentally of plasmonic phase-control is relevant for the future development of *in situ* tunable metasurfaces [237], modulators and holds great promise for novel sensor concepts.

Our device is based on a heterostructure of graphene encapsulated between two layers of hexagonal boron nitride (h-BN), [18] which serves to preserve the lifetime of the graphene plasmons. The device was assembled by the polymer-free van der Waals assembling technique [7] and then transferred onto 15 nm thin AuPd local gates. The so-called "phase shifter gate" has a length of 150 nm and the gaps to the other gates are 100 nm each. Using these local gates it is possible to spatially control the carrier density profile. A gold contact is connected by electrical side contact [7], allowing for gating of the graphene.

A $CO_2$ laser with a free space wavelength of $\lambda_0 = 10.6$ $\mu$m is focussed onto this elongated gold contact with a sharp edge. The polarization is perpendicular to the edge as sketched in Fig. 3.9. This edge provides the necessary momentum matching between far-field photons and plasmons and thus the light is partially converted into graphene plasmons propagating away from the edge as a plane wave in the electrostatically doped graphene [238, 157].

The effect of the plasmon propagation trough this spatial carrier density profile is depicted in Fig. 3.10a. The plasmon effective index $n = c/v_{\mathrm{ph}}$, with $v_{\mathrm{ph}}$ the plasmon phase velocity and $c$ the speed of light, is related to the gate-induced charge density: $v_{\mathrm{ph}} \propto \lambda_{\mathrm{pl}} \propto \sqrt{n_{\mathrm{s}}}$ [18]. The voltage on the phase shifter gate $V_{\mathrm{PS}}$ controls $n$ in the graphene above this gate. After the plasmons propagate through this velocity-tunable (and thus phase-shifting) region their optical path length (Fig. 3.10b) can be expressed as

$$L(V_{\mathrm{PS}}) = \int_a^b n(x, V_{\mathrm{PS}}) dx \tag{3.239}$$

where $x$ is the position and $a = 0\,\mathrm{nm}$ and $b = 485\,\mathrm{nm}$ are the start and end points of the phase-shifting

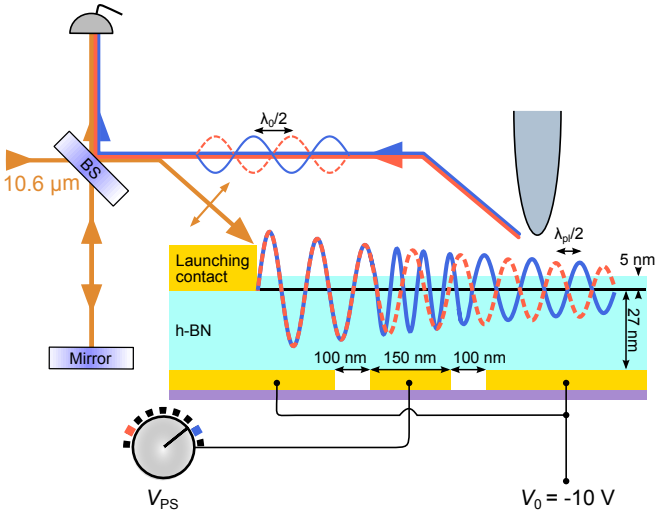


Figure 3.9: Device sketch and measurement principle. The three local gates are used to independently tune the carrier concentration in the different graphene regions. The phase shifter voltage $V_{\mathrm{PS}}$ is tuned and during all experiments $V_0 = -10\,\mathrm{V}$ is kept constant. The gate thickness is 15 nm. The plasmons propagate from the launching contact over the phase shifter region and are ultimately scattered into far-field light using a metallized AFM tip, and subsequently interfered with the incoming light.

region respectively,[239] where the carrier density profile does not change any more when $V_{\mathrm{PS}}$ is changed.

The carrier density profile is simulated by the electrostatic Laplace equation taking into account the full anisotropic DC permittivity of h-BN as well as the spatial gate profile [240]. For each $V_{\mathrm{PS}}$ the carrier density profile is simulated and $n(x, V_{\mathrm{PS}})$ is then calculated taking into account the full dielectric environment. The carrier-density-dependent graphene conductivity is calculated using the zero-temperature non-local random phase approximation [241]. As the out-of-plane decay length of the plasmons is much smaller than the thickness of the bottom h-BN the spatial profile of the metal gates does not need to be taken into account.

Due to the different optical path lengths for different $V_{\mathrm{PS}}$ the plasmons accumulate a different phase $\phi$ after propagating through the phase shifter region. The phase difference $\Delta\phi$ between different optical path lengths can be estimated using the optical path difference,

$$\Delta\phi(V_{\mathrm{PS}}) = k_0 \Delta L = k_0 \left(L(V_{\mathrm{PS}}) - L(-10\,\mathrm{V})\right). \tag{3.240}$$

In Fig. 3.10c we show how the optical path difference $\Delta L$ translates into a different phase for different $V_{\mathrm{PS}}$ as they exit the phase shifter region. The wavelength reduction in the phase shifter region is clear. In order to experimentally observe the phase shift between different $V_{\mathrm{PS}}$ we use a metallized atomic force microscopy probe tip to scan across the sample. The plasmons are scattered from the probe tip and then recorded as the out-scattered light signal in the far-field by scattering-type scanning near-field optical microscopy (s-SNOM) (Fig. 3.9). The measurement is performed in homodyne configuration, where the light passes trough interferometric arms with a constant length. While scanning the tip across the sample we observe a plasmon fringe pattern, as shown in Fig. 3.11a, with the full plasmon wavelength $\lambda_{\mathrm{pl}}$ launched by the sharp metal edge on the left. This fringe pattern is measured because the incident electric field interferes with the plasmon field [238, 157]. We do not observe any plasmons reflected by the gold contact. We also observe a fringe pattern with $\lambda_{\mathrm{pl}}/2$ at the graphene edge due to edge reflected plasmons interfering with the plasmons launched by the tip [17, 16, 18]. The extracted plasmon wavelength at a gate voltage of $V_0 = -10$ V is $\lambda_{\mathrm{pl}} = (126 \pm 4)$ nm for both launched and reflected plasmons (Fig. 3.11a), in good agreement with the theoretically calculated 128 nm [18]. The drop of the optical signal at the gap position is mainly explained by the change in dielectric environment below the surface. Gold is known to have a high optical signal however the missing gold in the gaps leads to a drop of the optical signal.

By changing $V_{\mathrm{PS}}$ we observe a change in position of the launched plasmon fringes to the right of the phase shifter region (Fig. 3.11b). The phase shift can be extracted from the data using the simple

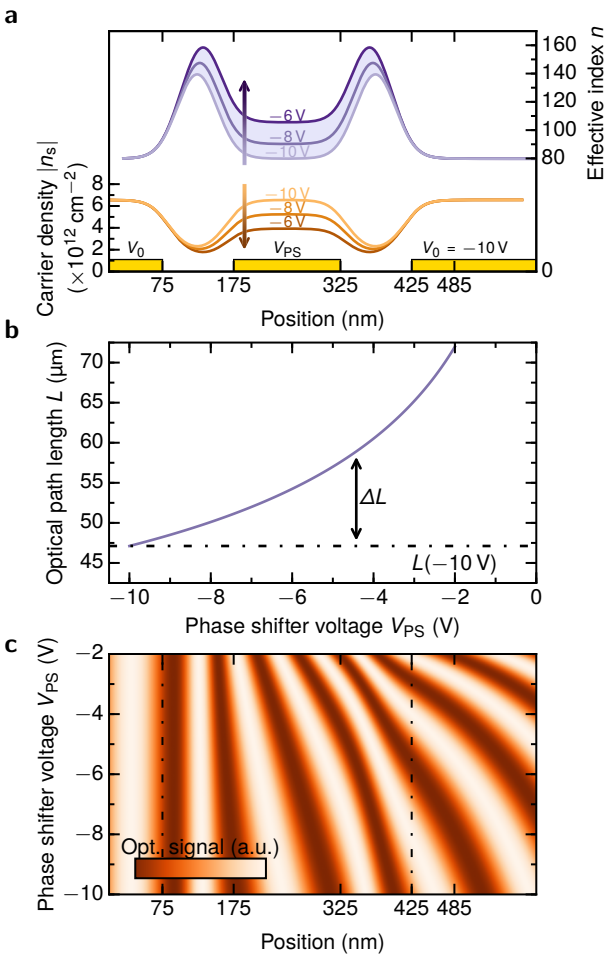


Figure 3.10: Working principle. Panel (a) Simulated spatial carrier density profile and the corresponding spatial profile of the plasmon effective index $n$, for a range of $V_{\mathrm{PS}}$. Varying $V_{\mathrm{PS}}$ leads to different optical path lengths $L$. The shaded area indicates the optical path difference $\Delta L = 7$ $\mu$m between $V_{\mathrm{PS}} = -10$ V and $V_{\mathrm{PS}} = -6$ V, equivalent to a phase shift of $\Delta\phi = 4/3\pi$ at $\lambda_0 = 10.6$ $\mu$m. The position of the local gates is indicated at the bottom. Panel (b) Calculated optical path length $L$ from 0 to 485 nm for a changing $V_{\mathrm{PS}}$ and a constant $V_0 = -10$ V. The optical path difference for the different configurations is indicated as $\Delta L$. Panel (c) Plasmons propagate from the left and start accumulating a different phase for different $V_{\mathrm{PS}}$ inside the phase shifting region (indicated by the two dashed lines) due to their different optical path lengths $L(V_{\mathrm{PS}})$.

relationship $\Delta\phi = k_{\mathrm{pl}}\Delta x$, with $k_{\mathrm{pl}} = 2\pi/\lambda_{\mathrm{pl}}$. We find that the wavelength of the plasmons to the right of the phase shifting region is independent of $V_{\mathrm{PS}}$. This confirms that that the carrier density is well defined for the region where we extract the light phase, and that the phase-shift only occurs in the phase-shifting region for positions from 100 to 350 nm.

In order to extract $\phi$ for different $V_{\mathrm{PS}}$ we remove the background optical signal by subtracting the smoothed optical signal both from data and fitting function. We then fit launched and edge reflected fringes using $\Re e(re^{i\phi}e^{ikx})$, where $\phi$ is the phase we are interested in and $r$ a real valued amplitude. The plasmon wavevector $k = k_{\mathrm{pl}} + k_{\mathrm{i}}i = 2\pi/126\mathrm{nm} - 1.5i$ $\mu\mathrm{m}^{-1}$ is fixed in order to capture the phase fully in $\phi$. The extracted inverse damping ratio $\gamma_{\mathrm{p}}^{-1} = k_{\mathrm{pl}}/k_{\mathrm{i}} \sim 30$ is in accordance with previous studies on high quality graphene encapsulated in h-BN at room temperature [18]. In order to compensate for small drifts in the interferometric arm length which can lead to a change in the fringe position, we measure the phase of the launched plasmons relative to the phase of the edge reflected plasmons. The edge reflected plasmons are not influenced by $V_{\mathrm{PS}}$ as the graphene edge is $\sim 2.7$ $\mu$m away (and thus more than the plasmon decay length) from the phase shifter gate (Fig. 3.11a). The phase of the

edge reflected plasmons is measured relative to the graphene edge from the simultaneously measured topography [18]. In Fig. 3.12a we show the measured phase shift $\Delta\phi$ relative to the plasmon phase

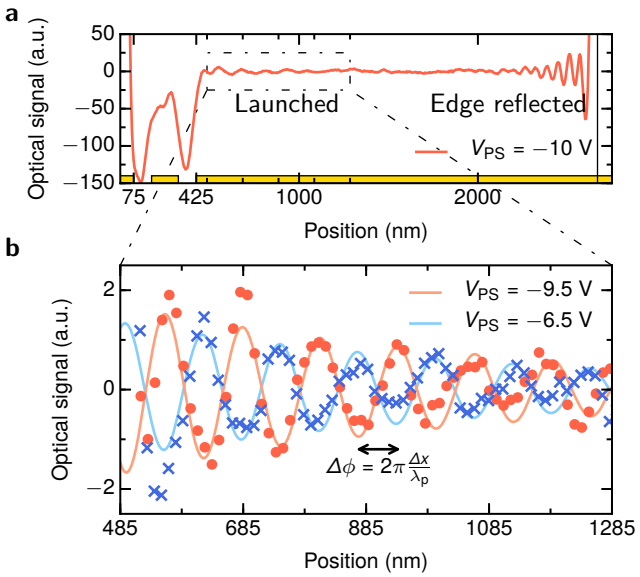


Figure 3.11: Measurement of full device and a phase shift of $\pi$. Panel (a) Optical signal of the full device with the launching contact at 0 nm and the position of all the gates indicated. For clarity a polynomial background was subtracted. The edge of the graphene is indicated as vertical solid line at 2670 nm. anel (b) Measurement (data points) and fits (solid lines) of the absolute value of the fourth harmonic of the optical signal with a smoothed optical signal background subtracted from both. The phase shift between $V_{PS} = -9.5$ V and $V_{PS} = -6.5$ V is $(1.04 \pm 0.11)\pi$.

measured at $V_{PS} = V_0 = -10$ V. We observe a fully tunable phase shift from 0 to $2\pi$ for a 6 V range. The blue line is the phase shift calculated from the optical path length approximation (OPLA) [239] using eq. 3.240, without fitting parameters. A good agreement with experiments is reached for small $V_{PS} - V_0$ but stronger deviation is clearly visible for larger $V_{PS} - V_0$. In order to quantitatively understand the behaviour of the phase shift, we employ the scattering approach described in Section 3.2. This approach reduces to the OPLA when the plasmon wavelength is much smaller than the length scale over which the carrier density changes. As for our device, these two lengthscales are comparable, the LS-RPA approach is required. Numerical results obtained with the LS-RPA approach as shown in Fig. 3.12a are in excellent agreement with experimental data. The essence of the LS-RPA approach is the following: We start by considering an inhomogeneous system where spatial variations of the carrier density profile are confined to a limited region of space. The propagating plasmon modes outside this region define the incoming and outgoing plane wave modes [199]. Complex transmission and reflection coefficients are evaluated from a long-wavelength expansion of the proper density-density linear response function. This is the point where the Random Phase Approximation (RPA) for an inhomogeneous electron system [199] is carried out, to approximate the proper density response function with the non-interacting one. Keeping only the leading term in the long-wavelength limit, one recovers the local approximation, [197] where only the local frequency-dependent conductivity function matters. A more quantitative understanding of the data, however, requires the first non-local correction to the long-wavelength expansion.

Using this approach we also calculate the expected optical rejection ratio $|r|^2$ for this device which is very small (Fig. 3.12b), owing to the smooth change of the plasmon wavelength. This makes this type of device an ideal candidate as a modulator as unwanted reflections are minimal. Indeed we do not observe plasmons reflected by the split gate as there are no plasmon fringes with spacing $\lambda_{pl}/2$ observed next to the phase shifting region.

One important figure-of-merit of a phase modulator is the half-wave voltage $V_\pi$, the voltage that needs to be applied to change the phase by $\pi$. Smaller voltages means more efficient operation. The voltage-length product $V_\pi l$ reached is 2.5 V $\mu$m, more than an order of magnitude smaller than for

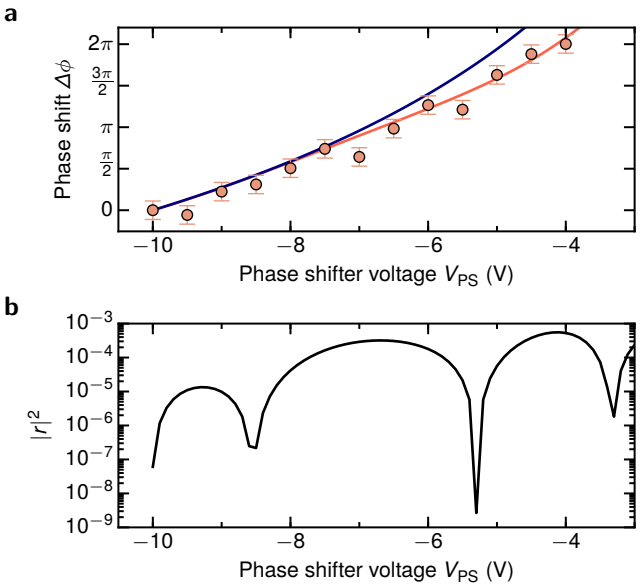


Figure 3.12: Phase shift $\Delta\phi$ and reflection magnitude. Panel (a) Calculated and measured phase shift with respect to the phase of the transmitted plasmon at a gate voltage of $-10\,\mathrm{V}$ applied to both the large gates and the phase shifter gate. The blue line is the phase shift calculated from $\Delta\phi = k_0\Delta L$ using the calculated optical path difference $\Delta L$. The red line is the phase shift calculated from Lippmann-Schwinger theory (see supplement). The error bar length of $\pm 0.11\pi$ is the standard deviation of the extracted phase of the launched plasmon for 12 measurements with $V_{\mathrm{PS}} = V_0 = -10\,\mathrm{V}$. Panel (b) Calculated reflection magnitude from the phase shifting device for a plane wave plasmon coming in from the left.

plasmonic phase modulators based on other materials (60 V $\mu$m) [242]. It is also much smaller than for diffraction limited phase modulators based on pin-photodiodes (360 V $\mu$m) [243] or pin-diodes with a photonic crystal (50 V $\mu$m) [244]. Commercially used lithium niobate modulators have much larger voltage-length products on the order of $\mathrm{V}\cdot\mathrm{cm}$. By decreasing the thickness of the bottom h-BN $V_\pi$ can even be further reduced. We have modelled our modulator using an equivalent circuit model (see supplement) and find that the cutoff frequency can be up to $\sim 1$ THz, but the real switching time will be limited be limited by other processes. We remark that the coupling efficiency from light to plasmons for these devices is very low. Improved matching schemes and resonant structures [237] are required for the development of practical modulators or metasurfaces.

## 3.4 Conclusion

In summary, we have presented a general theoretical framework to calculate the scattering properties of 2D plasmons in different inhomogeneous geometries.

In the interface problem discussed in Sect. 3.1 we considered only a sharp variation of the local conductivity, while in the scattering geometries discussed in Sect. 3.2 we considered more general types of perturbations. These include perturbations coupling to density, current, and real-spin operators. Moreover, non-local effects and exchange-correlation effects beyond the RPA are take into account. Since our scattering theory requires as an input the proper density-density response function of an inhomogeneous electron system, this is calculated in Appendix B.1 for a parabolic band electron gas and in Appendix B.2 for the Massless Dirac Fermion liquid in graphene.

We emphasize, for the sake of completeness, that the present theory has also been very successfully used to explain experimental data related to a plasmonic phase shifter realized by using encapsulated graphene [19].

The working principle and practical implementation of this device is carefully discussed in Sect. 3.3.

# Chapter 4

# Plasmons in topological materials

Recent years have witnessed a tremendous interest in the topological properties of matter, culminated with the 2016 Nobel prize awarded to D.J. Thouless, F.D M. Haldane, and J.M. Kosterlitz "For theoretical discoveries of topological phase transitions and topological phases of matter".

Electron transport is indeed affected by the topology of the band structure as discussed in Refs. [245, 246, 247]. More recently the interesting interplay of band-structure topology and electron-electron interactions was studied [248, 249, 204].

In particular the authors of Ref. [204] first showed that topologically non-trivial materials can host edge plasmon modes with a non-reciprocal dispersion relation. These modes have been dubbed Chiral Berry Plasmons (CBPs).

From the point of view of the long-wavelength electromagnetic response, the most important feature of topological materials is the appearance of a finite off-diagonal conductivity $\sigma_{xy}(\omega) \neq 0$ even in absence of a magnetic field [247, 61, 204, 205]. The latter is proportional to the Berry flux, which is the integral over the Fermi sphere of the Berry curvature of Bloch wavefunctions. It is therefore directly related to the geometrical properties of the band structure.

In this Chapter we generalize the theory of Ref. [204] to an arbitrary interface between two 2D materials having different normal conductivities and different Berry fluxes, and using different types of electron-electron interactions. We moreover calculate reflection and transmission coefficients for bulk modes through the interface. This provides an alternative way to probe the chirality of materials.

We finally discuss the impact of a finite damping rate, stemming for example from electron-phonon interactions, on the lifetime of CBPs.

## 4.1 Semiclassical theory of plasmons in the presence of a Berry flux

Plasmon excitations in two-dimensional (2D) materials can be described, at long wavelength, using semiclassical equations of motions for charge and current densities coupled to the electric field. These are the continuity equation

$$-i\omega\rho(\boldsymbol{r},\omega) + \partial_i J_i(\boldsymbol{r},\omega) = 0 \ , \tag{4.1}$$

where $\rho(\boldsymbol{r},\omega)$ is the excess *charge* density and $\boldsymbol{J}(\boldsymbol{r},\omega)$ is the *electric* current density, and the constitutive relation for the conductivity

$$J_i(\boldsymbol{r},\omega) = -\sigma_{ij}(\boldsymbol{r},\omega)\partial_j\phi(\boldsymbol{r},\omega) \ . \tag{4.2}$$

Here $\phi(\boldsymbol{r},\omega)$ is the *total* electric potential and $\sigma_{ij}(\boldsymbol{r},\omega)$ is a local conductivity which we parametrize in the following way

$$\sigma_{ij}(\boldsymbol{r},\omega) = \frac{i}{\pi\omega}\mathcal{D}(\boldsymbol{r})\delta_{ij} + \frac{e^2}{\hbar}\mathcal{F}(\boldsymbol{r})\epsilon_{ij} \ , \tag{4.3}$$

where $\mathcal{D}(\boldsymbol{r})$ is a spatially dependent Drude weight, $\mathcal{F}(\boldsymbol{r})$ is a spatially dependent Berry flux, and the tensors $\delta_{ij}$ and $\epsilon_{ij}$ are the 2D Kronecker and Levi-Civita tensors respectively.

Combining Eqs. (4.1-4.2-4.3) we obtain

$$\begin{aligned} -i\omega\rho(\boldsymbol{r},\omega) = \partial_i[\sigma_{ij}(\boldsymbol{r})\partial_j\phi(\boldsymbol{r},\omega)] = \frac{i}{\pi\omega}\mathcal{D}(\boldsymbol{r})\partial_i\partial_i\phi(\boldsymbol{r},\omega) \\ +\frac{i}{\pi\omega}\partial_i\mathcal{D}(\boldsymbol{r})\partial_i\phi(\boldsymbol{r},\omega) + \frac{e^2}{\hbar}\epsilon_{ij}\partial_i\mathcal{F}(\boldsymbol{r})\partial_j\phi(\boldsymbol{r},\omega) \ . \end{aligned} \tag{4.4}$$

Please note that only the gradient of $\mathcal{F}(\boldsymbol{r})$ appears in Eq. (4.4), therefore a spatially uniform Berry flux has no impact on plasmon propagation. This is in contrast to what happens in the presence of magnetic field where a gap is opened in plasmon dispersion even with a spatially uniform magnetic field.

To close the problem and calculate the spectrum of density oscillations we need another relation between the two fields $\phi(\boldsymbol{r},\omega)$ and $\rho(\boldsymbol{r},\omega)$. This is provided by electrostatics and is in general in the form of an integral relation of the type

$$\phi(\boldsymbol{r},\omega) = \int d\boldsymbol{r}' L(\boldsymbol{r}-\boldsymbol{r}')\rho(\boldsymbol{r}',\omega) \ . \tag{4.5}$$

Here the kernel $L(\boldsymbol{r})$ takes into account the screening of the Coulomb interaction by the surrounding dielectric environment.

In the following we will discuss three different forms of this relation and compare the corresponding results.

### 4.1.1 Interface Model

We now specialize Eq. (4.4) to a system formed by two half planes filled by different media separated by a sharp interface located at $x = 0$. The Drude weight has the form

$$\mathcal{D}(\boldsymbol{r}) = \mathcal{D}_0\left[1 + \frac{\Delta}{2}\ \mathrm{sgn}(x)\right] \ , \tag{4.6}$$

since the Drude weight is a semi-positive defined quantity only values of $|\Delta| \leq 2$ are meaningful. However, since considering $\Delta < 0$ is equivalent to a reflection $x \mapsto -x$ we will consider only $0 \leq \Delta \leq 2$. In a similar way the spatial variation of the Berry flux is described by

$$\mathcal{F}(\boldsymbol{r}) = \mathcal{F}_0 + \frac{\Delta_{\mathcal{F}}}{2}\ \mathrm{sgn}(x) \ , \tag{4.7}$$

where $\Delta_{\mathcal{F}}$ can now take any real value. Thanks to translational invariance in the $y$ direction we can write the charge density and the electric potential as

$$\phi(\boldsymbol{r},\omega) = e^{iqy}\phi(x,q,\omega) \ , \tag{4.8}$$

and

$$\rho(\boldsymbol{r},\omega) = e^{iqy}\rho(x,q,\omega) \ . \tag{4.9}$$

We now decompose the potential and density profile on the two sides of the interface according to

$$\phi(x,q,\omega) = \Theta(-x)\phi_<(x,q,\omega) + \Theta(x)\phi_>(x,q,\omega) \ , \tag{4.10}$$

and

$$\begin{aligned} \rho(x,q,\omega) = \Theta(-x)\rho_<(x,q,\omega) + \Theta(x)\rho_>(x,q,\omega) \\ + \delta(x)\rho_{\mathrm{I}}(q,\omega) \ . \end{aligned} \tag{4.11}$$

Here we allowed the potential to have at most a simple discontinuity at $x = 0$, while the charge density is allowed to have a delta function singularity at $x = 0$ describing the build-up of an interface charge density $\rho_{\mathrm{I}}(q,\omega)$. Away from the origin Eq. (4.4) reduces to

$$-i\omega\rho_{\lessgtr}(x,q,\omega) = \frac{i\mathcal{D}_0}{\pi\omega}\left(1 \mp \frac{\Delta}{2}\right)\left(\partial_x^2 - q^2\right)\phi_{\lessgtr}(x,q,\omega) \ . \tag{4.12}$$

Integrating Eq. (4.4) around the origin we obtain a matching boundary condition

$$-\frac{\omega^2\pi}{\mathcal{D}_0}\rho_{\rm I}(q,\omega) = \left(1+\frac{\Delta}{2}\right)\partial_x\phi_>(0,q,\omega) - \left(1-\frac{\Delta}{2}\right)\partial_x\phi_<(0,q,\omega) + \frac{q\omega}{\Omega_0}\left[\left(\mathcal{F}_0+\frac{\Delta_\mathcal{F}}{2}\right)\phi_>(0,q,\omega) - \left(\mathcal{F}_0-\frac{\Delta_\mathcal{F}}{2}\right)\phi_<(0,q,\omega)\right] . \tag{4.13}$$

where $\Omega_0 \equiv \hbar\mathcal{D}_0/(e^2\pi)$.

We now need an electrostatic interaction of the type

$$\phi(x,q,\omega) = \int dx' L(x-x',q)\rho(x',q,\omega) . \tag{4.14}$$

In the following we analyze separately three possible forms of the interaction kernel $L(x,q)$. The first one is the so-called Local Capacitance Approximation (LCA)

$$L_{\rm LCA}(x,q) = \frac{1}{C}\delta(x) . \tag{4.15}$$

This approximation works well when interactions are screened by a conducting gate near the plane of the 2D electron system and predicts the existence of acoustic plasmon modes in bulk 2D materials.

We then consider an approximated kernel proposed by Fetter to reproduce the long-wavelength behavior of Coulomb interaction but allowing for analytical solution of the resulting equations. This reads

$$L_{\rm Fetter}(x,q) = \sqrt{2}\pi e^{-\sqrt{2}|q||x|} . \tag{4.16}$$

Finally we consider the full Coulomb interaction. In Fourier transform with respect to the $y$ direction this reads

$$L_{\rm Coulomb}(x,q) = 2K_0(|q||x|) . \tag{4.17}$$

This last case will require the Wiener-Hopf solution, discussed in Chapter 3, of the corresponding integro-differential equation.

### 4.1.2 Local capacitance approximation

In this case we set the boundary charge $\rho_{\rm I}(q,\omega)$ to zero because building a localized charge density with the LCA electrostatic interaction would cost infinite energy. Making use of LCA Eq. (4.12) becomes

$$\left[\partial_x^2 + \frac{\omega^2}{v_\lessgtr^2} - q^2\right]\phi_\lessgtr(x,q,\omega) = 0 , \tag{4.18}$$

where $v_\lessgtr = v_0\sqrt{1\mp\Delta/2}$ and $v_0 = \sqrt{\mathcal{D}_0/(\pi C)}$. This equation is a one-dimensional (1D) wave equation that has propagating solutions in the left (right) half-plane if $\omega^2 > v_\lessgtr^2 q$, and localized solutions if $\omega^2 < v_\lessgtr^2 q$. In the remaining part of this section we will analyze the propagating and bound solutions of Eq. (4.18) with the boundary condition (4.13) for arbitrary values of $\Delta$ and $\Delta_\mathcal{F}$. The case of $\Delta = 2$ corresponding to an interface with a non-conducting medium in the left half-plane is singular and will be handled separately.

#### Interface between conducting media ($0 \le \Delta < 2$)

We can identify three different regimes of the solutions of Eq. (4.18) corresponding to three different regions of the $q$-$\omega$ diagram in Fig. 4.1a. For $\omega^2 > v_> q$ (dark shaded region in Fig. 4.1a) the solution of (4.18) has an oscillating behavior on both sides of the interface. This represents plasmons propagating from one side of the interface to the other. We define $k_\lessgtr = \sqrt{\omega^2/v_\lessgtr^2 - q^2}$ and look for a solution of the type

$$\phi(x,q,\omega) = \begin{cases} e^{ik_< x} + re^{-ik_< x} & x < 0 \\ te^{ik_> x} & x > 0 , \end{cases} \tag{4.19}$$

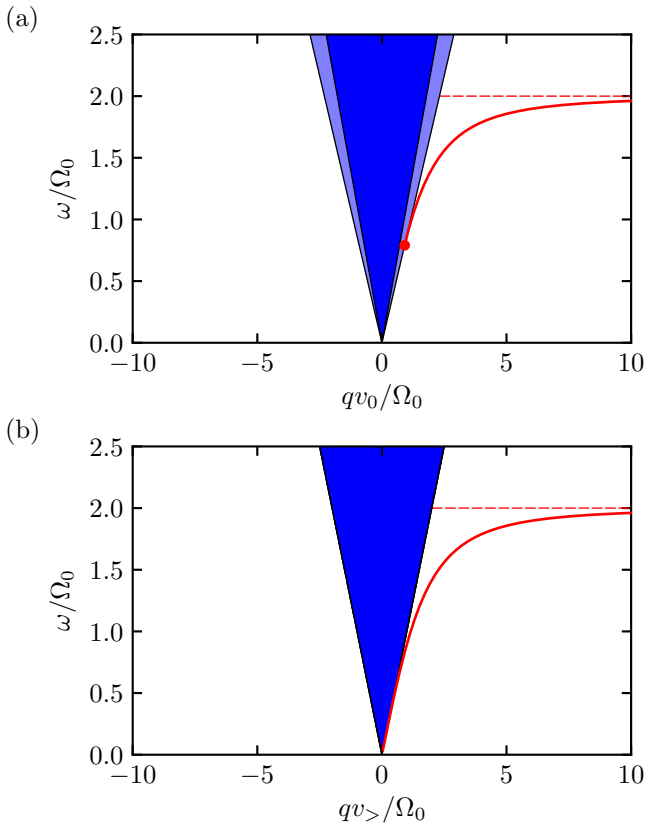


Figure 4.1: Panel (a) shows the bound state dispersion for $\Delta = 0.5$, $\Delta_{\mathcal{F}} = 1$ (red thick line), the dark shaded region represents the continuum of propagating states, the light shaded region represents the continuum of TIR states. The red dashed line is the asymptotic value of the bound mode frequency for large values of $q$. Panel (b) is the same as panel (a) but for either $\Delta = 0$ or $\Delta = 2$, and $\Delta_{\mathcal{F}} = 1$.

corresponding to an impinging wave plus a reflected wave in the left-half plane and a transmitted wave in the right half plane. Enforcing the continuity of the potential at $x = 0$ and the the boundary condition (4.13) we obtain the reflection coefficient

$$r = \frac{-\frac{\Delta}{2} - \frac{k_> - k_<}{k_< + k_>} + i\frac{q\omega\Delta_{\mathcal{F}}}{\Omega_0(k_< + k_>)}}{1 + \frac{\Delta(k_> - k_<)}{2(k_< + k_>)} - i\frac{q\omega\Delta_{\mathcal{F}}}{\Omega_0(k_< + k_>)}} \ , \tag{4.20}$$

and the transmission coefficient

$$t = \frac{\left(1 - \frac{\Delta}{2}\right)\frac{2k_<}{k_< + k_>}}{1 + \frac{\Delta(k_> - k_<)}{2(k_< + k_>)} - i\frac{q\omega\Delta_{\mathcal{F}}}{\Omega_0(k_< + k_>)}} \ . \tag{4.21}$$

If $v_> q > \omega^2 > v_< q$ (light-shaded area in Fig. 4.1a) the solution of Eq. (4.18) is a propagating wave for $x < 0$ and an evanescent wave for $x > 0$. This corresponds to Total Internal Reflection (TIR) of plasmon impinging from the left side. In this case we look for a solution of the type

$$\phi(x, q, \omega) = \begin{cases} e^{ik_< x} + re^{-ik_< x} & x < 0 \\ (1 + r)e^{-\lambda_>^{-1} x} & x > 0 \ , \end{cases} \tag{4.22}$$

where $\lambda_>^{-1} \equiv \sqrt{q^2 - \omega^2/v_>^2}$ and we explicitly enforced the continuity of potential at $x = 0$. Making use of the boundary condition (4.13) we obtain

$$r = \frac{\frac{1}{2}\left(1 - \frac{i}{k_<\lambda_>}\right) - \frac{\Delta}{4}\left(1 + \frac{i}{k_<\lambda_>}\right) + i\frac{q\omega\Delta_{\mathcal{F}}}{2k_<\Omega_0}}{\frac{1}{2}\left(1 + \frac{i}{k_<\lambda_>}\right) - \frac{\Delta}{4}\left(1 - \frac{i}{k_<\lambda_>}\right) - i\frac{q\omega\Delta_{\mathcal{F}}}{2k_<\Omega_0}} \ . \tag{4.23}$$

In the region of the $q$-$\omega$ plane where $\omega^2 < v_<^2 q^2$ (white area of Fig. 4.1a) the solutions of the wave equation (4.18) are evanescent waves on the two sides of the interface. This means that bound plasmonic states can occur in this region. This states have the form

$$\phi(x, q, \omega) = \begin{cases} e^{\lambda_<^{-1} x} & x < 0 \\ e^{-\lambda_>^{-1} x} & x > 0 \ , \end{cases} \tag{4.24}$$

where $\lambda_<^{-1} \equiv \sqrt{q^2 - \omega^2/v_<^2}$. Enforcing the boundary condition (4.13) we conclude that bound states can occur for values of $q$ and $\omega$ that solve the following equation

$$\frac{q\omega\Delta_{\mathcal{F}}}{\Omega_0} = \left(1 + \frac{\Delta}{2}\right)\lambda_>^{-1} + \left(1 - \frac{\Delta}{2}\right)\lambda_<^{-1} \ . \tag{4.25}$$

A solution to this equation exists if $|q|$ exceeds the critical value

$$q_{\rm cr} = \sqrt{\frac{\Delta(2 + \Delta)}{\Delta_{\mathcal{F}}^2(2 - \Delta)}}\frac{\Omega_0}{v_0} \ , \tag{4.26}$$

and is given by

$$\omega = \Omega_0 \mathrm{sgn}(q\Delta_{\mathcal{F}}) \times \\ \times \sqrt{\frac{(\Delta^2 + 4)\Delta_{\mathcal{F}}^2 q^4 v_0^4 + 4\Delta^2 q^2 v_0^2 \Omega_0^2 + \mathrm{sgn}(q\Delta_{\mathcal{F}})\Delta_{\mathcal{F}} q^3 v_0^3 \sqrt{(4 - \Delta^2)[q^2 v_0^2 \Delta_{\mathcal{F}}^2(4 - \Delta^2) - 8\Delta^2\Omega_0^2]}}{2\left(\Delta^2\Omega_0^4 + \Delta_{\mathcal{F}}^4 q^4 v_0^4 + 4\Delta_{\mathcal{F}}^2 q^2 v_0^2 \Omega_0^2\right)}} \ . \tag{4.27}$$

A plot of this dispersion relation for $\Delta = 1$ and $\Delta_{\rm F} = 1$ is shown in Fig. 4.1a. The frequency of the bound mode ranges from $\pm\omega_{\rm cr}$

$$\omega_{\rm cr} = \sqrt{\frac{\Delta(2 + \Delta)}{2\Delta_{\mathcal{F}}^2}}\Omega_0 \ , \tag{4.28}$$

corresponding to the point where the mode detaches from the continuum of TIR states, to its asymptotic value $\omega_\infty$, where

$$\omega_\infty = \frac{2\Omega_0}{|\Delta_{\mathcal{F}}|} \ . \tag{4.29}$$

**Homogeneous normal conductivity ($\Delta = 0$)**

It is worthwhile considering the case of uniform normal conductivity. In this case $v_< = v_> = v_0$, the TIR region is shrunk down to a line and the expression for propagating and bound modes are simplified considerably. Reflection and transmission coefficients are given by

$$r = \frac{i\eta}{1 - i\eta} \ , \tag{4.30}$$

and

$$t = \frac{1}{1 - i\eta} \ , \tag{4.31}$$

where

$$\eta = \frac{q\omega}{2k\Omega_0}\Delta\mathcal{F} \ . \tag{4.32}$$

The critical wavevector value $q_{\rm cr}$ vanishes and the bound mode becomes gapless, with the simpler dispersion relation

$$\omega = \frac{qv_0 \ \mathrm{sgn}(\Delta_\mathcal{F})}{\sqrt{1 + \frac{q^2 v_0^2 \Delta_\mathcal{F}^2}{4\Omega_0^2}}} \ . \tag{4.33}$$

It is also interesting to consider a more general case of this type of interface. We assume to have a material with a uniform Drude weight $\mathcal{D}_0$ and a Berry flux that depends only on $x$, i. e. $\mathcal{F}(\boldsymbol{r}) = \mathcal{F}(x)$. Under these conditions and applying LCA we obtain an equation for the electric potential

$$-\partial_x^2\phi(x,q,\omega - \frac{\omega q}{\Omega_0}\partial_x\mathcal{F}(x)\phi(x,q,\omega) = \left(\frac{\omega^2}{v_0^2} - q^2\right)\phi(x,q,\omega) \ , \tag{4.34}$$

that is analogous to the Schrödinger equation for a particle of mass $m$ in one spatial dimension with a scalar potential $2mU(x)/\hbar^2 = -(\omega q/\Omega_0)\partial_x\mathcal{F}(x)$. We can therefore use theorems on existence of a bound state in 1D quantum mechanics to draw general conclusion on the existence of plasmonic bound states at an interface even if the spatial variation of $\mathcal{F}(x)$ is spread over some finite length.

**Insulator-conductor interface ($\Delta = 2$)**

In this case $v_< = 0$, therefore $\phi_<(x) = \rho_<(x) = 0$ and the boundary condition (4.13) reduces to

$$2\partial_x\phi_>(0,q,\omega) + \frac{q\omega}{\Omega_0}\mathcal{F}_>\phi_>(0,q,\omega) = 0 \ . \tag{4.35}$$

where $\mathcal{F}_> = \mathcal{F}_0 + \Delta_\mathcal{F}/2$.

For $\omega^2 > q^2 v_>^2$ the system supports propagating modes of the form

$$\phi(x,q,\omega) = e^{-ik_> x} + e^{ik_> x}\frac{1 + i\eta}{1 - i\eta} \tag{4.36}$$

where

$$\eta = \frac{q\omega}{2k\Omega_0}\mathcal{F}_> \ . \tag{4.37}$$

For $\omega^2 < q^2 v_>^2$ we obtain from (4.13) the following condition for the existence of bound modes

$$-\frac{1}{\lambda_>} + \frac{q\omega\mathcal{F}_>}{2\Omega_0} = 0 \ . \tag{4.38}$$

This leads to the dispersion relation

$$\omega = \frac{qv_> \ \mathrm{sgn}\left(\mathcal{F}_>\right)}{\sqrt{1 + \frac{v_>^2 \mathcal{F}_>^2 q^2}{4\Omega_0^2}}} \ . \tag{4.39}$$

### 4.1.3 Fetter interaction

The integral relation (4.14) with the approximated kernel (4.16) proposed by Fetter[127, 128] can be easily inverted yielding a purely differential relation between the charge density and the electric potential

$$\rho(x,q,\omega) = \frac{1}{4\pi|q|}(2q^2 - \partial_x^2)\phi(x,q,\omega) \ . \tag{4.40}$$

Substitution into (4.12) gives a second order differential equation for the potential at each side of the interface

$$\partial_x^2\phi_{\lessgtr}(x,q,\omega) + q^2\frac{2\omega^2 - 4\mathcal{D}_0|q|(1\mp\Delta/2)}{4\mathcal{D}_0|q|(1\mp\Delta/2)-\omega^2}\phi_{\lessgtr}(x,q,\omega) = 0 \ . \tag{4.41}$$

If the coefficient of the second term of the above equation is positive the solutions are traveling waves, while if this coefficient is negative the solutions are exponentially localized. Therefore, propagating modes exist in the left (right) plane for values of $\omega$ such that

$$\sqrt{2\mathcal{D}_0(1\mp\Delta/2)|q|} < |\omega| < \sqrt{4\mathcal{D}_0(1\mp\Delta/2)|q|} \ . \tag{4.42}$$

Note that this approximate interaction predicts the existence of an *unphysical* upper boundary of the continuum of propagating states.

The solutions of Eq. (4.41) on the two sides of the interface must be matched according to a suitable boundary condition.

The convolution of the well behaved functions $\phi_{\lessgtr}(x,q,\omega)$ with the interaction kernel (4.16) gives a function with continuous derivative, while the potential generated by the interface charge density $\rho_{\rm I}(q,\omega)$ has a discontinuous derivative at $x=0$. The discontinuity of the derivative of the potential is therefore given by

$$\partial_x\phi_>(0,q,\omega) - \partial_x\phi_<(0,q,\omega) = -4\pi|q|\rho_{\rm I}(q,\omega) \ . \tag{4.43}$$

Making use of the continuity of the potential on the two sides of the interface

$$\phi_>(0,q,\omega) = \phi_<(0,q,\omega) \ , \tag{4.44}$$

and substituting (4.43) into the general boundary condition (4.13) yields

$$-\left(1 - \frac{\omega^2}{4\mathcal{D}_0|q|} + \frac{\Delta}{2}\right)\partial_x\phi_>(0,q,\omega) + \left(1 - \frac{\omega^2}{4\mathcal{D}_0|q|} - \frac{\Delta}{2}\right)\partial_x\phi_<(0,q,\omega) = \frac{q\omega\Delta_{\mathcal{F}}}{\Omega_0}\phi_>(0,q,\omega) \ , \tag{4.45}$$

In the remainder of this section we analyze separately the three relevant cases as done with the LCA interaction. First of all we solve the general case $0 \le \Delta < 2$, then we analyze in more detail the case $\Delta = 0$, and finally we solve separately the singular case $\Delta = 2$. For each case we calculate transmission and reflection coefficients for travelling modes and the dispersion relation of bound modes.

#### Interface between conducting media ($0 \le \Delta < 2$)

For values of $\omega$ in the range

$$\sqrt{2\mathcal{D}_0(1+\Delta/2)|q|} < |\omega| < \sqrt{4\mathcal{D}_0(1-\Delta/2)|q|} \ , \tag{4.46}$$

the solution to Eq. (4.41) is a travelling wave on both sides of the interface. In this region of the $q$-$\omega$ plane (blue-shaded region in Fig. 4.2) we can define the $x$ component of the wavevector as the *real* and positive value

$$k_{\lessgtr} = |q|\sqrt{\frac{2\omega^2 - 4\mathcal{D}_0|q|(1\mp\Delta/2)}{4\mathcal{D}_0|q|(1\mp\Delta/2)-\omega^2}} \ . \tag{4.47}$$

We look for a solution of the type described in (4.19). Using the boundary conditions (4.44-4.45) we obtain the reflection coefficient

$$r = \frac{-\frac{\Delta}{2} - \left(1 - \frac{\omega^2}{4\mathcal{D}_0|q|}\right)\frac{k_>-k_<}{k_<+k_>} + i\frac{q\omega\Delta_{\mathcal{F}}}{\Omega_0(k_<+k_>)}}{1 - \frac{\omega^2}{4\mathcal{D}_0|q|} + \frac{\Delta(k_>-k_<)}{2(k_<+k_>)} - i\frac{q\omega\Delta_{\mathcal{F}}}{\Omega_0(k_<+k_>)}} \ , \tag{4.48}$$

and the transmission coefficient

$$t = \frac{\left(1 - \frac{\omega^2}{4\mathcal{D}_0|q|} - \frac{\Delta}{2}\right)\frac{2k_<}{k_< + k_>}}{1 - \frac{\omega^2}{4\mathcal{D}_0|q|} + \frac{\Delta(k_> - k_<)}{2(k_< + k_>)} - i\frac{q\omega\Delta_\mathcal{F}}{\Omega_0(k_< + k_>)}} \ . \tag{4.49}$$

The continuum of TIR states lies in the region

$$\sqrt{2\mathcal{D}_0(1+\Delta/2)|q|} < |\omega| < \min\left\{\sqrt{4\mathcal{D}_0(1-\Delta/2)|q|}, \sqrt{2\mathcal{D}_0(1+\Delta/2)|q|}\right\} \ , \tag{4.50}$$

(light-shaded ragion if Fig. 4.2). Here we look for a solution of the type (4.22), and we obtain, for the reflection coefficient

$$r = \frac{\frac{1}{2}\left(1 - \frac{\omega^2}{4\mathcal{D}_0|q|}\right)\left(1 - \frac{i}{k_<\lambda_>}\right) - \frac{\Delta}{4}\left(1 + \frac{i}{k_<\lambda_>}\right) + i\frac{q\omega\Delta_\mathcal{F}}{2k_<\Omega_0}}{\frac{1}{2}\left(1 - \frac{\omega^2}{4\mathcal{D}_0|q|}\right)\left(1 + \frac{i}{k_<\lambda_>}\right) - \frac{\Delta}{4}\left(1 - \frac{i}{k_<\lambda_>}\right) - i\frac{q\omega\Delta_\mathcal{F}}{2k_<\Omega_0}} \ . \tag{4.51}$$

Bound states can exist when $\omega^2 < 2\mathcal{D}_0|q|(1-\Delta/2)$. Defining the decay lengths as

$$\lambda_\lessgtr = |q|\sqrt{\frac{4\mathcal{D}_0|q|(1 \mp \Delta/2) - 2\omega^2}{4\mathcal{D}_0|q|(1 \mp \Delta/2) - \omega^2}} \ , \tag{4.52}$$

we look for solutions in the same form as in (4.24). Using the boundary contition (4.45) we obtain the bound state equation

$$\frac{1 - \frac{\omega^2}{4\mathcal{D}_0|q|} + \frac{\Delta}{2}}{\lambda_>} + \frac{1 - \frac{\omega^2}{4\mathcal{D}_0|q|} - \frac{\Delta}{2}}{\lambda_<} = \frac{q\omega\Delta_\mathcal{F}}{\Omega_0} \ . \tag{4.53}$$

We can rewrite it in terms of the dimensionless variables

$$x \equiv \frac{\omega}{\sqrt{4\mathcal{D}_0|q|}} \ , \tag{4.54}$$

$$y \equiv \frac{\mathrm{sgn}(q)\sqrt{4\mathcal{D}_0|q|}\Delta_\mathcal{F}}{2\Omega_0} \ , \tag{4.55}$$

obtaining

$$\sqrt{1 - x^2 + \frac{\Delta}{2}}\sqrt{1 - 2x^2 + \frac{\Delta}{2}} + \sqrt{1 - x^2 - \frac{\Delta}{2}}\sqrt{1 - 2x^2 - \frac{\Delta}{2}} = 2xy \ , \tag{4.56}$$

This is equivalent to the third degree equation for $x^2$

$$x^6 - \frac{48y^2 + 16y^4 + 9\Delta^2}{32y^2}x^4 + \frac{4y^2 + (3+y^2)\Delta^2}{8y^2}x^2 = \frac{\Delta^2}{8y^2} \ , \tag{4.57}$$

under the conditions

$$x < \frac{2-\Delta}{4} \ , \tag{4.58}$$

$$xy > 0 \ , \tag{4.59}$$

$$|4x^2 - 3 - 2y^2| < \sqrt{1 - 2\Delta^2 + 12y^2 + 4y^4} \ , \tag{4.60}$$

Eq. 4.57 has at most one acceptable solution $x_0^2(y)$ for a given valuee of $y$ that we calculate numerically. The dispersion relation of the bound mode is then obtained as

$$\omega = \sqrt{4\mathcal{D}_0|q|}\mathrm{sgn}(q\Delta_\mathcal{F})\sqrt{x_0^2\left(\frac{\mathrm{sgn}(q)\sqrt{4\mathcal{D}_0|q|}\Delta_\mathcal{F}}{2\Omega_0}\right)} \tag{4.61}$$

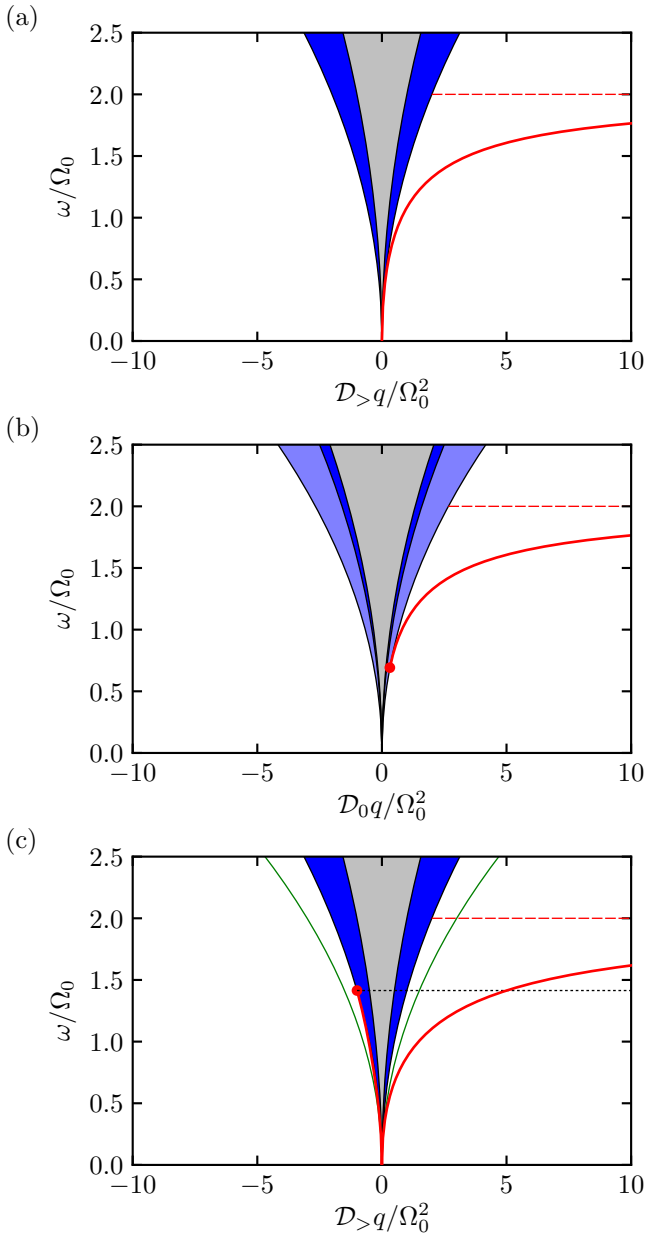


Figure 4.2: Dispersion relation of the bound state (red thcik lines) calculated using Fetter approximate interaction for different values of the parameter $\Delta$: panel (a) $\Delta = 0$ and $\Delta_{\mathcal{F}} = 1$, panel (b) $\Delta = 0.5$ and $\Delta_{\mathcal{F}} = 1$, panel (c) $\Delta = 2$ and $\Delta_{\mathcal{F}} = 1$. Red dashed lines mark the asymptotic frequency $\Omega_\infty = 2\Omega_0/\Delta_{\mathcal{F}}$, blue shaded regions represent the continuum of propagating states, the light-blue shaded region in panel (b) is the continuum of TIR states, the gray-shaded regions are the regions where the Fetter interaction fails to represent continuum states. Red dots mark the positions where the bound mode merges into the continuum. In panel (c) the black dotted line marks the treshold frequency $\omega_{\mathrm{T}}$ above wich only a forward-moving mode is present, while the green thin lines represent the bound states at $\Delta_{\mathcal{F}} = 0$.

**Homogeneous normal conductivity ($\Delta = 0$)**

In this particular case (Fig. 4.2a) the TIR states are not present and the expressions for $r$ and $t$ simplify to

$$r = \frac{i\eta}{1 - \frac{\omega^2}{4\mathcal{D}_0|q|} - i\eta} \ , \tag{4.62}$$

and

$$t = \frac{1 - \frac{\omega^2}{4\mathcal{D}_0|q|}}{1 - \frac{\omega^2}{4\mathcal{D}_0|q|} - i\eta} \ . \tag{4.63}$$

Where $\eta$ is given by (4.32).

A bound state can exist for $\omega^2 < 2\mathcal{D}_0|q|$. Defining

$$\lambda^{-1} = |q|\sqrt{\frac{1 - \frac{\omega^2}{2\mathcal{D}_0|q|}}{1 - \frac{\omega^2}{4\mathcal{D}_0|q|}}} \ , \tag{4.64}$$

we obtain the bound-state equation

$$\frac{2}{\lambda}\left(1 - \frac{\omega^2}{4\mathcal{D}_0|q|}\right) = \frac{q\omega\Delta_{\mathcal{F}}}{\Omega_0} \ , \tag{4.65}$$

that we can rewrite in terms of the dimension-less variables previously defined as

$$\sqrt{1-x^2}\sqrt{1-2x^2} = xy \ , \tag{4.66}$$

This is equivalent to

$$x^4 - \frac{3+y^2}{2}x^2 + \frac{1}{2} = 0 \ , \tag{4.67}$$

under the conditions

$$xy > 0 \ , \tag{4.68}$$

$$|x| < \frac{1}{2} \ . \tag{4.69}$$

The only acceptable solution is therefore

$$x_0^2(y) = \frac{3 + y^2 - \sqrt{1 + 6y^2 + y^4}}{4} \ , \tag{4.70}$$

which leads to the dispersion relation

$$\begin{aligned} \omega &= \mathrm{sgn}(q\Delta_{\mathcal{F}})\sqrt{\mathcal{D}_0|q|\left[3 + \frac{\mathcal{D}_0\Delta_{\mathcal{F}}^2|q|}{\Omega_0^2} - \sqrt{1 + 6\frac{\mathcal{D}_0\Delta_{\mathcal{F}}^2|q|}{\Omega_0^2} + \left(\frac{\mathcal{D}_0\Delta_{\mathcal{F}}^2|q|}{\Omega_0^2}\right)^2}\right]} \approx \\ &\approx \mathrm{sgn}(q\Delta_{\mathcal{F}})\begin{cases}\sqrt{2\mathcal{D}_0|q|} & |q| \to 0 \\ \omega_\infty & |q| \to \infty \ .\end{cases} \end{aligned} \tag{4.71}$$

**Insulator-conductor interface ($\Delta = 2$)**

This section makes contact with Ref. [204] reproducing its calculations. In this case plasmons can propagate only for $x > 0$. Travelling states are in the form

$$\phi(x, q, \omega) = e^{-ik_> x} + e^{ik_> x}\frac{1 + i\eta}{1 - i\eta} \tag{4.72}$$

where

$$\eta = \frac{\frac{\omega^2\sqrt{2}}{8\mathcal{D}_0 k_>} + \frac{q\omega}{2k_>\Omega_0}\Delta_{\mathcal{F}}}{1 - \frac{\omega^2}{8\mathcal{D}_0|q|}} \ . \tag{4.73}$$

The bound state equation reads

$$\frac{2-\frac{\omega^2}{4\mathcal{D}_0|q|}}{\lambda_>}-\frac{\omega^2}{4\mathcal{D}_0|q|}\sqrt{2}|q|=\frac{q\omega\Delta_{\mathcal{F}}}{\Omega_0}\ , \tag{4.74}$$

that is equivalent, using dimension-less variables to

$$\sqrt{1-x^2}\sqrt{1-\frac{x^2}{2}}=\frac{x^2}{\sqrt{2}}+xy\ , \tag{4.75}$$

This reduces to the third degree equation

$$x^3+\frac{3+2y^2}{2\sqrt{2}y}x^2-\frac{1}{\sqrt{2}y}=0\ , \tag{4.76}$$

under the condition

$$x\left(y+\frac{x}{\sqrt{2}}\right)>0\ , \tag{4.77}$$

For $q\omega\Delta_{\mathcal{F}}<0$ a bound mode exist for $|q|<q_{\rm T}$ and $|\omega|<\omega_{\rm T}$, with threshold values given by $q_{\rm T}=\Omega_0^2/(2\mathcal{D}_0\Delta_{\mathcal{F}}^2)$ and $\omega_{\rm T}=\sqrt{2}\Omega_0/|\Delta_{\mathcal{F}}|$.

### 4.1.4 Coulomb interaction

The inverse of the full 2D Coulomb interaction kernel is not a simple differential operator. To solve the resulting integro-differential equation in this case a more advanced mathematical technique due to Wiener and Hopf is needed. This is discussed in detail in Ref. [130] and in Section 3.1 of this Thesis.

Here we summarize the results for the bound states.

#### Interface between conducting media ($0<\Delta<2$)

For this case the Wiener-Hopf technique leads to the equation for the bound states

$$\frac{\Delta\coth[I(x)]}{2x}=\mathrm{sgn}(q)\Delta_{\mathcal{F}}\frac{\sqrt{2\mathcal{D}_0|q|}}{2\Omega_0}. \tag{4.78}$$

Here, $x=\omega/\sqrt{2\mathcal{D}_0|q|}$, with $|x|<\sqrt{1-\Delta/2}$,

$$2I(x)=\ln\left(\frac{1+\Delta/2}{1-\Delta/2}\right)+f\left(\frac{x}{\sqrt{1-\Delta/2}}\right)-f\left(\frac{x}{\sqrt{1+\Delta/2}}\right), \tag{4.79}$$

and the function $f(x)$ is defined by the integral

$$f(x)=-\frac{2}{\pi}\int_0^{\pi/2}d\theta\ln(1-x^2\sin\theta). \tag{4.80}$$

The latter must in general be evaluated numerically. We note however that $f(0)=0$ and $f(1)=\ln(2)+4\boldsymbol{G}/\pi$ where $\boldsymbol{G}\approx 0.916$ is the Catalan constant. We consider only positive values of $x$ since negative frequency solutions are redundant and can be obtained by inverting frequency and wavevector. For positive values of $x$ the left hand side of (4.78) has codomain $[b,\infty]$ with $b=\Delta\coth[I(\sqrt{1-\Delta/2})]/(2\sqrt{1-\Delta/2})$. Eq. (4.78) has therefore solutions only if the right hand side is larger than $b$. This happens when $\mathrm{sgn}(q\Delta_{\mathcal{F}})>0$ and $|q|>q_T$ where the treshold wavevector is given by

$$q_T=\frac{2\Omega_0^2b^2}{\mathcal{D}_0\Delta_{\mathcal{F}}^2}. \tag{4.81}$$

For small values of $x$ the left hand side of (4.78) can be approximated by $1/x$. For large values of $|q|$ the bound mode approaches therefore the asymptotic frequency

$$\omega_\infty=\frac{2\Omega_0}{|\Delta_{\mathcal{F}}|}. \tag{4.82}$$

The numerical results for a specific example are shown in Fig. 4.3-b.

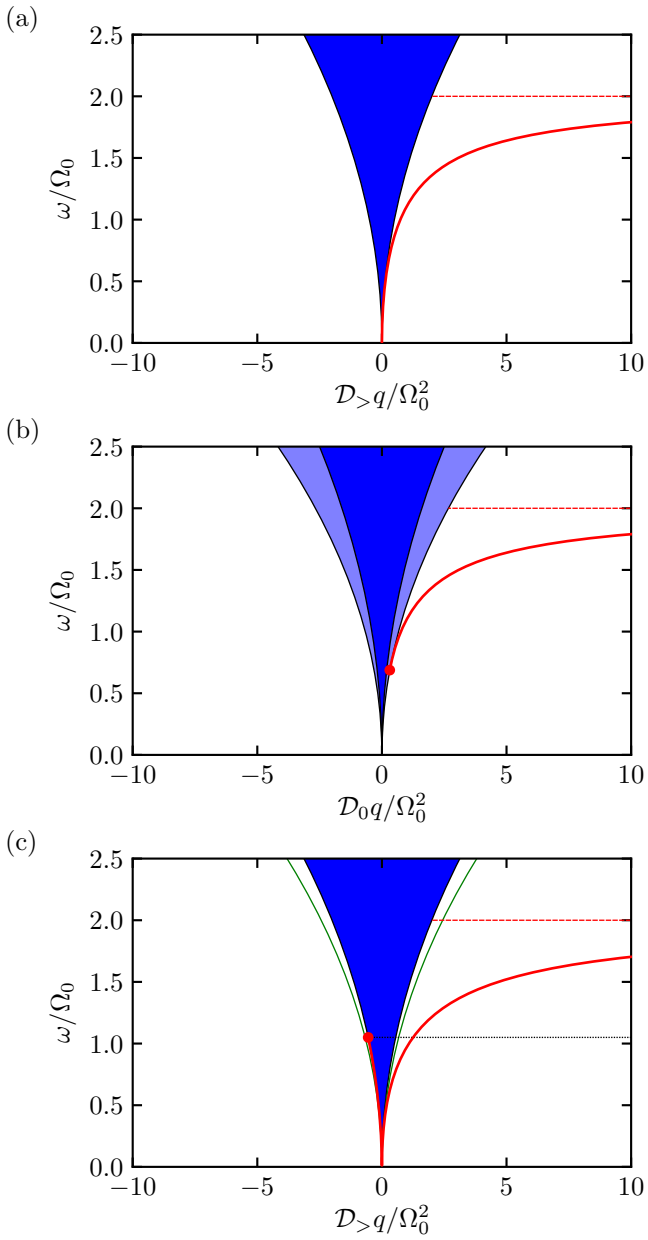


Figure 4.3: Dispersion relation of the bound state (red thcik lines) calculated using the full Coulomb interaction for different values of the parameter $\Delta$: panel (a) $\Delta = 0$ and $\Delta_{\mathcal{F}} = 1$, panel (b) $\Delta = 0.5$ and $\Delta_{\mathcal{F}} = 1$, panel (c) $\Delta = 2$ and $\Delta_{\mathcal{F}} = 1$. Red dashed lines mark the asymptotic frequency $\Omega_\infty = 2\Omega_0/\Delta_{\mathcal{F}}$, blue shaded regions represent the continuum of propagating states, the light-blue shaded region in panel (b) is the continuum of TIR states. Red dots mark the positions where the bound mode merges into the continuum. In panel (c) the black dotted line marks the treshold frequency $\omega_{\mathrm{T}}$ above wich only a forward-moving mode is present, while the green thin lines represent the bound states at $\Delta_{\mathcal{F}} = 0$.

**Homogeneous normal conductivity ($\Delta = 0$)**

This particular case can be solved directly without resorting to the Wiener-Hopf technique. We obtain a simpler bound-state equation

$$\frac{\sqrt{1-x^4}}{2x[1-\frac{1}{\pi}\arccos(x^2)]} = \mathrm{sgn}(q)\Delta_{\mathcal{F}}\frac{\sqrt{2\mathcal{D}|q|}}{2\Omega_0}, \tag{4.83}$$

where $x = \omega/\sqrt{2\mathcal{D}_0|q|}$. Since for positive values of $x$ the left hand side spans the whole interval $[0,\infty]$. This equation has therefore a positive solution for every wavevector such that $\mathrm{sgn}(q)\Delta_{\mathcal{F}} > 0$. For large values of $|q|$ the bound mode approaches therefore the asymptotic frequency

$$\omega_\infty = \frac{2\Omega_0}{|\Delta_{\mathcal{F}}|}. \tag{4.84}$$

The numerical results for a specific example are shown in Fig. 4.3-a.

**Insulator-conductor interface ($\Delta = 2$)**

For a physical edge the bound-state equation is

$$\frac{\tanh[\tilde{I}(x)]}{x} = \mathrm{sgn}(q)\Delta_{\mathcal{F}}\frac{\sqrt{2\mathcal{D}_>|q|}}{2\Omega_0}. \tag{4.85}$$

where

$$\tilde{I}(x) = -\ln(x^2/2)/2 - f(x)/2, \tag{4.86}$$

$f(x)$ is defined in (4.80), and $x = \omega/\sqrt{2D_>|q|}$.

The function on the left hand side vanishes for $x = x_0 \approx 0.906$. In absence of Berry flux a bound states exists with $\omega = x_0\sqrt{2\mathcal{D}_>|q|}$. The codomain of the left hand side of (4.85) is $[-g,+\infty]$ with $g = \tanh(2\boldsymbol{G}/\pi) \approx 0.525$.

This means that for $\mathrm{sgn}(q\Delta_{\mathcal{F}}) > 0$ Eq. (4.85) always has a solution, while for $\mathrm{sgn}(q\Delta_{\mathcal{F}}) < 0$ it has solution only for $|q| < q_T$, where

$$q_T = \frac{2\Omega_0^2 g^2}{\mathcal{D}_>\Delta_{\mathcal{F}}^2}, \tag{4.87}$$

corresponding to the frequency

$$\omega_T = \frac{2\Omega_0 g}{|\Delta_{\mathcal{F}}|}. \tag{4.88}$$

For large values of $|q|$ the frequency of the bound state tends to the limiting value

$$\omega_\infty = \frac{2\Omega_0}{|\Delta_{\mathcal{F}}|}. \tag{4.89}$$

### 4.1.5 Impact of a finite damping rate

We now consider the impact on bound modes dispersion and lifetime of a finite damping rate. We consider a conductivity in the form

$$\sigma_{ij}(\boldsymbol{r},\omega) = \frac{i}{\pi(\omega+i\gamma)}\mathcal{D}(\boldsymbol{r})\delta_{ij} + \frac{e^2}{\hbar}\mathcal{F}(\boldsymbol{r})\epsilon_{ij}\ , \tag{4.90}$$

With $\mathcal{D}(\boldsymbol{r})$ and $\mathcal{F}(\boldsymbol{r})$ having the same form as (4.6-4.7). For the sake of simplicity we consider only the Local Capacitance Approximation case. Eq. (4.18) becomes

$$\left[\partial_x^2 + \frac{\omega(\omega+i\gamma)}{v_{\lessgtr}^2} - q^2\right]\phi_{\lessgtr}(x,q,\omega) = 0\ , \tag{4.91}$$

while the boundary condition (4.13) reads in this case

$$\begin{aligned}&\left(1+\frac{\Delta}{2}\right)\partial_x\phi_>(0,q,\omega)-\left(1-\frac{\Delta}{2}\right)\partial_x\phi_<(0,q,\omega)=\\&=-\frac{q(\omega+i\gamma)}{\Omega_0}\left[\left(\mathcal{F}_0+\frac{\Delta_\mathcal{F}}{2}\right)\phi_>(0,q,\omega)-\left(\mathcal{F}_0-\frac{\Delta_\mathcal{F}}{2}\right)\phi_<(0,q,\omega)\right]\ .\end{aligned}\tag{4.92}$$

We solve explicitely only the case of a physical edge ($\Delta=2$). In this case the result is

$$\omega=-i\Gamma+\ \mathrm{sgn}\left(q\mathcal{F}_>\right)\sqrt{\Omega^2\left[1+\frac{\gamma^2\mathcal{F}^2}{4\Omega_0^2}\right]-\Gamma^2}\ ,\tag{4.93}$$

where $\Omega$ is the solution in absence of damping

$$\Omega=\frac{qv_>\ \mathrm{sgn}\left(\mathcal{F}_>\right)}{\sqrt{1+\frac{v_>^2\mathcal{F}_>^2q^2}{4\Omega_0^2}}}\ ,\tag{4.94}$$

and

$$\Gamma=\frac{\gamma}{2}\frac{1+\frac{v_>^2\mathcal{F}_>^2q^2}{2\Omega_0^2}}{1+\frac{v_>^2\mathcal{F}_>^2q^2}{4\Omega_0^2}}\ .\tag{4.95}$$

This means that the plasmon lifetime is

$$\tau_\mathrm{p}(q)\equiv\frac{1}{2\Gamma}=\frac{1}{\gamma}\frac{1+\frac{v_>^2\mathcal{F}_>^2q^2}{4\Omega_0^2}}{1+\frac{v_>^2\mathcal{F}_>^2q^2}{2\Omega_0^2}}\ .\tag{4.96}$$

Note that the lifetime of this bound mode ranges from $\gamma^{-1}$, as for normal bulk plasmons, to half this value. No effect of "topological protection" can be seen in this situation.

## 4.2 Conclusions

In this Chapter we developed a general theory of Chiral Berry Plasmons at a generic interface and using three different types of electron-electron interaction. For the Local Capacitance interaction and for the Fetter approximated interaction the problem was amenable to the solution of Ordinary Differential Equations. For the case of the full Coulomb interaction the more advanced Wiener-Hopf technique described in Section 3.1 was used. The results obtained for the dispersion of the bound modes are compared in Figs. 4.1-4.2-4.3. The asymptotic frequency of the bound modes $\omega_\infty=2\Omega_0/|\Delta_\mathcal{F}|$ is shown to be independent on the electron-electron interaction.

We moreover calculated reflection and transmission coefficient for propagating modes. These are shown to depend, at finite incidence angle, on the chirality of the material, and show a non-reciprocal behavior, as recently pointed out also in Ref. [250].

The lifetime of CBPs was calculated in Sect. 4.1.5 in the simplest approximation and was shown not to benefit from any topological protection.

Our result are relevant for near-field optical experiments involving topologically non-trivial materials like narrow-gap Dirac materials [205].

# Appendix A

# Plasmons in 2D materials including retardation

## A.1 Constitutive equations

We suppose that our two-dimensional material is positioned in the $z = 0$ plane. The $z < 0$ half-space –from now on region 1– is filled with an homogeneous and isotropic dielectric material with electric permeability $\epsilon_1$ and magnetic permeability $\mu_1$, while the region with $z > 0$ is occupied by a material with constants $\epsilon_2$ and $\mu_2$. The current response of a 2D system can be described by the two-dimensional conductivity:

$$\sigma_{2Dij}(\boldsymbol{q}, \boldsymbol{q}', \omega) = (ie^2/\omega)\tilde{\chi}^J_{ij}(\boldsymbol{q}, \boldsymbol{q}', \omega) \ , \tag{A.1}$$

that relates the current density induced in the two-dimensional material to the *total* in-plane electric field. In the following we neglect the coupling between the magnetic field and the spin of the electrons considering only its effects on orbital motion. For $z > 0$ and $z < 0$ the fields are described by Maxwell equations in a uniform dielectric:

$$\begin{aligned} &\left[\partial_z^2 - q^2 + \frac{\omega^2 n^2_{(j)}}{c^2}\right] \boldsymbol{F}_{(j)}(\boldsymbol{q}, z, \omega) = 0 \ , \\ &[\hat{\boldsymbol{z}}\partial_z + i\boldsymbol{q}] \cdot \boldsymbol{F}_{(j)}(\boldsymbol{q}, z, \omega) = 0 \ . \end{aligned} \tag{A.2}$$

Where $\boldsymbol{F}$ is the electric or the magnetic field in the $j$ region, and $n^2_{(j)} = \epsilon_j \mu_j$ is the corresponding refraction index. The above equations must be supplemented by boundary conditions at $z = 0$:

$$\begin{aligned} &[\boldsymbol{B}(\boldsymbol{q}, 0+, \omega) - \boldsymbol{B}(\boldsymbol{q}, 0-, \omega)] \cdot \hat{\boldsymbol{z}} = 0 \ , \\ &[\boldsymbol{E}(\boldsymbol{q}, 0+, \omega) - \boldsymbol{E}(\boldsymbol{q}, 0-, \omega)] \times \hat{\boldsymbol{z}} = 0 \ , \\ &[\epsilon_2 \boldsymbol{E}(\boldsymbol{q}, 0+, \omega) - \epsilon_1 \boldsymbol{E}(\boldsymbol{q}, 0-, \omega)] \cdot \hat{\boldsymbol{z}} = \frac{4\pi}{\omega} \boldsymbol{q} \cdot \boldsymbol{J}_{2D}(\boldsymbol{q}, \omega) \ , \\ &\left[\frac{\boldsymbol{B}(\boldsymbol{q}, 0+, \omega)}{\mu_2} - \frac{\boldsymbol{B}(\boldsymbol{q}, 0-, \omega)}{\mu_1}\right] \times \hat{\boldsymbol{z}} = -\frac{4\pi}{c} \boldsymbol{J}_{2D}(\boldsymbol{q}, \omega) \ . \end{aligned} \tag{A.3}$$

## A.2 Homogeneous system

We restrict now to an homogeneous an isotropic 2D material. In this case $\boldsymbol{J}_{2D}(\boldsymbol{q}, \omega)$ depends only on the $\boldsymbol{q}$ Fourier component of the electric field and different in-plane wavevectors are decoupled. Moreover $\sigma_{2D}(\boldsymbol{q}, \omega)$ can be separated in a longitudinal and a transverse part:

$$\begin{aligned} &J_{2Di}(\boldsymbol{q}, \omega) = \sigma_{2Dij}(\boldsymbol{q}, \omega) E_j(\boldsymbol{q}, z = 0, \omega) = \\ &\left[\sigma_L(q, \omega) \frac{q_i q_j}{q^2} + \sigma_T(q, \omega) \left(\delta_{ij} - \frac{q_i q_j}{q^2}\right)\right] E_j(\boldsymbol{q}, z = 0, \omega) \ , \end{aligned} \tag{A.4}$$

where longitudinal (transverse) means parallel (orthogonal) to the in-plane wavevector $\boldsymbol{q}$. Since the system is symmetric under rotations about the $\hat{\boldsymbol{z}}$ axis, in the following we can assume that $\boldsymbol{q}$ is in the $\hat{\boldsymbol{x}}$ direction with no loss of generality.

### A.2.1 Confined modes

We can write the electric field of confined modes as:

$$\boldsymbol{E}_{(j)}(\boldsymbol{r},t) = \boldsymbol{a}_{(j)} e^{iqx \pm \beta_{(j)} z - i\omega t} + c.c. \ , \tag{A.5}$$

where $\beta_{(j)} = \sqrt{q^2 - \omega^2 n_{(j)}^2/c^2}$ is the propagation constant along $z$ in the $j$ region and $\Re e[\beta_{(j)}] > 0$. To enforce the condition $\nabla \cdot \boldsymbol{E} = 0$, the z components of $\boldsymbol{a}_{(j)}$ must be:

$$a_{(j)z} = \mp \frac{iq}{\beta_{(j)}} a_{(j)x} \ , \tag{A.6}$$

where the upper (lower) sign applies to region 1 (2). The in-plane components of $\boldsymbol{a}_{(1)}$ and $\boldsymbol{a}_{(2)}$ must be equal to satisfy the homogeneous boundary conditions and will be designed simply by $a_x$ and $a_y$. The associated magnetic fields are:

$$\begin{aligned} \boldsymbol{B}_{(j)}(\boldsymbol{r},t) = &\left[ \mp \beta_{(j)} a_y \hat{\boldsymbol{x}} \mp \frac{\omega^2 n_{(j)}^2}{c^2 \beta_{(j)}} a_x \hat{\boldsymbol{y}} + iq a_y \hat{\boldsymbol{z}} \right] \times \\ &\left( \frac{-ic}{\omega} \right) e^{iqx + \beta_{(j)} z - i\omega t} + c.c. \ , \end{aligned} \tag{A.7}$$

Inserting Eqs. (A.4-A.5-A.7) in (A.3) the system of boundary conditions reduces to:

$$\begin{bmatrix} 1 + \frac{4\pi i \sigma_L(q,\omega)\beta_1\beta_2}{\omega(\epsilon_2\beta_1 + \epsilon_1\beta_2)} & 0 \\ 0 & 1 - \frac{4\pi i \omega \sigma_T(q,\omega)\mu_1\mu_2}{(\mu_1\beta_2 + \mu_2\beta_1)c^2} \end{bmatrix} \begin{bmatrix} a_x \\ a_y \end{bmatrix} = 0 \ . \tag{A.8}$$

This system can have two types of non-trivial solutions corresponding to Transverse Magnetic (TM) or Transverse Electric (TE) field configurations.

#### TM modes

Modes with $a_x \neq 0$ and $a_y = 0$ have non-vanishing $x$ and $z$ components of the electric field and magnetic field directed along $y$. These are called TM modes or longitudinal modes because they are determined by the behaviour of $\sigma_L(q,\omega)$. They exist if:

$$1 + \frac{4\pi i \sigma_L(q,\omega)\beta_1\beta_2}{\omega(\epsilon_1\beta_2 + \epsilon_2\beta_1)} = 0 \ . \tag{A.9}$$

An example of such modes is given by the 2D plasmons-polaritons. If in the long-wavelength limit $\sigma_L$ can be approximated by a simple (dissipation-less) Drude conductivity:

$$\sigma_L(q,\omega) = \frac{iD_0/\pi}{\omega} = \frac{ic\Omega_{\rm pp}}{2\pi\omega} \ , \tag{A.10}$$

where we introduced the plasmon-polariton characteristic frequency $\Omega_{\rm pp} = 2D_0/c$, we obtain a dispersion relation for the normal modes of a suspended sample ($\epsilon_j = \mu_j = 1$):

$$\omega = \Omega_{\rm pp} \sqrt{\frac{1}{2}\left( \sqrt{1 + \frac{4c^2q^2}{\Omega_{\rm pp}^2}} - 1 \right)} \ . \tag{A.11}$$

This relation can be interpreted as the hybridisation of 2D plasmons with the modes of the electromagnetic field (i.e. 2D plasmon polaritons). For $q \gg \Omega_{\rm pp}/c^2$ i.e. in the electrostatic limit we recover the 2D plasmon dispersion $\omega = \Omega_{\rm pp}\sqrt{qc/\Omega_{\rm pp}}$.

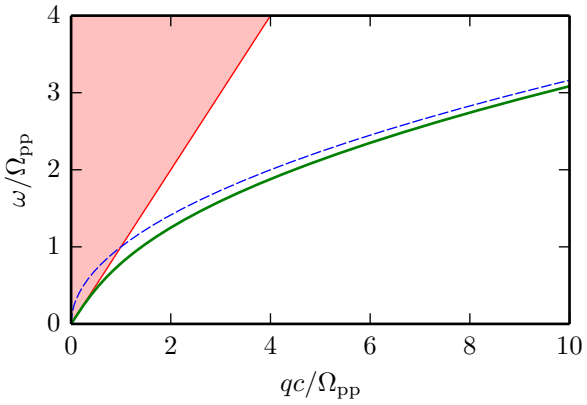


Figure A.1: Dispersion relation of 2D plasmon-polartiton (green solid line), the blue-dashed line is the electrostatic plasmon dispersion, while the red thin line marks the boundary of the light cone. Modes are confined in the $z$ direction only outside the red-shaded region.

It must be noted that all these modes are confined, for a suspended sample, only if $q > \omega/c$, i.e. outside the lightcone. Inside this region the modes are strongly mixed with the radiation of the far field. On the other side far-field experiments (trasmission or reflection experiments) can probe only the region inside the lightcone. In graphene the frequency $\Omega_{\rm pp}$ is given by:

$$\Omega_{\rm pp} = \frac{2D_0}{c} = \frac{e^2}{\hbar c}\frac{2E_{\rm F}}{\hbar} = \alpha\Omega_{\rm Inter} = \\ 2.52\ 10^{12}\ \text{Rad/s}\sqrt{n[10^{12}\ \text{cm}^{-2}}\ . \tag{A.12}$$

Here $\Omega_{\rm Inter}$ is the onset of interband optical transitions.

### TE modes

Solutions of Eq (A.8) with $a_x = 0$ and $a_y \neq 0$ have the electric field directed along $y$ and magnetic field with non-vanishing $x$ and $z$ components. These are called TE modes or transverse modes because they are determined by the behaviour of $\sigma_T(q,\omega)$. They exist if:

$$1 - \frac{4\pi i\omega\sigma_T(q,\omega)\mu_1\mu_2}{c^2(\mu_1\beta_1 + \mu_2\beta_2)} = 0\ . \tag{A.13}$$

In this case if we use a simple Drude expression for the conductivity we get no solution because of the wrong sign of the imaginary part of $\sigma$. This happens because no charge density is induced in the sample resulting in no Coulomb force sustaining the oscillations of the transverse modes.

Solutions of Eq. (A.13) can be found if a different form of the conductivity is assumed.

One possibility is to consider a 2D electron system with a finite shear modulus [35, 175] $\mathcal{S}$, that is a conductivity in the form:

$$\sigma_T(q,\omega) = \frac{iD_0/\pi}{\omega^2\left(1 - \frac{q^2 s_T^2}{\omega^2}\right)}\ , \tag{A.14}$$

where $s_T = \sqrt{\mathcal{S}/(m\bar{n})}$ is the velocity of a shear wave. In this case we obtain solutions corresponding to shear waves hybridised with photons. For 2DEGs and graphene the non-interacting shear-wave velocity is [102, 175] $s = v_{\rm F}/2$, causing the shear waves to disappear because of Landau damping. The shear waves can emerge from the electron hole continuum thanks to exchange-correlation effects at very low densities in parabolic-band 2DEGs ($r_{\rm S} > 14$) when the electron liquid is approaching Wigner crystallisation.

In graphene TE modes can be sustained by interband effects. Ziegler and Mikhailov [154] showed that taking into account the inter-band contribution to $\sigma_T$ a TE modes must exist near the inter-band electron-hole continuum.

### A.2.2 Transmission and reflection coefficients

In the region $q < n_i\omega/c$ a beam of light arriving at the interface from region 1 at an angle $\theta_i$ with the $z$ direction is partially transmitted to region 2, partially reflected to region 1 and partially absorbed by the 2D material at the interface. Here we calculate the transmission and reflection coefficients for the electric field of the wave as well as the reflection, transmission and absorption coefficient for the energy carried by the light beam. Results depend on light polarisation. We therefore analyse separately the cases of TE and TM fields. At $\theta_i = 0$, that is at normal incidence, the results will be equal.

#### TE fields

Figure A.2 shows the directions and labelling of field in the case of TE incidence. The transmission coefficient defined as $t = E_t/E_i$ is found to be:

$$t = \frac{2\frac{n_1}{\mu_1}\cos(\theta_i)}{\frac{n_1}{\mu_1}\cos(\theta_i) + \frac{n_2}{\mu_2}\cos(\theta_t) + \frac{4\pi}{c}\sigma_T} \ , \tag{A.15}$$

where $\sigma_T = \sigma_T(\omega n_1 \sin(\theta_1)/c, \omega/c)$. We can calculate the reflection coefficient $r = E_r/E_i$ using the relation, valid for TE fields, $r = t - 1$:

$$r = \frac{\frac{n_1}{\mu_1}\cos(\theta_i) - \frac{n_2}{\mu_2}\cos(\theta_t) - \frac{4\pi}{c}\sigma_T}{\frac{n_2}{\mu_2}\cos(\theta_t) + \frac{n_1}{\mu_1}\cos(\theta_i) + \frac{4\pi}{c}\sigma_T} \ . \tag{A.16}$$

The reflection coefficient for energy is simply $R = |r|^2$ because the reflected light travels in the same

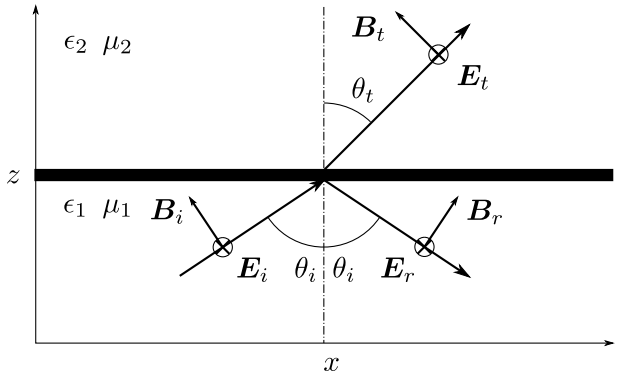


Figure A.2: Fields direction and labelling for TE incidence

medium and at the same angle with the interface as the incoming light.

$$R = \left| \frac{\frac{n_1}{\mu_1}\cos(\theta_i) - \frac{n_2}{\mu_2}\cos(\theta_t) - \frac{4\pi}{c}\sigma_T}{\frac{n_2}{\mu_2}\cos(\theta_t) + \frac{n_1}{\mu_1}\cos(\theta_i) + \frac{4\pi}{c}\sigma_T} \right|^2 \tag{A.17}$$

The trasmission coefficient of energy is instead given by $T = n_2\mu_1\cos(\theta_t)|t|^2/(n_1\mu_2\cos(\theta_i))$. This leads to:

$$T = \frac{4\frac{n_1 n_2}{\mu_1\mu_2}\cos(\theta_i)\cos(\theta_t)}{\left|\frac{n_2}{\mu_2}\cos(\theta_t) + \frac{n_1}{\mu_1}\cos(\theta_i) + \frac{4\pi}{c}\sigma_T\right|^2} \ . \tag{A.18}$$

The absorption coefficient of the 2D material can be defined as $A = 1 - R - T$ and is equal to:

$$A = \frac{4\frac{n_1}{\mu_1}\cos(\theta_i)\frac{4\pi}{c}\Re e\left[\sigma_T\left(\frac{n_1\omega}{c}\sin(\theta_i), \omega\right)\right]}{\left|\frac{n_2}{\mu_2}\cos(\theta_t) + \frac{n_1}{\mu_1}\cos(\theta_i) + \frac{4\pi}{c}\sigma_T\left(\frac{n_1\omega}{c}\sin(\theta_i), \omega\right)\right|^2} \ . \tag{A.19}$$

**TM fields**

Field reflection and transmission coefficients are defined in the same way as in the TE case. Now $\sigma_L$ is a shorthand for $\sigma_L(\omega n_1 \sin(\theta_1)/c, \omega/c)$. Labelling an directions of fields are shown in Fig. A.3. The field

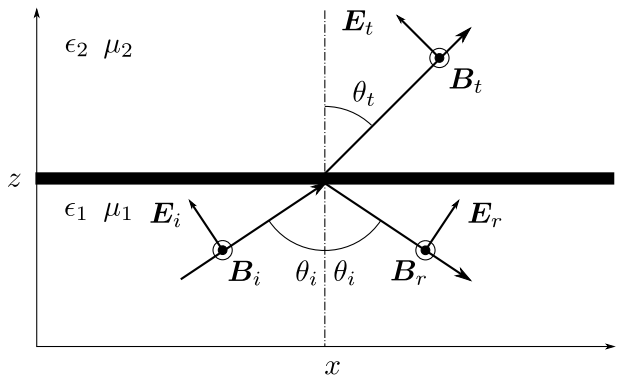


Figure A.3: Fields direction and labelling for TM incidence

transmission coefficient is now:

$$t = \frac{\frac{2n_1}{\mu_1}\cos(\theta_i)}{\frac{n_2}{\mu_2}\cos(\theta_i) + \frac{n_1}{\mu_1}\cos(\theta_t) + \frac{4\pi}{c}\cos(\theta_i)\cos(\theta_t)\sigma_L} \ , \tag{A.20}$$

and is related to $r$ by: $r = 1 - t\frac{\cos(\theta_t)}{\cos(\theta_i)}$. The reflection coefficient is hence:

$$r = \frac{\frac{n_2}{\mu_2}\cos(\theta_i) - \frac{n_1}{\mu_1}\cos(\theta_t) + \frac{4\pi}{c}\cos(\theta_i)\cos(\theta_t)\sigma_L}{\frac{n_2}{\mu_2}\cos(\theta_i) + \frac{n_1}{\mu_1}\cos(\theta_t) + \frac{4\pi}{c}\cos(\theta_i)\cos(\theta_t)\sigma_L} \ . \tag{A.21}$$

We can obtain the reflection, transmission and absorption coefficients from the same relations valid in the TE case. The results are:

$$T = \frac{4\frac{n_1 n_2}{\mu_1 \mu_2}\cos(\theta_i)\cos(\theta_t)}{\left|\frac{n_2}{\mu_2}\cos(\theta_i) + \frac{n_1}{\mu_1}\cos(\theta_t) + \frac{4\pi}{c}\cos(\theta_i)\cos(\theta_t)\sigma_L\right|^2} \ , \tag{A.22}$$

$$R = \frac{\left|\frac{n_2}{\mu_2}\cos(\theta_i) - \frac{n_1}{\mu_1}\cos(\theta_t) + \frac{4\pi}{c}\cos(\theta_i)\cos(\theta_t)\sigma_L\right|^2}{\left|\frac{n_2}{\mu_2}\cos(\theta_i) + \frac{n_1}{\mu_1}\cos(\theta_t) + \frac{4\pi}{c}\cos(\theta_i)\cos(\theta_t)\sigma_L\right|^2} \ , \tag{A.23}$$

$$A = \frac{4\frac{n_1}{\mu_1}\cos(\theta_i)\cos^2(\theta_t)\frac{4\pi}{c}\Re e\left[\sigma_L\right]}{\left|\frac{n_2}{\mu_2}\cos(\theta_i) + \frac{n_1}{\mu_1}\cos(\theta_t) + \frac{4\pi}{c}\cos(\theta_i)\cos(\theta_t)\sigma_L\right|^2} \ . \tag{A.24}$$

**Normal incidence**

The above formulas simplify for normal incidence. TE and TM fields are identical in this case. We obtain for the fields coefficients:

$$\begin{aligned} t &= \frac{2\frac{n_1}{\mu_1}}{\frac{n_1}{\mu_1} + \frac{n_2}{\mu_2} + \frac{4\pi}{c}\sigma} \ , \\ r &= \frac{\frac{n_1}{\mu_1} - \frac{n_2}{\mu_2} - \frac{4\pi}{c}\sigma_T}{\frac{n_2}{\mu_2} + \frac{n_1}{\mu_1} + \frac{4\pi}{c}\sigma} \ . \end{aligned} \tag{A.25}$$

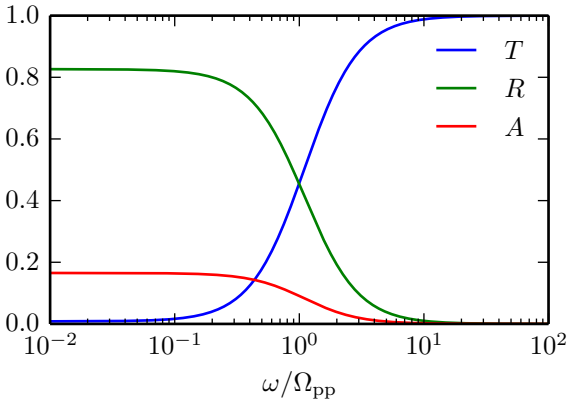


Figure A.4: Transmission,reflection and absorption coefficients at normal incidence for a 2D material described by a Drude conductivity with $\gamma = 0.1\ \Omega_{\rm pp}$.

While the energy coefficients are:

$$\begin{aligned} T &= \frac{4\frac{n_1 n_2}{\mu_1 \mu_2}}{\left|\frac{n_2}{\mu_2} + \frac{n_1}{\mu_1} + \frac{4\pi}{c}\sigma\right|^2}\ , \\ R &= \frac{\left|\frac{n_2}{\mu_2} - \frac{n_1}{\mu_1} + \frac{4\pi}{c}\sigma\right|^2}{\left|\frac{n_2}{\mu_2} + \frac{n_1}{\mu_1} + \frac{4\pi}{c}\sigma\right|^2}\ , \\ A &= \frac{4\frac{n_1}{\mu_1}\frac{4\pi}{c}\Re e\left[\sigma\right]}{\left|\frac{n_2}{\mu_2} + \frac{n_1}{\mu_1} + \frac{4\pi}{c}\sigma\right|^2}\ . \end{aligned} \tag{A.26}$$

For a suspended sample of a two-dimensional material described by a Drude conductivity $\sigma = ic\Omega_{\rm pp}/(\omega + i\gamma)$ the coefficients become:

$$\begin{aligned} R &= \frac{\Omega_{\rm pp}^2}{(\Omega_{\rm pp}+\gamma)^2 + \omega^2}\ , \\ T &= \frac{\omega^2 + \gamma^2}{(\Omega_{\rm pp}+\gamma)^2 + \omega^2}\ , \\ A &= \frac{2\gamma\Omega_{\rm pp}}{(\Omega_{\rm pp}+\gamma)^2 + \omega^2}\ . \end{aligned} \tag{A.27}$$

As an example we show in Fig. A.4 the behaviour of these coefficients for a material with $\gamma = 0.1\ \Omega_{\rm pp}$.

# Appendix B

# Density-density response functions of inhomogeneous electron systems

## B.1 Non-interacting density-density response function of an inhomogeneous electron liquid

The proper density-density response function of the inhomogeneous 2D electron system under study is a crucial input for the microscopic calculation of the scattering kernel in Eq. (3.132).

In this Section we first consider a parabolic-band 2D electron gas [35] subject to *three* different types of perturbations that break translational and rotational invariance. We calculate the proper density-density response function within the aforementioned RPA [35]. Our results have the form of a rigorous expansion in inverse powers of the frequency $\omega$. We calculate the leading and next-to-leading terms of this expansion. Section B.2 below will be devoted to the case of an inhomogeneous graphene sheet.

The proper density-density response function $\tilde{\chi}_{nn}(\boldsymbol{q},\boldsymbol{q}',\omega)$ is defined in Eq. (3.119). In the RPA, this complicated function is brutally replaced by the density-density response function $\chi_{\rm H}(\boldsymbol{q},\boldsymbol{q}',\omega)$ of a formally non-interacting system usually termed the "Hartree system" [35]. In the case of a 2D parabolic-band electron gas, the energy eigenstates of the Hartree system are determined by the Hamiltonian

$$\mathcal{H} = \frac{1}{2m}\left[\boldsymbol{p} + \frac{e}{c}\boldsymbol{A}(\boldsymbol{r})\right]^2 + U_{\rm tot}(\boldsymbol{r}) + \boldsymbol{Z}(\boldsymbol{r})\cdot\boldsymbol{\sigma}\ . \tag{B.1}$$

Here $m$ is the electron band mass, $-e$ the electron charge, $c$ the speed of light,

$$U_{\rm tot}(\boldsymbol{r}) = U_{\rm ext}(\boldsymbol{r}) + U_{\rm H}(\boldsymbol{r}) \tag{B.2}$$

is the sum of an external scalar potential $U_{\rm ext}(\boldsymbol{r})$ and the self-consistent Hartree potential [35] $U_{\rm H}(\boldsymbol{r})$, $\boldsymbol{A}(\boldsymbol{r})$ is an external vector potential, and, finally, $\boldsymbol{Z}(\boldsymbol{r})$ is an external Zeeman field that couples to spin degrees of freedom. In Eq. (B.1), $\boldsymbol{\sigma}$ is a vector of spin-1/2 Pauli matrices, $\sigma^\alpha$ with $\alpha = x, y, z$. Without loss of generality, we work in the Coulomb gauge for the vector potential, i.e. $\nabla\cdot\boldsymbol{A}(\boldsymbol{r}) = 0$. In 2D, the electron orbital motion is influenced only by the perpendicular component of the magnetic field $B_z(\boldsymbol{r})$, while the Zeeman field $\boldsymbol{Z}(\boldsymbol{r})$ couples to all three components of the electron's spin.

For homogeneous electron systems $U_{\rm H}$ is cancelled exactly by the background potential and the Hartree system reduces to the corresponding homogeneous non-interacting electron system [35].

Following Ref. [35], we express $\chi_{\rm H}(\boldsymbol{q},\boldsymbol{q}',\omega)$ in terms of a density-density correlator at different times:

$$\chi_{\rm H}(\boldsymbol{q},\boldsymbol{q}',\omega) = \frac{-i}{S\hbar}\lim_{\eta\to 0^+}\int_0^\infty d\tau\, e^{i(\omega+i\eta)\tau}\langle[n_{\boldsymbol{q}}(\tau), n_{-\boldsymbol{q}'}]\rangle\ , \tag{B.3}$$

where the density operator at time $\tau$ is defined via the usual Heisenberg time evolution operator, i.e. $n_{\boldsymbol{q}}(\tau) = \exp(i\mathcal{H}\tau/\hbar)n_{\boldsymbol{q}}\exp(-i\mathcal{H}\tau/\hbar)$, and $n_{\boldsymbol{q}}$ is given by

$$n_{\boldsymbol{q}} = e^{-i\boldsymbol{q}\cdot\boldsymbol{r}}\ . \tag{B.4}$$

In Eq. (B.3), the average must be taken over the ground state of the Hamiltonian (B.1) and $[\dots,\dots]$ denotes a commutator. Now, the key point is that this average can be expanded [35] in a Taylor series for small values of $\tau$:

$$\langle [n_{\boldsymbol{q}}(\tau), n_{-\boldsymbol{q}'}] \rangle = \sum_{\ell=0}^{\infty} \frac{\tau^\ell}{\ell!} \langle [n_{\boldsymbol{q}}^{(\ell)}, n_{-\boldsymbol{q}'}] \rangle \ , \tag{B.5}$$

where, for any operator $\mathcal{O}$,

$$\mathcal{O}^{(0)} \equiv \mathcal{O} \ , \tag{B.6}$$

and for integer values of $\ell \geq 1$ the $\ell$-th time derivative of the operator $\mathcal{O}$ is defined by

$$\mathcal{O}^{(\ell)} \equiv \frac{i}{\hbar} [\mathcal{H}, \mathcal{O}^{(\ell-1)}] \ . \tag{B.7}$$

In the following, we make use of three useful identities involving time derivatives of operators. For any $\ell \geq 1$ the expectation value of the $\ell$-th time derivative of an operator, calculated over the ground state (or any other equilibrium state), vanishes:

$$\langle \mathcal{O}^{(\ell)} \rangle = \frac{i}{\hbar} \langle \mathcal{H}\mathcal{O}^{(\ell-1)} - \mathcal{O}^{(\ell-1)}\mathcal{H} \rangle = 0 \ . \tag{B.8}$$

Products of operators are differentiated with respect to time according to the Leibniz rule:

$$(AB)^{(1)} = \frac{i}{\hbar} \left( \mathcal{H}AB - A\mathcal{H}B + A\mathcal{H}B - AB\mathcal{H} \right) = A^{(1)}B^{(0)} + A^{(0)}B^{(1)} \ . \tag{B.9}$$

Combining Eq. (B.8) and (B.9), we obtain the "integration by parts" rule:

$$\langle A^{(n+1)} B^{(m)} \rangle = -\langle A^{(n)} B^{(m+1)} \rangle \ . \tag{B.10}$$

After integration over time $\tau$, Eq. (B.5) translates into an expansion of $\chi_{\rm H}(\boldsymbol{q}, \boldsymbol{q}', \omega)$ in inverse powers of $\omega$:

$$\chi_{\rm H}(\boldsymbol{q}, \boldsymbol{q}', \omega) = \sum_{\ell=0}^{\infty} \frac{M^{(\ell)}(\boldsymbol{q}, \boldsymbol{q}')}{\omega^{\ell+1}} \tag{B.11}$$

where

$$M^{(\ell)}(\boldsymbol{q}, \boldsymbol{q}') \equiv \frac{i^\ell}{\hbar S} \langle [n_{\boldsymbol{q}}^{(\ell)}, n_{-\boldsymbol{q}'}] \rangle \ . \tag{B.12}$$

The following reciprocity relations hold for the coefficients $M^{(\ell)}(\boldsymbol{q}, \boldsymbol{q}')$:

$$M^{(2\ell)}(\boldsymbol{q}, \boldsymbol{q}') = -[M^{(2\ell)}(-\boldsymbol{q}, -\boldsymbol{q}')]^* \ , \tag{B.13}$$

$$M^{(2\ell+1)}(\boldsymbol{q}, \boldsymbol{q}') = [M^{(2\ell+1)}(-\boldsymbol{q}, -\boldsymbol{q}')]^* \ , \tag{B.14}$$

and

$$M^{(\ell)}(\boldsymbol{q}, \boldsymbol{q}') = [M^{(\ell)}(-\boldsymbol{q}', -\boldsymbol{q})]_t \ . \tag{B.15}$$

In Eq. (B.15), $[\dots]_t$ represents time inversion.

We now proceed to calculate the coefficients $M^{(\ell)}(\boldsymbol{q}, \boldsymbol{q}')$ of the expansion in Eq. (B.11) up to $\ell = 3$ for the system described by the Hamiltonian (B.1).

For later convenience, we introduce the *kinetic* momentum operator $\boldsymbol{\Pi}$ with Cartesian components

$$\Pi_\alpha \equiv p_\alpha + \frac{e}{c} A_\alpha(\boldsymbol{r}) \ . \tag{B.16}$$

The kinetic momentum operator has the same commutation relation with the position operator as the *canonical* momentum operator,

$$[r_\alpha, \Pi_\beta] = i\hbar\delta_{\alpha\beta} \ . \tag{B.17}$$

However, different Cartesian components of $\boldsymbol{\Pi}$ do not commute with each other [35]:

$$[\Pi_\alpha, \Pi_\beta] = -\frac{ie\hbar}{c} \epsilon_{\alpha\beta} \partial_\alpha A_\beta(\boldsymbol{r}) = -\frac{ie\hbar}{c} B_z(\boldsymbol{r}) \ , \tag{B.18}$$

where $B_z(\boldsymbol{r})$ is the magnetic field in the $\hat{\boldsymbol{z}}$ direction at position $\boldsymbol{r}$ in space. A sum over repeated indices is intended in Eq. (B.18) and below.

Introducing the kinetic momentum operator, we can rewrite the Hamiltonian (B.1) in the following manner:

$$\mathcal{H} = \frac{1}{2m} \Pi_\alpha \Pi_\alpha + U_{\rm tot}(\boldsymbol{r}) + Z_\alpha(\boldsymbol{r}) \otimes \sigma^\alpha \ . \tag{B.19}$$

### B.1.1 Calculation of $M^{(0)}$

As we have seen above in Eq. (B.6), the zeroeth-order derivative of an operator coincides with the operator itself: $n_{\boldsymbol{q}}^{(0)} = n_{\boldsymbol{q}}$. Density operators commute among each other because they are functions of the position operator only,

$$[n_{\boldsymbol{q}}, n_{-\boldsymbol{q}'}] = 0 \ . \tag{B.20}$$

We therefore conclude that $M^{(0)}(\boldsymbol{q}, \boldsymbol{q}')$ vanishes identically.

### B.1.2 Calculation of $M^{(1)}$

The first non-trivial term of the expansion (B.11) is determined by $M^{(1)}$. The time derivative of the density operator can be easily calculated:

$$n_{\boldsymbol{q}}^{(1)} = \frac{i}{\hbar}\,[\mathcal{H}, n_{\boldsymbol{q}}] = \frac{i}{2\hbar m}\,[\Pi_\alpha \Pi_\alpha, n_{\boldsymbol{q}}] = -iq_\alpha J_{\boldsymbol{q},\alpha} \ . \tag{B.21}$$

In deriving the second equality we made use of the fact that the scalar and Zeeman terms of the Hamiltonian (B.19) commute with the density operator. In deriving the third equality, we made use of the following commutator

$$[\Pi_\alpha, n_{\boldsymbol{q}}] = [p_\alpha, n_{\boldsymbol{q}}] = -\hbar q_\alpha n_{\boldsymbol{q}} \tag{B.22}$$

and introduced the *physical* (i.e. gauge-invariant) current operator in Fourier space:

$$J_{\boldsymbol{q},\alpha} \quad = \quad \frac{1}{2m}\{\Pi_\alpha, n_{\boldsymbol{q}}\} \ , \tag{B.23}$$

where $\{\dots,\dots\}$ denotes an anticommutator. Note that Eq. (B.21) is the operator version of the continuity equation.

Using Eqs. (B.22)-(B.23) we calculate $M^{(1)}(\boldsymbol{q}, \boldsymbol{q}')$ finding:

$$M^{(1)}(\boldsymbol{q}, \boldsymbol{q}') = \frac{i}{\hbar S}\langle[-iq_\alpha J_{\boldsymbol{q},\alpha}, n_{-\boldsymbol{q}'}]\rangle = \frac{q_\alpha q'_\alpha}{mS}\langle n_{\boldsymbol{q}-\boldsymbol{q}'}\rangle \ . \tag{B.24}$$

For $\boldsymbol{q} = \boldsymbol{q}'$, Eq. (B.11) for $\ell = 1$ and Eq. (B.24) reduce to the usual f-sum rule for homogeneous electron systems [119, 35].

### B.1.3 Calculation of $M^{(2)}$

Using Eq. (B.21), we immediately see that the second derivative of the density operator is proportional to the first derivative of the current operator,

$$n_{\boldsymbol{q}}^{(2)} = -iq_\alpha J_{\boldsymbol{q},\alpha}^{(1)} \ . \tag{B.25}$$

The latter can be calculated by repeated use of the commutation relations (B.17), (B.18), (B.20), and (B.22) and reads as following:

$$J_{\boldsymbol{q},\alpha}^{(1)} = -\frac{iq_\beta}{m}\left(T_{\boldsymbol{q},\alpha\beta} - \frac{\hbar^2 q_\alpha q_\beta}{4m} n_{\boldsymbol{q}}\right) + \frac{1}{m}F_{\boldsymbol{q},\alpha} - \frac{1}{m}\partial_\alpha U_{\rm tot} n_{\boldsymbol{q}} - \frac{1}{m}\partial_\alpha Z_\beta S_{\boldsymbol{q},\beta} \ . \tag{B.26}$$

In Eq. (B.26) we introduced the stress tensor operator

$$T_{\boldsymbol{q},\alpha\beta} \equiv \frac{1}{4m}\{\{\Pi_\alpha, \Pi_\beta\}, n_{\boldsymbol{q}}\} \ , \tag{B.27}$$

the Lorentz force-density operator

$$F_{\boldsymbol{q},\alpha} \equiv -\frac{e\epsilon_{\alpha\beta}}{4mc}\{\{\Pi_\beta, B_z(\boldsymbol{r})\}, n_{\boldsymbol{q}}\} \ , \tag{B.28}$$

and the spin-density operator

$$S_{\boldsymbol{q},\alpha} \equiv n_{\boldsymbol{q}}\sigma^\alpha \ . \tag{B.29}$$

Taking the commutator in Eq. (B.12) with the density operator at wavevector $-\boldsymbol{q}'$ we obtain the final result

$$\begin{aligned} M^{(2)}(\boldsymbol{q},\boldsymbol{q}') &= q_\alpha q'_\alpha q_\beta \frac{2}{mS}\langle J_{\boldsymbol{q}-\boldsymbol{q}',\beta}\rangle - \epsilon_{\alpha\beta} q_\alpha q'_\beta \frac{ie}{m^2 cS}\langle B_z(\boldsymbol{r}) n_{\boldsymbol{q}-\boldsymbol{q}'}\rangle \\ &= \frac{q_\alpha q'_\alpha (q_\beta + q'_\beta)}{mS}\langle J_{\boldsymbol{q}-\boldsymbol{q}',\beta}\rangle - \epsilon_{\alpha\beta} q_\alpha q'_\beta \frac{ie}{m^2 cS}\langle B_z(\boldsymbol{r}) n_{\boldsymbol{q}-\boldsymbol{q}'}\rangle \ . \end{aligned} \tag{B.30}$$

In the second step we used the continuity equations (B.21) and the identity (B.8) (the aim of this manipulation was to put the result in a more symmetric form).

### B.1.4 Calculation of $M^{(3)}$

The calculation of the third moment, $M^{(3)}(\boldsymbol{q},\boldsymbol{q}')$, is quite cumbersome. It can be simplified by using an "integration by parts" described in Eq. (B.10), together with Eqs. (B.25) and (B.21):

$$M^{(3)}(\boldsymbol{q},\boldsymbol{q}') = -\frac{i}{\hbar S}\langle [n^{(3)}_{\boldsymbol{q}}, n_{-\boldsymbol{q}'}]\rangle = \frac{i}{\hbar S}\langle [n^{(2)}_{\boldsymbol{q}}, n^{(1)}_{-\boldsymbol{q}'}]\rangle = \frac{i}{\hbar S} q_\alpha q'_\beta \langle [J^{(1)}_{\boldsymbol{q},\alpha}, J_{-\boldsymbol{q}',\beta}]\rangle \ . \tag{B.31}$$

We then evaluate the commutator $[J^{(1)}_{\boldsymbol{q},\alpha}, J_{-\boldsymbol{q}',\beta}]$ by using Eqs. (B.23)-(B.26) and the commutation rules (B.17), (B.18), (B.20), and (B.22). We find

$$\begin{aligned} M^{(3)}(\boldsymbol{q},\boldsymbol{q}') &= q_\gamma q'_\gamma q_\alpha q'_\beta \frac{3}{m^2 S}\langle T_{\boldsymbol{q}-\boldsymbol{q}',\alpha\beta}\rangle + q_\alpha q'_\alpha \frac{\hbar^2}{m^3 S}\Big\{\frac{3}{4}[q_\beta(q_\beta - q'_\beta)][q'_\beta(q_\beta - q'_\beta)] + \frac{1}{4}(q_\beta q'_\beta)^2\Big\}\langle n_{\boldsymbol{q}-\boldsymbol{q}'}\rangle \\ &+ q_\alpha q'_\beta \frac{1}{m^2 S}\langle \partial_\alpha \partial_\beta U_{\rm tot}(\boldsymbol{r}) n_{\boldsymbol{q}-\boldsymbol{q}'}\rangle + q_\alpha q'_\beta \frac{1}{m^2 S}\langle \partial_\alpha \partial_\beta Z_\gamma(\boldsymbol{r}) S_{\boldsymbol{q}-\boldsymbol{q}',\gamma}\rangle + q_\alpha q'_\alpha \frac{e^2}{m^3 c^2 S}\langle B_z^2(\boldsymbol{r}) n_{\boldsymbol{q}-\boldsymbol{q}'}\rangle \\ &+ \frac{3}{2}\left(q_\beta q'_\beta q_\alpha - q^2 q'_\alpha\right)\frac{i}{m^2 S}\langle F_{\boldsymbol{q}-\boldsymbol{q}',\alpha}\rangle + q_\alpha q'_\gamma \epsilon_{\alpha\beta}\frac{e}{m^2 cS}\langle L_{\boldsymbol{q}-\boldsymbol{q}',\beta\gamma}\rangle + q_\alpha q'_\beta \epsilon_{\alpha\beta}\frac{e}{m^2 cS}\langle L_{\boldsymbol{q}-\boldsymbol{q}',\gamma\gamma}\rangle \ . \end{aligned} \tag{B.32}$$

Because of the presence of a non-uniform magnetic field, Eq. (B.32) contains two terms that involve the tensor

$$L_{\boldsymbol{q},\alpha\beta} = \frac{1}{4m}\{\{\Pi_\alpha, \partial_\beta B_z(\boldsymbol{r})\}, n_{\boldsymbol{q}}\} \ . \tag{B.33}$$

## B.2 On inhomogeneous 2D electron systems in graphene

The technique used in the previous Section to calculate the density-density response function of an inhomogeneous parabolic-band electron liquid cannot be applied directly to graphene. The main reason is that the high-frequency expansion (B.11) is invalidated by the presence of particle-hole excitations of arbitrarily large energy, which are associated to inter-band transitions [219, 251].

In this case, instead of calculating microscopically the density-density response function of an inhomogeneous system of 2D massless Dirac fermions [31], we choose a more humble approach. We find a semi-phenomenological expression for $\chi_{\rm H}(\boldsymbol{q},\boldsymbol{q}',\omega)$ which is able to capture, even if in an approximate way, nonlocal effects. The functional dependence of $\chi_{\rm H}(\boldsymbol{q},\boldsymbol{q}',\omega)$ on wavevectors and frequency is chosen is such a way that it respects the following requirements: (i) it is equivalent to a local spatially-dependent conductivity [197] at second order in the wavevectors; (ii) it reduces to

$$\chi_{\rm H}(\boldsymbol{q},\boldsymbol{q}',\omega) = \delta_{\boldsymbol{q},\boldsymbol{q}'}\left[\frac{E_{\rm F} q^2}{\pi\hbar^2\omega^2} - \frac{E_{\rm F}^{-1} q^2}{4\pi} + \frac{3 v_{\rm F}^2 E_{\rm F} q^4}{4\pi\hbar^2\omega^4}\right] \tag{B.34}$$

in the homogeneous limit; (iii) it contains terms $\mathcal{O}(q^4)$ (i.e. it takes into account nonlocal effects); (iv) it depends only on the spatially-dependent ground-state electron density $n(\boldsymbol{r})$.

We propose the following simple expression that meets all the requirements (i)-(iv):

$$\chi_{\rm H}(\boldsymbol{q},\boldsymbol{q}',\omega) = \frac{E_{\rm F}(\boldsymbol{q}-\boldsymbol{q}')\boldsymbol{q}\cdot\boldsymbol{q}'}{\pi S\hbar^2\omega^2} - \frac{E_{\rm F}^{-1}(\boldsymbol{q}-\boldsymbol{q}')\boldsymbol{q}\cdot\boldsymbol{q}'}{4\pi S} + \frac{3 v_{\rm F}^2 E_{\rm F}(\boldsymbol{q}-\boldsymbol{q}')(\boldsymbol{q}\cdot\boldsymbol{q}')^2}{4\pi S\hbar^2\omega^4} \ . \tag{B.35}$$

Here $E_{\rm F}(\boldsymbol{q})$ is defined by

$$E_{\rm F}(\boldsymbol{q}) \equiv \int d\boldsymbol{r}\ e^{-i\boldsymbol{q}\cdot\boldsymbol{r}} \hbar v_{\rm F}\ \mathrm{sgn}[n(\boldsymbol{r})]\sqrt{\pi|n(\boldsymbol{r})|}\ , \tag{B.36}$$

where $v_{\rm F}$ is the graphene Fermi velocity [31] and $n(\boldsymbol{r})$ the local carrier density. Similarly,

$$E_{\rm F}^{-1}(\boldsymbol{q}) \equiv \int d\boldsymbol{r}\ e^{-i\boldsymbol{q}\cdot\boldsymbol{r}} \left[\hbar v_{\rm F}\ \mathrm{sgn}[n(\boldsymbol{r})]\sqrt{\pi|n(\boldsymbol{r})|}\right]^{-1}\ . \tag{B.37}$$

Eq. (B.35) has been successfully used in Ref. [19] to calculate the the transmission coefficient in an experimental geometry of the type sketched in Fig. 3.1(b).

# Appendix C

# Static density-stress tensor response of a two-dimensional electron liquid

In this Appendix we calculate the stress tensor of a 2D electron system subject to an external scalar potential.

We consider Eq. (B.27) with $\boldsymbol{A}(\boldsymbol{r}) = \boldsymbol{0}$. The average value of the stress-tensor operator is given, up to linear order in the external field, by

$$\langle T_{\boldsymbol{q},\alpha\beta} \rangle = \langle T_{\boldsymbol{q},\alpha\beta} \rangle_0 + \sum_{\boldsymbol{q}} \chi_{\alpha\beta}(\boldsymbol{q}) U_{\rm ext}(\boldsymbol{q}) \ , \tag{C.1}$$

where $\langle \dots \rangle_0$ indicates an average over the ground state of the homogeneous electron liquid, and $\chi_{\alpha\beta}(\boldsymbol{q})$ is the static density-stress tensor response function. The latter can be expressed using Kubo formula [35]:

$$\chi_{\alpha\beta}(\boldsymbol{q}) = -\frac{i}{\hbar S} \lim_{\eta \to 0^+} \int_0^\infty d\tau e^{-\eta t} \langle [T_{\boldsymbol{q},\alpha\beta}(\tau), n_{-\boldsymbol{q}}] \rangle_0 \ , \tag{C.2}$$

where $T_{\boldsymbol{q},\alpha\beta}(\tau)$ is the stress tensor operator at time $\tau$ in the Heisenberg representation—see Sect. B.1—and the expectation value must be taken over the ground state of the unperturbed *interacting* electron liquid.

In the RPA, we can replace the response function of the interacting electron system with

$$\chi_{\alpha\beta}(\boldsymbol{q}) = \frac{\chi^{(0)}_{\alpha\beta}(\boldsymbol{q})}{1 - v(q, \omega = 0)\chi_0(q, \omega = 0)} \ , \tag{C.3}$$

where $\chi^{(0)}_{\alpha\beta}(\boldsymbol{q})$ is the static density-stress tensor response function of the non-interacting electron system and $\chi_0(q, \omega = 0)$ is the non-interacting static density-density response function [35].

For a non-interacting 2D parabolic-band electron system, the right-hand side of Eq. (C.2) can be easily calculated. We find

$$\chi^{(0)}_{\alpha\beta}(\boldsymbol{q}) = \frac{g}{S} \sum_{\boldsymbol{k}} \frac{f_{\boldsymbol{k}} - f_{\boldsymbol{k}+\boldsymbol{q}}}{\epsilon_{\boldsymbol{k}} - \epsilon_{\boldsymbol{k}+\boldsymbol{q}}} \langle \boldsymbol{k} | T_{\boldsymbol{q},\alpha\beta} | \boldsymbol{k} + \boldsymbol{q} \rangle = -\frac{2g}{S} \sum_{\boldsymbol{k}} \frac{f_{\boldsymbol{k}}}{\frac{\hbar^2}{2m}\left[q^2 + 2\boldsymbol{k}\cdot\boldsymbol{q}\right]} \langle \boldsymbol{k} | T_{\boldsymbol{q},\alpha\beta} | \boldsymbol{k} + \boldsymbol{q} \rangle \ , \tag{C.4}$$

where $g = 2$ is a spin degeneracy factor, $f_{\boldsymbol{k}} = \Theta(k_{\rm F} - k)$ is the usual zero-temperature Fermi step, and $\epsilon_{\boldsymbol{k}} = \hbar^2 \boldsymbol{k}^2/(2m)$ is the band energy.

Making use of the following matrix element of the stress tensor between plane-wave states,

$$\langle \boldsymbol{k} | T_{\boldsymbol{q},\alpha\beta} | \boldsymbol{k} + \boldsymbol{q} \rangle = E_{\rm F} \left( 2\bar{k}_\alpha \bar{k}_\beta + \bar{q}_\alpha \bar{k}_\beta + \bar{k}_\alpha \bar{q}_\beta + \bar{q}_\alpha \bar{q}_\beta \right) \ , \tag{C.5}$$

where $\bar{q} = q/k_{\rm F}$, $\bar{k} = k/k_{\rm F}$, and assuming, without loss of generality, that $\boldsymbol{q}$ lies in the $\hat{\boldsymbol{x}}$ direction, we

| $n$ | $\ell$ | $\psi^{(n,\ell)}(z)$ |
|---|---|---|
| 0 | 0 | $z-\lambda\sqrt{z^2-1}$ |
| 2 | 0 | $\frac{2}{3}z^3-\frac{\lambda(1+2z^2)}{3}\sqrt{z^2-1}$ |
| 0 | 1 | $z^2-\frac{1}{2}-\lambda z\sqrt{z^2-1}$ |
| 0 | 2 | $\frac{4}{3}z^3-z+\frac{\lambda(1-4z^2)}{3}\sqrt{z^2-1}$ |

Table C.1: Explicit expressions for the functions $\psi^{(n,\ell)}(z)$. Here $\lambda = \text{sign}[\Re e\ (z^*\sqrt{z^2-1})]$, and the function sign$(x)$ evaluates to 0 in $x=0$.

get:

$$\begin{aligned}
&\chi^{(0)}_{\alpha\beta}(\hat{\boldsymbol{x}}q) = \\
&= -\frac{2E_{\rm F}N_0}{\bar{q}}\int_0^1 d\bar{k}\bar{k}\int_{-\pi}^{\pi}\frac{d\theta}{2\pi}\frac{2\bar{k}^2\cos^2(\theta)\delta_{\alpha x}\delta_{\beta x}+2\bar{k}^2\sin^2(\theta)\delta_{\alpha y}\delta_{\beta y}+2\bar{q}\bar{k}\cos(\theta)\delta_{\alpha x}\delta_{\beta x}+\bar{q}^2\delta_{\alpha x}\delta_{\beta x}}{\frac{\bar{q}}{2}+\bar{k}\cos(\theta)} \\
&= -E_{\rm F}N_0\frac{(-2)}{\bar{q}}\int_0^1 d\bar{k}\bar{k}\int_{-\pi}^{\pi}\frac{d\theta}{2\pi}\frac{\delta_{\alpha\beta}\left(\bar{k}^2+\bar{k}\bar{q}\cos(\theta)+\frac{1}{2}\bar{q}^2\right)+\sigma^{(3)}_{\alpha\beta}\left(\bar{k}^2\cos(2\theta)+\bar{k}\bar{q}\cos(\theta)+\frac{1}{2}\bar{q}^2\right)}{-\frac{\bar{q}}{2}-\bar{k}\cos(\theta)} \\
&= -N_0E_{\rm F}[f_{\rm s}\left(\bar{q}\right)\delta_{\alpha\beta}+f_{\rm a}\left(\bar{q}\right)\sigma^{(3)}_{\alpha\beta}]\ .
\end{aligned} \tag{C.6}$$

Here, the functions $f_{\rm s/a}(\bar{q})$ can be expressed in terms of the auxiliary functions $\psi^{(n,\ell)}(z)$ defined by

$$\psi^{(n,\ell)}(z) \equiv \int_0^1 dx\ x^{1+n+\ell}\int_{-\pi}^{\pi}\frac{d\theta}{2\pi}\frac{\cos(\ell\theta)}{z-x\cos(\theta)}\ . \tag{C.7}$$

Explicit expressions for these functions are provided in Table C.1.

Putting everything together, we finally obtain

$$f_{\rm s}(\bar{q}) = \bar{q}\psi^{(0,0)}\left(\frac{\bar{q}}{2}\right)-2\psi^{(0,1)}\left(\frac{\bar{q}}{2}\right)+\frac{2}{\bar{q}}\psi^{(2,0)}\left(\frac{\bar{q}}{2}\right) = 1+\frac{\bar{q}^2}{6}-\frac{1}{3|\bar{q}|}\left(\frac{\bar{q}^2}{2}+1\right)\Theta(\bar{q}-2)\sqrt{\bar{q}^2-4} \tag{C.8}$$

and

$$f_{\rm a}(\bar{q}) = \bar{q}\psi^{(0,0)}\left(\frac{\bar{q}}{2}\right)-2\psi^{(0,1)}\left(\frac{\bar{q}}{2}\right)+\frac{2}{\bar{q}}\psi^{(0,2)}\left(\frac{\bar{q}}{2}\right) = \frac{\bar{q}^2}{3}-\frac{1}{3|\bar{q}|}\left(\bar{q}^2-1\right)\Theta(\bar{q}-2)\sqrt{\bar{q}^2-4}\ . \tag{C.9}$$

The quantities $f_{x/y}(q)$ defined in Eqs. (3.232)-(3.233) are related to $f_{\rm s}$ and $f_{\rm a}$ by $f_{x/y}(q) = [f_{\rm s}(q/k_{\rm F}) \pm f_{\rm a}(q/k_{\rm F})]/2$.

# Appendix D

# Mathematical theorems used in the interface plasmon problem

## D.1 Fourier transform theorems

In this paper we used the standard definition for the spatial Fourier transform

$$\hat{f}(q_x) \equiv \mathcal{F}_x[f(x)](q_x) = \int_{-\infty}^{+\infty} dx e^{-iq_x x} f(x). \tag{D.1}$$

We defined also the right (left) Fourier transform

$$\hat{f}_{R/L}(q_x) \equiv \mathcal{F}_x^{R/L}[f(x)](q_x) = \int_{-\infty}^{\infty} dx e^{-iq_x x} f(x)\Theta(\pm x), \tag{D.2}$$

using integration by parts we can derive the property

$$\mathcal{F}_x^{R/L}[\partial_x f(x)] = iq_x \mathcal{F}_x^{R/L}[f(x)] \mp f(0). \tag{D.3}$$

## D.2 Complex analysis theorems

i)The right (left) Fourier transform of a function is analytic in the lower (upper) half of the complex plane, including the real line, its inverse Fourier transform vanishes when its argument is smaller (larger) than zero.

The converse is also true. If a function is analityc in the lower (upper) half of the complex plane

ii) If two functions $A(q)$ and $B(q)$ are analytical, respectively, for $\Im m(q_z) \geq 0$ and $\Im m(q_z) \leq 0$, and satisfy $A(q) = B(q)$ for $\Im m(q) = 0$, then there exist a unique function $C(q)$ analytical everywhere which coincides with $A(q)$ ($B(q)$) for $\Im m(q_z) \geq 0$ ($\Im m(q) \leq 0$).

iii) Given $\tilde{A}$ and $p \geq 0$ constants (with $p$ an integer), if $A(q)$ is an integral function such that $|A(q)| \leq \tilde{A}|q|^p$ for $|q| \to \infty$, then $A(q)$ is a polynomial of degree $\leq p$.

iv) Assume $A(q_z)$ to be an analytic function in an open set containing the real line and for $|\Re e(q)| \to \infty$, $|A(q)| < \tilde{A}|q|^{-p}$ (with $p > 0$ and $\tilde{A}$ a constant). Then $A(q)$ can be written as

$$A(q) = A_R(q) + A_L(q) \ , \tag{D.4}$$

where $A_R(q)$ is regular for $\Im m(q) \leq 0$ and $A_L(q)$ is regular for $\Im m(q_z) \geq 0$, with

$$\begin{aligned} A_{R/L}(q) &= \mp \int_{-\infty}^{\infty} \frac{dq'_x}{2\pi i} \frac{A(q')}{q' - q \pm i\eta} \\ &= \frac{1}{2} A(q) \pm i\mathcal{P} \int_{-\infty}^{\infty} \frac{dq'_x}{2\pi} \frac{A(q')}{q' - q}, \end{aligned} \tag{D.5}$$

v) Assume $B(q)$ to be analytic and *positive* in an open set containing the real line, and such that, for $|\Re e(q)| \to \infty$, $|B(q_z)| \to 1$. Then $B(q_z)$ can be written as

$$B(q) = \frac{B_R(q)}{B_L(q)}, \tag{D.6}$$

where $B_R(q)$ is analytic for $\Im m(q) \leq 0$ and $B_L(q)$ is analytic for $\Im m(q) \geq 0$, with $B_{R/L}(q)$ given by

$$\begin{aligned} B_{R/L}(q) &= \exp\left[-\int_{-\infty}^{+\infty} \frac{dq'}{2\pi i} \frac{\ln[B(q')]}{q' - q \pm i\eta}\right] \\ &= [B(q)]^{\pm\frac{1}{2}} \exp\left[i\mathcal{P}\int_{-\infty}^{\infty} \frac{dq'}{2\pi} \frac{\ln[B(q')}{q' - q}\right] , \end{aligned} \tag{D.7}$$

From the second line of this equation it is evident that $|B_{R/L}(q)| = [|B(q)|]^{\pm\frac{1}{2}}$. This theorem is a corollary of the previous one, when the latter is applied to the function $A(q) = \ln B(q)$.

# Appendix E

# Mathematical and computational details of the two-dimensional plasmon scattering problem

## E.1 Effective interaction

The effective interaction satisfies Eq. (3.140). Assuming that $W_{\rm h}^{-1}(q,\omega)$ has only one simple zero at $q_{\rm pl}$, the most general solution of this *distributional* equation is

$$W_{\rm h}(q,\omega) = \mathcal{P}\frac{1}{W_{\rm h}^{-1}(q,\omega)} + A\delta(q-q_{\rm pl}) \ . \tag{E.1}$$

Here $\mathcal{P}$ stands for Cauchy principal value, while the constant $A$ must be chosen to satisfy the required boundary conditions. To see what is the correct choice of $A$ to have an outgoing wave, we look at the asymptotic behavior of $W_{\rm h}$ in real space for large $r$.

To begin with, we can single out the divergent part of the interaction by rewriting Eq. (E.1) as

$$W_{\rm h}(q,\omega) = C(\omega)\left[\mathcal{P}\frac{1}{q_{\rm pl}-q} + B\delta(q_{\rm pl}-q) + \frac{1}{q} + \frac{\mathcal{W}(q,\omega)}{q_{\rm pl}}\right] \ . \tag{E.2}$$

Since the last term in Eq. (E.2) is regular at $q = q_{\rm pl}$, it does not affect the asymptotic behavior of the effective interaction at large distances, i.e. for $rq_{\rm pl}(\omega) \gg 1$. We can therefore write

$$\begin{aligned} W_{\rm h}(r \gg q_{\rm pl}^{-1},\omega) &\simeq C(\omega)\int \frac{d\boldsymbol{q}}{(2\pi)^2} e^{i\boldsymbol{q}\cdot\boldsymbol{r}}\left[\mathcal{P}\frac{1}{q_{\rm pl}-q} + B\delta(q_{\rm pl}-q) + \frac{1}{q}\right] \\ &= C(\omega)q_{\rm pl}\left\{\frac{1}{2}\,Y_0(q_{\rm pl}r) + \frac{B}{2\pi}\,J_0(q_{\rm pl}r) + \frac{1}{4}\left[\mathbf{H}_0(q_{\rm pl}r) - Y_0(q_{\rm pl}r)\right]\right\} \ , \end{aligned} \tag{E.3}$$

where $J_0(x)$ and $Y_0(x)$ are the first and second kind Bessel functions and $\mathbf{H}_0(x)$ is the Struve function. The term in square bracket goes to zero like $r^{-1}$ for large $r$, while $J_0(x)$ and $Y_0(x)$ are oscillating functions whose amplitudes decay like $r^{-1/2}$ for large $r$.

The correct combination for an outgoing (ingoing) cylindrical wave is obtained by setting $B = \mp\pi i$, a choice which yields the first (second) Hankel function $H_0^{(1\text{-}2)}(x) = J_0(x) \pm i\, Y_0(x)$. With this choice of $B$ the asymptotic behavior of $W_{\rm h}$ is

$$W_{\rm h}^{(\pm)}(r \gg q_{\rm pl}^{-1},\omega) \simeq \frac{\mp i}{2} q_{\rm pl} C(\omega)\, H_0^{(1\text{-}2)}(q_{\rm pl}r) \simeq \frac{\mp i}{\sqrt{2\pi r}}\sqrt{q_{\rm pl}}C(\omega)e^{\pm i(q_{\rm pl}r - \frac{\pi}{4})} \ , \tag{E.4}$$

where we dropped all terms decaying faster than $r^{-1/2}$ and made use of the asymptotic behavior of Hankel's functions.

If we neglect the correction $\mathcal{W}$, the effective interaction in real space is

$$W_{\rm h}^{(\pm)}(r,\omega) = C(\omega)q_{\rm pl}\left\{\mp\frac{i}{2}\,H_0^{(1\text{-}2)}(q_{\rm pl}r) + \frac{1}{4}\left[\mathbf{H}_0(q_{\rm pl}r) - Y_0(q_{\rm pl}r)\right]\right\} \ . \tag{E.5}$$

## E.2 Real space formulation of the scattering equations

### E.2.1 Geometry in Fig. 3.1(a)

To make a connection between the scattering amplitude $f(\theta_{\boldsymbol{r}}, \theta, \omega)$ and the solutions of the scattering equation in momentum space it is useful to rewrite the latter equation in real space. The real-space version of Eq. (3.133) reads as following:

$$\int d^2\boldsymbol{r}' W_{\rm h}^{-1}(|\boldsymbol{r}-\boldsymbol{r}'|,\omega) V_{\rm sc}(\boldsymbol{r}',\omega) = \frac{1}{S}\int d^2\boldsymbol{r}' \Delta(\boldsymbol{r},\boldsymbol{r}',\omega) V_{\rm sc}(\boldsymbol{r}',\omega)\ , \tag{E.6}$$

while Eq. (3.138) becomes

$$V_{\rm sc}(\boldsymbol{r},\omega) = V^{(0)}(\boldsymbol{r},\omega) + \int d\boldsymbol{r}' W_{\rm h}^{(+)}(|\boldsymbol{r}-\boldsymbol{r}'|,\omega)\frac{1}{S}\int d\boldsymbol{r}'' \Delta(\boldsymbol{r}',\boldsymbol{r}'',\omega) V_{\rm sc}(\boldsymbol{r}'',\omega)\ . \tag{E.7}$$

Since the inhomogeneity is localized in a finite region of space of radius $a$, $\Delta(\boldsymbol{r},\boldsymbol{r}',\omega)$ vanishes if $r$ or $r'$ are bigger than $a$. For $r \gg a, q_{\rm pl}^{-1}$ we can also approximate $|\boldsymbol{r}-\boldsymbol{r}'| \simeq r - \boldsymbol{r}\cdot\boldsymbol{r}'/r$. Setting $V^{(0)}(\boldsymbol{r},\omega) = \exp(i\boldsymbol{q}_{\rm pl}\cdot\boldsymbol{r})$ we obtain

$$\begin{aligned}
V_{\rm sc}(\boldsymbol{r},\omega) &\simeq e^{i\boldsymbol{q}_{\rm pl}\cdot\boldsymbol{r}} + \int_{r'<a} d^2\boldsymbol{r}' W_{\rm h}^{(+)}(r-\hat{\boldsymbol{r}}\cdot\boldsymbol{r}',\omega)\int_{r''<a} d^2\boldsymbol{r}''\frac{1}{S}\Delta(\boldsymbol{r}',\boldsymbol{r}'',\omega)V_{\rm sc}(\boldsymbol{r}'',\omega)\\
&\simeq e^{i\boldsymbol{q}_{\rm pl}\cdot\boldsymbol{r}} - C(\omega)\int_{r'<a} d^2\boldsymbol{r}' \frac{i\sqrt{q_{\rm pl}}}{\sqrt{2\pi r}} e^{i[q_{\rm pl}(r-\hat{\boldsymbol{r}}\cdot\boldsymbol{r}')-\frac{\pi}{4}]}\int_{r''<a} d^2\boldsymbol{r}''\frac{1}{S}\Delta(\boldsymbol{r}',\boldsymbol{r}'',\omega)V_{\rm sc}(\boldsymbol{r}'',\omega)\\
&\simeq e^{i\boldsymbol{q}_{\rm pl}\cdot\boldsymbol{r}} - \frac{\sqrt{q_{\rm pl}}e^{i\frac{\pi}{4}}}{\sqrt{2\pi r}}C(\omega)e^{iq_{\rm pl}r}\int_{r'<a} d^2\boldsymbol{r}' e^{-iq_{\rm pl}\hat{\boldsymbol{r}}\cdot\boldsymbol{r}'}\int_{r''<a} d^2\boldsymbol{r}''\frac{1}{S}\Delta(\boldsymbol{r}',\boldsymbol{r}'',\omega)V_{\rm sc}(\boldsymbol{r}'',\omega)\\
&\simeq e^{i\boldsymbol{q}_{\rm pl}\cdot\boldsymbol{r}} - \frac{\sqrt{q_{\rm pl}}e^{i\frac{\pi}{4}}}{\sqrt{2\pi r}}C(\omega)e^{iq_{\rm pl}r}\int_{r'<a} d^2\boldsymbol{r}' e^{-iq_{\rm pl}\hat{\boldsymbol{r}}\cdot\boldsymbol{r}'}T(\boldsymbol{r}',\theta,\omega)\\
&\simeq e^{i\boldsymbol{q}_{\rm pl}\cdot\boldsymbol{r}} - \frac{\sqrt{q_{\rm pl}}e^{i\frac{\pi}{4}}}{\sqrt{2\pi r}}C(\omega)e^{iq_{\rm pl}r}T(q_{\rm pl}\hat{\boldsymbol{r}},\theta,\omega).
\end{aligned} \tag{E.8}$$

In the second approximate equality we used the asymptotic expression in Eq.(E.4).

Comparing Eq. (3.136) in the main text with the result of Eq. (E.8), we finally obtain Eq. (3.158).

### E.2.2 Geometry in Fig. 3.1(b)

The Lippmann-Schwinger equation for this geometry is

$$V_{\rm sc}(x,\theta,\omega) = V^{(0)}(x,\theta,\omega) + \int dx' W_{\rm h}^{(+)}(x-x', q_{\rm pl}\sin(\theta),\omega)\int\frac{dx''}{L_x}\Delta(x',x'',q_{\rm pl}\sin(\theta),\omega)V_{\rm sc}(x'',\theta,\omega), \tag{E.9}$$

where

$$W_{\rm h}^{(\pm)}(x,q_y,\omega) = \int\frac{dq_x}{2\pi}e^{iq_x x}W_{\rm h}^{(\pm)}(q,\omega)\ , \tag{E.10}$$

with $q$ defined as right after Eq. (3.189), and

$$\begin{aligned}
&W_{\rm h}^{(\pm)}(\sqrt{q_{\rm pl}^2\sin^2(\theta)+q_x^2},\omega) =\\
&= \frac{C(\omega)}{\cos(\theta)}\left[\mathcal{P}\frac{1}{q_{\rm pl}\cos(\theta)+q_x} + \mathcal{P}\frac{1}{q_{\rm pl}\cos(\theta)-q_x} \mp i\pi\delta(q_{\rm pl}\cos(\theta)-q_x) \mp i\pi\delta(q_{\rm pl}\cos(\theta)+q_x)\right]\\
&+ C(\omega)\left[\frac{\sqrt{q_{\rm pl}^2\sin^2(\theta)+q_x^2}-q_{\rm pl}}{q_{\rm pl}^2\cos^2(\theta)-q_x^2} + \frac{1}{\sqrt{q_{\rm pl}^2\sin^2(\theta)+q_x^2}} + \frac{\mathcal{W}\left(\sqrt{q_{\rm pl}^2\sin^2(\theta)+q_x^2},\omega\right)}{q_{\rm pl}}\right]\ .
\end{aligned} \tag{E.11}$$

The asymptotic behavior for $|x| \gg (q_{\rm pl}\cos\theta)^{-1}$ is completely controlled by the divergent terms in the first line. Fourier transforming only this part, we obtain the asymptotic behavior:

$$W_{\rm h}^{(\pm)}(x,q_{\rm pl}\sin(\theta),\omega) \simeq \mp\frac{iC(\omega)}{\cos(\theta)}e^{\pm iq_{\rm pl}\cos(\theta)|x|}\ . \tag{E.12}$$

Using Eq. (E.12) in Eq. (E.9), we finally find:

$$
\begin{aligned}
&V_{\rm sc}(x,\theta,\omega) \simeq \\
&\simeq \begin{cases} e^{iq_{\rm pl}\cos\theta x} - \frac{iC(\omega)}{\cos\theta} e^{iq_{\rm pl}\cos\theta x} \int dx' e^{-iq_{\rm pl}\cos\theta x} \frac{1}{L_x} \int dx'' \Delta(x',x'',q_{\rm pl}\sin\theta,\omega) V_{\rm sc}(x'',\theta,\omega), \;\; x \to +\infty \\ e^{iq_{\rm pl}\cos\theta x} - \frac{iC(\omega)}{\cos\theta} e^{-iq_{\rm pl}\cos\theta x} \int dx' e^{+iq_{\rm pl}\cos\theta x} \frac{1}{L_x} \int dx'' \Delta(x',x'',q_{\rm pl}\sin\theta,\omega) V_{\rm sc}(x'',\theta,\omega), \;\; x \to -\infty \end{cases} \\
&\simeq \begin{cases} e^{iq_{\rm pl}\cos\theta x} \left(1 - \frac{iC(\omega)}{\cos\theta}\right) T(q_{\rm pl}\cos\theta,\theta,\omega), \;\; x \to +\infty \\ e^{iq_{\rm pl}\cos\theta x} - \frac{iC(\omega)}{\cos\theta} T(-q_{\rm pl}\cos\theta,\theta,\omega) e^{-iq_{\rm pl}\cos\theta x}, \;\; x \to -\infty \; . \end{cases}
\end{aligned}
\tag{E.13}
$$

Comparing this result with Eq. (3.137) in the main text, we obtain the desired expressions for the transmission and reflection coefficients listed in Eqs. (3.166) and (3.167).

## E.3 Numerical solution of Eq. 3.165

First of all we introduce dimensionless variables defining

$$t(q,\theta,\omega) \equiv C(\omega) T(qq_{\rm P},\theta,\omega) \; , \tag{E.14}$$

$$u(q,q',\theta,\omega) \equiv C(\omega) U(qq_{\rm P}, q'q_{\rm P}, q_{\rm P}\sin(\theta),\omega) \; , \tag{E.15}$$

$$w(q,\omega) \equiv \frac{q_{\rm P}}{C(\omega)} W^{(+)}_{\rm hom}(q_{\rm P}q,\omega) \; , \tag{E.16}$$

With these substitutions Eq. 3.165 becomes

$$t(q,\theta,\omega) = u(q,\cos(\theta),\theta,\omega) + \frac{1}{2\pi}\int_{-\infty}^{\infty} dq' u(q,q',\theta,\omega) w\left(\sqrt{\sin^2(\theta)+q'^2},\omega\right) t(q',\theta,\omega) \; . \tag{E.17}$$

Given a set of $N+2$ points $q_0 \dots q_{N+1}$ on the real axis we define $N$ basis function as

$$\phi_i(q) = \varphi(q-q_i, q_i - q_{i-1}, q_{i+1} - q_i) \; , \tag{E.18}$$

where $1 \le i \le N$, and the tent function is defined by

$$\varphi(x,\Delta_L,\Delta_R) = \begin{cases} 1 + \frac{x}{\Delta_L} & \text{if} \quad -\Delta_L < x < 0 \\ 1 - \frac{x}{\Delta_R} & \text{if} \quad 0 \le x < \Delta_R \\ 0 & \text{otherwise} \end{cases} \; . \tag{E.19}$$

We now substitute the functions $t$ and $u$ with their piecewise linear approximations on the gird defined by the points $q_i$.

$$t(q,\theta,\omega) = \phi_i(q) t_i(q,\theta,\omega) \; , \tag{E.20}$$

$$u(q,q',\theta,\omega) = \phi_i(q)\phi_j(q') u_{ij}(\theta,\omega) \; . \tag{E.21}$$

The superposition coefficients can be written as

$$u_{ij}(\theta,\omega) = M^{-1}_{ik} M^{-1}_{lj} \int dq \int dq' \phi_k(q)\phi_l(q') u(q,q',\theta,\omega) \approx u(q_i,q_j,\theta,\omega) \; , \tag{E.22}$$

where the overlap matrix of the basis function is

$$M_{ij} = \int dq \phi_i(q)\phi_j(q) \; . \tag{E.23}$$

We obtain the linear system

$$\left[\delta_{jl} - \frac{1}{2\pi} u_{jk} w_{kl}(\theta,\omega)\right] t_l(\theta,\omega) = u_{jk}(\theta,\omega)\phi_k(\cos(\theta)) \; , \tag{E.24}$$

where

$$
\begin{aligned}
w_{kl}(\theta,\omega) &= \int_{-\infty}^{\infty} dq' \phi_k(q') w\left(\sqrt{\sin^2(\theta)+q'^2},\omega\right)\phi_l(q') \\
&= \int_{-\infty}^{\infty} dq' \phi_k(q')\phi_l(q')\Bigg\{ \frac{1+\sqrt{q'^2+\sin^2(\theta)}}{2\cos(\theta)}\left(\frac{\mathcal{P}}{q'+\cos(\theta)} - \frac{\mathcal{P}}{q'-\cos(\theta)}\right) \\
&- \frac{i\pi}{|\cos(\theta)|}\left[\delta(q'-\cos(\theta)+\delta(q'+\cos(\theta))\right] + w_{\mathrm{reg}}\left(\sqrt{q'^2+\sin^2(\theta)},\omega\right)\Bigg\}
\end{aligned}
\tag{E.25}
$$

and we singled out the singular part of the effective interaction

$$
W^{(+)}_{\mathrm{hom}}(q,\omega) = \frac{C(\omega)}{q_{\mathrm{p}}}\left[\mathcal{P}\frac{1}{1-\frac{q}{q_{\mathrm{P}}}} - i\pi\delta\left(1-\frac{q}{q_{\mathrm{P}}}\right)\right] + W_{\mathrm{reg}}(q,\omega)\ . \tag{E.26}
$$

## E.4 Numerical solution of Eq. 3.203

$$
t_{mm'}(q,\omega) \equiv C(\omega) q_{\mathrm{P}} T_{mm'}(q q_{\mathrm{P}},\omega) \tag{E.27}
$$

$$
u_{mm'}(q,q',\omega) \equiv C(\omega) q_{\mathrm{P}} U_{mm'}(q q_{\mathrm{P}}, q' q_{\mathrm{P}},\omega) \tag{E.28}
$$

$$
w(q,\omega) \equiv \frac{q_{\mathrm{P}}}{C(\omega)} W^{(+)}_{\mathrm{hom}}(q_{\mathrm{P}} q,\omega) \tag{E.29}
$$

Following the same steps as in the above section gives

$$
(t_{mm'})_j(\omega) = (u_{mm'})_{jk}(q,\omega)\phi_k(1) + \sum_{n=-\infty}^{\infty} \frac{1}{2\pi}(u_{mn})_{jk}(q,\omega) w_{kl}(\omega)(t_{nm'})_l(\omega) \tag{E.30}
$$

$$
w_{kl}(\omega) = \int_0^{\infty} dq' q' \phi_k(q') w\left(q',\omega\right)\phi_l(q') \tag{E.31}
$$

# Bibliography


[1] K. S. Novoselov, A. K. Geim, S. V. Morozov, D. Jiang, Y. Zhang, S. V. Dubonos, I. V. Grigorieva, and A. A. Firsov, *Electric Field Effect in Atomically Thin Carbon Films*, Science **306**, 666 (2004).

[2] K. S. Novoselov, D. Jiang, F. Schedin, T. J. Booth, V. V. Khotkevich, S. V. Morozov, and A. K. Geim, *Two-dimensional atomic crystals*, Proc. Nat. Acad. Sci. U.S.A. **102**, 10451 (2005).

[3] M. Xu, T. Liang, M. Shi, and H. Chen, *Graphene-Like Two-Dimensional Materials*, Chemical Reviews **113**, 3766 (2013).

[4] A. K. Geim and I. V. Grigorieva, *Van der Waals heterostructures*, Nature **499**, 419 (2013).

[5] K. S. Novoselov, A. Mishchenko, A. Carvalho, and A. H. Castro Neto, *2D materials and van der Waals heterostructures*, Science **353** (2016).

[6] C. Dean, A. F. Young, I. Meric, C. Lee, L. Wang, S. Sorgenfrei, K. Watanabe, T. Taniguchi, P. Kim, K. Shepard, and J. Hone, *Boron nitride substrates for high-quality graphene electronics*, Nature Nanotechnology **5**, 722 (2010).

[7] L. Wang, I. Meric, P. Y. Huang, Q. Gao, Y. Gao, H. Tran, T. Taniguchi, K. Watanabe, L. M. Campos, D. A. Muller, J. Guo, P. Kim, J. Hone, K. L. Shepard, and C. R. Dean, *One-Dimensional Electrical Contact to a Two-Dimensional Material*, Science **342**, 614 (2013).

[8] M. J. M. de Jong and L. W. Molenkamp, *Hydrodynamic electron flow in high-mobility wires*, Phys. Rev. B **51**, 13389 (1995).

[9] R. N. Gurzhi, *Minimum of Resistance in Impurity-free Conductors*, JETP **17**, 521 (1963).

[10] R. N. Gurzhi, *Hydrodynamic effects in solids at low temperature*, Soviet Physics Uspekhi **11**, 255 (1968).

[11] D. A. Bandurin, I. Torre, R. K. Kumar, M. Ben Shalom, A. Tomadin, A. Principi, G. H. Auton, E. Khestanova, K. S. Novoselov, I. V. Grigorieva, L. A. Ponomarenko, A. K. Geim, and M. Polini, *Negative local resistance caused by viscous electron backflow in graphene*, Science **351**, 1055 (2016).

[12] R. Krishna Kumar, D. Bandurin, F. Pellegrino, Y. Cao, A. Principi, H. Guo, G. Auton, M. Ben Shalom, L. Ponomarenko, G. Falkovich, K. Watanabe, T. Taniguchi, I. Grigorieva, L. Levitov, M. Polini, and A. Geim, *Superballistic flow of viscous electron fluid through graphene constrictions*, Nat. Phys. **13**, 1182 (2017).

[13] J. Crossno, J. K. Shi, K. Wang, X. Liu, A. Harzheim, A. Lucas, S. Sachdev, P. Kim, T. Taniguchi, K. Watanabe, T. A. Ohki, and K. C. Fong, *Observation of the Dirac fluid and the breakdown of the Wiedemann-Franz law in graphene*, Science **351**, 1058 (2016).

[14] P. J. W. Moll, P. Kushwaha, N. Nandi, B. Schmidt, and A. P. Mackenzie, *Evidence for hydrodynamic electron flow in PdCoO2*, Science **351**, 1061 (2016).

[15] L. Ju, B. Geng, J. Horng, C. Girit, M. Martin, Z. Hao, H. A. Bechtel, X. Liang, A. Zettl, Y. R. Shen, and F. Wang, *Graphene plasmonics for tunable terahertz metamaterials*, Nature Nanotechnology **6**, 630 (2011).

[16] J. Chen, M. Badioli, P. Alonso-Gonzalez, S. Thongrattanasiri, F. Huth, J. Osmond, M. Spasenovic, A. Centeno, A. Pesquera, P. Godignon, A. Zurutuza Elorza, N. Camara, F. J. G. de Abajo, R. Hillenbrand, and F. H. L. Koppens, *Optical nano-imaging of gate-tunable graphene plasmons*, Nature **487**, 77 (2012).

[17] Z. Fei, A. S. Rodin, G. O. Andreev, W. Bao, A. S. McLeod, M. Wagner, L. M. Zhang, Z. Zhao, M. Thiemens, G. Dominguez, M. M. Fogler, A. H. C. Neto, C. N. Lau, F. Keilmann, and D. N. Basov, *Gate-tuning of graphene plasmons revealed by infrared nano-imaging*, Nature **487**, 82 (2012).

[18] A. Woessner, M. B. Lundeberg, Y. Gao, A. Principi, P. Alonso-González, M. Carrega, K. Watanabe, T. Taniguchi, G. Vignale, M. Polini, J. Hone, R. Hillenbrand, and F. H. L. Koppens, *Highly confined low-loss plasmons in graphene–boron nitride heterostructures*, Nature Materials **14**, 421 (2015).

[19] A. Woessner, Y. Gao, I. Torre, M. B. Lundeberg, C. Tan, K. Watanabe, T. Taniguchi, R. Hillenbrand, J. Hone, M. Polini, and F. H. L. Koppens, *Electrical 2π phase control of infrared light in a 350-nm footprint using graphene plasmons*, Nat. Photon. **11**, 421 (2017).

[20] A. K. Geim and K. S. Novoselov, *The rise of graphene*, Nature Materials **6**, 183 (2007).

[21] L. A. Ponomarenko, A. K. Geim, A. A. Zhukov, R. Jalil, S. V. Morozov, K. S. Novoselov, I. V. Grigorieva, E. H. Hill, V. V. Cheianov, V. I. Fal/'ko, K. Watanabe, T. Taniguchi, and R. V. Gorbachev, *Tunable metal-insulator transition in double-layer graphene heterostructures*, Nat Phys **7**, 958 (2011).

[22] S. J. Haigh, A. Gholinia, R. Jalil, S. Romani, L. Britnell, D. C. Elias, K. S. Novoselov, L. A. Ponomarenko, A. K. Geim, and R. Gorbachev, *Cross-sectional imaging of individual layers and buried interfaces of graphene-based heterostructures and superlattices*, Nat Mater **11**, 764 (2012).

[23] A. H. Castro Neto, F. Guinea, N. M. R. Peres, K. S. Novoselov, and A. K. Geim, *The electronic properties of graphene*, Rev. Mod. Phys. **81**, 109 (2009).

[24] C. Lee, X. Wei, J. W. Kysar, and J. Hone, *Measurement of the Elastic Properties and Intrinsic Strength of Monolayer Graphene*, Science **321**, 385 (2008).

[25] A. A. Balandin, S. Ghosh, W. Bao, I. Calizo, D. Teweldebrhan, F. Miao, and C. N. Lau, *Superior Thermal Conductivity of Single-Layer Graphene*, Nano Letters **8**, 902 (2008).

[26] L. A. Falkovsky and S. S. Pershoguba, *Optical far-infrared properties of a graphene monolayer and multilayer*, Phys. Rev. B **76**, 153410 (2007).

[27] D. S. L. Abergel and V. I. Fal'ko, *Optical and magneto-optical far-infrared properties of bilayer graphene*, Phys. Rev. B **75**, 155430 (2007).

[28] L. A. Falkovsky, *Optical properties of graphene*, Journal of Physics: Conference Series **129**, 012004 (2008).

[29] N. M. R. Peres, *Colloquium: The transport properties of graphene: An introduction*, Rev. Mod. Phys. **82**, 2673 (2010).

[30] D. N. Basov, M. M. Fogler, A. Lanzara, F. Wang, and Y. Zhang, *Colloquium: Graphene spectroscopy*, Rev. Mod. Phys. **86**, 959 (2014).

[31] V. N. Kotov, B. Uchoa, V. M. Pereira, F. Guinea, and A. H. Castro Neto, *Electron-Electron Interactions in Graphene: Current Status and Perspectives*, Rev. Mod. Phys. **84**, 1067 (2012).

[32] S. Reich, J. Maultzsch, C. Thomsen, and P. Ordejón, *Tight-binding description of graphene*, Phys. Rev. B **66**, 035412 (2002).

[33] J. C. Slater and G. F. Koster, *Simplified LCAO Method for the Periodic Potential Problem*, Phys. Rev. **94**, 1498 (1954).

[34] A. Bostwick, T. Ohta, J. L. McChesney, T. Seyller, K. Horn, and E. Rotenberg, *Renormalization of graphene bands by many-body interactions*, Solid State Communications **143**, 63 (2007).

[35] G. F. Giuliani and G. Vignale, *Quantum Theory of the Electron Liquid*, Cambridge University Press, Cambridge (2005).

[36] M. C. Lemme, T. J. Echtermeyer, M. Baus, and H. Kurz, *A Graphene Field-Effect Device*, IEEE Electron Device Letters **28**, 282 (2007).

[37] J. Xia, F. Chen, J. Li, and N. Tao, *Measurement of the quantum capacitance of graphene*, Nat Nano **4**, 505 (2009).

[38] L. Britnell, R. V. Gorbachev, R. Jalil, B. D. Belle, F. Schedin, A. Mishchenko, T. Georgiou, M. I. Katsnelson, L. Eaves, S. V. Morozov, N. M. R. Peres, J. Leist, A. K. Geim, K. S. Novoselov, and L. A. Ponomarenko, *Field-Effect Tunneling Transistor Based on Vertical Graphene Heterostructures*, Science **335**, 947 (2012).

[39] F. Parhizgar, A. Qaiumzadeh, and R. Asgari, *Quantum capacitance of double-layer graphene*, Phys. Rev. B **96**, 075447 (2017).

[40] J. Martin, N. Akerman, G. Ulbricht, T. Lohmann, J. H. Smet, K. von Klitzing, and A. Yacoby, *Observation of electron-hole puddles in graphene using a scanning single-electron transistor*, Nature Physics **4**, 144 (2008).

[41] A. S. Mayorov, D. C. Elias, I. S. Mukhin, S. V. Morozov, L. A. Ponomarenko, K. S. Novoselov, A. K. Geim, and R. V. Gorbachev, *How Close Can One Approach the Dirac Point in Graphene Experimentally?*, Nano Letters **12**, 4629 (2012).

[42] A. Lucas, J. Crossno, K. C. Fong, P. Kim, and S. Sachdev, *Transport in inhomogeneous quantum critical fluids and in the Dirac fluid in graphene*, Phys. Rev. B **93**, 075426 (2016).

[43] B. Wunsch, T. Stauber, F. Sols, and F. Guinea, *Dynamical polarization of graphene at finite doping*, New Journal of Physics **8**, 318 (2006).

[44] A. Principi, M. Polini, and G. Vignale, *Linear response of doped graphene sheets to vector potentials*, Phys. Rev. B **80**, 075418 (2009).

[45] N. D. Mermin, *Lindhard Dielectric Function in the Relaxation-Time Approximation*, Phys. Rev. B **1**, 2362 (1970).

[46] P. F. Maldague, *Many-body corrections to the polarizability of the two-dimensional electron gas*, Surface Science **73**, 296 (1978).

[47] M. B. Lundeberg, Y. Gao, R. Asgari, C. Tan, B. Van Duppen, M. Autore, P. Alonso-González, A. Woessner, K. Watanabe, T. Taniguchi, R. Hillenbrand, J. Hone, M. Polini, and F. H. L. Koppens, *Tuning quantum nonlocal effects in graphene plasmonics*, Science **357**, 187 (2017).

[48] D. C. Elias, R. R. Nair, T. M. G. Mohiuddin, S. V. Morozov, P. Blake, M. P. Halsall, A. C. Ferrari, D. W. Boukhvalov, M. I. Katsnelson, A. K. Geim, and K. S. Novoselov, *Control of Graphene's Properties by Reversible Hydrogenation: Evidence for Graphane*, Science **323**, 610 (2009).

[49] J. T. Robinson, J. S. Burgess, C. E. Junkermeier, S. C. Badescu, T. L. Reinecke, F. K. Perkins, M. K. Zalalutdniov, J. W. Baldwin, J. C. Culbertson, P. E. Sheehan, and E. S. Snow, *Properties of Fluorinated Graphene Films*, Nano Letters **10**, 3001 (2010).

[50] A. N. Grigorenko, M. Polini, and K. S. Novoselov, *Graphene plasmonics*, Nat Photon **6**, 749 (2012).

[51] K. Watanabe, T. Taniguchi, and H. Kanda, *Direct-bandgap properties and evidence for ultraviolet lasing of hexagonal boron nitride single crystal*, Nature Materials **3**, 404 (2004).

[52] R. Geick, C. H. Perry, and G. Rupprecht, *Normal Modes in Hexagonal Boron Nitride*, Phys. Rev. **146**, 543 (1966).

[53] Y. Cai, L. Zhang, Q. Zeng, L. Cheng, and Y. Xu, *Infrared reflectance spectrum of BN calculated from first principles*, Solid State Communications **141**, 262 (2007).

[54] J. D. Caldwell, A. V. Kretinin, Y. Chen, V. Giannini, M. M. Fogler, Y. Francescato, C. T. Ellis, J. G. Tischler, C. R. Woods, A. J. Giles, M. Hong, K. Watanabe, T. Taniguchi, S. A. Maier, and K. S. Novoselov, *Sub-diffractional volume-confined polaritons in the natural hyperbolic material hexagonal boron nitride*, Nature Communications **5**, 5221 (2014).

[55] A. Kumar, T. Low, K. H. Fung, P. Avouris, and N. X. Fang, *Tunable Light–Matter Interaction and the Role of Hyperbolicity in Graphene–hBN System*, Nano Letters **15**, 3172 (2015).

[56] K. F. Mak, C. Lee, J. Hone, J. Shan, and T. F. Heinz, *Atomically Thin* $MoS_2$*: A New Direct-Gap Semiconductor*, Phys. Rev. Lett. **105**, 136805 (2010).

[57] B. Radisavljevic, A. Radenovic, J. Brivio, V. Giacometti, and A. Kis, *Single-layer MoS2 transistors*, Nature Nanotechnology **6**, 147 (2011).

[58] K. F. Mak, K. He, C. Lee, G. H. Lee, J. Hone, T. F. Heinz, and J. Shan, *Tightly bound trions in monolayer MoS2*, Nat Mater **12**, 207 (2013).

[59] H. Zeng, J. Dai, W. Yao, D. Xiao, and X. Cui, *Valley polarization in MoS2 monolayers by optical pumping*, Nature Nanotechnology **7**, 490 (2012).

[60] K. F. Mak, K. He, J. Shan, and T. F. Heinz, *Control of valley polarization in monolayer MoS2 by optical helicity*, Nature Nanotechnology **7**, 494 (2012).

[61] K. F. Mak, K. L. McGill, J. Park, and P. L. McEuen, *The valley Hall effect in MoS2 transistors*, Science **344**, 1489 (2014).

[62] L. Li, Y. Yu, G. J. Ye, Q. Ge, X. Ou, H. Wu, D. Feng, X. H. Chen, and Y. Zhang, *Black phosphorus field-effect transistors*, Nature Nanotechnology **9**, 372 (2014).

[63] H. Liu, A. T. Neal, Z. Zhu, Z. Luo, X. Xu, D. Tomanek, and P. D. Ye, *Phosphorene: An Unexplored 2D Semiconductor with a High Hole Mobility*, ACS Nano **8**, 4033 (2014).

[64] A. N. Rudenko and M. I. Katsnelson, *Quasiparticle band structure and tight-binding model for single- and bilayer black phosphorus*, Phys. Rev. B **89**, 201408 (2014).

[65] J. Qiao, X. Kong, Z.-X. Hu, F. Yang, and W. Ji, *High-mobility transport anisotropy and linear dichroism in few-layer black phosphorus*, Nat. Comm. **5**, 4475 (2014).

[66] C. Gong, L. Li, Z. Li, H. Ji, A. Stern, Y. Xia, T. Cao, W. Bao, C. Wang, Y. Wang, Z. Q. Qiu, R. J. Cava, S. G. Louie, J. Xia, and X. Zhang, *Discovery of intrinsic ferromagnetism in two-dimensional van der Waals crystals*, Nature **546**, 265 (2017).

[67] B. Huang, G. Clark, E. Navarro-Moratalla, D. R. Klein, R. Cheng, K. L. Seyler, D. Zhong, E. Schmidgall, M. A. McGuire, D. H. Cobden, W. Yao, D. Xiao, P. Jarillo-Herrero, and X. Xu, *Layer-dependent ferromagnetism in a van der Waals crystal down to the monolayer limit*, Nature **546**, 270 (2017).

[68] N. D. Mermin and H. Wagner, *Absence of Ferromagnetism or Antiferromagnetism in One- or Two-Dimensional Isotropic Heisenberg Models*, Phys. Rev. Lett. **17**, 1133 (1966).

[69] R. V. Gorbachev, A. K. Geim, M. I. Katsnelson, K. S. Novoselov, T. Tudorovskiy, I. V. Grigorieva, A. H. MacDonald, S. V. Morozov, K. Watanabe, T. Taniguchi, and L. A. Ponomarenko, *Strong Coulomb drag and broken symmetry in double-layer graphene*, Nat Phys **8**, 896 (2012).

[70] A. Avsar, J. Y. Tan, T. Taychatanapat, J. Balakrishnan, G. K. W. Koon, Y. Yeo, J. Lahiri, A. Carvalho, A. S. Rodin, E. C. T. O'Farrell, G. Eda, A. H. Castro Neto, and B. Özyilmaz, *Spin-orbit proximity effect in graphene*, Nature Communications **5**, 4875 (2014).

[71] H. B. Heersche, P. Jarillo-Herrero, J. B. Oostinga, L. M. Vandersypen, and A. F. Morpurgo, *Induced superconductivity in graphene*, Solid State Communications **143**, 72 (2007).

[72] Z. Wang, C. Tang, R. Sachs, Y. Barlas, and J. Shi, *Proximity-Induced Ferromagnetism in Graphene Revealed by the Anomalous Hall Effect*, Phys. Rev. Lett. **114**, 016603 (2015).

[73] L. Landau and E. M. Lifshitz, *Course of Theoretical Physics: Fluid Mechanics*, Pergamon, New York (1987).

[74] L. Landau and E. M. Lifshitz, *Course of Theoretical Physics: Physical Kinetics*, Pergamon, New York (1981).

[75] M. Dyakonov and M. Shur, *Shallow water analogy for a ballistic field effect transistor: New mechanism of plasma wave generation by dc current*, Phys. Rev. Lett. **71**, 2465 (1993).

[76] M. I. Dyakonov and M. S. Shur, *Choking of electron flow: A mechanism of current saturation in field-effect transistors*, Phys. Rev. B **51**, 14341 (1995).

[77] M. Dyakonov and M. Shur, *Detection, Mixing and Frequency Multiplication of Terahertz Radiation by Two Dimensional Electronic Fluid*, IEEE Transactions on Electronic Devices **43**, 380 (1996).

[78] M. Dyakonov and M. Shur, *Plasma Wave Electroics: Novel Terahertz Devices using Two Dimensional Electron Fluid*, IEEE Transactions on Electronic Devices **43**, 1640 (1996).

[79] A. O. Govorov and J. J. Heremans, *Hydrodynamic Effects in Interacting Fermi Electron Jets*, Phys. Rev. Lett. **92**, 026803 (2004).

[80] M. Müller and S. Sachdev, *Collective cyclotron motion of the relativistic plasma in graphene*, Phys. Rev. B **78**, 115419 (2008).

[81] M. Müller, J. Schmalian, and L. Fritz, *Graphene: A Nearly Perfect Fluid*, Phys. Rev. Lett. **103**, 025301 (2009).

[82] R. Bistritzer and A. H. MacDonald, *Hydrodynamic theory of transport in doped graphene*, Phys. Rev. B **80**, 085109 (2009).

[83] A. V. Andreev, S. A. Kivelson, and B. Spivak, *Hydrodynamic Description of Transport in Strongly Correlated Electron Systems*, Phys. Rev. Lett. **106**, 256804 (2011).

[84] M. Mendoza, H. J. Herrmann, and S. Succi, *Preturbulent Regimes in Graphene Flow*, Phys. Rev. Lett. **106**, 156601 (2011).

[85] M. Mendoza, H. J. Herrmann, and S. Succi, *Hydrodynamic Model for Conductivity in Graphene*, Sci. Rep. **3** (2013).

[86] D. Svintsov, V. Vyurkov, S. Yurchenko, T. Otsuji, and V. Ryzhii, *Hydrodynamic model for electron-hole plasma in graphene*, Journal of Applied Physics **111**, 083715 (2012).

[87] B. N. Narozhny, I. V. Gornyi, M. Titov, M. Schütt, and A. D. Mirlin, *Hydrodynamics in graphene: Linear-response transport*, Phys. Rev. B **91**, 035414 (2015).

[88] U. Briskot, M. Schütt, I. V. Gornyi, M. Titov, B. N. Narozhny, and A. D. Mirlin, *Collision-dominated nonlinear hydrodynamics in graphene*, Phys. Rev. B **92**, 115426 (2015).

[89] B. N. Narozhny, I. V. Gornyi, A. D. Mirlin, and J. Schmalian, *Hydrodynamic Approach to Electronic Transport in Graphene*, Ann. Phys. page 1700043 (2017).

[90] A. Tomadin and M. Polini, *Theory of the plasma-wave photoresponse of a gated graphene sheet*, Phys. Rev. B **88**, 205426 (2013).

[91] A. Tomadin, G. Vignale, and M. Polini, *Corbino Disk Viscometer for 2D Quantum Electron Liquids*, Phys. Rev. Lett. **113**, 235901 (2014).

[92] A. Lucas, *Stokes paradox in electronic Fermi liquids*, Phys. Rev. B **95**, 115425 (2017).

[93] G. F. Giuliani and J. J. Quinn, *Lifetime of a quasiparticle in a two-dimensional electron gas*, Phys. Rev. B **26**, 4421 (1982).

[94] A. A. Abrikosov and I. M. Khalatnikov, *The theory of a fermi liquid (the properties of liquid 3 He at low temperatures)*, Reports on Progress in Physics **22**, 329 (1959).

[95] A. S. Mayorov, R. V. Gorbachev, S. V. Morozov, L. Britnell, R. Jalil, L. A. Ponomarenko, P. Blake, K. S. Novoselov, K. Watanabe, T. Taniguchi, and A. K. Geim, *Micrometer-Scale Ballistic Transport in Encapsulated Graphene at Room Temperature*, Nano Letters **11**, 2396 (2011).

[96] I. Torre, A. Tomadin, A. K. Geim, and M. Polini, *Nonlocal transport and the hydrodynamic shear viscosity in graphene*, Phys. Rev. B **92**, 165433 (2015).

[97] L. Molenkamp and M. de Jong, *Observation of Knudsen and Gurzhi transport regimes in a two-dimensional wire*, Solid-State Electronics **37**, 551 (1994).

[98] L. W. Molenkamp and M. J. M. de Jong, *Electron-electron-scattering-induced size effects in a two-dimensional wire*, Phys. Rev. B **49**, 5038 (1994).

[99] M. Knudsen, *Die Gesetze der Molekularströmung und der inneren Reibungsströmung der Gase durch Röhren*, Ann. Phys. **333**, 75 (1909).

[100] L. Pfeiffer and K. West, *The role of MBE in recent quantum Hall effect physics discoveries*, Physica E: Low-dimensional Systems and Nanostructures **20**, 57 (2003).

[101] M. J. Manfra, *Molecular Beam Epitaxy of Ultra-High-Quality AlGaAs/GaAs Heterostructures: Enabling Physics in Low-Dimensional Electronic Systems*, Annual Review of Condensed Matter Physics **5**, 347 (2014).

[102] A. Principi, G. Vignale, M. Carrega, and M. Polini, *Bulk and shear viscosities of the two-dimensional electron liquid in a doped graphene sheet*, Phys. Rev. B **93**, 125410 (2016).

[103] D. A. Abanin, S. V. Morozov, L. A. Ponomarenko, R. V. Gorbachev, A. S. Mayorov, M. I. Katsnelson, K. Watanabe, T. Taniguchi, K. S. Novoselov, L. S. Levitov, and A. K. Geim, *Giant Nonlocality Near the Dirac Point in Graphene*, Science **332**, 328 (2011).

[104] F. M. D. Pellegrino, I. Torre, A. K. Geim, and M. Polini, *Electron hydrodynamics dilemma: Whirlpools or no whirlpools*, Phys. Rev. B **94**, 155414 (2016).

[105] M. Beconcini, S. Valentini, R. K. Kumar, G. H. Auton, A. K. Geim, L. A. Ponomarenko, M. Polini, and F. Taddei, *Scaling approach to tight-binding transport in realistic graphene devices: The case of transverse magnetic focusing*, Phys. Rev. B **94**, 115441 (2016).

[106] J. C. W. Song and L. S. Levitov, *Energy-Driven Drag at Charge Neutrality in Graphene*, Phys. Rev. Lett. **109**, 236602 (2012).

[107] C. W. J. Beenakker and H. van Houten, *Quantum Transport in Semiconductor Nanostructures*, Solid State Physics **44**, 1 (1991).

[108] Y. V. Sharvin, *A Possible Method for Studying Fermi Surfaces*, JETP **21**, 655 (1965).

[109] H. Guo, E. Ilseven, G. Falkovich, and L. Levitov, *Stokes Paradox, Back Reflections and Interaction-Enhanced Conduction*, ArXiv e-prints (2016).

[110] H. Guo, E. Ilseven, G. Falkovich, and L. S. Levitov, *Higher-than-ballistic conduction of viscous electron flows*, Proc. Nat. Acad. Sci. U.S.A **114**, 3068 (2017).

[111] M. Müller, L. Fritz, and S. Sachdev, *Quantum-critical relativistic magnetotransport in graphene*, Phys. Rev. B **78**, 115406 (2008).

[112] L. Fritz, J. Schmalian, M. Müller, and S. Sachdev, *Quantum critical transport in clean graphene*, Phys. Rev. B **78**, 085416 (2008).

[113] M. Müller, L. Fritz, S. Sachdev, and J. Schmalian, *Relativistic magnetotransport in graphene*, AIP Conference Proceedings **1134**, 170 (2009).

[114] M. Müller, J. Schmalian, and L. Fritz, *Graphene: A Nearly Perfect Fluid*, Phys. Rev. Lett. **103**, 025301 (2009).

[115] R. Franz and G. Wiedemann, *Ueber die Wärme-Leitungsfähigkeit der Metalle*, Annalen der Physik **165**, 497 (1853).

[116] A. Principi and G. Vignale, *Violation of the Wiedemann-Franz Law in Hydrodynamic Electron Liquids*, Phys. Rev. Lett. **115**, 056603 (2015).

[117] C. W. Hicks, A. S. Gibbs, A. P. Mackenzie, H. Takatsu, Y. Maeno, and E. A. Yelland, *Quantum Oscillations and High Carrier Mobility in the Delafossite* $PdCoO_2$, Phys. Rev. Lett. **109**, 116401 (2012).

[118] H.-J. Noh, J. Jeong, J. Jeong, E.-J. Cho, S. B. Kim, K. Kim, B. I. Min, and H.-D. Kim, *Anisotropic Electric Conductivity of Delafossite* $PdCoO_2$ *Studied by Angle-Resolved Photoemission Spectroscopy*, Phys. Rev. Lett. **102**, 256404 (2009).

[119] D. Pines and P. Nozières, *The Theory of Quantum Liquids*, W. A. Benjamin Inc., New York (1963).

[120] A. Sommerfeld, *Ueber die Fortpflanzung elektrodynamischer Wellen längs eines Drahtes*, Ann. Phys. **303**, 233 (1899).

[121] A. Otto, *Excitation of nonradiative surface plasma waves in silver by the method of frustrated total reflection*, Z. Phys. A **216**, 398 (1968).

[122] E. Kretschmann and H. Raether, *Radiative Decay of Non Radiative Surface Plasmons Excited by Light*, Z. Naturforsch. Teil A **23**, 2135 (1968).

[123] C. F. Hirjibehedin, A. Pinczuk, B. S. Dennis, L. N. Pfeiffer, and K. W. West, *Evidence of electron correlations in plasmon dispersions of ultralow density two-dimensional electron systems*, Phys. Rev. B **65**, 161309 (2002).

[124] R. H. Ritchie, *Plasma Losses by Fast Electrons in Thin Films*, Phys. Rev. **106**, 874 (1957).

[125] C. C. Grimes and G. Adams, *Observation of Two-Dimensional Plasmons and Electron-Ripplon Scattering in a Sheet of Electrons on Liquid Helium*, Phys. Rev. Lett. **36**, 145 (1976).

[126] D. B. Mast, A. J. Dahm, and A. L. Fetter, *Observation of Bulk and Edge Magnetoplasmons in a Two-Dimensional Electron Fluid*, Phys. Rev. Lett. **54**, 1706 (1985).

[127] A. L. Fetter, *Edge magnetoplasmons in a bounded two-dimensional electron fluid*, Phys. Rev. B **32**, 7676 (1985).

[128] A. L. Fetter, *Edge magnetoplasmons in a two-dimensional electron fluid confined to a half-plane*, Phys. Rev. B **33**, 3717 (1986).

[129] G. Eliasson, J.-W. Wu, P. Hawrylak, and J. Quinn, *Magnetoplasma modes of a spatially periodic two-dimensional electron gas*, Solid State Communications **60**, 41 (1986).

[130] V. A. Volkov and S. A. Mikhailov, *Edge magnetoplasmons: low frequency weakly damped excitations in inhomogeneous two-dimensional electron systems*, Sov. Phys.-JETP **67**, 1639 (1988).

[131] X. Xia and J. J. Quinn, *Multipole edge plasmons of two-dimensional electron-gas systems*, Phys. Rev. B **50**, 8032 (1994).

[132] X. Xia and J. J. Quinn, *Edge magnetoplasmons of two-dimensional electron-gas systems*, Phys. Rev. B **50**, 11187 (1994).

[133] R. F. Oulton, V. J. Sorger, T. Zentgraf, R.-M. Ma, C. Gladden, L. Dai, G. Bartal, and X. Zhang, *Plasmon lasers at deep subwavelength scale*, Nature **461**, 629 (2009).

[134] J. N. Anker, W. P. Hall, O. Lyandres, N. C. Shah, J. Zhao, and R. P. Van Duyne, *Biosensing with plasmonic nanosensors*, Nat Mater **7**, 442 (2008).

[135] A. V. Akimov, A. Mukherjee, C. L. Yu, D. E. Chang, A. S. Zibrov, P. R. Hemmer, H. Park, and M. D. Lukin, *Generation of single optical plasmons in metallic nanowires coupled to quantum dots*, Nature **450**, 402 (2007).

[136] S. A. Maier, *Plasmonics: Fundamentals and Applications*, Springer, New York (2007).

[137] F. H. L. Koppens, D. E. Chang, and F. J. García de Abajo, *Graphene plasmonics: a platform for strong light–matter interactions*, Nano letters **11**, 3370 (2011).

[138] P. A. D. Gonçalves and N. M. R. Peres, *An Introduction to Graphene Plasmonics*, World Scientific, Singapore (2016).

[139] M. Jablan, H. Buljan, and M. Soljačić, *Plasmonics in graphene at infrared frequencies*, Phys. Rev. B **80**, 245435 (2009).

[140] S. Thongrattanasiri, F. H. L. Koppens, and F. J. García de Abajo, *Complete Optical Absorption in Periodically Patterned Graphene*, Phys. Rev. Lett. **108**, 047401 (2012).

[141] A. Y. Nikitin, F. Guinea, F. J. Garcia-Vidal, and L. Martin-Moreno, *Surface plasmon enhanced absorption and suppressed transmission in periodic arrays of graphene ribbons*, Phys. Rev. B **85**, 081405 (2012).

[142] L. Vicarelli, M. S. Vitiello, D. Coquillat, A. Lombardo, A. C. Ferrari, W. Knap, M. Polini, V. Pellegrini, and A. Tredicucci, *Graphene field-effect transistors as room-temperature terahertz detectors*, Nat Mater **11**, 865 (2012).

[143] E. H. Hwang and S. Das Sarma, *Dielectric function, screening, and plasmons in two-dimensional graphene*, Phys. Rev. B **75**, 205418 (2007).

[144] H. Yan, T. Low, W. Zhu, Y. Wu, M. Freitag, X. Li, F. Guinea, P. Avouris, and F. Xia, *Damping pathways of mid-infrared plasmons in graphene nanostructures*, Nat Photon **7**, 394 (2013).

[145] A. Principi, G. Vignale, M. Carrega, and M. Polini, *Impact of disorder on Dirac plasmon losses*, Phys. Rev. B **88**, 121405 (2013).

[146] E. H. Hwang, R. Sensarma, and S. Das Sarma, *Plasmon-phonon coupling in graphene*, Phys. Rev. B **82**, 195406 (2010).

[147] A. Principi, M. Carrega, M. B. Lundeberg, A. Woessner, F. H. L. Koppens, G. Vignale, and M. Polini, *Plasmon losses due to electron-phonon scattering: The case of graphene encapsulated in hexagonal boron nitride*, Phys. Rev. B **90**, 165408 (2014).

[148] A. Principi, G. Vignale, M. Carrega, and M. Polini, *Intrinsic lifetime of Dirac plasmons in graphene*, Phys. Rev. B **88**, 195405 (2013).

[149] A. Vakil and N. Engheta, *Transformation Optics Using Graphene*, Science **332**, 1291 (2011).

[150] L. Wu, H. S. Chu, W. S. Koh, and E. P. Li, *Highly sensitive graphene biosensors based on surface plasmon resonance*, Opt. Express **18**, 14395 (2010).

[151] D. Rodrigo, O. Limaj, D. Janner, D. Etezadi, F. J. García de Abajo, V. Pruneri, and H. Altug, *Mid-infrared plasmonic biosensing with graphene*, Science **349**, 165 (2015).

[152] T. Low, A. Chaves, J. D. Caldwell, A. Kumar, N. X. Fang, P. Avouris, T. F. Heinz, F. Guinea, L. Martin-Moreno, and F. Koppens, *Polaritons in layered two-dimensional materials*, Nat Mater **16**, 182 (2017).

[153] Y. V. Bludov, A. Ferreira, N. M. R. Peres, and M. I. Vasilevskiy, *A primer on surface plasmon-polaritons in graphene*, International Journal of Modern Physics B **27**, 1341001 (2013).

[154] S. A. Mikhailov and K. Ziegler, *New Electromagnetic Mode in Graphene*, Phys. Rev. Lett. **99**, 016803 (2007).

[155] S. G. Menabde, D. R. Mason, E. E. Kornev, C. Lee, and N. Park, *Direct optical probing of transverse electric mode in graphene*, Scientific reports **6**, 21523 (2016).

[156] N. Peres, Y. V. Bludov, A. Ferreira, and M. I. Vasilevskiy, *Exact solution for square-wave grating covered with graphene: surface plasmon-polaritons in the terahertz range*, Journal of Physics: Condensed Matter **25**, 125303 (2013).

[157] P. Alonso-González, A. Y. Nikitin, F. Golmar, A. Centeno, A. Pesquera, S. Vélez, J. Chen, G. Navickaite, F. Koppens, A. Zurutuza, F. Casanova, L. E. Hueso, and R. Hillenbrand, *Controlling graphene plasmons with resonant metal antennas and spatial conductivity patterns*, Science **344**, 1369 (2014).

[158] A. Woessner, P. Alonso-González, M. B. Lundeberg, Y. Gao, J. E. Barrios-Vargas, G. Navickaite, Q. Ma, D. Janner, K. Watanabe, A. W. Cummings, T. Taniguchi, V. Pruneri, S. Roche, P. Jarillo-Herrero, J. Hone, R. Hillenbrand, and F. H. L. Koppens, *Near-field photocurrent nanoscopy on bare and encapsulated graphene*, Nature Communications **7**, 10783 (2016).

[159] A. Y. Nikitin, P. Alonso-González, S. Vélez, S. Mastel, A. Centeno, A. Pesquera, A. Zurutuza, F. Casanova, L. E. Hueso, F. H. L. Koppens, and R. Hillenbrand, *Real-space mapping of tailored sheet and edge plasmons in graphene nanoresonators*, Nature Photonics **10**, 239 (2016).

[160] P. Alonso-González, A. Y. Nikitin, Y. Gao, A. Woessner, M. B. Lundeberg, A. Principi, N. Forcellini, W. Yan, S. Vélez, A. J. Huber, K. Watanabe, T. Taniguchi, F. Casanova, L. E. Hueso, M. Polini, J. Hone, F. H. L. Koppens, and R. Hillenbrand, *Acoustic terahertz graphene plasmons revealed by photocurrent nanoscopy*, Nat. Nanotech. **12**, 31 (2017).

[161] C. Hoyos and D. T. Son, *Hall Viscosity and Electromagnetic Response*, Phys. Rev. Lett. **108**, 066805 (2012).

[162] A. Cortijo, Y. Ferreirós, K. Landsteiner, and M. A. H. Vozmediano, *Visco elasticity in 2D materials*, 2D Materials **3**, 011002 (2016).

[163] B. Bradlyn, M. Goldstein, and N. Read, *Kubo formulas for viscosity: Hall viscosity, Ward identities, and the relation with conductivity*, Phys. Rev. B **86**, 245309 (2012).

[164] T. Scaffidi, N. Nandi, B. Schmidt, A. P. Mackenzie, and J. E. Moore, *Hydrodynamic Electron Flow and Hall Viscosity*, Phys. Rev. Lett. **118**, 226601 (2017).

[165] D. T. Son and A. O. Starinets, *Viscosity, Black Holes, and Quantum Field Theory*, Annual Review of Nuclear and Particle Science **57**, 95 (2007).

[166] P. K. Kovtun, D. T. Son, and A. O. Starinets, *Viscosity in Strongly Interacting Quantum Field Theories from Black Hole Physics*, Phys. Rev. Lett. **94**, 111601 (2005).

[167] T. Schäfer and D. Teaney, *Nearly perfect fluidity: from cold atomic gases to hot quark gluon plasmas*, Reports on Progress in Physics **72**, 126001 (2009).

[168] B. V. Jacak and B. Müller, *The Exploration of Hot Nuclear Matter*, Science **337**, 310 (2012).

[169] C. Cao, E. Elliott, J. Joseph, H. Wu, J. Petricka, T. Schäfer, and J. E. Thomas, *Universal Quantum Viscosity in a Unitary Fermi Gas*, Science **331**, 58 (2011).

[170] E. Elliott, J. A. Joseph, and J. E. Thomas, *Anomalous Minimum in the Shear Viscosity of a Fermi Gas*, Phys. Rev. Lett. **113**, 020406 (2014).

[171] S. Cremonini, *The shear viscosity to entropy ratio: A status report*, Modern Physics Letters B **25**, 1867 (2011).

[172] M. Katsnelson, *Graphene: Carbon in Two Dimensions*, Cambridge University Press, Cambridge (2012).

[173] G. E. H. Reuter and E. H. Sondheimer, *The theory of the anomalous skin effect in metals*, Proc. R. Soc. London A **195**, 336 (1948).

[174] L. Levitov and G. Falkovich, *Electron viscosity, current vortices and negative nonlocal resistance in graphene*, Nature Physics **12**, 672 (2016).

[175] S. Conti and G. Vignale, *Elasticity of an electron liquid*, Phys. Rev. B **60**, 7966 (1999).

[176] A. Lucas, *Hydrodynamic transport in strongly coupled disordered quantum field theories*, New Journal of Physics **17**, 113007 (2015).

[177] I. Torre, A. Tomadin, R. Krahne, V. Pellegrini, and M. Polini, *Electrical plasmon detection in graphene waveguides*, Phys. Rev. B **91**, 081402 (2015).

[178] A. Levchenko, H.-Y. Xie, and A. V. Andreev, *Viscous magnetoresistance of correlated electron liquids*, Phys. Rev. B **95**, 121301 (2017).

[179] G. Falkovich and L. Levitov, *Linking Spatial Distributions of Potential and Current in Viscous Electronics*, Phys. Rev. Lett. **119**, 066601 (2017).

[180] T. V. Phan, J. C. W. Song, and L. S. Levitov, *Ballistic Heat Transfer and Energy Waves in an Electron System*, ArXiv e-prints (2013).

[181] S. Selberherr, *Analysis and Simulation of Semiconductor Devices*, Springer-Verlag/Wien, Wien (1984).

[182] D. Vasileska and S. Goodnick, *Computational Electronics*, Morgan & Claypool, USA (2006).

[183] J. E. Avron, R. Seiler, and P. G. Zograf, *Viscosity of Quantum Hall Fluids*, Phys. Rev. Lett. **75**, 697 (1995).

[184] I. V. Tokatly and G. Vignale, *Lorentz shear modulus of a two-dimensional electron gas at high magnetic field*, Phys. Rev. B **76**, 161305 (2007).

[185] I. V. Tokatly and G. Vignale, *Lorentz shear modulus of fractional quantum Hall states*, Journal of Physics: Condensed Matter **21**, 275603 (2009).

[186] N. Read, *Non-Abelian adiabatic statistics and Hall viscosity in quantum Hall states and $p_x + ip_y$ paired superfluids*, Phys. Rev. B **79**, 045308 (2009).

[187] N. Read and E. H. Rezayi, *Hall viscosity, orbital spin, and geometry: Paired superfluids and quantum Hall systems*, Phys. Rev. B **84**, 085316 (2011).

[188] F. D. M. Haldane, *Geometrical Description of the Fractional Quantum Hall Effect*, Phys. Rev. Lett. **107**, 116801 (2011).

[189] M. Sherafati, A. Principi, and G. Vignale, *Hall viscosity and electromagnetic response of electrons in graphene*, Phys. Rev. B **94**, 125427 (2016).

[190] P. S. Alekseev, *Negative Magnetoresistance in Viscous Flow of Two-Dimensional Electrons*, Phys. Rev. Lett. **117**, 166601 (2016).

[191] M. S. Steinberg, *Viscosity of the Electron Gas in Metals*, Phys. Rev. **109**, 1486 (1958).

[192] T. Taychatanapat, K. Watanabe, T. Taniguchi, and P. Jarillo-Herrero, *Electrically tunable transverse magnetic focusing in graphene*, Nat Phys **9**, 225 (2013).

[193] F. M. D. Pellegrino, I. Torre, and M. Polini, *Nonlocal transport and the Hall viscosity of two-dimensional hydrodynamic electron liquids*, Phys. Rev. B **96**, 195401 (2017).

[194] L. V. Delacretaz and A. Gromov, *Transport signatures of Hall viscosity*, arXiv preprint arXiv:1706.03773 (2017).

[195] D. N. Basov, M. M. Fogler, and F. J. García de Abajo, *Polaritons in van der Waals materials*, Science **354** (2016).

[196] D. N. Basov and M. M. Fogler, *Plasmonic imaging is gaining momentum*, Science **357**, 132 (2017).

[197] J. L. Garcia-Pomar, A. Y. Nikitin, and L. Martin-Moreno, *Scattering of Graphene Plasmons by Defects in the Graphene Sheet*, ACS Nano **7**, 4988 (2013).

[198] B.-Y. Jiang, G. X. Ni, C. Pan, Z. Fei, B. Cheng, C. N. Lau, M. Bockrath, D. N. Basov, and M. M. Fogler, *Tunable Plasmonic Reflection by Bound 1D Electron States in a 2D Dirac Metal*, Phys. Rev. Lett. **117**, 086801 (2016).

[199] I. Torre, M. I. Katsnelson, A. Diaspro, V. Pellegrini, and M. Polini, *Lippmann-Schwinger theory for two-dimensional plasmon scattering*, Phys. Rev. B **96**, 035433 (2017).

[200] Z. Fei, A. S. Rodin, W. Gannett, S. Dai, W. Regan, M. Wagner, M. K. Liu, A. S. McLeod, G. Dominguez, M. Thiemens, A. H. Castro Neto, F. Keilmann, A. Zettl, R. Hillenbrand, M. M. Fogler, and D. N. Basov, *Electronic and plasmonic phenomena at graphene grain boundaries*, Nat. Nanotech **8**, 821 (2013).

[201] Z. Fei, G.-X. Ni, B.-Y. Jiang, M. M. Fogler, and D. N. Basov, *Nanoplasmonic Phenomena at Electronic Boundaries in Graphene*, ACS Photonics **4**, 2971 (2017).

[202] B.-Y. Jiang, G.-X. Ni, Z. Addison, J. K. Shi, X. Liu, S. Y. F. Zhao, P. Kim, E. J. Mele, D. N. Basov, and M. M. Fogler, *Plasmon Reflections by Topological Electronic Boundaries in Bilayer Graphene*, Nano Letters **17**, 7080 (2017).

[203] J. Chen, M. L. Nesterov, A. Y. Nikitin, S. Thongrattanasiri, P. Alonso-González, T. M. Slipchenko, F. Speck, M. Ostler, T. Seyller, I. Crassee, F. H. L. Koppens, L. Martin-Moreno, F. J. García de Abajo, A. B. Kuzmenko, and R. Hillenbrand, *Strong Plasmon Reflection at Nanometer-Size Gaps in Monolayer Graphene on SiC*, Nano Letters **13**, 6210 (2013).

[204] J. C. W. Song and M. S. Rudner, *Chiral plasmons without magnetic field*, Proc. Nat. Acad. Sci. U.S.A. **113**, 4658 (2016).

[205] J. C. W. Song and M. A. Kats, *Giant Hall Photoconductivity in Narrow-Gapped Dirac Materials*, Nano Letters **16**, 7346 (2016).

[206] A. Principi, M. I. Katsnelson, and G. Vignale, *Edge Plasmons in Two-Component Electron Liquids in the Presence of Pseudomagnetic Fields*, Phys. Rev. Lett. **117**, 196803 (2016).

[207] A. Principi, R. Asgari, and M. Polini, *Acoustic plasmons and composite hole-acoustic plasmon satellite bands in graphene on a metal gate*, Solid State Communications **151**, 1627 (2011).

[208] B. Noble, *Methods based on the Wiener-Hopf technique for the solution of partial differential equations*, Chelsea Pub. Co., New York (1988).

[209] B. Rejaei and A. Khavasi, *Scattering of surface plasmons on graphene by a discontinuity in surface conductivity*, Journal of Optics **17**, 075002 (2015).

[210] S. Farajollahi, B. Rejaei, and A. Khavasi, *Reflection and transmission of obliquely incident graphene plasmons by discontinuities in surface conductivity: observation of the Brewster-like effect*, Journal of Optics **18**, 075005 (2016).

[211] A. V. Shchegrov, I. V. Novikov, and A. A. Maradudin, *Scattering of Surface Plasmon Polaritons by a Circularly Symmetric Surface Defect*, Phys. Rev. Lett. **78**, 4269 (1997).

[212] J. A. Sánchez-Gil and A. A. Maradudin, *Near-field and far-field scattering of surface plasmon polaritons by one-dimensional surface defects*, Phys. Rev. B **60**, 8359 (1999).

[213] A. Y. Nikitin, F. López-Tejeira, and L. Martín-Moreno, *Scattering of surface plasmon polaritons by one-dimensional inhomogeneities*, Phys. Rev. B **75**, 035129 (2007).

[214] G. Brucoli and L. Martín-Moreno, *Comparative study of surface plasmon scattering by shallow ridges and grooves*, Phys. Rev. B **83**, 045422 (2011).

[215] D. K. Efimkin, Y. E. Lozovik, and A. A. Sokolik, *Collective excitations on a surface of topological insulator*, Nanoscale Research Letters **7**, 163 (2012).

[216] B. K. Ishmukhametov, *Collective Oscillations of Atomic Electrons in the Statistical Theory of Atoms*, physica status solidi (b) **45**, 669 (1971).

[217] B. K. Ishmukhametov and K. M. I., Fiz. Met. Metalloved **40**, 736 (1975).

[218] J. J. Sakurai, *Modern Quantum Mechanics*, Addison-Wesley, New York (1994).

[219] S. H. Abedinpour, G. Vignale, A. Principi, M. Polini, W.-K. Tse, and A. H. MacDonald, *Drude weight, plasmon dispersion, and ac conductivity in doped graphene sheets*, Phys. Rev. B **84**, 045429 (2011).

[220] T. Ando, A. B. Fowler, and F. Stern, *Electronic properties of two-dimensional systems*, Rev. Mod. Phys. **54**, 437 (1982).

[221] A. Tomadin, A. Principi, J. C. W. Song, L. S. Levitov, and M. Polini, *Accessing Phonon Polaritons in Hyperbolic Crystals by Angle-Resolved Photoemission Spectroscopy*, Phys. Rev. Lett. **115**, 087401 (2015).

[222] C. A. Ullrich and G. Vignale, *Time-dependent current-density-functional theory for the linear response of weakly disordered systems*, Phys. Rev. B **65**, 245102 (2002).

[223] F. Stern, *Polarizability of a Two-Dimensional Electron Gas*, Phys. Rev. Lett. **18**, 546 (1967).

[224] F. M. Dickey, *Laser Beam Shaping: Theory and Techniques*, CRC Press.

[225] J. B. Pendry, D. Schurig, and D. R. Smith, *Controlling Electromagnetic Fields*, Science **312**, 1780 (2006).

[226] J. Sun, E. Timurdogan, A. Yaacobi, E. S. Hosseini, and M. R. Watts, *Large-scale nanophotonic phased array*, Nature **493**, 195 (2013).

[227] N. Yu and F. Capasso, *Flat optics with designer metasurfaces*, Nat Mater **13**, 139 (2014).

[228] M. Takeda, H. Ina, and S. Kobayashi, *Fourier-transform method of fringe-pattern analysis for computer-based topography and interferometry*, J. Opt. Soc. Am. **72**, 156 (1982).

[229] G. T. Reed, G. Mashanovich, F. Y. Gardes, and D. J. Thomson, *Silicon optical modulators*, Nat Photon **4**, 518 (2010).

[230] K. Liu, C. R. Ye, S. Khan, and V. J. Sorger, *Review and perspective on ultrafast wavelength-size electro-optic modulators*, Laser & Photonics Reviews **9**, 172 (2015).

[231] A. V. Kildishev, A. Boltasseva, and V. M. Shalaev, *Planar Photonics with Metasurfaces*, Science **339** (2013).

[232] J. A. Dionne, K. Diest, L. A. Sweatlock, and H. A. Atwater, *PlasMOStor: A Metal−Oxide−Si Field Effect Plasmonic Modulator*, Nano Letters **9**, 897 (2009).

[233] M. Mohsin, D. Neumaier, D. Schall, M. Otto, C. Matheisen, A. Lena Giesecke, A. A. Sagade, and H. Kurz, *Experimental verification of electro-refractive phase modulation in graphene*, Sci. Rep. **5**, 10967 (2015).

[234] Z. Sun, A. Martinez, and F. Wang, *Optical modulators with 2D layered materials*, Nat Photon **10**, 227 (2016).

[235] P. L. Phillips, J. C. Knight, J. M. Pottage, G. Kakarantzas, and P. S. J. Russell, *Direct measurement of optical phase in the near field*, Applied Physics Letters **76**, 541 (2000).

[236] M. L. M. Balistreri, J. P. Korterik, L. Kuipers, and N. F. van Hulst, *Local Observations of Phase Singularities in Optical Fields in Waveguide Structures*, Phys. Rev. Lett. **85**, 294 (2000).

[237] Z. Li, K. Yao, F. Xia, S. Shen, J. Tian, and Y. Liu, *Graphene Plasmonic Metasurfaces to Steer Infrared Light*, Sci. Rep. **5**, 12423 (2015).

[238] A. Huber, N. Ocelic, D. Kazantsev, and R. Hillenbrand, *Near-field imaging of mid-infrared surface phonon polariton propagation*, Applied Physics Letters **87**, 081103 (2005).

[239] M. Born and E. Wolf, *Principles of Optics*, Cambridge University Press, Cambridge (1999).

[240] M.-H. Liu, *Theory of carrier density in multigated doped graphene sheets with quantum correction*, Phys. Rev. B **87**, 125427 (2013).

[241] M. Polini, R. Asgari, G. Borghi, Y. Barlas, T. Pereg-Barnea, and A. H. MacDonald, *Plasmons and the spectral function of graphene*, Phys. Rev. B **77**, 081411 (2008).

[242] C. Haffner, W. Heni, Y. Fedoryshyn, J. Niegemann, A. Melikyan, D. L. Elder, B. Baeuerle, Y. Salamin, A. Josten, U. Koch, C. Hoessbacher, F. Ducry, L. Juchli, A. Emboras, D. Hillerkuss, M. Kohl, L. R. Dalton, C. Hafner, and J. Leuthold, Nat. Photonics **9**, 525 (2015).

[243] W. M. J. Green, M. J. Rooks, L. Sekaric, and Y. A. Vlasov, *Ultra-compact, low RF power, 10 Gb/s silicon Mach-Zehnder modulator*, Opt. Express **15**, 17106 (2007).

[244] A. Hosseini, X. Xu, H. Subbaraman, C.-Y. Lin, S. Rahimi, and R. T. Chen, *Large optical spectral range dispersion engineered silicon-based photonic crystal waveguide modulator*, Opt. Express **20**, 12318 (2012).

[245] D. Xiao, M.-C. Chang, and Q. Niu, *Berry phase effects on electronic properties*, Rev. Mod. Phys. **82**, 1959 (2010).

[246] G. Sundaram and Q. Niu, *Wave-packet dynamics in slowly perturbed crystals: Gradient corrections and Berry-phase effects*, Phys. Rev. B **59**, 14915 (1999).

[247] D. J. Thouless, M. Kohmoto, M. P. Nightingale, and M. den Nijs, *Quantized Hall Conductance in a Two-Dimensional Periodic Potential*, Phys. Rev. Lett. **49**, 405 (1982).

[248] A. Srivastava and A. m. c. Imamoğlu, *Signatures of Bloch-Band Geometry on Excitons: Nonhydrogenic Spectra in Transition-Metal Dichalcogenides*, Phys. Rev. Lett. **115**, 166802 (2015).

[249] J. Zhou, W.-Y. Shan, W. Yao, and D. Xiao, *Berry Phase Modification to the Energy Spectrum of Excitons*, Phys. Rev. Lett. **115**, 166803 (2015).

[250] L.-k. Shi and J. C. W. Song, *Plasmon geometric phase and plasmon Hall shift*, ArXiv e-prints (2017).

[251] J. Sabio, J. Nilsson, and A. H. Castro Neto, *$f$-sum rule and unconventional spectral weight transfer in graphene*, Phys. Rev. B **78**, 075410 (2008).